

AD A068514

DDC FILE COPY



LEVEL III

8031697

014521  
P

*Preliminary Reports, Memoranda  
and Technical Notes of the  
Materials Research Council  
Summer Conference*

*La Jolla, California*



July 1978

This document has been approved  
for public release and sale; its  
distribution is unlimited.

Sponsored by  
Defense Advanced Research Projects Agency  
ARPA Order No. 2341/6

Department of Materials and Metallurgical Engineering

79 04 17 056

6

12

PRELIMINARY REPORTS, MEMORANDA AND TECHNICAL NOTES  
of the

MATERIALS RESEARCH COUNCIL SUMMER CONFERENCE,  
La Jolla, California,

11 July 1978

12 306p.

DDC  
REF ID: A651179  
MAY 11 1979  
C

DARPA Order Number: 2341/6  
Program Code Number: 8D10

Contractor: The Regents of The University of Michigan

Effective Date of Contract: 30 June 1978

Contract Expiration Date: 30 June 1979

Amount of Contract: \$300,000

Contract Number: MDA03-76C-0250, DARPA Order-2341  
Principal Investigator: Associate Dean Maurice J. Sinnott

10 College of Engineering  
The University of Michigan  
Ann Arbor, Michigan 48109  
(313) 763-0242

This document has been approved  
for public release and sale; its  
distribution is unlimited.

407 222

LB

The views and conclusions contained in this document are those of the authors and should not be interpreted as necessarily representing the official policies, either expressed or implied, of the Defense Advanced Research Projects Agency or the U.S. Government.

## TABLE OF CONTENTS

- I. Foreword
- II. Steering Committee
- III. Participants
- IV. Guest Consultants
- V. Preliminary Reports, Memoranda and Technical Notes

The following papers fall into two categories; (1) papers in a state ready for publication, and (2) reports and memoranda for limited distribution representing work in progress. The former category is available for general distribution and in some cases are in the process of publication in the appropriate technical journals. The limited distribution reports and memoranda represent initial ideas, problem suggestions, position papers, and status reports and are aimed primarily to stimulate discussion with the Council. However, they are available subject to the author's release by request to the Project Director.

<u>TITLE</u>	<u>PAGE</u>
Report of a Meeting on Fundamentals of Cohesion, Adsorption and the Strength of Material Interfaces A. G. Evans, J. P. Hirth and J. R. Rice . . . . .	1
Progress and Opportunities in RSR E. E. Hucke . . . . .	19
Potential Application of Rapid Solidification Metallurgy to Small, High-Performance Turbine Rotors M. Cohen. . . . .	24
Liquid Metal Electron and Ion Sources R. Gomer. . . . .	26
Dynamic Elastic Crack Tip Stresses and Displacements for Computing Fracture F. A. McClintock. . . . .	67
Shock Front Propagation and the Stability of Imploding Surfaces J. J. Gilman. . . . .	99

Access Number	Volume	Section	<input type="checkbox"/>
N.S.	1	Section	<input type="checkbox"/>
DOC	2	Section	<input type="checkbox"/>
UNANNO. NO. 9	3	Section	<input type="checkbox"/>
JUSTIFICATION			
BY			
DISTRIB. HIGHWAY AGENCY COSTS			
SPECIAL			
Date			

*free*

*A*

<u>TITLE</u>	<u>PAGE</u>
On the Kink Mode of Failure of Fiber Reinforced Composites D. C. Drucker and A. G. Evans . . . . .	104
On the Thermodynamics of Adsorption at Interfaces As It Influences Decohesion J. P. Hirth and J. R. Rice. . . . .	108
Contact Problems in Ceramic Components A. G. Evans and F. A. McClintock. . . . .	131
High Temperature Cavity Growth in Ceramics A. G. Evans . . . . .	141
Use of Nuclear Magnetic Resonance to Measure Cooling Rates in Rapidly Solidified Metals H. Reiss. . . . .	167
Damage Thresholds in Ceramics Caused By Water Drop Impact A. G. Evans . . . . .	193
A Remark on Some Reported Measurements of the Viscosity of Water at Very High Pressures G. H. Vineyard. . . . .	214
Source Monochromaticity Considerations for Optical Interferometry Amnon Yariv . . . . .	220
Method for Measuring Shock Front Risetimes J. J. Gilman and A. Yariv . . . . .	236
Acoustic Waveguides for Undersea Acoustic Detectors and Transmitters G. S. Kino. . . . .	240
The Pressure Sensitivity of a Clad Optical Fiber B. Budiansky, D. C. Drucker, G. S. Kino & J. R. Rice. .	250
Three Dimensional VLSI Devices G. S. Kino. . . . .	262
A Proposed Technique for Measurements of Imminent Failures in Ceramic Turbines in Operation G. S. Kino. . . . .	271
Covalent Bonded Metals R. L. Coble . . . . .	273

<u>TITLE</u>	<u>PAGE</u>
Design of High Current Brushes J. L. Margrave. . . . .	275
A Chemical Interpretation of the Effect of Oxygen Additions to CF <sub>4</sub> in Plasma-Etching of Silicon, Silicon Oxides or Silicon Nitrides J. L. Margrave. . . . .	277
Extension of Fiber Sensor Response to Extremely High Frequencies H. Winsor . . . . .	281
First Principles Band Theoretic and Pair Potential Calculations of Theoretical Tensile Stress - Abstract H. Ehrenreich . . . . .	287
As Technologies Approach Their Limit - Abstract E. W. Montroll. . . . .	288
The Relation Between Imaging, Tomography and Far Field Inversion Techniques - Abstract G. S. Kino. . . . .	289

### Foreword

This collection of papers does not constitute a formal reporting of the activities of the DARPA Materials Research Council Summer Conference. Each report, memoranda or technical note is a draft of the author or authors and is their work alone. The Steering Committee, in conjunction with the authors, will decide how this material can best be presented as a formal report to DARPA.

Steering Committee

Professor Willis H. Flygare  
Secretary of the Steering Committee  
Department of Chemistry  
University of Illinois  
Urbana, Illinois 61801

Professor Bernard Budiansky  
Division of Engineering and Applied Science  
Harvard University  
Cambridge, Massachusetts 02138

Professor Morris Cohen  
Department of Materials Science and Engineering  
Massachusetts Institute of Technology  
Cambridge, Massachusetts 02139

Dr. John J. Gilman, Director  
Materials Research Center  
Allied Chemical Corporation  
Morristown, New Jersey 07960

Professor Paul L. Richards  
Department of Physics  
University of California  
Berkeley, California 94720

Dr. Robb M. Thomson  
National Bureau of Standards  
Office of Programs  
Washington, D.C. 20234

Professor Amnon Yariv  
Electrical Engineering Department  
California Institute of Technology  
Pasadena, California 91125

Project Director

Associate Dean Maurice J. Sinnott  
College of Engineering  
The University of Michigan  
Ann Arbor, Michigan 48109

Participants

Professor Nico Bloembergen  
Division of Engineering and Applied Physics  
Harvard University  
Cambridge, Massachusetts 02138

Professor Robert Coble  
Materials Science Department  
Massachusetts Institute of Technology  
Cambridge, Massachusetts 02139

Dean Daniel C. Drucker  
Engineering College  
University of Illinois  
Urbana, Illinois 61801

Professor Henry Ehrenreich  
Harvard University  
Cambridge, Massachusetts 02138

Professor Anthony G. Evans  
Materials Department  
University of California  
Berkeley, California 94720

Professor Robert Gomer  
James Franck Institute  
University of Chicago  
Chicago, Illinois 60637

Professor Alan J. Heeger  
Department of Physics  
University of Pennsylvania  
Philadelphia, Pennsylvania 19104

Professor John P. Hirth  
Metallurgical Engineering Department  
Ohio State University  
Columbus, Ohio 43201

Professor Gordon S. Kino  
Microwave Laboratory  
Stanford University  
Stanford, California 94305

Professor Walter Kohn  
Department of Physics  
University of California  
La Jolla, California 92037

Professor James A. Krumhansl  
Department of Physics  
Cornell University  
Ithaca, New York 14850

Professor John L. Margrave  
Department of Chemistry  
Rice University  
Houston, Texas 77001

Professor Frank A. McClintock  
Department of Mechanical Engineering  
Massachusetts Institute of Technology  
Cambridge, Massachusetts 02139

Professor Elliott W. Montroll  
Department of Physics and Astronomy  
University of Rochester  
Rochester, New York 14534

Professor Howard Reiss  
Department of Chemistry  
University of California  
Los Angeles, California 90024

Professor James R. Rice  
Division of Engineering  
Brown University  
Providence, Rhode Island 02912

Dr. George H. Vineyard  
Brookhaven National Laboratory  
Upton, Long Island, New York 11973

GUEST CONSULTANTS

Farid F. Abraham  
IBM Research Lab  
M33/281  
San Jose, CA

Daniel E. Altman  
U.S. NOSC  
Bldg. 33, Code 8115  
San Diego, CA 92152

Robert J. Asaro  
Brown University  
Barus & Holley  
Providence, RI 02912

Neil Ashcroft  
LASSP  
Cornell University  
Clark Hall  
Ithaca, NY 14853

Marvin E. Backman  
Naval Weapons Center  
Code 3831  
China Lake, CA 93555

Willi Baginski  
Staff Engineer  
Litton Industries  
Woodland Hills, CA 91364

Robert R. Baker  
Ford Motor Company  
E3172, Sci. Res. Lab.  
Dearborn, MI 48121

John F. Barnes  
Los Alamos Scientific Lab  
Mail Stop 210  
Los Alamos, NM 87545

Michael K. Barnoski  
Hughes Research Labs  
3011 Malibu Canyon Rd.  
Malibu, CA 92065

James C. Beetle  
U.S. Army ARRADCOM  
Bldg. 355, Rm. 25  
Dover, NJ 07801

Arden L. Bement  
Materials Sciences Office  
DARPA  
1400 Wilson Blvd.  
Arlington, VA 22209

Larry Bertholf  
Sandia Labs  
Division 5162  
Albuquerque, NM 87185

Arthur Bienenstock  
Dept. of Materials Science  
Stanford University  
Stanford, CA 94305

J. V. Biggers  
Pennsylvania State University  
Materials Research Lab  
University Park, PA 16802

J. E. Blue  
Naval Research Lab  
P.O. Box 8337  
Orlando, FL 32806

Joseph A. Bucaro  
Naval Research Lab  
Code 8113  
Washington, DC 20375

Michael J. Buckley  
Materials Sciences Office  
DARPA  
1400 Wilson Blvd.  
Arlington, VA 22209

W. Murray Bullis  
National Bureau of Standards  
Tech A353  
Washington, DC 20234

James W. Butler  
Naval Research Lab  
Code 6670  
Washington, DC 20375

Rowland M. Cannon, Jr.  
Massachusetts Inst. Technology  
Room 13-4026  
Cambridge, MA 02139

Brice Carnahan  
Chemical Engineering Dept.  
The University of Michigan  
Ann Arbor, MI 48109

Pallab Chatterjee  
Texas Instruments, Inc.  
MS 134, Box 225936  
Dallas, TX 75265

Joseph Chovan  
General Electric Company  
Bldg. 3, Electronics Park  
Syracuse, NY

Rodney J. Clifton  
Brown University  
Div. of Engineering  
Providence, RI 02912

Arthur R. Cox  
Suprv. Advanced Materials Tech.  
Pratt & Whitney Aircraft  
P.O. Box 2691  
West Palm Beach, FL 33402

L. E. Cross  
Materials Research Lab  
Pennsylvania State University  
University Park, PA 16802

Roger E. Dewanes  
Rockwell International  
Science Center  
P.O. Box 1085  
Thousand Oaks, CA 91360

John E. Donovan  
Naval Research Lab  
P.O. Box 8337  
Orlando, FL 32856

Wilfred Dukes  
Bell Aerospace Company  
New Orleans, LA

Fred Eisen  
Rockwell International  
Science Center  
P.O. Box 1085  
Thousand Oaks, CA 91360

Larry L. Fehrenbacher  
Asst. to Chief Scientist  
Air Force Systems Command  
AFSC1DLZ Andrews AFB  
Washington, DC 20334

Trangott E. Fischer  
Exxon Research Engineering Co.  
P.O. Box 45  
Linden, NY 07036

G. Richard Fowles  
Washington State University  
Phys. Science 948-B  
Pullman, WA 99164

Edward Fuller  
National Bureau of Standards  
Room A355, Bldg. 223  
Washington, DC 20234

Michael N. Gardos  
Tech. Group Leader  
Hughes Aircraft Company  
Bldg. 6/D-133  
Culver City, CA 90230

Richard Gentilman  
Raytheon Company  
Research Division  
Waltham, MA 02154

Thomas Giallorenzi  
NRL  
Code 5572  
Washington, DC

Henry C. Graham  
Air Force Materials Lab  
AFML/LLM  
Wright Patterson AFB  
Ohio 45433

Don Groves  
NAS  
JH406  
Washington, DC 20418

Pradeep K. Gupta  
Program Manager  
Mechanical Technology, Inc.  
968 Albany-Shaker Rd.  
Latham, NY

H. Tracy Hall  
Brigham Young University  
Room 26, B-41  
Provo, UT 84601

Robert J. Hansen  
Naval Research Lab  
Code 8441  
Washington, DC 20375

John Harper  
AiResearch Manufacturing Co.  
503-4  
Phoenix, AZ 85034

Joe N. Harris  
Georgia Institute of Technology  
Hinman Research Bldg.  
Atlanta, GA 30332

Ralph J. Harrison  
AMMRC  
Bldg. 292  
Watertown, MA 02172

Edward W. Hart  
Cornell University  
228 Bard Hall  
Ithaca, NY 14853

Peter Havstad  
Ford Motor Company  
Scientific Research  
Dearborn, MI 48121

Walter Herrmann  
Sandia Labs  
Dept. 5160  
Albuquerque, NM 87185

Richard G. Hoagland  
Battelle Columbus Labs  
505 King Avenue  
Columbus, OH 43201

Paul R. Holiday  
Project Metallurgist  
Pratt & Whitney Aircraft  
Government Products Division  
West Palm Beach, FL 33402

Tim James  
Engineering Department  
University of California  
Santa Barbara, CA 93017

Leif Johansson  
SSRL  
SLAC, Bin 69  
P.O. Box 4349  
Stanford, CA 94305

R. N. Katz  
AMMRC  
Bldg. 313N  
Watertown, MA 02172

Bernard H. Kear  
Senior Consulting Scientist  
United Technologies Res. Ctr.  
Silver Lane  
East Hartford, CT 06108

R. D. Ketchpel  
Rockwell International  
Science Center  
P.O. Box 1085  
Thousand Oaks, CA 91360

R. W. Keyes  
IBM Research  
P.O. Box 218  
Yorktown Hgts., NY

Albert S. Kobayashi  
University of Washington  
MEB 261  
Seattle, WA 98195

G. Edward Kuhl  
USAF  
AFML/LPO  
Wright-Patterson AFB  
OH 45433

John W. Kury  
3575 Blackhawk Rd.  
Danville, CA

F. F. Lange  
Rockwell International  
Science Center  
P.O. Box 1085  
Thousand Oaks, CA 91360

U. S. Lindholm  
Southwest Research Institute  
San Antonio, TX 78231

H. L. Luo  
Applied Physics & Information  
Science (C-014)  
University of California  
La Jolla, CA 92093

Peter Mannerling  
La Jolla Institute  
McKellar Plaza  
La Jolla, CA 92037

Frank Markarian  
Naval Weapons Center  
China Lake, CA

David A. Matuska  
Air Force Armaments Lab  
DLJW  
Elgin AFB, FL 32542

John H. Mattingly  
Naval Air Systems Command  
JP2, Rm. 812, Code 53621C  
Washington, DC 20361

Bobby D. McConnell  
Technical Area Manager  
Air Force Materials Lab  
B-56  
Wright-Patterson AFB  
OH 45433

T. C. McGill  
California Institute of Tech.  
M.S. 116-81  
Pasadena, CA 91125

A. M. McLean  
Ford Motor Company  
Engineering & Research Staff  
Dearborn, MI 48121

Charles J. McMahon, Jr.  
University of Pennsylvania  
205 LRSM-K1  
Philadelphia, PA 19104

I. R. McNab  
Westinghouse  
Research & Development Ctr.  
Pittsburgh, PA 15235

John T. Mendel  
Hughes Aircraft Company  
Torrance, CA

John F. Mescall  
U.S. Army ARRADCOM  
Bldg. 350  
Dover, NJ 07821

Kenneth A. Meyer  
LASL  
MS 232  
Los Alamos, NM 87544

P. A. Miles  
Raytheon Company  
Bedford, MA

John R. Miner  
Technology Manager  
Mechanical Components and  
Systems Programs  
Pratt & Whitney Aircraft  
P.O. Box 2691  
West Palm Beach, FL 33402

F. Milstein  
Dept. Mechanical Engineering  
University of California  
Santa Barbara, CA 93106

Joseph B. Moore  
Director  
Materials Technology & Control  
Pratt & Whitney Aircraft  
P.O. Box 2691  
West Palm Beach, FL 33402

Solomon Musikant  
General Electric Company  
3198 Chestnut Street  
Philadelphia, PA 19101

Robert Newnham  
Pennsylvania State University  
Materials Research Lab  
University Park, PA 16802

Douglas Pinnow  
Hughes Research Labs  
Bldg. 250, Room 2100  
Malibu, CA 92152

Robert Pohanka  
Naval Research Lab/ONR  
Code G361  
Washington, DC 20375

H. Posen  
USAF/RADC-Deputy For  
Electronic Technology  
Solid State Sciences  
Bedford, MA 01731

G. M. Pound  
Materials Science Dept.  
Stanford University  
Stanford, CA 94305

Rishi Raj  
Cornell University  
Bard Hall  
Ithaca, NY 14853

Glen Randers-Pehrson  
U.S. Army ARRADCOM  
Bldg. 350  
Dover, NJ 07821

Howard Rast  
Naval Ocean Systems Center  
NOSC, Bldg. A-4, Room 128  
San Diego, CA 92152

Roy Rice  
Naval Research Lab  
404-42 Code 6360  
Washington, DC 20375

Richard Reynolds  
Materials Sciences Office  
DARPA  
1400 Wilson Blvd.  
Arlington, VA 22209

Don Roy  
Coors Porcelain Company  
600 Ninth St.  
Golden, CO 80415

Arthur L. Ruoff  
Cornell University  
230 Bard Hall  
Ithaca, NY 14853

Eugene L. Rusert  
McDonnell Douglas  
Astronautics Company  
P.O. Box 516  
E457, Bldg. HQ M.S. 24  
St. Louis, MO 63133

S. C. Sanday  
Naval Research Lab  
Washington, DC 20375

R. L. Seliger  
Hughes Research Labs  
3011 Malibu Canyon Rd.  
Malibu, CA 90265

David M. Sharp  
LASL  
P.O. Box 1663  
Los Alamos, NM 87544

D. A. Shockey  
SRI International  
Menlo Park, CA 94025

L. B. Sibley  
Manager, Tribology Projects  
SKF Industries, Inc.  
1100 First Avenue  
King of Prussia, PA 19406

Glen A. Slack  
General Electric Company  
Schenectady, NY 12302

Harold Sliney  
Lubricants Research Section  
NASA Lewis Research Center  
M5 23-2  
21000 Brookpark Rd.  
Cleveland, OH 44135

Henry I. Smith  
MIT, Lincoln Lab  
E-145  
P.O. Box 73  
Lexington, MA 02173

Wallace A. Smith  
Philips Labs  
345 Scarborough Rd.  
Briarcliff Manor, NY 10510

F. Blake Wallace  
Garrett  
111 S. 36th St.  
Phoenix, AZ 85034

Richard M. Spriggs  
Lehigh University  
Alumni Memorial Bldg. 27  
Bethlehem, PA 18015

Philip Weinberg  
Materials Engineer  
Naval Air Systems Command  
AIR-52032E  
Washington, DC 20361

C. Martin Stickley  
Dept. of Energy  
Washington, DC 20545

Harry V. Winsor  
Materials Science Office  
DARPA  
1400 Wilson Blvd.  
Arlington, VA 22209

B. R. Suydam  
Los Alamos Scientific Lab  
MS 233  
Los Alamos, NM 87545

T. W. Wright  
Ballistic Research Lab  
Aberdeen Proving Ground  
MD 21005

Lewis R. Swank  
Ford Motor Company  
E3172 Sci. Lab  
P.O. Box 2053  
Dearborn, MI 48121

Paul Wynblatt  
Ford Motor Company  
S-2046 Research Lab Bldg.  
P.O. Box 2053  
Dearborn, MI 48121

R. J. Talham  
General Electric Company  
FRP-1-A5  
Syracuse, NY

T. Yonushonis  
AiResearch Manufacturing Co.  
93-393-503-4Y  
Phoenix, AZ 85034

Norman M. Tallan  
Air Force Materials Lab  
AFML/LL  
Wright-Patterson AFB  
Dayton, OH

Larry F. Thompson  
Bell Telephone Labs  
6F225-600 Mountain Ave.  
Murray Hill, NJ 07954

Dennis J. Viechnicki  
AMMRC  
Watertown, MA 02172

V. Vitek  
Dept. of Metallurgy and  
Materials Science  
University of Pennsylvania  
Philadelphia, PA 19104

REPORT OF A MEETING ON FUNDAMENTALS OF COHESION,  
ADSORPTION AND THE STRENGTH OF MATERIAL INTERFACES

A. G. Evans, J. P. Hirth and J. R. Rice

ABSTRACT

A 2½ day conference on the title subject was held during the July 1978 meeting of the MRC. The 17 presentations were divided among three sessions with the following titles:

(i) Atomistic calculations of cohesive properties of lattices and interfaces; (ii) Adsorption, cohesion of interfaces, and fracture processes; and (iii) Diffusive processes of grain boundary cavitation at elevated temperatures. The full meeting report includes the program, list of participants, and a summary of important points drawn from the presentations, together with a list of research needs.

REPORT OF A MEETING ON FUNDAMENTALS OF COHESION,  
ADSORPTION AND THE STRENGTH OF MATERIAL INTERFACES

A. G. Evans, J. P. Hirth and J. R. Rice

INTRODUCTION

A meeting on the title subject was held during the July 1978 MRC meeting. Presentations were divided into sessions on:

- I. Atomistic calculations of cohesive properties of lattices and interfaces;
- II. Adsorption, cohesion of interfaces, and fracture processes; and
- III. Diffusive processes of grain boundary cavitation at elevated temperature.

The list of participants (in addition to MRC members) and the meeting program are attached as Appendices. In the following three sections we list important points that emerged from presentations in each of the three areas, and also list some research needs in each area.

I. Atomistic Calculations of Cohesive Properties of Lattices and Interfaces

A. Important Points

1. It was clear that there has been considerable recent progress in the development of pair potentials. In addition to van der Waals, ionic and covalent materials, where

such potentials are fairly accurate representations of solids, more realistic potentials are emerging for simple metals using ion-core interaction potentials together with a pseudopotential representation of electron screening (discussed by Ashcroft). Also, for transition metals, a renormalized electron approach (developed by Ehrenreich and co-workers) can be used to obtain first-principles, energy-displacement curves for a strained solid, and the energy relation then can be inverted to define a pair potential of the same range as the energy relation. Indeed, given any energy displacement relation, this inversion technique can be used to generate a pair-potential. In this method, volume dependence is automatically included but any oscillations of the pseudopotential type are averaged out. The extent of applicability of such potentials remains largely to be explored.

2. Reliable first-principle calculations in terms of density functional theory (discussed by Kohn) are available for surface energies of free surfaces and internal interfaces (grain boundaries and stacking faults).

3. There has been some progress, which is continuing, in development of pair potentials. Users of such potentials for atomic calculations should be aware that pair-potentials which reflect to some extent first-principle relations are now becoming available. For complex configurations such as the cores of dislocations and crack tips, it seems likely that further developments involving directional pair interactions (bond angles) may be required for a realistic representation. Indeed,

the latter interactions would be required to accurately match the elastic constants for materials such as metals where there are large deviations from a fit to the Cauchy conditions that hold for all purely radial pairwise potentials. As an interim position, the use of some of the more recent pair-potentials for computations of defects such as vacancies, dislocations and grain boundaries, where the change in density from a perfect lattice is not dramatic, is a fair approximation of reality. Unless modified to match surface properties and to include large-scale volume change dependence and directional bonding effects, however, the use of such potentials for problems such as crack-tips and voids, where free surfaces are present, is probably a poor approximation.

4. The time is past for use of simple spline fit potentials such as the Johnson potential. Work over the past decade using such potentials has provided valuable guidelines on the characterization and motion of defects in solids. However, a correlation of behavior with real crystals is now needed and the newer potentials should be used which are based on first-principle calculations.

5. Classes of behavior of materials can be established independently of the accuracy of the pair potential used. Results showing atomic symmetries at grain boundaries (Vitek), the presence of a lattice trapping barrier (Thomson) and the pressure of lattice instabilities at fixed strains (Milstein) are examples. Milstein illustrated that modest strains (of the

order of twenty percent) can change on fcc configuration to a bcc configuration: other crystal structures can be formed similarly. As pointed out by Drucker, these strains represent upper bounds, independent of potential, that can be sustained in a stable manner by a given crystal structure. Further, Milstein's calculations based on a Morse potential showed that instabilities can occur much earlier, e.g., at shear angles on the order of 8°. Thus, in considering large strains at a crack tip, near a boundary, or in a uniformly strained region, the possibility of a stress induced transformation should not be overlooked, and it is important that artificial geometric constraints not be imposed on the calculation.

#### B. Needed Research

1. For problems such as the atomic simulation of cracks and voids involving free surfaces, it was suggested that a dual pair potential approach be used. One potential would be developed as usual for the bulk, while another would be used for the surface region, with the latter matched to appropriate surface properties such as the surface energy calculations mentioned above. A prototype of such an approach is the treatment of adsorption of Group IV species on metals by a combination of molecular orbital models for surface bonds with pseudopotential for the underlying metal.

2. Different paths of decohesion of a solid along an internal interface can be imagined. One of these if the hypothetical separation of rigid bulk phases in a path normal to the

interface. The appropriate force constant for small displacements is determined from a weighted average of phonon frequencies\* instead of the elastic constant appropriate to a tensile extension of both bulk and interface. Phonon dispersion data are needed for such displacements and are also important in determining the surface pair potential mentioned above.

3. Given that all pair potentials are perforce to some extent approximate, they should be matched to as many parameters as possible, including those sensitive to both long-range and short-range atomic interactions. These include parameters such as elastic constants (second and higher order), phonon frequency spectra (in both unstressed and stressed states), cohesive energy, free surface energy, stacking fault energy, defect formation and motion energies, and pressure dependence of junction tunneling and both Raman and infrared absorption. This extensive matching is particularly important for those potentials which are generated empirically.

4. All atomic calculations to date on dislocations, crack tips and grain boundaries have been two-dimensional in the sense of considering planar boundaries and straight dislocations or crack tips with periodic boundary conditions imposed in the direction of the line, and most of these have been at 0°K. Valuable information has been obtained, for example, on the Peierls potential barrier to dislocation motion and the lattice trapping barrier to crack propagation. These should be updated

\*E. Zaremba, Solid State Commun. 23, 347 (1977).

for the newer potentials that are emerging and should be extended to at least room temperature. Also, it is now necessary to extend the calculations to three dimensions to determine kink or jog formation energies for dislocations and crack tips. These are needed to predict rates of defect motion and to determine in detail the competition between sharp crack propagation and crack-tip blunting by dislocation emission. Methods are now available to match three-dimensional defects compatibly to a surrounding elastic continuum.

## II. Adsorption, Cohesion of Interfaces and Fracture Processes

### A. Important Points

1. A fundamental question is that of whether a given lattice or interface (e.g., grain boundary) can sustain an atomistically sharp crack. If such a crack configuration is stable against dislocation blunting up to loads corresponding to separation of crack tip bonds, brittle behavior is possible and the lattice or interface will be capable of cleaving--provided that a crack can be nucleated. Conversely, if dislocation blunting occurs first, cleavage will generally not be possible and failure must occur according to some more ductile mechanism. Although the final resolution of brittle vs. ductile response must rely on atomistic considerations, an approximate criterion can be phrased in terms of the work of interfacial separation, possibly as altered by adsorption, and dislocation parameters such as core size and energy of the step formed in tip blunting. The latter are also subject to alteration by adsorption.

2. The time scale of interfacial separation in, e.g., temper-embrittled steels at low temperatures, is such that there is an effectively constant composition of the temper-embrittling segregants (Pb, Sn, Sb, P, etc.) during separation. These circumstances are well removed from those of surface creation at composition equilibrium of the separating interface with the bulk, and appropriately different methods are required for calculation of the effect of segregation on the "ideal" work of separation. It is established that within the approximation of local equilibrium of the segregant at the separating interface, classical thermodynamic methods can be applied to calculate the effect of adsorption at constant composition. The work in this case (for a single segregant of surface concentration  $\Gamma$  and local potential  $\mu$ ) is

$$\bar{\omega} = \omega_0 - \int_0^\Gamma [\mu_{\text{int}}(\Gamma) - \mu_{\text{surf}}(\Gamma)] d\Gamma$$

where  $\omega_0$  is the work in the absence of segregation and where  $\mu = \mu_{\text{int}}(\Gamma)$ ,  $\mu = \mu_{\text{surf}}(\Gamma)$  are the respective equations of the adsorption isotherms for an unstressed interface and for the pair of free surfaces created by separation. The important question, still unresolved, is that of how much error is introduced by modelling the segregant as being in local equilibrium during separation. For comparison, the ideal work of separation at the opposite extreme of full composition equilibrium (with a source at potential  $\mu$ ) during separation is given by a simple

generalization of the Gibbs adsorption theorem:

$$\hat{\omega} = \omega_0 - \int_{-\infty}^{\mu} [\Gamma_{\text{surf}}(\mu) - \Gamma_{\text{int}}(\mu)] d\mu .$$

Here  $\Gamma = \Gamma_{\text{surf}}(\mu)$  and  $\Gamma = \Gamma_{\text{int}}(\mu)$  are the inverted equations of the two adsorption isotherms mentioned above.

3. Observations suggest that interfacial decohesion is an important micromechanism of fracture in many systems, including metals that ultimately fail by ductile hole coalescence. Specific examples for "brittle" fracture modes were provided by the work of MacMahon on intergranular fractures of temper-embrittled steels and by Evans on structural ceramics. Further, a key step in "ductile" fracture of metals is the nucleation of voids from precipitates or other inclusions and this often involves failure along the particle-matrix interface. An additional type of interfacial failure was shown by Asaro to be of importance in ductile fracture of spherodized steel. Here the fissures that nucleated at the spherodized carbides, typically on a grain or sub-grain boundary, were observed to grow along that boundary. In fact, Asaro showed evidence that the effect of dissolved hydrogen on ductile fracture in these steels can be explained through the concept that hydrogen aids the grain-boundary-splitting mode of cavity growth.

4. In the cases of intergranular separation noted above, it is not known definitively whether the crack remains atomistically sharp very near its tip (i.e., no dislocation

blunting, although nearby dislocations could move in the crack tip stress field) or whether, instead, the observed intergranular mode is a result of some kind of plastic "slipping-off" process. If the crack does indeed remain atomistically sharp, then it appears to be possible that the crack could grow with appreciable plastic dissipation by the motion of nearby dislocations. This involves the "screening" effect proposed by Thomson, and elaborated upon at the meeting by MacMahon and Vitek, whereby the macroscopic energy release rate can be far in excess of the ideal work,  $\omega$ , of interfacial separation. Nevertheless, it is important to understand that the size of  $\omega$  controls the size of the overall plastic dissipation and, in this case, alterations of  $\omega$  by absorption, for example, are expected to lead to corresponding alterations in the (much larger) macroscopic energy release rate.

5. The "regular solution model" seems to be successful in a qualitative sense in describing alloy systems that lead to segregation. The model as described by Wynblatt assumes that entropy effects can be described by a simple mixing expression. Thus surface and bulk concentrations are related in the form

$$x_A^s/x_B^s = (x_A^b/x_B^b) \exp(-\Delta H/kt) ,$$

and the enthalpy difference  $\Delta H$  between surface and bulk includes contributions from surface energy differences for the two constituents in pure form, from the enthalpy of mixing, and from

the misfit elastic strain energy A in B. Abraham and Pound, in computer simulations of segregation, demonstrate reasonable agreement with the model, with greatest disagreement when the solute A is smaller than B and the misfit energy is overestimated.

#### B. Research Needs

1. A major problem is that of how to properly pose and resolve the question of ductile vs. brittle response of an interface, including the effects of impurity segregation. Thermo-dynamic methods can be applied to analyze some parameters, specifically  $\omega$ , relevant to this competition, as described above. There remains the problem of assessing the effects of local departures from equilibrium composition during separation and of the kinetics of mass transport in the case of environmental or bulk solute embrittlement. Further, the effects of adsorption may, in some cases, be as important for alterations of the dislocation nucleation process as for alterations of  $\omega$ . The principles underlying such effects are not yet well understood.

2. The observations reported on ductile fracture mechanisms in spheroidized steels suggest a greater contribution of a "brittle" separation mode to cavity growth than previously understood. This needs further study to define the nature of the grain boundary splitting process and the relevance to ductile fracture mechanisms in other alloy systems.

3. The case of brittle crack growth with appreciable near tip dislocation motion remains incompletely understood.

Recent attempts at the problem have been reported and these need to be developed further.

4. To the extent that interfacial energy reductions are indeed important to fracture processes, there is need for better coordinated experimental and theoretical work on equilibrium segregation, including multi-component adsorption. The adsorption isotherms for such cases allow the thermodynamic calculations of  $\omega$  by the formulae given earlier (appropriately generalized to the multi-component case). Essentially, measurements (e.g., Auger) of surface and interface compositions are needed as a function of equilibrating potential, or suitable theoretical isotherm models are needed from which such segregation can be predicted confidently.

### III. High Temperature Cavity Growth

#### A. Important Points

1. Relative roles of boundary/interface energy and boundary diffusivity. The growth of cavities by diffusion depends on both the ratio  $\zeta$  of the boundary energy to the surface energy and the boundary diffusivity  $D_b \delta_b$ : in the sense that the growth rate is enhanced as  $\zeta$  or  $D_b \delta_b$  are increased. Most alloy additions tend to increase both the boundary energy and the boundary diffusivity, and thus enhance the material's susceptibility to high temperature cavity growth. However, some systems have been noted in which the low temperature boundary embrittlement is enhanced while the high temperature cavity growth is

retarded (inferring a decrease in boundary diffusivity). These influences of alloy additions on boundary energy and boundary diffusivity clearly have very important implications for the design of alloys required to perform at high temperatures.

2. One aspect of cavity growth calculations and data interpretation that has not been considered is the possible occurrence of interface processes, that restrict the availability of the vacancies required to extend the cavities, i.e., interface control. There are two indications that interface control may be an important consideration. Firstly, most diffusion creep data indicate that there is a threshold stress for the onset of creep, that can be plausibly attributed to a threshold for the continuous activation of vacancy sources (for a variety of possible reasons). Since prolific vacancy production is also required for cavity growth (especially in the equilibrium mode), related threshold characteristics might be anticipated. Secondly, direct observations of the configurations of boundary dislocations using high resolution techniques have inferred that a local vacancy supersaturation develops in the low stress limit, again suggesting the existence of interface control. The existence of interface control has two important implications; it can yield stress dependencies of the cavity growth rate that vary (continuously) from the predicted value, as the local stresses approach the threshold: it can encourage non-equilibrium cavity growth (which requires fewer vacancies) to occur at appreciably lower velocities than anticipated by present analyses.

3. Most of the present analyses of cavity growth pertain to the extension of uniform arrays of cavities. There are many important situations in which the primary time to failure is expended while the material contains a small number of isolated non-equilibrium cavities. The growth rates that pertain to this mode of cavity growth need to be analyzed, including conditions under which a liquid phase is contained near the crack tip. Two analyses, by Chuang and Rice and by Vitek, have been conducted; these must be extended to include crack configurations of interest (axi-symmetric, branching at triple points, etc.).

4. The analyses of cavity growth do not yet include the possibility of dislocation plasticity near or between cavities. The relaxation times associated with the presence of plastic zones are considerably larger than elastic relaxation times. This could influence the relative roles of the diffusivities on the cavity growth, including the transition between the equilibrium and non-equilibrium modes.

#### B. Research Needs

1. The implication that certain alloy additions can retard boundary diffusion (whereas an enhanced diffusion is usually expected) suggests an approach for reducing the susceptibility to high temperature cavity growth. Specifically, an attempt to identify alloy constituents that appreciably reduce the boundary diffusivity, without causing a counteracting increase in the boundary energy, is clearly merited. The search for

suitable alloy additions could involve atomistic modeling of the boundary energy and boundary diffusivity, at the most advanced levels discussed in Section I, coupled with empirical studies.

2. The possible incidence of interface control suggests that test data be obtained over a sufficiently wide range of stress/temperature conditions that trends indicative of a threshold become apparent; in a manner analogous to that used to resolve the existence of the phenomenon in creep experiments (Burton and Reynolds). A threshold could also be introduced into cavity growth calculations, to anticipate the specific influence of interface control on both the stress dependence of the growth rate and the transition from equilibrium to non-equilibrium growth.

3. An important cavity growth regime, the growth of a small number of relatively large isolated non-equilibrium cavities, has received little theoretical attention. More extensive analyses of this mode of cavity growth are urged. Similarly the incidence of dislocation plasticity on the modes of cavity growth needs to be explored.

## Appendix I

### COHESION, ADSORPTION & THE STRENGTH OF MATERIAL INTERFACES

#### Guest Participants

Farid F. Abraham  
IBM Research Lab.  
M33/281  
San Jose, CA

Robert J. Asaro  
Brown University  
Barus and Holley  
Providence, RI

Neil Ashcroft  
LASSP  
Cornell University  
Clark Hall  
Ithaca, NY 14853

Arthur Bienenstock  
Dept. of Materials Science  
Stanford University  
Stanford, CA 94305

Trangott E. Fischer  
Exxon Res. Eng. Co.  
P.O. Box 45  
Linden, NJ 07036

Ed Fuller  
National Bureau of Standards  
Room A355, Bldg. 223  
Washington, DC 20234

Ralph J. Harrison  
Army Materials & Mechanics  
Research Center  
Building 292  
Watertown, MA 02172

Tim James  
Engineering  
Univ. of California  
Santa Barbara, CA 93017

H. L. Luo  
Applied Physics & Information  
Science (C-014)  
University of California  
La Jolla, CA 92093

Charles J. MacMahon, Jr.  
University of Pennsylvania  
205 LRSM-K1  
Philadelphia, PA 19104

F. Milstein  
Dept. of Mechanical Engineering  
University of California  
Santa Barbara, CA 93106

H. Posen  
USAF/RADC - Deputy for  
Electronic Technology  
Solid State Sciences  
Bedford, MA 01731

G. M. Pound  
Materials Science Department  
Stanford University  
5506 Peterson  
Stanford, CA 94305

Rishi Raj  
Cornell University  
Bard Hall  
Ithaca, NY 14853

V. Vitek  
Dept. of Metallurgy and  
Materials Science  
University of Pennsylvania  
Philadelphia, PA 19104

Paul Wynblatt  
Ford Motor Company  
S 2046 Res. Lab. Bldg.  
P.O. Box 2053  
Dearborn, MI 48121

## Appendix II

### MEETING ON FUNDAMENTALS OF COHESION, ADSORPTION AND THE STRENGTH OF MATERIAL INTERFACES

July 1978

#### Session I - Atomistic Calculations of Cohesive Properties of Lattices and Interfaces

- N. Ashcroft (Cornell University) - general review of interatomic potentials
- H. Ehrenreich (Harvard University) - re-normalized atom method for cohesion in transition metals
- W. Kohn (University of California, San Diego) - overview of atomic calculations for free surfaces
- F. Milstein (University of California, Santa Barbara) - theoretical strength calculations
- V. Vitek (University of Pennsylvania) - atomistic structure of grain boundaries
- R. Thomson (National Bureau of Standards) - lattice effects in crack propagation

#### Session II - Adsorption, Cohesion of Interfaces, and Fracture Processes

- J. R. Rice (Brown University) - adsorption and embrittlement of material interfaces
- J. P. Hirth (Ohio State University) - solute adsorption to dislocations and cracks
- C. J. MacMahon (University of Pennsylvania) - grain boundary fracture of temper-embrittled steels
- R. J. Asaro (Brown University) - grain boundary effects in hydrogen embrittlement
- T. E. Fischer (Exxon Research and Engineering) - chemisorption and chemical bond effects
- P. Wynblatt (Ford Research Laboratories) - surface segregation in alloys
- A. Bienenstock (Stanford Linear Accelerator Center) - synchrotron radiation surface analysis
- G. M. Pound (Stanford University) and F. Abraham (IBM) - computer simulation of segregation

Session III - Diffusive Processes in Grain Boundar Cavitation  
at Elevated Temperatures

- R. Raj (Cornell University) - nucleation and growth of cavities at grain interfaces
- J. R. Rice (Brown University) - crack-like modes of diffusive rupture
- A. G. Evans (University of California, Berkeley) - grain boundary fracture in ceramic processing

## PROGRESS AND OPPORTUNITIES IN RSR

E. E. Hucke

A review of some of the outstanding accomplishments and areas of further opportunity arising from RSR methods was held.

The accomplishments of the Pratt and Whitney program offer an excellent example of the chain reaction benefits that can be derived from a materials processing advance such as RSR. In this case the end goal is increasing efficiency and/or performance of gas turbine driven aircraft through the benefits of better microstructure and properties of the high temperature components. However, the final improvement can be magnified by the additional freedoms possible with RSR in choosing alloys and processing which allow more than commensurate gains in final performance, due to easier thermomechanical processing, wider design choices, and fabrication economies.

The major enabling factor in this case has been the successful operation, with many alloys on a large scale, of the RSR powder-making equipment giving high yields of conveniently sized material solidified at rates at or exceeding  $10^5$  K/sec. The structures obtained have more than met expectations in producing very fine dendrite spacing (DAS) and even homogeneous crystalline alloys which have in almost all cases yielded materials superplastically deformable to near net shapes or workable to

sheet. Additional important benefits have arisen from the elimination of segregation phases in many alloys, and in other cases the ability to maintain in solution larger alloy concentrations of beneficial elements. The first factor allows important increases to be realized in re-melt temperature which substantially aids in thermomechanical processing (i.e., faster solution and better working) and particularly in the ability to practically apply the technique of directional recrystallization which is responsible for dramatic improvements in high temperature strength. Also, cobalt, previously partially helpful in raising the re-melt temperature, can be reduced thereby offering economy and conservation of strategic material. The ability to retain alloy in solution allows consideration of much higher refractory metal contents for high-temperature matrix strengthening without facing the usual consequences of non-workability.

In short, it was quickly perceived that RSR would contribute worthwhile improvements to the more usual superalloy compositions but that far more could be gained by exploiting the newly found alloying freedoms. Notably, it was possible to simultaneously gain strength with much higher  $\gamma$  contents without loss of fabricability by using higher Al giving better oxidation resistance even though eliminating substantial amounts of strategically important Cr. These changes have already allowed an overall improvement in metal temperature capability of 200°F compared to the best alloys now available, but with the added

advantages of sheet rollability. The latter factor enables a very important flexibility in engine design.

Previous favorable engine designs with elaborately channeled blades for transpirational and convective cooling have awaited the availability of an alloy rollable to sheet, but then transformable to a creep-resistant material. The present realization of this goal allows an alloy with 200°F improvement in metal-temperature capability to raise the turbine inlet temperature by ~400°F with additional cooling still further benefiting inlet temperature to a total of 630°F at equivalent life. Besides the usual benefits to performance and/or economy, such dramatic increases allow reconsideration of engine design factors, such as elimination of stages and return to pure jet engines with enormous savings in total engine parts. Indeed, the known performance/fuel savings of higher inlet-temperature lighter engines open many possibilities to new aircraft designs (e.g., VSTOL) which have been long awaiting the emergence of suitable performance engine packages.

In summary, this example of R&D aptly shows the down-stream multiplying effect of materials processing improvements.

There has been considerable interest since the inception of the ARPA program in RSR in determining whether glassy materials could be reconstructed into bulk form while retaining their desirable properties. This would obviously extend the potential range of useful application. From the report of preliminary studies carried out by Dr. Carl Cline of Lawrence Livermore

Laboratories, it is clear that at least a qualified success has already been achieved. Cline reported a number of interesting techniques that have:

1. Explosively welded together metallic glass ribbons.
2. Explosively welded a metallic glass layer to carbon steel.
3. Explosively compacted powder metallic glass powder.
4. Dynapact compacted at modest temperature metallic glass powder.
5. HIPed at low temperature (below Tg) metallic glass powder.

In all cases it was possible to define process variables which retained the glassy structure while obtaining full densification. At this time it is not possible to definitely state that no embrittlements have taken place, but the initial indications are indeed encouraging. At this time it appears that reconsolidation is going to be much easier than envisioned several years ago, even in cases such as explosive compaction where short temperature bursts well above Tg exist. Further definition of surface cleanliness requirements and full property determination on a range of glasses of interest remains. At this time further progress appears to be limited by availability of suitable powder material.

Interesting examples of consolidation of non-glassy RSR alloys, i.e., Ni superalloys and a wide range of difficult to fabricate ceramics such as AlN and B were reported. There appears

to be a good chance that this method can yield a polycrystalline diamond material (carbonado), possibly without binder metals such as Co and Si.

POTENTIAL APPLICATION OF RAPID SOLIDIFICATION  
METALLURGY TO SMALL, HIGH-PERFORMANCE TURBINE ROTORS

M. Cohen

Considerable attention has been devoted to the pros and cons of achieving higher operating temperatures in relatively small, high-performance, short-lifetime turbines. Looking ahead beyond present superalloy technology, there is much interest in the feasibility of ceramic turbines, and thought has also been given to prospects for carbon/graphite turbines (see E. E. Hucke in this report). The point of the present note is to offer a more modest suggestion, based on advanced in superalloy metallurgy at Pratt and Whitney, Florida. This approach shows promise of allowing a 200°F increase in turbine-blade temperature (perhaps a 400°F increase in turbine-inlet temperature), and yet it seems quite realistic from the practical standpoints of processing, reliability, and engineering experience.

Recent rapidly-solidified alloy development at Pratt and Whitney has led to the following compositions:

		<u>Ni</u>	<u>Al</u>	<u>Mo</u>	<u>Ta</u>	<u>W</u>
RSR	143	Bal	6	14	6	--
RSR	185	Bal	6.8	14	0	6

These alloys not only have superior high-temperature strength, but they are superplastic and can be isothermally forged to complex, near-final shapes. As emphasized in our previous Council reports, the RSR method permits extensions into alloy regimes which would otherwise result in undue brittleness and lack of fabricability. The rapid solidification sustains a sufficiently high degree of compositional and structural uniformity that new and desirable combinations of formability and high-temperature properties come into existence. At the same time, there is a significant raising of the incipient melting point (from 2330° to 2470°F) because of the suppression of segregation. The strength at elevated temperatures is also made possible by the grain-coarsening treatments which can be applied to these alloys prior to testing or service.

In the light of such progress, serious consideration might now be given to the use of RSR technology with its newly-available superalloy compositions for next-generation, high-performance, small turbine rotors. In this approach, it would also seem feasible to take advantage of the accompanying superplasticity to produce the rotor blades integral with the hub by isothermal forging.

## LIQUID METAL ELECTRON AND ION SOURCES

R. Gomer

### ABSTRACT

The mechanisms of electron and ion generation from Taylor cones of liquid metals are discussed. In the case of electron emission the vacuum arcing mechanism of Swanson and Schwind, which accounts for the observed high current repetitive pulsing is briefly reviewed. Mechanisms from onset to the high current regime are proposed for ion emission. It is concluded that at onset ions are generated exclusively by field desorption. A theory to account for the observed emitter heating is advanced, and it is concluded that high currents result from field ionization of thermally evaporated atoms. It is shown that space charge becomes important even at very low ion currents and is instrumental in providing stabilization in all regimes of ion emission.

## LIQUID METAL ELECTRON AND ION SOURCES

R. Gomer

### INTRODUCTION

Liquid metal ion sources have been studied by several investigators since at least 1967.<sup>1-7</sup> These sources provide a high brightness, quasi-point source of metal ions for high resolution ion beam lithography and other potential applications. The details of the ion generating mechanism seem very incompletely understood. Recently Swanson and Schwind<sup>8</sup> have also investigated liquid metal field emission sources. The mechanism in this case, as proposed by these authors, seems straightforward but will be briefly included here since it provides an interesting contrast to the ion emission case and serves to throw some light on the matter.

A liquid metal ionization or electron source typically consists of a fine tungsten capillary (0.02 to 0.002 cm in diameter) or of a capillary with a tungsten needle projecting through it, and an extraction electrode in front of this assembly. The tungsten assembly is cleaned, for instance by sputtering, so that it is wetted by the liquid metal used, which is then forced into the capillary by a suitable arrangement. When a critical voltage, generally 5-10 kV, is applied between capillary and

extractor the liquid metal is pulled outward by the electrostatic forces at its surface. It was shown in 1964 by Sir G. Taylor<sup>9</sup> that the balance between electric and surface tension stresses leads to the formation of a cone of half-angle  $49.3^\circ$ , at a critical voltage  $V_c$  which depends on the electrode configuration and the surface tension. In principle this cone should become infinitely sharp at its apex. Under some conditions dynamic instabilities occur and jetting with the ejection of liquid droplets is observed. For many liquid metals of low ionization potential it is possible however to minimize droplet formation. If the liquid metal electrode is made positive with respect to the extractor, relatively stable, d.c. ion emission results for such metals with currents ranging from a few microamperes to milliamperes. For Ga at currents  $>10^5$  amperes Swanson<sup>10</sup> has observed incandescence of the liquid cone itself, and at slightly higher currents a glow is seen in front of the liquid cone; the glow region increases in size with increasing current. Its size seems to be  $\sim 1\mu\text{m}$  or slightly larger. These effects seem to occur with all metals.

Ion emission has been reported for Ga,<sup>4</sup> alkali metals,<sup>2, 4, 5</sup> Au,<sup>6</sup> Si-Sn-Cd (Wood's metal),<sup>3</sup> Hg,<sup>6</sup> and others.<sup>6</sup> Some authors<sup>4</sup> mention energy spreads of  $\sim 10\text{eV}$  for ions. For alkali ions both singly and to a lesser extent doubly charged ions, as well as dimer and multimer ions have been reported.<sup>3</sup> In one instance a space charge limited, i.e.,  $i \propto V^{3/2}$  current voltage relation has been reported.<sup>2</sup>

If the polarity is reversed Swanson and Schwind<sup>8</sup> find, with an applied d.c. voltage that emission consists of nano-second pulses, the current per pulse reaching values of 200-300 amperes (!). The pulse repetition rate appears to be limited by the charging time of the power supply.

Since the formation of the emitter cone depends on electric forces, ion sources of this kind have also been called EHD (electrohydrodynamic) ion sources, and presumably the same, rather misleading, designation could also be applied to these configurations when used for electron emission.

#### MECHANISM OF ELECTRON EMISSION

The mechanism proposed by Swanson and Schwind<sup>8</sup> seems to explain the phenomenon and is here given very briefly. On application of the critical Taylor voltage a liquid cone of very high curvature at its apex is formed and since the field near this apex is of the correct sign for field emission, electron tunneling occurs. The current initially emitted (as seen in oscilloscope traces) is of the order of several milliamperes. This leads to heating of the apex region, thermal evaporation of metal atoms, and their ionization by field emitted electrons, which gain sufficient kinetic energy at very small distances from the cone ( $10-100\text{\AA}$ ). The resultant positive ions are attracted toward the cone where they (a) reduce electron space charge thus increasing field emission and (b) cause the sputter desorption of additional ions and neutrals. The result is an explosive increase

in net current and destruction, literally blowing apart, of the cone apex. This phenomenon, vacuum arcing,<sup>11</sup> can be observed equally well with solid metal field emitters but is then a single event, requiring the preparation of a new tip for its repetition. In the present case, on the other hand, the cone apex reforms very quickly under the electric stress on the liquid conductor and the process repeats itself.

#### ION EMISSION

We turn next to the case where the cone is made positive and ion emission is observed. The principal questions are:

- 1) What is the mechanism of ion generation?
- 2) Why is it stable, unlike the electron emission case?
- 3) Why is heating of the cone observed at quite small currents?
- 4) Is the "plasma" region in front of the cone incidental to or central to the ion generating mechanism(s)?

#### The Taylor Cone

We start by considering briefly the Taylor voltage, the electric field near the cone apex, and the forces acting on the cone. The condition for stress equilibrium on the surface of a curved conducting liquid with an electric field  $E$  at its surface is

$$\gamma(1/r_1 + 1/r_2) = (E/300)^2/8\pi \quad (1)$$

where  $\gamma$  is surface tension of the liquid in dynes/cm,  $r_1$  and  $r_2$  the principal radii of curvature and  $E$  the field in volts/cm.

For a sphere  $r_1 = r_2$  and the left side of Eq. (1) takes the familiar form  $2\gamma/r$ , while for a cone there is only one radius, which increases linearly with distance from the cone apex.

Taylor<sup>9</sup> showed that Eq. (1) could be met by an electric potential of the form

$$V = Ar^{\frac{1}{2}} P_{\frac{1}{2}}(\cos\theta) \quad (2)$$

where  $r$  is the radius vector in spherical polar coordinates and  $P_{\frac{1}{2}}$  the Legendre polynomial of order  $\frac{1}{2}$  and  $A$  a constant; this potential gives an outward normal field with the required  $r$  dependence and satisfies Laplace's equation. In order to satisfy the requirement that  $V = 0$  on the cone surface,  $P_{\frac{1}{2}}(\cos\theta)$  must be 0 on the cone, which is the case for  $(0 \leq \theta < \pi)$   $\theta = 130.7^\circ$ , giving a cone half-angle of  $49.3^\circ$ . The outward normal field on the cone turns out to be<sup>9</sup>

$$\begin{aligned} E &= (1/r) dV/d\theta = Ar^{-\frac{1}{2}} (dP_{\frac{1}{2}}/d\theta)_{130^\circ} \\ &= 0.974 Ar^{-\frac{1}{2}} \end{aligned} \quad (3)$$

and thus from Eq. (1) the critical cone-forming voltage is given by

$$V_c = 1.432 \cdot 10^3 \gamma^{\frac{1}{2}} R_o^{\frac{1}{2}} \quad (4)$$

where  $R_o$  is the value of  $r$  at  $\theta = 0$  for the counter electrode (extractor) assuming that the latter has the idealized shape

$$r = R_o \left[ P_{\frac{1}{2}}(\cos\theta) \right]^{-2} \quad (5)$$

For actual geometries which do not conform to this shape  $R_o$  can be thought of as a form factor of the order of the electrode spacing. To get some feeling for  $V_c$  let us assume  $R_o \sim 0.1\text{cm}$ ,  $\gamma = 700 \text{ dy/cm}$  (a value appropriate for liquid Ga, but typical of most of the metals under consideration). We then find  $V_c = 11\text{kV}$  in good agreement with the observed values, considering the uncertainty in  $R_o$ .

For voltages less than  $V_c$  no cone will be formed and for voltages in excess of  $V_c$  the net electric force exceeds the surface tension force so that the cone will be unstable. In reality it seems possible to exceed  $V_c$  considerably without the formation of droplets or the ejection of liquid jets in the case of ionization in vacuum. This point will be considered in more detail later.

It is evident from the Taylor argument that a rounded cone apex must be unstable at  $V_c$  relative to elongation into a true cone since the electrostatic forces will always exceed the surface tension forces. Thus any rounding will either have to be the result of a balance between the rate of removal of atoms and ions at the apex and the rate of supply of liquid, or must result from a reduction in apex field by space charge effects.

#### Apex Field

It is important to know the electric field at the (rounded) cone apex. This can be obtained by the method of Dyke et al:<sup>12</sup> A "core" consisting of a conducting sphere on a con-

ducting cone is chosen. For this geometry the potential is given by

$$V(r, \theta) = (V_R / R_O^n) (r^n - a^{2n+1} r^{-(n+1)}) P_n(\cos \theta) \quad (6)$$

where  $r$  is the radius vector in polar coordinates,  $R_O$  has the same meaning as in Eq. (4) and  $a$  is the radius of the core-sphere.  $n$  is chosen to make  $V = 0$  along the cone, i.e.,  $n = \frac{1}{2}$  in the present case. One then constructs an equipotential surface by picking a value of  $V = \text{constant}$  in such a way that this equipotential approximates the real geometry, in our case a cone of half-angle  $49.3^\circ$  terminated by a spherical cap. Using  $n = \frac{1}{2}$  and Eq. (6) one obtains

$$P_{\frac{1}{2}}(\cos \theta) = \frac{1 - k^2}{x^{\frac{1}{2}}(1 - k^2/x^2)} \quad (7)$$

as the equation of an equipotential, where use has been made of the fact that  $P_{\frac{1}{2}}(\theta = 0) = 1$ .  $k$  and  $x$  are defined by

$$k = a/r_O \quad (8)$$

$$x = r/r_O \quad (9)$$

and  $r_O$  is the distance from the origin to the equipotential at  $\theta = 0$ . Eq. (7) can easily be solved for pairs of  $(\theta, r)$  values once a given  $k$  has been picked, so that a polar plot of the equipotential can be constructed. It was found that a good approximation to the desired geometry was obtained by the choice  $k = 0.5$ , as shown in Fig. 1. The best sphere inscribable does not however

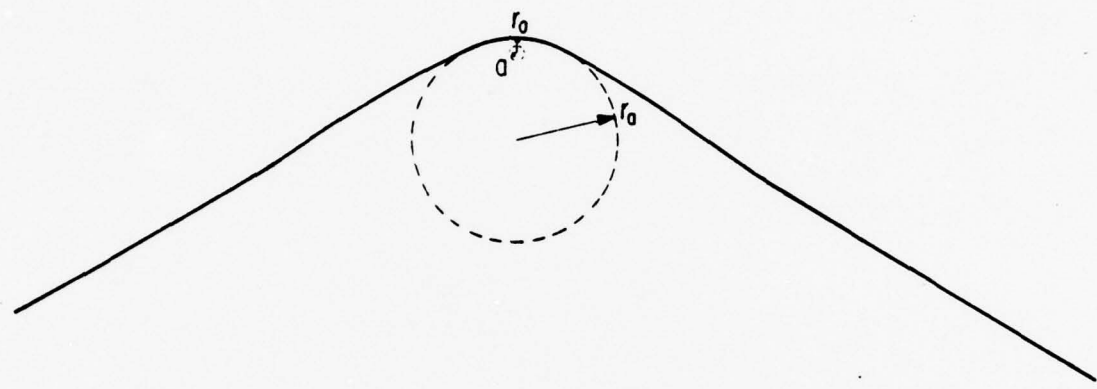


Figure 1. Equipotential simulating shape of cone terminated by spherical apex cap based on Eq. (7) with  $k = 0.0$ .  
 $a$  radius of core-sphere;  $r_0$  distance from origin to equipotential at  $\theta = 0$ ;  $r_a$  radius of best inscribable sphere.

have radius  $r_o$  but  $7.0 r_o$ . We designate this as the apex radius  $r_a$ :

$$r_a = 7r_o \quad (10)$$

The field-voltage proportionality constant for  $\theta = 0$ ,  $\beta_o = E(r_o, 0)/V_{\text{applied}}$  is then given by

$$\beta_o = \frac{(1 + 3k^2)}{R_o^{\frac{1}{2}} r_o^{\frac{1}{2}}} \cdot \frac{1}{1 - \left(\frac{r_o}{R_o}\right)^{\frac{1}{2}} (1 - k^2)} \quad (11)$$

For  $r_o/R_o \ll 1$  the last term on the right side of Eq. (11) is 1 and, in terms of  $r_a$ , and for  $k = 0.5$

$$\beta_o \approx 2.32 (R_o r_a)^{-\frac{1}{2}} \quad (12)$$

It is interesting to compare this value with  $\beta$  for a sphere of the same radius,  $r_a'$

$$\beta_{\text{sphere}} = 1/r_a \quad (13)$$

so that we have

$$\beta_o \text{ cone}/\beta_{\text{sphere}} = 2.32 (r_a/R_o)^{\frac{1}{2}} \quad (14)$$

Using Eqs. (4) for  $V_c$  and Eq. (12) for  $\beta_o$  we find for  $V = V_c$  an apex field  $E_o$

$$E_o = 3322 (\gamma/r_a)^{\frac{1}{2}} \text{ volts/cm} \quad (15)$$

If  $\gamma = 700 \text{ dy/cm}$ ,  $r_a = 2 \times 10^{-7} \text{ cm}$ ,  $E_o = 2 \times 10^8 \text{ volts/cm}$ . It will be shown presently that this is of the order required for field desorption.

### Force on the Cone

In the absence of space charge the steady state configuration of the apex region would be determined by balance between the removal of atoms and ions and their resupply under the unbalanced electrostatic force. The latter is therefore of some interest. The net outward force along the cone axis of symmetry is given in the absence of space charge by the net outward force over the truncated region of the cone, since along the cone electric and surface tension forces balance at  $V = V_c$ .

Assuming a spherical cap tangent to the cone where sphere and cone join the force  $F$  would be given by

$$\begin{aligned} F &= 0.6\pi r_a^2 (\epsilon_0^2 - 2\gamma/r_a) \\ &= 0.6\pi r_a^2 \left[ \frac{(E_0/300)^2}{8\pi} - \frac{2\gamma}{r_a} \right] \\ &= 5.43 r_a \gamma \text{ dynes} \end{aligned} \tag{16}$$

where use of Eqs. (1) and (15) has been made. For  $\gamma = 700 \text{ dy/cm}$ ,  $r_a = 2 \times 10^{-7} \text{ cm}$   $F = 7.6 \times 10^{-4} \text{ dynes}$ .

### Supply of Liquid

If viscous forces within the cone itself can be neglected the mass flow  $\frac{dv}{dt}$  under this force would be given by the net negative pressure acting on the supply capillary of radius  $r_c$  from Poiseuille's equation

$$\frac{dv}{dt} = r_c^2 F / (8\eta l) \text{ cm}^3/\text{sec} \tag{17}$$

If  $F$  is taken as  $8 \times 10^{-4}$  dynes and  $r_c = 10^{-2}$  cm  $\eta \approx 0.01$  poise,  $l = 0.1$  cm one finds  $dv/dt = 10^{-5} \text{ cm}^3/\text{sec}$ . Converted into current, using  $\sim 3 \times 10^{-23} \text{ cm}^3$  as the volume of an atom and the fact that  $1 \text{ ion/sec} = 1.6 \times 10^{-19} \text{ amperes}$  we find an equivalent current of 0.05 amperes. This value is much larger than the ion currents just beyond onset which are  $\sim 10^{-5}$  amperes and would predict essentially no blunting by desorption since supply exceeds desorption by a factor of  $\sim 10^3$ . The electric field falls off from the  $\theta = 0$  value with increasing polar angle and this may reduce the total force by a factor of  $\sim 5$ . It is also possible that the effective length of the supply capillary has been underestimated. However it is still impossible to explain appreciable blunting on the basis of the above considerations alone. It will turn out that there is in fact some slight blunting and that this results from a reduction in  $E$  by space charge, rather than by supply limitation. Thus the conclusion of this section is that supply will always be adequate to provide the observed ion currents.

#### Mechanism of Ion Formation

We consider next the mechanism of ion formation, starting at current onset. It seems clear that at least the initial step of ion emission is field evaporation or field desorption.<sup>13, 14, 15</sup> Two mechanisms for this have been proposed. Müller<sup>13</sup> assumed that under conditions of very high field the "ionic" potential curve corresponding to the state Metal<sup>-</sup> + Ion fell below the "neutral" curve Metal + Atom with desorption occurring by the atom moving outward, being adiabatically ionized and desorbing

over the Schottky barrier of the field-deformed ionic curve (Fig. 2). At sufficiently high field the latter would present a negligible barrier and under these conditions the field required for desorption is obtainable from the relation

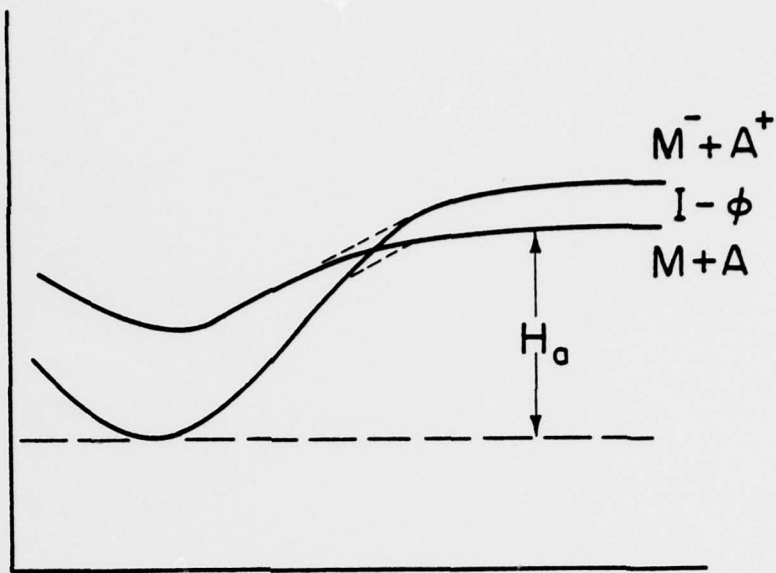
$$H_a + I_n - n\phi = (n^3 e^3 E)^{1/2} - (\alpha_a - \alpha_i) E^2 \quad (18)$$

essentially an energy balance equation, where  $E$  is field,  $H_a$  the atomic binding energy,  $I_n$  the appropriate sum of ionization potentials to produce an ion of charge  $n$ ,  $\phi$  the work function, and  $\alpha_a$  and  $\alpha_i$  atomic and ionic polarizabilities. This mechanism probably applied when  $I - \phi$  is small. When  $I \gg \phi$  Gomer and Swanson<sup>14,15</sup> have proposed a mechanism depicted schematically in Fig. 3, which consists of the intersection of neutral and ionic curves in such a way that (again for zero barrier height for desorption)

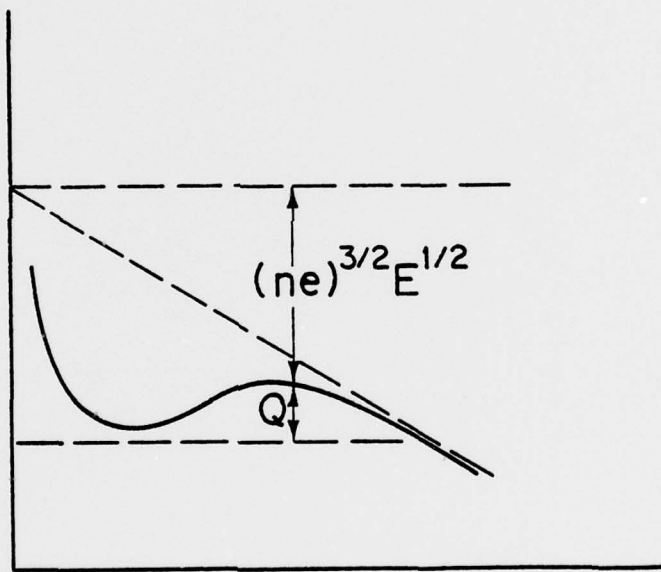
$$H_a + I_n - n\phi - n^2 e^2 / 4x_c = E e x_c - \frac{1}{2} (\alpha_a - \alpha_i) E^2 \quad (19)$$

Here  $x_c$  is the distance from the surface at which the intersection of the curves occurs, i.e.,  $\sim 2\text{\AA}$ . Both models indicate that fields of the order of one to several volts/Angstrom are required, depending on  $H_a$ ,  $I$  and  $\phi$  and this is confirmed by experiments on solid field emitters.

Since the quantitative validity of the image potential law at the fields involved is not clear, since  $x_c$  is increased from its zero field value by field penetration,<sup>15</sup> and since the effective polarizability of an atom in a metal surface is difficult

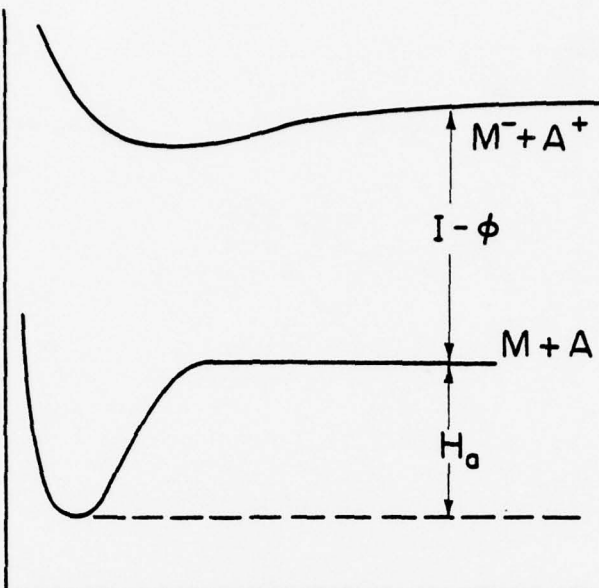


(a)

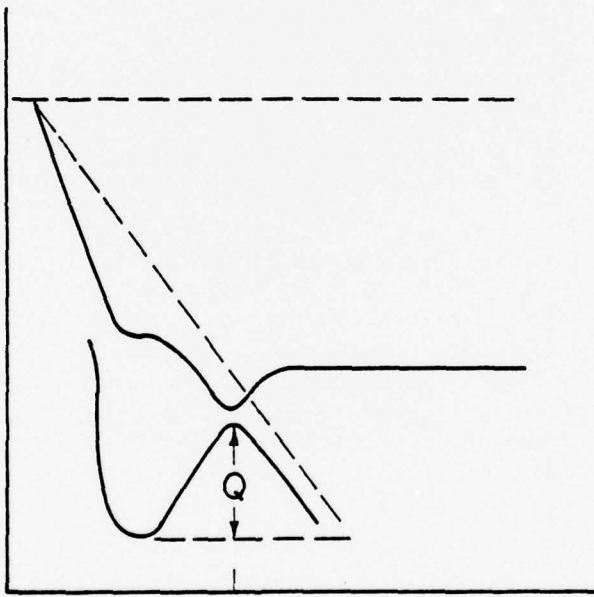


(b)

Figure 2. Potential energy diagram for field evaporation when  $1 - \phi$  is small. (a) No applied field; (2) applied field  $E$ . The diagrams drawn assume that the ground state is actually ionic, but this is not essential, as long as the field deformed curve at the maximum of the potential barrier is ionic.  $M + A$  neutral,  $M^- + A^+$  ionic curve.  $H_a$  heat of adsorption (or vaporization) relative to neutral metal + neutral atom in the absence of applied field.  $Q$  activation energy of field evaporation.



(a)



$$(b) \quad x_c \cong \frac{I - \phi + H_a - Q}{Ee}$$

Figure 3. Potential energy diagrams illustrating field desorption. (a) Field free case, (b) applied field  $E$ .  $M + A$  neutral curve,  $M^- + A^+$  ionic curve,  $H_a$  heat of vaporization,  $I$  ionization potential of atom A,  $\phi$  work function of metal,  $Q$  activation energy of desorption,  $x_c$  crossover of field deformed ionic and neutral curves.

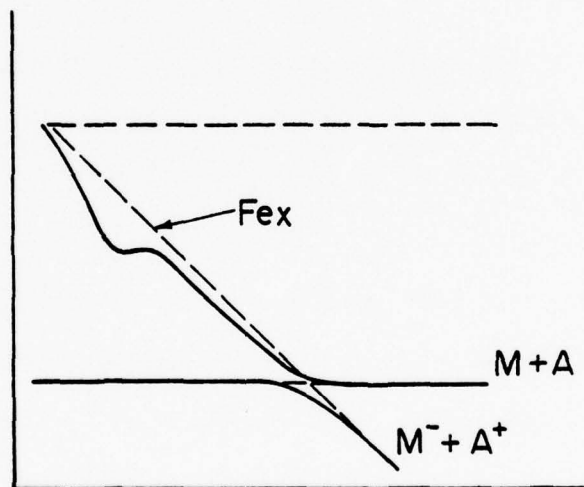
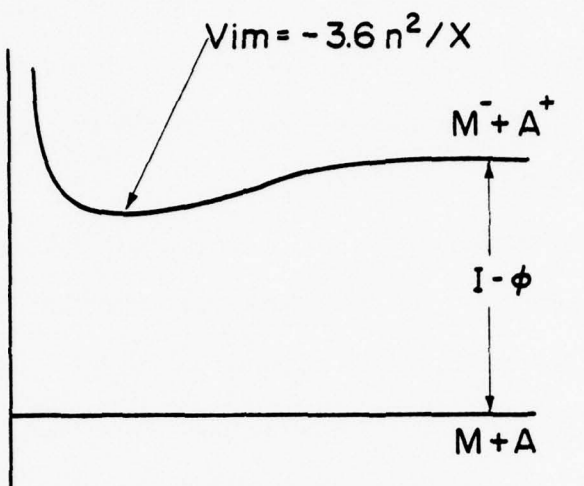
to calculate, it is not easy to go beyond semiquantitative estimates of desorption fields. This has nevertheless been attempted by Brandon,<sup>16</sup> who concludes that for  $Ga\ E = 1.16\text{ volts}/\text{\AA}$ , i.e.,  $1.16 \times 10^8\text{ volts}/\text{cm.}$

It will turn out that a related phenomenon, field ionization,<sup>17</sup> probably contributes most to current generation at high currents. This can be understood by analogy with field desorption, as indicated by Fig. 4, and consists of the intersection of an ionic and neutral curve at distances where the potential of the latter is sensibly zero. Looked at in terms of electrons, it amounts to tunneling of an electron out of a field deformed atomic potential.

In general the fields required for field desorption of an atom are considerably higher than those for field ionization of the same gas phase atom as is obvious from Figs. 3 and 4.

#### Space Charge Effects

We next consider space charge effects. For electron emission these become appreciable only at much higher currents than those involved here, but because of their mass ion velocities are less by a factor of  $\sim 300$  and space charge becomes important in the microampere range. An exact solution to the space charge problem for the cone is very difficult and we limit ourselves to the case of concentric spheres, that is, we replace emitter and collector by small and large spheres respectively. An approximate connection with the cone will be made via a scaling argument. Unlike the classical, thermionic, case treated by Langmuir<sup>18</sup>



$$X_c \approx \frac{I - \phi}{Ee}$$

Figure 4. Potential energy diagrams illustrating field ionization. All symbols as in Fig. 3. Correspondence with Fig. 3 can be made by assuming, in Fig. 3, a field so weak that intersection occurs in the flat portion of the neutral curve, i.e., to the right of the intersection shown there.

it is not permissible to set the field at the emitter equal to zero since, as we have seen, fields of the order of  $\text{volts}/\text{\AA}$  are in fact required there.

The basic equations are

$$\nabla^2 V = 4\pi\rho \quad (20)$$

with

$$\rho = \frac{i}{4\pi r^2 v} \quad (21)$$

and

$$v = (2Ve/m)^{1/2} + v_T \quad (22)$$

$$v_T \approx (2kT/m)^{1/2} \quad (23)$$

so that

$$r^2 \frac{d^2 V}{dr^2} + 2r \frac{dV}{dr} = i \left[ \left( \frac{2e}{m} \right)^{1/2} v^{1/2} + (kT/m)^{1/2} \right]^{-1} \quad (24)$$

Let  $x = r/r_a$  where  $r_a$  is the emitter radius. Define  $V_O$  as the applied voltage required, if there were no space charge, to produce the necessary field  $E_O$  at  $r_a$ :

$$E_O = V_O/r_a \quad (25)$$

Let  $V/V_O = y$ . Eq. (24) then becomes

$$x^2 \frac{d^2 y}{dx^2} + 2x \frac{dy}{dx} = \left( \frac{m}{2e} \right)^{1/2} i V_O^{-3/2} \left[ y^{1/2} + (v_T/V_O) \right]^{-1} \quad (26)$$

where

$$v_O \equiv (2V_O e/m)^{1/2} \quad (27)$$

For  $V$  in volts,  $i$  in amperes and  $m$  expressed as molecular weight  $M$ , Eq. (26) becomes

$$x^2 y'' + 2xy' = 6.49 \times 10^5 i M^{\frac{1}{2}} V_0^{-\frac{3}{2}} \left[ y^{\frac{1}{2}} + (kT/V_0 e)^{\frac{1}{2}} \right]^{-1} \quad (28)$$

with initial conditions

$$y(1) = 0 \quad (29)$$

$$y'(1) = 1 \quad (30)$$

If it were not for the appearance of  $V_0$  in the term  $(kT/V_0 e)^{\frac{1}{2}}$  in Eq. (28), the latter could be solved numerically without further ado for various values of  $i M^{\frac{1}{2}} V_0^{-\frac{3}{2}}$ , the integration being carried out until such values of  $x$  as yield a constant value of  $y \equiv y(\infty)$  (or until  $y' \approx 0$ ). By assuming a value, or values, of  $V_0$  the current would then be determined and also the voltage required to produce it, namely  $V_0 y(\infty)$ . The presence of the term  $(kT/V_0 e)^{\frac{1}{2}}$  forces us however to make some more explicit assumptions about the emission process. Specifically we first assume that the field is sufficiently high to make the lifetime of a surface atom with respect to ion desorption constant at a value  $\tau$ . The current is then given by

$$i = 4\pi r_a^2 10^{15} / \tau \text{ ions/sec} \quad (31)$$

where the number of atoms/cm<sup>2</sup> is taken as  $10^{15}$ . In units of amperes Eq. (31) becomes

$$i = 2.01 \times 10^{-3} r_a^2 / \tau \text{ amperes} \quad (32)$$

If we now pick a fixed value for  $E_o$  we can eliminate  $r_a$  from Eq. (32) by Eq. (25) and have

$$i = 2 \times 10^{-3} V_o^2 / (E_o^2 \tau) \quad (33)$$

Substitution of this expression for  $i$  in Eq. (28) yields

$$6.49 \times 10^5 i M^{\frac{1}{2}} V_o^{-\frac{3}{2}} = 1.30 \times 10^3 M^{\frac{1}{2}} V_o^{\frac{1}{2}} / (E_o^2 \tau) \quad (34)$$

and Eq. (28) becomes

$$x^2 y'' + 2xy' = 1.30 \times 10^3 M^{\frac{1}{2}} V_o^{\frac{1}{2}} / (E_o^2 \tau) \left[ y^{\frac{1}{2}} + \left( \frac{kT}{e} \right)^{\frac{1}{2}} V_o^{-\frac{1}{2}} \right]^{-1} \quad (35)$$

This procedure is equivalent to assuming that changes in  $i$  result from increases in  $r_a$  if  $\tau$  and  $E_o$  are considered to stay constant. With the explicit (and slightly arbitrary) choice  $E_o = 4 \times 10^8$  volts/cm,  $\tau = 10^{-13}$  sec,  $M = 70$  (corresponding to Ga), Eq. (35) finally becomes

$$x^2 y'' + 2xy' = 0.68 V_o^{\frac{1}{2}} [y^{\frac{1}{2}} + 0.16 V_o^{-\frac{1}{2}}]^{-1} \quad (36)$$

where  $T = 300K$  has been used. Eq. (36) was solved numerically for various values of  $V_o$  until  $y$  no longer increased appreciably with increasing  $x$ . The arbitrary cutoff was made at  $x = 10^4$ . The applied voltage  $V$  can now be found as  $V_o y(\infty)$ , where  $\infty$  is taken to be equivalent to  $x = 10^4$  and  $i$  can be obtained from Eq. (33). Table 1 shows the values of  $i$  vs. the corresponding applied voltage  $V$  for various values of  $V_o$  as well as  $V/V_o \equiv y(\infty)$ . Also shown are values of  $V^{\frac{3}{2}}/i$ . Fig. 5 shows plots of  $V(x)/V(\infty)$  vs  $x$  for some selected values of  $V_o$ . It is clear that the potential

TABLE I

Solutions of Eq. (36) in tabular form. Symbols as in text. For  $V_o \leq 1$  the term  $0.16 V_o^{-\frac{1}{2}}$  in Eq. (36) was calculated as if  $V_o = 20$  in that term.

$V_o$ (volts)	$V$ (volts)	$i$ (amperes)	$V/V_o$	$V^{\frac{3}{2}}/i$
0.01	0.0154	$1.2 \times 10^{-11}$	1.54	$1.6 \times 10^8$
0.5	1.81	$3.13 \times 10^{-8}$	3.62	$7.8 \times 10^7$
1.0	4.61	$1.25 \times 10^{-7}$	4.61	$7.9 \times 10^7$
5.0	40.5	$3.13 \times 10^{-6}$	8.1	$8.2 \times 10^7$
10.0	102	$1.25 \times 10^{-5}$	10.2	$8.2 \times 10^7$
20	258	$5.00 \times 10^{-5}$	12.9	$8.3 \times 10^7$
50	875	$3.13 \times 10^{-4}$	17.5	$8.3 \times 10^7$
100	2,280	$1.25 \times 10^{-3}$	22.8	$8.7 \times 10^7$
500	16,750	0.031	33.5	$7 \times 10^7$

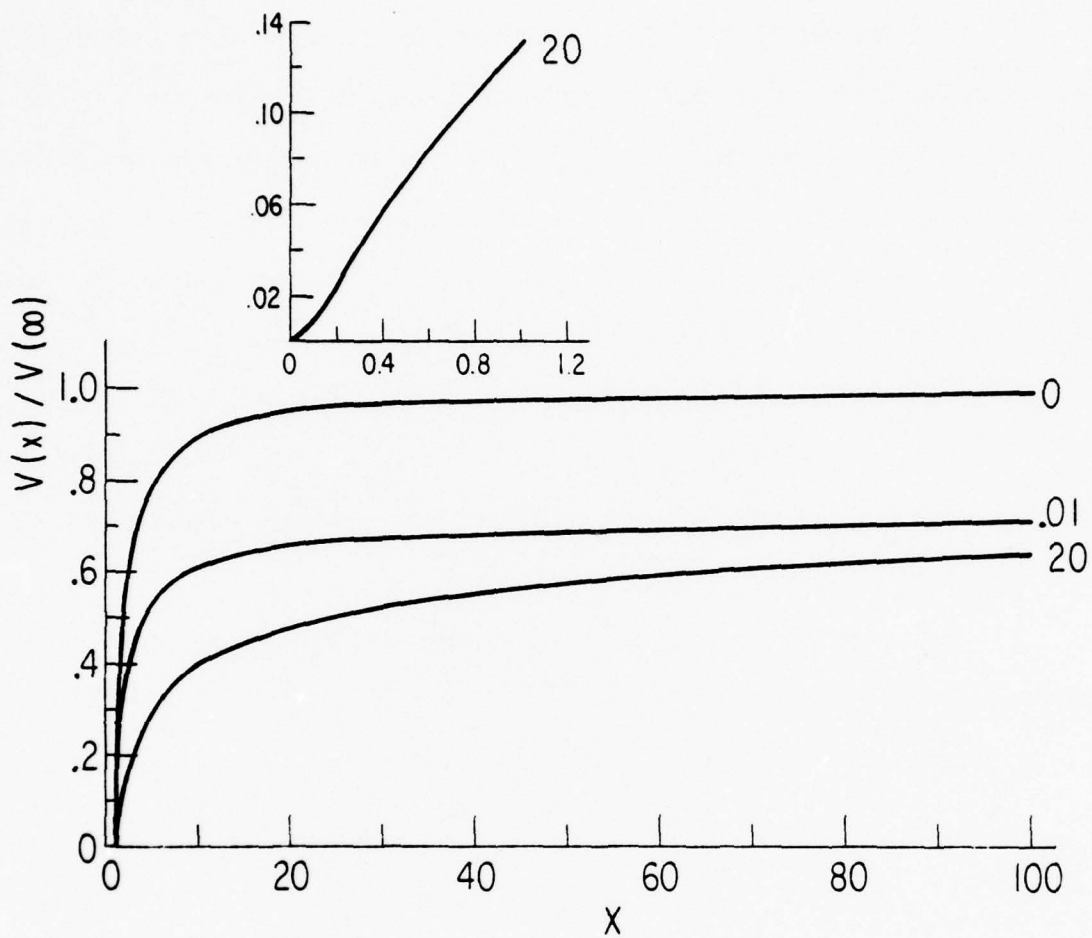


Figure 5. Plots of  $V(x)/V(\infty)$  vs.  $x$  for various values of  $V_0$ , shown on curves, based on solutions of Eq. (36). Insert shows region for  $1 \leq x \leq 2$  for  $V_0 = 20$ , to illustrate the fact that for appreciable space charge the field  $E$  will have its maximum at  $x > 1$ .

rises much less rapidly than in the absence of space charge.

Figure 6 shows the field relative to that at  $x = 1$ , vs.  $x$ .

If we now shed our scruples about the term  $(kT/V_O e)^{1/2}$  in Eq. (28) or (36) and assume that its exact magnitude is relatively unimportant so long as it is finite and thus prevents  $\nabla^2 V$  from becoming infinite at  $x = 1$ , we can also interpret the results in terms of fixed  $r_a$ , if we assume that the variation in  $E_O$  required to increase  $i$  is so small that a constant value of  $E_O$  can be assumed even when  $i$  is varied. In that case a fixed choice of  $V_O^{\text{true}} = E_O r_a$  suffices to obtain  $i$ , the values of  $V_O$  shown in Table I being now considered simply as numbers required to vary  $i$ . We call these  $V_O$  (parameter).

We have from Eq. (34) and the values of  $E_O$  and  $\tau$  used to obtain Eq. (36)

$$i = 1.26 \times 10^{-7} V_O^{3/2} V_O^{1/2} (\text{param}) \quad (37)$$

and

$$V = V_O y(\infty) \quad (38)$$

For a particular choice of  $V_O$ ,  $i$  is now obtained as a function of applied voltage  $V$  by picking a value of  $V_O$  (param) from Table I, using the appropriate value of  $y(\infty)$  to obtain  $V$  from Eq. (38) and the value of  $i$  from Eq. (37).

A plot of  $\log i$  vs.  $y(\infty) \equiv V/V_O$  for  $V_O = 20$  volts, obtained in this way, is shown in Fig. 7; space charge effects are still appreciable when  $i \approx 10^{-6}$  amperes, where  $V/V_O = 1.5$ .

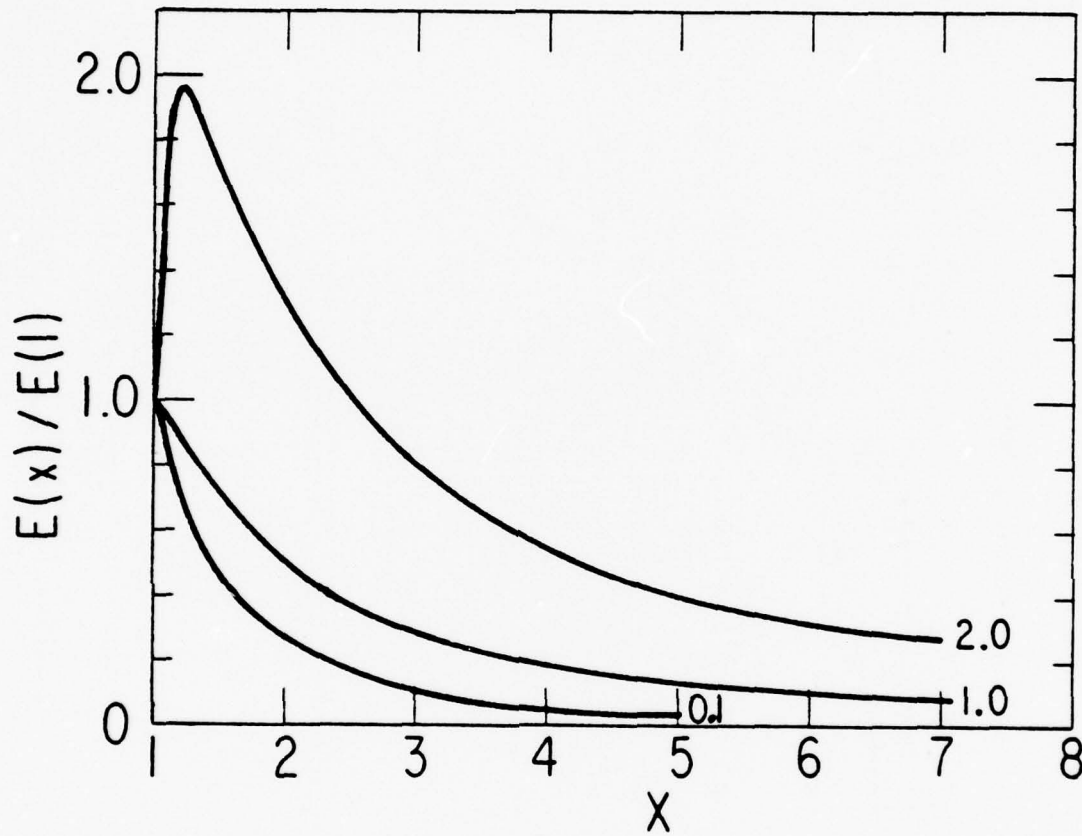


Figure 6.  $E(x)/E(1)$  vs.  $x$  for various values of  $V_0$ , based on solutions of Eq. (36). Note that for  $V_0 = 20$  the field  $E$  peaks at  $x = 1.2$ , and is almost  $2 E(1)$  at that point.

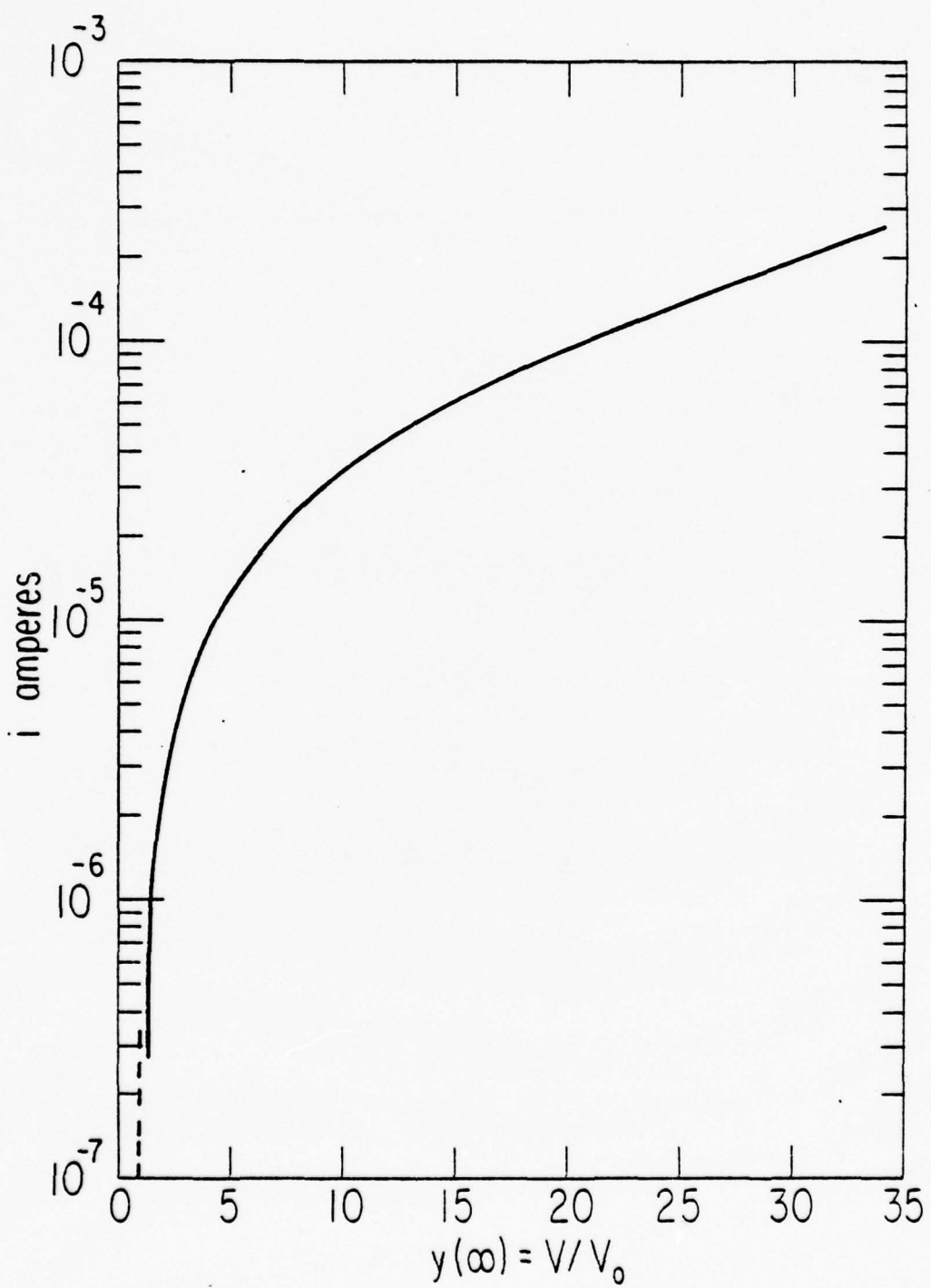


Figure 7. Log  $i$  vs.  $y(\infty) = V(\infty)/V_0$  for  $V_0 = 20$ , based on Eq. (37).

The choice  $V_o = 20$  volts corresponds to  $E_o = 1 \times 10^8$  v/cm for  $r_a = 2 \times 10^{-1}$  cm, or to  $2 \times 10^8$  v/cm for  $r_a = 10^{-7}$  cm.

It should be emphasized that the smallness of  $r_a$  is crucial to this result, although this is not directly obvious. An example will illustrate this. Suppose we choose  $E_o = 2 \times 10^8$  volt/cm and  $r_a = 10^{-6}$  rather than  $10^{-7}$  cm. We then have  $V_o = 200$  volts, instead of 20 volts and from Eq. (37) we see that the ratio  $V/V_o = 1.5$  now corresponds to  $i = 3 \times 10^{-5}$  amperes, or 30 times higher than for  $r_a = 10^{-7}$  cm. The physical reason is that higher currents are now required to produce the same current density.

We now adapt these results to the Taylor cone in a rough way by assuming (a) that the values of current for the sphere of same radius  $r_a$  as the cone apex must be divided by  $\sim 4$  to give the equivalent cone current, since the emitting area of the latter is  $\sim \pi r_a^2$  rather than  $4\pi r_a^2$  as for the sphere, and (b) that once this correction has been made the same ratio of  $V/V_o$  can be used for the cone as for the sphere. Table II lists some representative assumptions of  $r_a$ ,  $E_o$ , and values of  $i$  and  $V$  based on these assumptions, calculated by means of Eqs. (14), (37), (38) and the solutions of Eq. (36).

The numerical values of  $V$  listed in Table II depend not only on the quantitative validity of our extrapolation from sphere to cone but also on the exact value of  $R_o$  and must therefore be considered at best semiquantitative estimates. Despite this fact several conclusions emerge rather clearly: (1) Apex

TABLE II

Various combinations of  $r_a$ ,  $E_o$ ,  $i$ , and  $V$ . The values for  $i$  refer to a sphere and should be divided by  $\sqrt{4}$  for the cone. The values of  $V_o$  correspond to the voltage required to produce the field  $E_o$  at the surface of a sphere of radius  $r_a$  in the absence of space charge.

$r_a$ (cm)	$E_o$ (volts/cm)	$V_o$ (volts)	$i$ (amperes)	$V_{sphere}$ (volts)	$V_{cone}$ (volts)
$10^{-7}$	$10^8$	10	$4.0 \times 10^{-7}$	15	6,450
$10^{-7}$	$10^8$	10	$2.8 \times 10^{-6}$	36	15,566
$10^{-7}$	$2 \times 10^8$	20	$1.1 \times 10^{-6}$	30	9,302
$10^{-7}$	$2 \times 10^8$	20	$8.0 \times 10^{-6}$	72	21,900
$2 \times 10^{-7}$	$10^8$	20	$1.16 \times 10^{-6}$	30	9,120
$3 \times 10^{-7}$	$10^8$	30	$2.1 \times 10^{-6}$	45	11,200
$4 \times 10^{-7}$	$10^8$	40	$3.2 \times 10^{-6}$	60	12,930
$8 \times 10^{-7}$	$10^8$	80	$9.0 \times 10^{-6}$	75	18,430
$8 \times 10^{-7}$	$10^8$	80	$1.6 \times 10^{-6}$	96	14,600

fields of  $\geq 10^8$  volts/cm can only be obtained with very small apex radii, even in the absence of space charge, and (2) space charge effects become significant at currents of  $\geq 10^{-7}$  amperes. There is some trade-off between apex radius and  $V/V_o$ , as already pointed out, and also  $V_{cone}/V_{sphere}$  decreases with increasing  $r_a$  as indicated by Eq. (14). Nevertheless it seems clear that  $r_a$  values much in excess of  $100\text{\AA}$  would require voltages in considerable excess of experimentally observed values to produce the required apex fields. This conclusion is of considerable significance for ion-optic applications, since it implies a very small effective source size and consequent high brightness, as in fact observed experimentally. Since the apex is probably spheroidal rather than spherical, the effective source size is dependent on actual apex size.

We are also able now to estimate to what extent space charge can contribute to relaxation of the cone apex from infinite sharpness. From Eq. (1) we find for example if  $r_a = 2 \times 10^{-7}$  cm and  $\gamma = 700$  dynes/cm that the equilibrium field is  $E = 1.26 \times 10^8$  volts/cm. It is clear from Table II that even a modest current can suffice to reduce  $E_o$  to this value from that which would be present at  $V_c$  in the absence of space charge, say  $2 \times 10^8$  volts/cm. Thus such blunting as occurs seems to result entirely from reduction in apex field by space charge, rather than from any limitations on liquid supply, as already stated in an earlier section.

### Mechanisms of Current Generation and Stabilization

We are now ready to consider ion current formation from onset to high currents, as voltage is increased from 0. Clearly there can be no current at all below  $V_c$  since cone formation is a prerequisite. If the apex field at  $V_c$  (in the absence of ion current and hence space charge effects) is too small to allow field desorption, no ion current will be observed at  $V_c$ . Increases in  $V$  will then lead to droplet formation, possibly with concomitant ionization. This will be discussed in slightly greater detail in the next section. Assuming however that the apex field at  $V_c$  suffices for appreciable ion generation there will be a sharp onset of current at  $V_c$ . In the case of Ga, for instance the experimental onset value<sup>10</sup> appears to be 2-3 microamperes, and this implies that there will already be some space charge effects at onset. The cone apex will consequently assume a form corresponding to equilibrium between surface tension and electrostatic stress, the latter being reduced by space charge in the current generating region from the value which would obtain in the absence of current. As already pointed out the effective apex radius must be of the order of  $10-50\text{\AA}$  to account for the observed voltages required. In the current regime just beyond onset the mechanism of ionization must correspond to pure field desorption or evaporation, and consequently ion energy distributions will be narrow, and principally determined by quantum effects, i.e., uncertainties in the locus of ionization. These probably amount to  $\sim 1\text{eV}$ .

Emission in this current-voltage regime will be stable since space charge provides negative, i.e., stabilizing, feedback. If through some fluctuation  $r_a$  increases,  $E$  will decrease, and hence  $I$  will decrease. This causes a reduction in space charge so that  $E$  (for fixed  $V$ ) increases, pulls the apex into a sharper configuration (i.e., decreases  $r_a$ ), thereby causing more  $I$  and also more space charge screening, thus causing relaxation, etc.

We must consider next what happens as  $V$  is increased so that  $I$  increases to  $>10^{-5}$  amperes. It is found experimentally<sup>10</sup> for Ga, for instance, that the liquid cone is heated to  $>1000^\circ\text{C}$  at such currents. It is easy to show that ohmic heating at  $10^{-5}$  amperes is unimportant. (See, for instance, Swanson and Schwind<sup>8</sup>). On the other hand field desorption with short desorption times can lead to heating through an effect analogous to that observed when a solid is cleaved. The separation energy in that case always exceeds the surface energy of the surfaces created because the breaking of bonds can never be performed adiabatically and some energy is always imparted to the separated solids through "snapping back." In the present case, if the departing ion leaves very rapidly, the remanent liquid will not have time to assume its equilibrium configuration as the ion leaves. Thus the work of removing an ion exceeds the adiabatic value and the difference appears eventually as heat in the liquid. It turns out that only a very small amount of energy per ion formed is required to account for the temperature rises in fact observed at  $>10^{-5}$  amperes. Very approximately we have at steady state

$$K \frac{\Delta T}{x} = Q/\pi r_a^2 = \bar{Q} \quad (39)$$

where  $K$  is thermal conductivity,  $\Delta T$  the temperature rise at the apex,  $x$  a mean distance over which this rise decays,  $Q$  the heat generated per unit time and  $\bar{Q}$  the heat per unit time per unit area. Eq. (39) applies strictly speaking to a cylinder, not a truncated cone, but the correction factor will not exceed an order of magnitude. Taking liquid Ga as an example,  $K \approx 0.3$  watt sec<sup>-1</sup> cm<sup>-1</sup> deg<sup>-1</sup>. Taking  $x = 0.01$  cm we see that the required heat becomes, for  $\Delta T = 1000^\circ K$

$$\bar{Q} \approx 3 \times 10^4 = 10^{15} q\tau \quad \text{watts/sec/cm}^2 \quad (40)$$

where  $q$  is the heat generated per ion. Thus

$$\begin{aligned} q &= 3 \times 10^{-4} \tau \text{ ergs/atom} \\ &= 2 \times 10^{-8} \tau \text{ eV} \end{aligned} \quad (41)$$

If  $\tau = 10^{-12}$  sec,  $q = 2 \times 10^{-4}$  eV. Alternately (but equivalently, since  $i$ ,  $r_a$  and  $\tau$  are related by Eq. (32))

$$q \approx \frac{K\Delta t}{xi} \pi r_a^2 \times 1.6 \times 10^{-19} \quad (42)$$

where  $i$  is ion current. Taking  $i = 10^{-5}$  amperes we find

$$q = 10^{10} r_a^2 \text{ eV} \quad (43)$$

for  $r_a$  in cm. If  $r_a = 2 \times 10^{-7}$  cm,  $q = 4 \times 10^{-4}$  eV and for smaller radii  $q$  will be correspondingly smaller. This heating mechanism was pointed out to the author by Professor W. Kohn.

In the case of solids the relaxation can involve only elastic deformations. In the case of liquids on the other hand there is in addition an analogue to plastic deformation which can occur on the time scale of interest. If an atom were plucked out of a liquid surface by field evaporation the surface area would increase by  $\sim \pi r_{\text{atom}}^2 \approx 7 \times 10^{-16} \text{ cm}^2$  and the liquid would quickly get rid of this "hole", but not in the time of desorption. Thus there would be a relaxation energy of  $\gamma \pi r_{\text{atom}}^2$  ergs/ion, or for  $\gamma = 700 \text{ ergs/cm}^2$ ,  $5 \times 10^{-13} \text{ ergs/ion}$  or  $0.3 \text{ eV}$ . This value is probably an overestimate because of partial relaxation during field desorption. Further it should be remembered that the estimate of the required heat refers to a cylinder not a very blunt cone. Finally it must also be recalled that if the field is not high enough to allow field desorption with zero activation energy, the activation energy, which amounts to heat carried away by the desorbing particle, must be subtracted from the above value.

It is clear in any case that the effect just discussed can lead to sufficient heating to cause appreciable evaporation of neutral atoms. The discussion of space charge limited field desorption also indicates that the high currents obtained experimentally at voltages of order  $1.5 - 2V_c$  simply could not be obtained by field evaporation, since very much higher voltages would be needed to provide the required fields. Thus it seems clear that the high currents obtained at voltages above  $V_c$  must come from neutral atoms evaporated thermally and then ionized in some manner.

It is easy to find some limits on the product of area which must supply this vapor and the (equilibrium) vapor pressure involved. The evaporating flux from a surface at temperature  $T$  such that the equilibrium vapor pressure  $P$  is given by  $\dot{N}/A$

$$\dot{N}/A = P(2\pi mkT)^{-\frac{1}{2}} = 1.3 \times 10^{20} P_{\text{torr}} \text{ atoms/cm}^2/\text{sec} \quad (44)$$

for Ga at  $1300^{\circ}\text{K}$ , where  $A$  is area and  $P$  pressure. Thus if every evaporated atom were somehow ionized the resultant current would be

$$i_{\text{max}} = 21 P_{\text{torr}} \cdot A \text{ amperes} \quad (45)$$

Thus for  $i = 10^{-4}$  amperes,  $P \cdot A = 4.7 \times 10^{-6}$  torr- $\text{cm}^2$ . If  $P = 1$  torr, corresponding to  $T = 1350^{\circ}\text{C}$  for Ga,  $A = 4.7 \times 10^{-6} \text{ cm}^2$ , or if it is assumed to be given by  $\pi r^2$ ,  $r = 1.2 \times 10^{-3} \text{ cm}$ . If  $P = 760$  torr a value of  $r = 4 \times 10^{-5} \text{ cm}$  would result. Thus it is clear that an area much bigger than the hemispherical apex cap must contribute to current generation.

We show next that the ionization mechanism cannot be impact ionization of vapor by field desorbed ions. Let us assume for the moment that the pressure of vapor is uniform (which is, of course, incorrect) in order to estimate the mean free path with respect to excitation (or ionization). The cross section  $\sigma_i$  for inelastic collisions, i.e., electronic excitations in ion-atom collisions is  $\sigma_i = 10^{-19} - 10^{-20} \text{ cm}^2$  for ion energies in the range 1-5 KeV.<sup>19</sup> Since ions gain  $\sim 50\%$  of their final kinetic energy in  $\sim 10 r_a$  as indicated by Fig. 5 energies of the order of

0.1-5K eV are obviously the only ones of relevance. The mean free path for excitation is then  $\lambda_i$

$$\lambda_i = (\rho\sigma_i)^{-1} = kT/(P\sigma_i) \quad (46)$$

where  $\rho$  is gas density, or if  $P$  is expressed in torr

$$\lambda_i = 1.4 \times 10^{-16} / (\sigma P_{\text{torr}}) \quad (47)$$

where  $T = 1400\text{K}$  has been used. Thus, for  $\sigma = 10^{-19}\text{cm}^2$  we find, at  $P = 10^3$  torr (a value not likely to be achievable)  $\lambda_i = 1.4\text{cm}$ . If we assume that the region where vapor pressure is appreciable in dimensions of  $10^{-4}\text{ cm}$ , we see that  $10^{-4}$  ionizing collisions per field desorbed ion would occur. The situation would not be improved if  $P$  could somehow be raised: The cross-section for elastic collisions  $\sigma_e$  in which ion kinetic energy will be efficiently lost is  $\sigma_e \approx 10^{-15}\text{cm}^2$ , so that at  $P = 10^3$  torr the mean free path for elastic collisions is  $\lambda_e \approx 10^{-4}\text{ cm}$ . Increasing  $P$  would correspondingly decrease  $\lambda_e$  and thus ion kinetic energy, thereby increasing  $\lambda_i$ . Ion-atom collisions could therefore lead to substantial current increases only if every electron thereby released ionized on an average of  $10^5$  vapor atoms by avalanching. Since the cross-section for electron excitation is of order  $10^{-15}$  -  $10^{-16}\text{cm}^2$  (for electron energies of  $\sim 100\text{eV}$ ) and hence the mean free path for electron ionizing events also of order  $10^{-4}\text{ cm}$  at  $P = 10^3$  torr this seems impossible. Although the pressures to be expected in front of the apex can be substantially increased by polarization effects, it seems impossible to attain the values

necessary for impact ionization over a sufficient region of space to make this mechanism likely as a major contributor to current generation. At very high currents however, if secondary electrons from the cathode are able to reach the cone and its vicinity, electron impact ionization of metal vapor probably contributes substantially. Under these conditions however ion energies will show a wide spread, and the effective source size will also have increased substantially so that this regime is of little interest for ion-optical applications.

The most likely mechanism for current generation under conditions where space charge limited field evaporation cannot account for more than a fraction of the current is probably field ionization. The overall mechanism can be envisaged as follows. Metal atoms evaporating from the cone in the vicinity of the apex are drawn into the high field region by the polarization force,  $\frac{1}{2} \alpha \text{grad}E^2$  and are there field ionized. Thus supply from a region much larger than that corresponding to the immediate cone apex is utilized, and since impact ionization is not involved low steady state vapor densities present no difficulty. The electrons liberated by field ionization are accelerated to the cone and serve to heat it. The energy supplied in this way overcompensates that withdrawn by vaporization. The latter is  $\sim 5$  eV/atom; since the distances at which field ionization occurs probably lie between  $0.1 r_a$  and  $r_a$  from the surface the energy delivered per electron is necessarily much greater. The reason that runaway heating does not occur is probably that the total number of atoms evapo-

rating exceeds those being ionized by a sufficient factor. Under conditions where field ionization predominates, the field at the cone apex is probably reduced to the point where field desorption no longer occurs. Under conditions of appreciable space charge the potential drop between emitter and cathode is not concentrated near the emitter as in the absence of space charge but distributed over a larger distance (Fig. 5). Consequently high fields are also maintained over much larger distances, (Fig. 6) and sufficient fields for field ionization still to occur at  $1-5 r_a$  in front of the cone apex. The lifetime with respect to field ionization can be estimated very crudely<sup>17</sup> from

$$1/\tau = v_e e^{-6.8 \times 10^7 I^{3/2}/E} \quad (47)$$

where  $v_e$  is an electronic frequency,  $\sim 10^{15} \text{ sec}^{-1}$  and  $I$  the ionization potential of the atom being field ionized. For Ga  $I = 6 \text{ eV}$  and for  $E = 10^8 \text{ volts/cm}$   $\tau \approx 2 \times 10^{-11} \text{ sec}$ . In this time an atom moving with thermal velocity moves  $\sim 100 \text{ \AA}$ . In this distance the high field is not changing very much under space charge conditions and consequently the probability of field ionization is high.

Although the probability of impact ionization or excitations by ions is small as we have seen it should nevertheless suffice to account for the visible light seen for  $I > 10$  microamperes. At very high voltages and currents it is conceivable that pressures in the apex region are sufficiently high to allow enough multiplication of electron ionization to make field ionization

the minor and electron impact ionization the major current generating mechanism. As already indicated the primary source of electrons under these conditions may be secondaries released from the cathode under ion impact.

Unlike the electron emission case runaway is not observed for ion emission. The reason is that unlike the electron emission case there is sufficient negative feedback present in all regimes of ion emission. This is provided by space charge and by the fact that a decrease in apex field leads to an increase in apex radius, hence a further decrease in field and thus to decreases in emission which in turn reduce space charge thus lead to increases in field, etc. The reason space charge is effective in ion but not in electron emission is of course that the primary charge carriers in ion generation are massive and the counter charge carriers, which reduce space charge are light, with the opposite situation occurring in electron emission.

Although it seems certain that ion-atom collisions cannot contribute appreciably to ion current, such collisions may nevertheless lead to appreciable broadening of the ion energy distribution, since elastic and charge exchange collisions have very high cross-sections. Considerable broadening is also known to occur in field ionization<sup>17</sup> at high fields, since then the locus of ionization is distributed over an appreciable region of space, and hence of potential.

We must finally consider why it is possible to exceed the Taylor cone voltage  $V_c$  without destroying the cone. The

$$1394 \gamma^{\frac{1}{2}}/r^{\frac{1}{2}} < E_c \quad (48)$$

where  $E_c$  is the field for sufficient field desorption to give adequate space charge, i.e., to give a current of say  $10^{-6}$  amperes, and  $r$  is the radius of curvature of the cone slightly below its theoretical apex. If  $r$  is chosen as  $10^{-7}$  cm and  $\gamma = 700$  dynes/cm the left hand side of expression (48) gives  $E_c \leq 1.17 \cdot 10^8$  volts/cm. Thus very roughly we expect no droplet formation for metals for which the desorption field is of order 1 volt/ $\text{\AA}$  and would expect droplet formation for metals with appreciably higher evaporation fields.

#### CONCLUSION

The foregoing indicates that the processes entering into the operation of a liquid metal ion source are by no means simple and that at best a semiquantitative description of the various phenomena is possible. Nevertheless even a qualitative understanding of these sources is of some interest because of their potential value in ion optical applications of various kinds.

#### ACKNOWLEDGEMENTS

The author would like to thank Professor B. Carnahan for carrying out the computer solution of the space charge equation, and Professor W. Kohn for stimulating discussions. He would also like to thank Dr. L. W. Swanson for making available numerous results before publication. This research was supported by the

answer can be given only qualitatively, but must be that under space charge conditions the field is concentrated in the space charge region, i.e., lines of force are so concentrated that the field on the cone surface does not appreciably exceed the Taylor field. It is obviously not practical to attempt a calculation of equilibrium shape under space charge conditions without far more detailed knowledge of the actual current distribution than is available at present.

#### Droplet Formation

Finally droplet formation must be discussed since its occurrence is undesirable for ion formation but desirable if the object is "atomization," that is the deliberate formation of small droplets. It is clear that droplets must form if the field at the cone apex and down-shank from it exceeds the critical field. Thus, if at  $V_c$  the field in the apex region is insufficient for enough field evaporation to produce appreciable space charge, the cone apex will be pulled out into a jet and when the length of the latter exceeds  $2\pi r$ , where  $r$  is the jet radius, necking off and hence droplet formation will occur in accordance with well known classical theory.<sup>20</sup> It should be noted that the field at the apex is (in theory) infinite but of course this region has dimensions of less than a single atom. Thus the criterion just spelled out applies to the region immediately adjacent to the theoretical cone apex. Formally we may write from Eqs. (2), (3) and (4) that droplets will form if

Defense Advanced Research Projects Agency of the Department of Defense under Contract No. MDA903-76C-0250 with the University of Michigan.

### References

1. D. S. Swatik and C. D. Hendricks, AIAA J. 6, 1596 (1968).
2. J. F. Mahoney, A. T. Yahiku, H. L. Daley, R. D. Moore and J. Perel, J. Appl. Phys. 40, 5101 (1969).
3. B. W. Colby and C. A. Evans, Jr., Anal. Chem. 45, 1887 (1973).
4. V. E. Krohn and G. R. Ringo, Appl. Phys. Let. 27, 479 (1975).
5. R. Clampitt, K. L. Aitken, D. K. Jefferies, J. Vac. Sci. Technol. 12, 1208 (1975).
6. R. Clampitt, D. K. Jefferies, Nucl. Inst. and Methods 149, 739 (1978).
7. R. Clampitt, D. K. Jefferies, Inst. Phys. Conf. Ser. 38, 12 (1978).
8. L. W. Swanson and G. A. Schwind, J. Appl. Phys. (in press).
9. G. I. Taylor, Proc. Roy. Soc. (London) A280, 383 (1964).
10. L. W. Swanson, private communication.
11. W. W. Dolan, W. P. Dyke and J. K. Trolan, Phys. Rev. 91, 1504 (1953).
12. W. P. Dyke, J. K. Trolan, W. W. Dolan and G. Barnes, J. Appl. Phys. 24, 570 (1953).
13. E. W. Müller, Phys. Rev. 102, 618 (1956).
14. R. Gomer, J. Chem. Phys. 31, 341 (1959).
15. R. Gomer and L. W. Swanson, J. Chem. Phys. 38, 1613 (1963).
16. D. G. Brandon, Field Ion Microscopy, J. H. Hren and S. Ranganathan, eds., Plenum Press, N.Y., (1968), p. 28.
17. R. Gomer, Field Emission and Field Ionization, Harvard Press, Cambridge (1960).
18. I. Langmuir and K. T. Compton, Rev. Mol. Phys. 13, 191 (1931).
19. H. S. W. Massey and H. B. Gilbody, Electronic and Ionic Impact Phenomena, Vol. 4, Oxford Press (Oxford) (1974).
20. A. W. Adamson, Physical Chemistry of Surfaces, 3rd Ed., Wiley, N.Y. (1976).

DYNAMIC ELASTIC CRACK TIP STRESSES AND DISPLACEMENTS  
FOR COMPUTING FRACTURE

F. A. McClintock

ABSTRACT

For dynamic crack growth calculations in an elastic, homogeneous material, the crack velocity should be taken to be a function of the dynamic stress singularity. Existing equations for the necessary stress and displacement fields are plotted to show the very marked distortion that increases from 10% at 1/3 the Rayleigh wave velocity  $c_R$  to a factor of 2 at  $2/3 c_R$ . The crack opening between elements just behind the crack tip can be used with these results to obtain the dynamic stress singularity, and hence, from test data, the current crack velocity.

# DYNAMIC ELASTIC CRACK TIP STRESSES AND DISPLACEMENTS

## FOR COMPUTING FRACTURE

F. A. McClintock

### INTRODUCTION

A number of computer codes can treat elasto-dynamic problems in considerable detail. For brittle fracture, however, they often simply postulate that fracture occurs in an element when the stress in that element reaches a critical value. Such a criterion implies a value of the critical stress intensity factor which depends on the cell size of the finite element or finite difference code. For instance, for static elastic cracking, a square element of size  $d$  adjacent to a crack with stress intensity  $K_I$  will experience a stress at its center of

$$\sigma_{22} = K_I / \sqrt{2\pi(d/2)} . \quad (1)$$

With a critical fracture stress criterion, then, the critical stress intensity factor is in effect being assumed to be set by the fracture stress  $\sigma_f$  and cell size  $d$  from Eq. (1):

$$K_{Ic} = \sigma_f \sqrt{\pi d} . \quad (2)$$

Many static elastic codes account for this by introducing special elements which allow calculating the stress intensity factor in terms of the displacements of nearby elements (the

displacements seem to give better results than using the stresses in nearby elements).

For Mode I the stress singularity for a dynamic crack (Rice, 1968) and the general solution for a growing crack (Tsai, 1974) are already known. Plots for individual stress components have been presented for both orthotropy and isotropy (Achenbach and Bazant, 1975). It is the object of this note to gather the complete set of isotropic equations for the singularities in stress and displacement, to plot the results in more pictorial form, and incidentally to discuss the limitating behavior as the Reynolds number approaches unity.

#### Stress Fields Around Tips of Growing Cracks

The dynamic elastic stress and displacement fields for Mode I involve the ratio of shear wave speed  $c_s$  to uniaxial strain (longitudinal) wave speed,  $c_\ell$ , which is obtained from the ratio of shear to uniaxial strain moduli:

$$c_s/c_\ell = \sqrt{G(1+\nu)(1-2\nu)/(E(1\nu))} = \sqrt{(1-2\nu)/(2(1-\nu))} . \quad (3)$$

Consider physical  $x_1$ ,  $x_2$  and  $r$ ,  $\theta$  coordinates fixed to the tip of the crack, moving in the  $x_1$  direction:

$$x_1 = r \cos \theta, \quad x_2 = r \sin \theta . \quad (4)$$

It is convenient to define relativistic coordinates in terms of lateral contraction ratios, expressed in terms of the crack velocity  $V$  relative to the wave speeds:

$$\alpha_l^2 = 1 - (V/c_l)^2 , \quad (5)$$

$$\alpha_s^2 = 1 - (V/c_s)^2 .$$

Dilational and shear contracted coordinates are now defined:

$$\begin{aligned} \rho_l &\equiv r_l/r \equiv (\cos^2\theta + \alpha_l^2 \sin^2\theta)^{\frac{1}{2}}, & \theta_l &\equiv \tan^{-1}(\alpha_l \tan\theta) , \\ \rho_s &\equiv r_s/r \equiv (\cos^2\theta + \alpha_s^2 \sin^2\theta)^{\frac{1}{2}}, & \theta_s &\equiv \tan^{-1}(\alpha_s \tan\theta) . \end{aligned} \quad (6)$$

A constant coefficient D is in turn defined in terms of the contraction ratios:

$$D = (4\alpha_s \alpha_l - (1+\alpha_s^2)^2)/(1+\alpha_s^2) . \quad (7)$$

The results may be normalized in terms of the applied stress intensity  $K_I$  and radius r. Alternatively, for Mode I this normalization can be expressed through the approximate static plastic zone found from the elastic stress field. In terms of the tensile yield strength Y, define

$$r_{YI} = (K_I/Y)^2/(2\pi) . \quad (8)$$

(Numerical elastic-plastic results in Mode I, e.g., by Tracey (1976) give a maximum radius only about 10% larger than this.) Normalized this way, Rice (1968) gives the stress as

$$\frac{\sigma_{11}^I}{K_I/\sqrt{2\pi r}} = \frac{\sigma_{11}^I}{Y} \sqrt{\frac{r}{r_{YI}}} \equiv S_{11}^I = \frac{1}{D} \left[ (1+2\alpha_l^2 - \alpha_s^2) \frac{\cos(\theta_l/2)}{\rho_l^{\frac{1}{2}}} - \frac{4\alpha_s \alpha_l}{1+\alpha_s^2} \frac{\cos(\theta_s/2)}{\rho_s^{\frac{1}{2}}} \right] ,$$

$$\frac{\sigma_{22}^I}{K_I/\sqrt{2\pi r}} = \frac{\sigma_{22}^I}{Y} \sqrt{\frac{r}{r_{YI}}} \equiv S_{22}^I = \frac{1}{D} \left[ -(1+\alpha_s^2) \frac{\cos(\theta_l/2)}{\rho_l^{\frac{1}{2}}} + \frac{4\alpha_s \alpha_l}{1+\alpha_s^2} \frac{\cos(\theta_s/2)}{\rho_s^{\frac{1}{2}}} \right] ,$$

$$\frac{\sigma_{12}^I}{K_I/\sqrt{2\pi r}} = \frac{\sigma_{12}^I}{Y} \sqrt{\frac{r}{r_{YI}}} \equiv s_{12}^I = \frac{1}{D} \left[ 2 \left( \frac{\sin(\theta_\ell/2)}{\rho_\ell^{\frac{1}{2}}} - \frac{\sin(\theta_s/2)}{\rho_s^{\frac{1}{2}}} \right) \right]. \quad (9)$$

Note that in the limit as  $V/c \rightarrow 0$ , from Eqs. (5) and (7)

$$\begin{aligned} D &\rightarrow \left[ 4(1 - (V/c_s)^2/2)(1 - (V/c_\ell)^2/2) - (1 + 1 - (V/c_s)^2)^2 \right] / (1 + 1 - (V/c_s)^2) \\ &\rightarrow (V/c_s)^2 - (V/c_\ell)^2. \end{aligned} \quad (10)$$

Terms of similar order must be kept in the numerator to recover the static stress distribution.

For Mode II, Freund (1975) reports results that can be cast in the form

$$\begin{aligned} \frac{\sigma_{11}^{II}}{K_{II}/\sqrt{2\pi r}} &= \frac{\sigma_{11}^{II}}{Y} \sqrt{\frac{r}{r_{YII}}} \equiv s_{11}^{II} = \frac{-2\alpha_s}{D} \left[ \frac{1+2\alpha_\ell^2-\alpha_s^2}{1+\alpha_s^2} \frac{\sin(\theta_\ell/2)}{\rho_\ell^{\frac{1}{2}}} - \frac{\sin(\theta_s/2)}{\rho_s^{\frac{1}{2}}} \right], \\ \frac{\sigma_{22}^{II}}{K_{II}/\sqrt{2\pi r}} &= \frac{\sigma_{22}^{II}}{Y} \sqrt{\frac{r}{r_{YII}}} \equiv s_{22}^{II} = \frac{-2\alpha_s}{D} \left[ \frac{-\sin(\theta_\ell/2)}{\rho_\ell^{\frac{1}{2}}} + \frac{\sin(\theta_s/2)}{\rho_s^{\frac{1}{2}}} \right], \\ \frac{\sigma_{12}^{II}}{K_{II}/\sqrt{2\pi r}} &= \frac{\sigma_{12}^{II}}{Y} \sqrt{\frac{r}{r_{YII}}} = s_{12}^{II} = \frac{-2\alpha_s}{D} \left[ - \frac{2\alpha_\ell}{(1+\alpha_s^2)} \frac{\cos(\theta_\ell/2)}{\rho_\ell^{\frac{1}{2}}} \right. \\ &\quad \left. + \frac{(1+\alpha_s^2)}{2\alpha_s} \frac{\cos(\theta_s/2)}{\rho_s^{\frac{1}{2}}} \right], \end{aligned} \quad (11)$$

where  $r_{YII}$  is defined as  $K_{II}^2/(2\pi Y^2)$  and is about 1/3 the apparent plastic zone size calculated from the purely elastic distribution. For either mode in plane strain, the out-of-plane normal stress is

$$\sigma_{33} = v(\sigma_{11} + \sigma_{22}) . \quad (12)$$

Pending elastic-plastic and preferably strain-rate dependent solutions for cracks traveling at an appreciable fraction of sound speed, it may be helpful to visualize the stress with the contour lines at which yield would be exceeded if the elastic solution were valid. For Mode I static cracks this procedure, illustrated by McClintock and Irwin (1965), gave results which were surprisingly close to the numerical calculations of Levy et al. (1971) and Tracey (1976), perhaps because the plastic flow is off to the side. For Mode III, where as here the high equivalent stress is ahead of the crack, the actual plastic zone extends twice as far as expected from the elastic solution alone (McClintock and Irwin, 1969; Chitaley and McClintock, 1971). In any event, for both modes considered here, the yield criteria are

$$\left(\frac{\sigma}{Y}\right)^2 = \frac{r_{YI,II}}{r} \left[ \frac{1}{2} \left( (S_{11} - S_{22})^2 + (S_{22} - S_{33})^2 + (S_{33} - S_{11})^2 \right) + 3(S_{12})^2 \right]. \quad (13)$$

The non-dimensional apparent yield radii  $(r_Y/r_{YI})$  and  $(r_Y/r_{YII})$  are found as functions of  $\theta$  by equating Eq. (13) to unity, and introducing  $S_{ij}^I$  or  $S_{ij}^{II}$ , as desired.

#### Displacement Fields Around Tips of Growing Cracks

The displacement fields are useful in numerical calculations. For Mode I, Rice's (1968) Eqs. (145) and (146) give the functions  $\Phi$  and  $\Psi$  for the irrotational and solenoidal parts of displacement field in terms of the contracted coordinates and two coefficients A and B by

$$\frac{\Phi_0}{A} = r_l^{3/2} \cos \frac{3}{2} \theta_l, \quad \frac{\Psi_0}{A} = - \frac{B}{A} r_s^{3/2} \sin \frac{3}{2} \theta_l, \quad (14)$$

where in terms of the coefficient D of Eq. (7),

$$A = \frac{4}{3} \frac{K_I}{3\sqrt{2\pi}GD} \quad \text{and} \quad \frac{B}{A} = \frac{2\alpha_l}{1+\alpha_s^2}. \quad (15)$$

In terms of these functions, the displacement components are

$$u_1 = \frac{\partial \Phi_0}{\partial x_1} + \frac{\partial \Psi_0}{\partial x_2}, \quad u_2 = \frac{\partial \Phi_0}{\partial x_2} - \frac{\partial \Psi_0}{\partial x_1}. \quad (16)$$

A change of variable gives the derivatives in terms of the contracted coordinates of Eq. (6). For example,

$$\frac{\partial \Phi_0}{\partial x_1} = \frac{\partial \Phi_0}{\partial r_l} \frac{\partial r_l}{\partial x_1} + \frac{\partial \Phi_0}{\partial \theta_l} \frac{\partial \theta_l}{\partial x_1}. \quad (17)$$

The derivatives are found from the contracted coordinates expressed as functions of the original coordinates and the contraction ratios. For example, for the uniaxial strain (longitudinal) coordinates  $r_l, \theta_l$ ,

$$\begin{aligned} \frac{\partial r_l}{\partial x_1} &= x_1/r_l = \cos \theta_l, & \frac{\partial r_l}{\partial x_2} &= \alpha_l^2 x_2/r_l = \alpha_l \sin \theta_l, \\ \frac{\partial \theta_l}{\partial x_1} &= -\alpha_l x_2/r_l^2 = -\sin \theta_l/r_l, & \frac{\partial \theta_l}{\partial x_2} &= \alpha_l x_1/r_l^2 = \alpha_l \cos \theta_l/r_l. \end{aligned} \quad (18)$$

Carrying out the indicated operations and introducing the trigonometric identities for sums and differences of angles gives the four derivatives:

$$\begin{aligned}\frac{\partial \Phi_0}{\partial x_1} &= \frac{3}{2} r_\ell^{\frac{1}{2}} \cos(\theta_\ell/2), \quad \frac{\partial \Phi_0}{\partial x_2} = \frac{3}{2} r_\ell^{\frac{1}{2}} \alpha_\ell \sin(\theta_\ell/2) \\ \frac{\partial \Psi_0}{\partial x_1} &= -\frac{3}{2} \frac{B}{A} r_s^{\frac{1}{2}} \sin(\theta_s/2), \quad \frac{1}{A} \frac{\partial \Psi_0}{\partial x_2} = -\frac{3}{2} \frac{B}{A} r_s^{\frac{1}{2}} \alpha_s \cos(\theta_s/2).\end{aligned}\quad (19)$$

It is convenient to express the displacements by normalizing them in terms of the nominal static yield radius multiplied by yield strain. Dividing out also by the dimensionless radius and introducing the definitions of A and B (Eqs. 15) yields non-dimensional displacements as functions only of contracted coordinates:

$$\begin{aligned}\frac{u_1^I}{\sqrt{r/2\pi} K_I/E} &= \frac{u_1^I}{r_{YI}(Y/E)(r/r_{YI})^{\frac{1}{2}}} = \frac{4(1+\nu)}{D} \left( \rho_\ell^{\frac{1}{2}} \cos \frac{\theta_\ell}{2} - \frac{2\alpha_\ell}{1+\alpha_s^2} \rho_s^{\frac{1}{2}} \alpha_s \cos \frac{\theta_s}{2} \right), \\ \frac{u_2^I}{\sqrt{r/2\pi} K_I/E} &= \frac{u_2^I}{r_{YI}(Y/E)(r/r_{YI})^{\frac{1}{2}}} = \frac{4(1+\nu)}{D} \left( -\rho_\ell^{\frac{1}{2}} \alpha_\ell \sin \frac{\theta_\ell}{2} + \frac{2\alpha_\ell}{1+\alpha_s^2} \rho_s^{\frac{1}{2}} \sin \frac{\theta_s}{2} \right).\end{aligned}$$

Again terms of order  $(V/c)^2$  must be kept in the numerator to recover the static displacement field.

For Mode II, Freund (1975) gives the displacements, which may be presented in the form

$$\begin{aligned}\frac{u_1}{\sqrt{r/2\pi} K_{II}/E} &= \frac{u_1}{r_{YII}(Y/E)(r/r_{YII})^{\frac{1}{2}}} = \frac{4(1+\nu)\alpha_s}{D} \left[ \frac{2}{1+\alpha_s^2} \rho_\ell^{\frac{1}{2}} \sin(\theta_\ell/2) \right. \\ &\quad \left. - \rho_s^{\frac{1}{2}} \sin(\theta_s/2) \right] \\ \frac{u_2}{r_{YII}(Y/E)(r/r_{YII})^{\frac{1}{2}}} &= \frac{4(1+\nu)}{D} \left[ \frac{2\alpha_\ell \alpha_s}{1+\alpha_s^2} \rho_\ell^{\frac{1}{2}} \cos(\theta_\ell/2) - \rho_s^{\frac{1}{2}} \cos(\theta_s/2) \right]\end{aligned}\quad (21)$$

## Results

The stress and displacement fields were evaluated for constant fractions of the Rayleigh (surface) wave speed, related to the shear wave speed by a cubic equation which can be stated in the form (Flügge, 1962)

$$c_R^2/c_s^2 = 1 - \frac{(2-c_R^2/c_s^2)^4}{16(1-(c_R^2/c_s^2)(c_s^2/c^2))} . \quad (22)$$

Rather than solve the cubic of Eq. (22), it seemed quicker to evaluate it by successive approximations, initially using an approximation of 0.9 in the right hand side, and then repeatedly substituting the result into the right hand side until convergence, using a programmable calculator.

The stresses and displacements for Modes I and II, from Eqs. (9), (11), (13), (20), and (21), are presented in Tables 1.1 and 1.2 for various Mach numbers relative to the Rayleigh wave velocity,  $c_R$ . Values of Poisson's ratio were taken at regular intervals corresponding roughly to ionic solids ( $\nu = 2/8$ ), steel ( $\nu = 2/7$ ), and aluminum ( $\nu = 2/6$ ). Since the effect of Poisson's ratio was regular, and only changed the results by 10% from the median value, its effect is given in Tables 2.1 and 2.2 only for  $\nu/c_R = 0.01$  and  $0.99$ .

The stress is of interest primarily for a fracture criterion, which really depends on non-linear atomic or plastic processes. Because these are still uncertain, and may depend on shear as well as normal components on either radial or arbitrary

planes, we present complete information on the stress in pictorial form, Figs. 1 and 2. The yield tendency is indicated by the normalized radius at which yield would occur if the elastic stress distribution held (Fig. 1). Statically the stress is biaxial in front of the crack and the only yield tendency comes from out-of-plane strain due to compressibility. At high Mach numbers it appears that the shear stress above and below the crack tip has less effect on the material ahead of the crack, so the circumferential stress falls off, leaving uniaxial tension in front of the crack. This gives a tongue of apparent yielding, an extended zone ahead of the crack. In the limit at high speeds, the radii to the apparent plastic zone vary as  $1/(1-V/c_R)^2$ , and the stress at a given radius as  $1/(1-Vc_R)$ .

The components of stress are illustrated by the principal stress vectors at the apparent elastic-plastic boundary, shown in Fig. 2. Large values occur where the stress is nearly biaxial, and the plastic zone is close to the crack tip. In the limit as  $V/c_R \rightarrow 1$ , the stress is almost, but definitely not quite, biaxial for  $\theta$  between  $72^\circ$  and  $73^\circ$ . There are sudden changes in principal stress directions wherever the stress is nearly biaxial, but the stress components still vary gradually.

The displacement field, like the stress field, is relatively unaffected for Rayleigh Mach numbers below 0.4. Above that speed the displacements increase, ultimately varying as  $1/(1-V/c_R)$ . The displacements in front of the crack then become

drawn in, as expected from the uniaxial stress field that develops there.

The results for Mode II are presented in Table 1.2 and Figs. 5-8. Again the stress and displacement vary in the limit as  $1/(1-V/c_R)$ , shear effects do not penetrate far ahead of the crack tip, and there is a rather sudden change in the displacement field near  $V/c_R = 0.9$ , before settling down to the limit. The results agree with the plots of Achenbach and Bazant (1975) obtained from the limiting orthotropic case, except for their apparent error in the sign of  $u_2$ . A downward displacement in front of the crack is necessary to match the static limit (e.g., Rice, 1968, and others) and, considering the curvilinear coordinates, to give the positive shear stress which is found.

#### Use of the Dynamic Stress and Displacement Fields

In interpreting test data, the applied loads and the macroscopic crack geometry are known. Hence a dynamic numerical analysis provides displacements near the crack tip. Displacements might also be obtained experimentally. Equations (20) and (21) should then yield the dynamic stress intensity factors,  $K_{Id}$  and  $K_{IId}$ , for that velocity. From a series of specimens at different applied loads, or from a single specimen with relatively slowly varying velocity, the dependence of  $K_d$  on crack Mach number can be obtained.

To use these data predictively, one could use a set of relative displacement components at radii  $r$  around the crack tip to provide an estimate of  $K$  from the extrapolated crack position

and velocity:  $u(K, r, V)$ . The subsequent crack velocity would then be found from the stress intensity factor. The process could be iterated.

It does not appear that the fracture criteria required to predict crack branching are available. What is needed is to apply computer codes to some of the best experiments available and see what fracture criteria will adequately predict the mirror surface, the roughening region, observed crack velocities, and forking, as well as, for example, the breaking out of a chip at the back side of a specimen (Kinra and Kolsky, 1976). (The reader can observe the phenomenon by breaking a piece of chalk.) With these predictions made and verified, one should have fair faith in the fracture criteria and in the code.

### Conclusions

Dynamic effects reach 10% at about  $1/3$  the Rayleigh wave velocity ( $1/5$  the uniaxial strain or longitudinal wave velocity). They reach a factor of 2 at about  $2/3$  the Rayleigh ( $2/5$  the longitudinal) wave velocity. In the limit, stress and displacement vary as  $1/(1-V/c_R)$ .

The main distortion of the stress field consists of a uniaxial stress ahead of the crack, in the direction of crack growth, tending to produce a tongue of plastic strain.

It appears possible to find stress intensity as a function of velocity from experiments by measuring or analyzing for displacements behind the tip of a growing crack. Such data could then be used in numerical calculations to predict crack

velocity as a function of load history in untested parts.

Questions of micro or macro crack branching await the combination of such studies with fracture criteria, to see whether the usual assumption of cracking at a critical intensity on a radial plane is still adequate.

#### ACKNOWLEDGEMENTS

This research was supported by the Defense Advanced Research Projects Agency of the Department of Defense under Contract No. MDA903-76C-0250 with The University of Michigan.

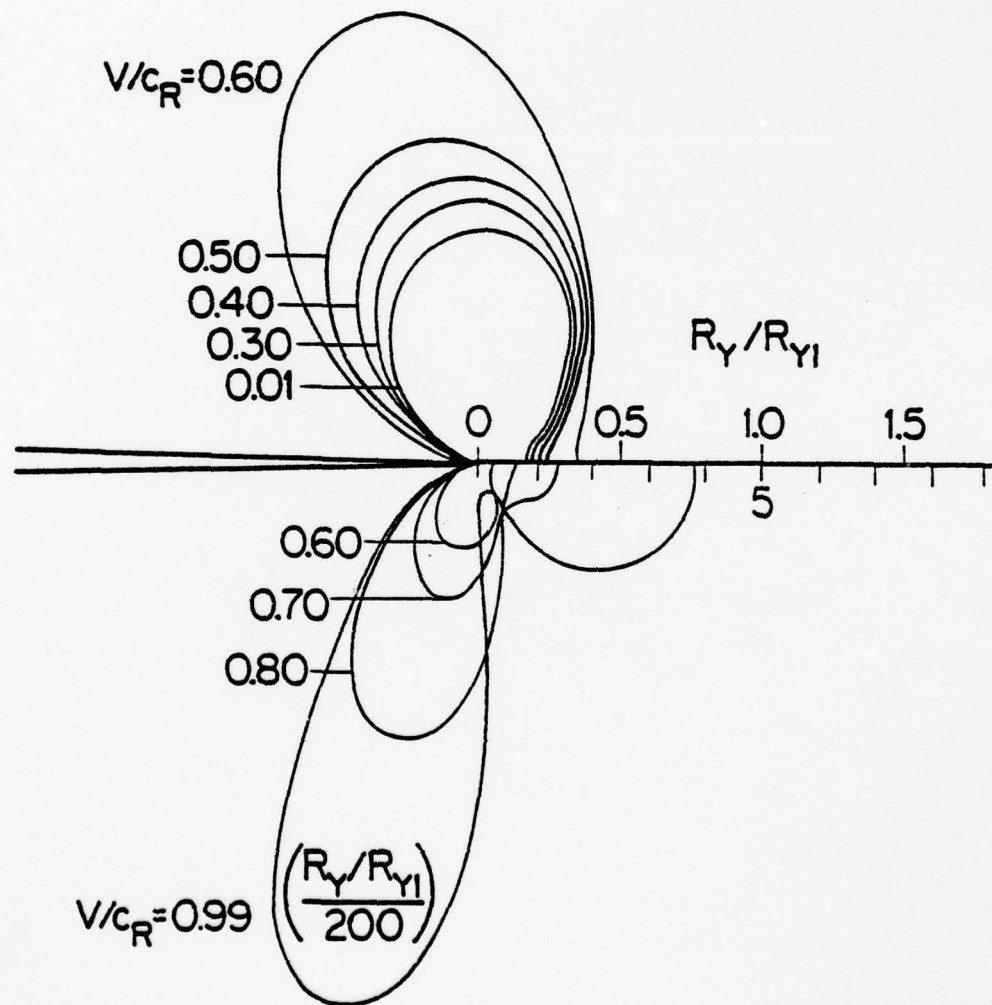


Figure 1. Apparent plastic zone radius for Mode I normalized by static value  $R_{YI} = (K_I/Y)^2/2\pi$ .  $\nu = 2/7$ .

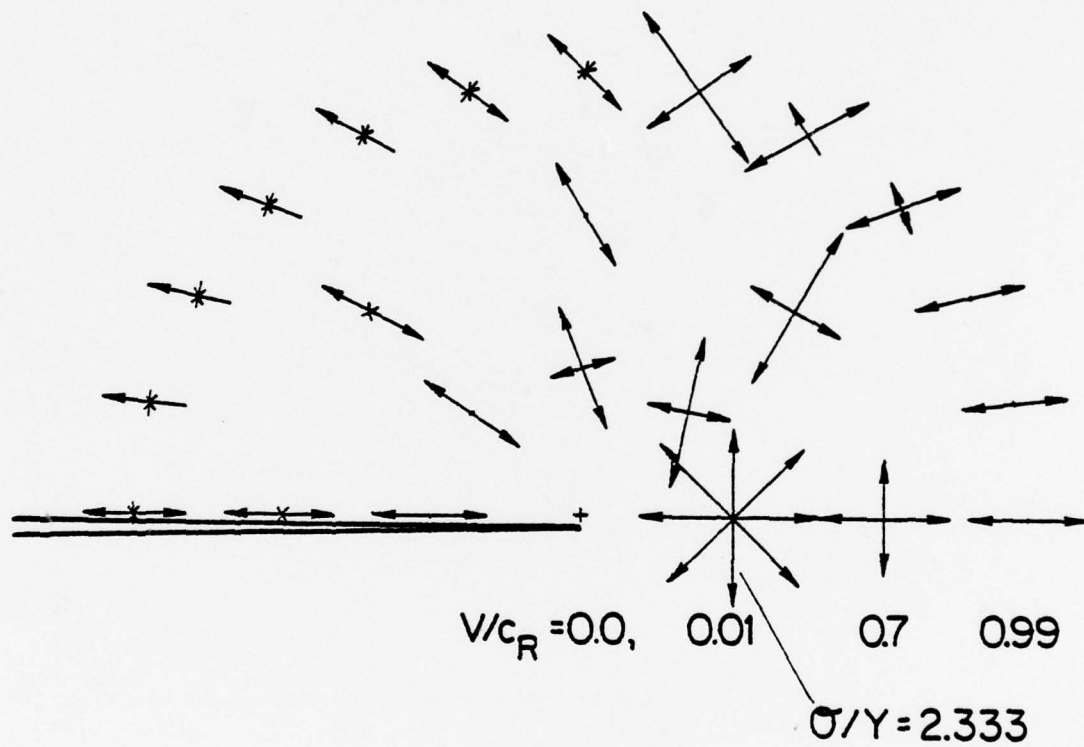


Figure 2. Principal stress components at apparent yield for Mode I,  $\sigma_1/Y$ ,  $\sigma_2/Y$ .  $\nu = 2/7$ .

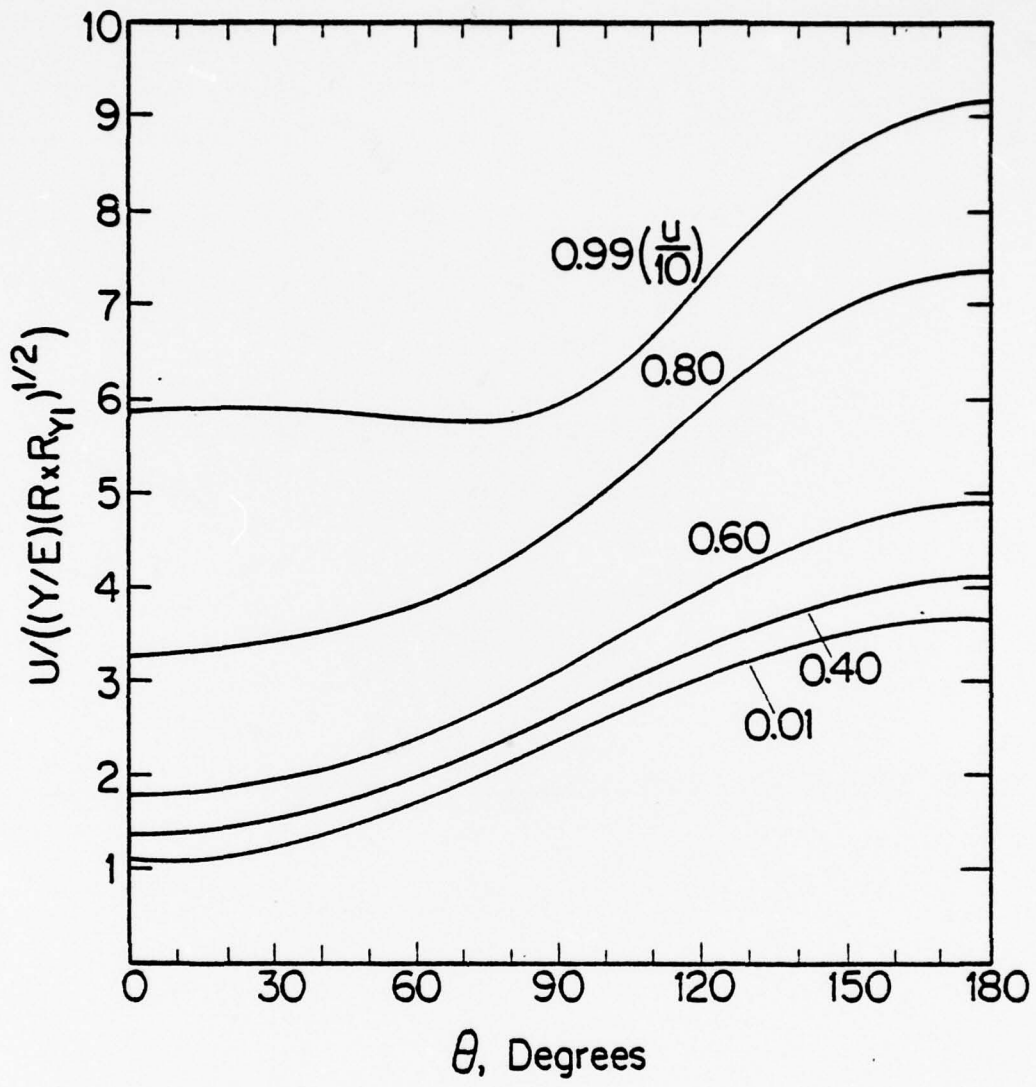


Figure 3. Normalized displacement magnitudes for Mode I,  
 $v = 2/7$ .

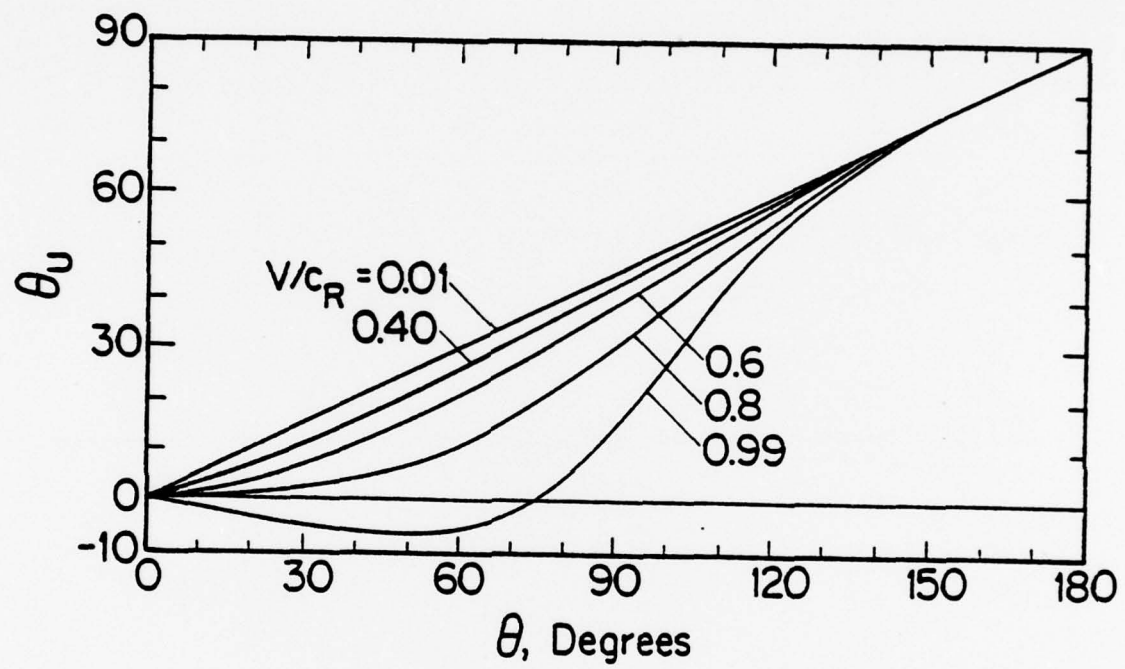


Figure 4. Displacement directions for Mode I,  $v = 2/7$ .

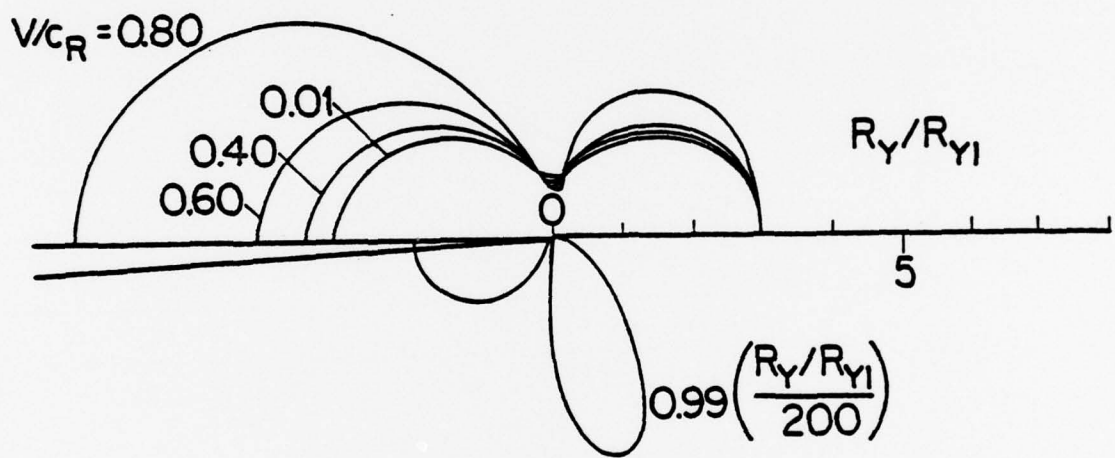


Figure 5. Apparent plastic zone radius for Mode II normalized by static value  $R_{YI} = (K_I/Y)^2/2\pi$ .  $\nu = 2/7$ .

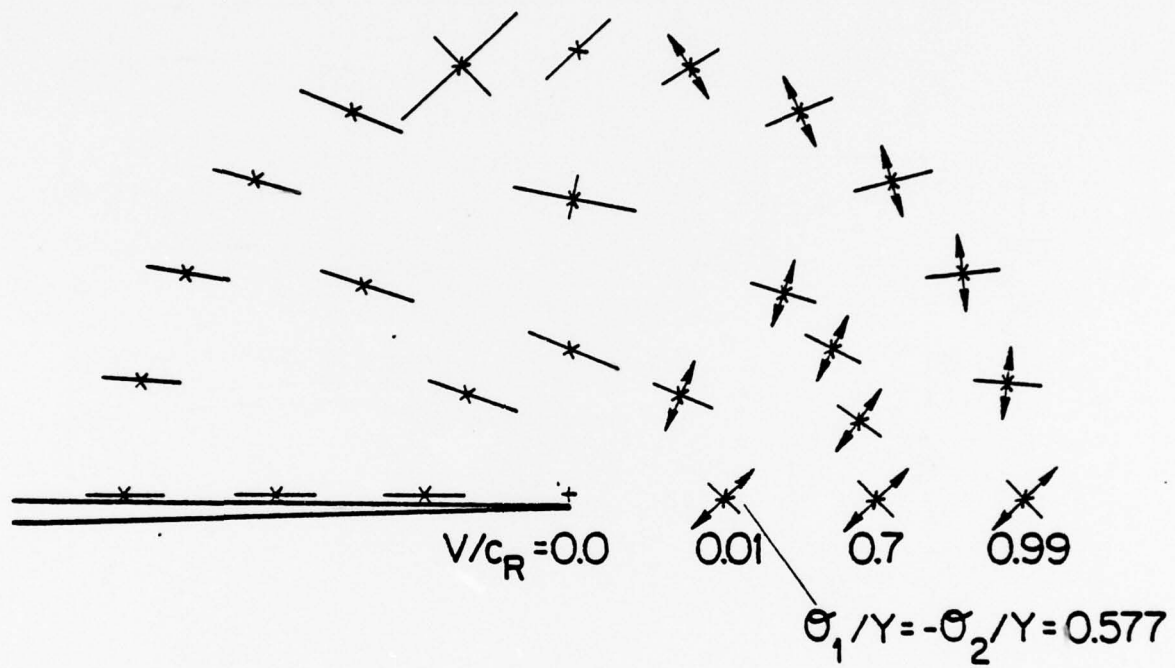


Figure 6. Principal stress components at apparent yield for Mode II,  $\sigma_1/Y$ ,  $\sigma_2/Y$ .  $\nu = 2/7$ .

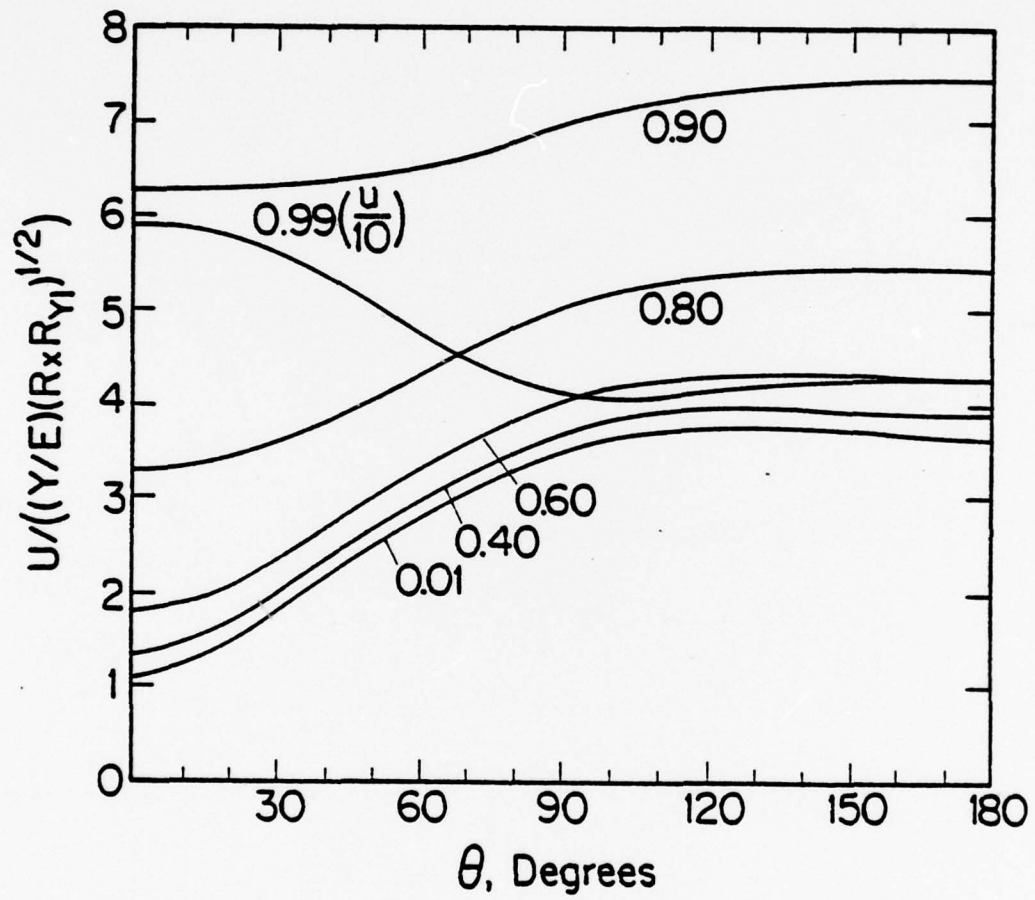


Figure 7. Normalized displacement magnitudes for Mode II,  
 $v = 2/7$ .

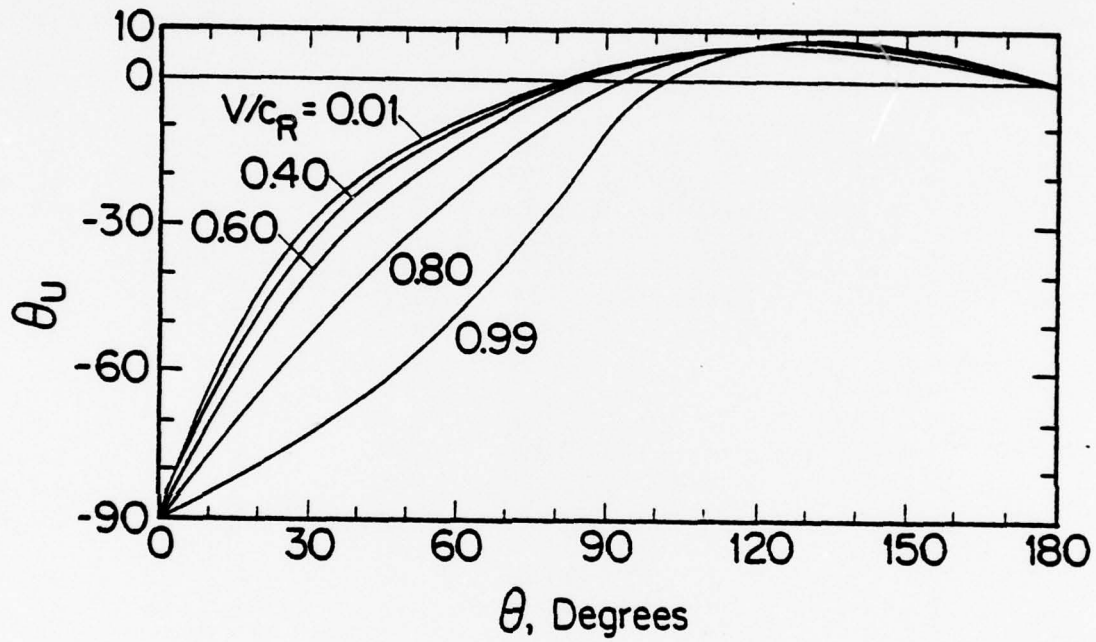


Figure 8. Displacement directions for Mode II,  $v = 2/7$ .

TABLE 1.1 STRESS AND DISPLACEMENT FOR DYNAMIC MODE I CRACK TIP

POISSON'S RATIO, NU = 2/7, CR/CL = 0.506734, CR/CS = 0.925165

$$((\text{PRIM STRESS})/Y)(R/RYI)^{0.5} \quad U/((Y/E)(R+RYI)^{0.5})$$

THETA	RY/RYI	S1	S2	THETA 1	U	THETA U
<i>V/CR = 0.01</i>						
0.1	0.1837	2.3354	2.3313	44.0	1.1022	0.0
15.0	0.2308	2.3332	1.7945	56.2	1.1460	7.5
30.0	0.3589	2.0298	1.1952	67.5	1.2744	15.0
45.0	0.5318	1.7518	0.7821	78.7	1.4787	22.5
60.0	0.7003	1.5524	0.5175	90.0	1.7450	30.0
75.0	0.8154	1.4135	0.3437	101.3	2.0551	37.5
90.0	0.8419	1.3156	0.2257	112.5	2.3879	45.0
105.0	0.7679	1.2459	0.1435	123.8	2.7207	52.5
120.0	0.6085	1.1961	0.0858	135.0	3.0308	60.0
135.0	0.4020	1.1613	0.0459	146.3	3.2971	67.5
150.0	0.1998	1.1383	0.0197	157.5	3.5014	75.0
165.0	0.0534	1.1251	0.0048	168.8	3.6299	82.5
179.9	0.0000	1.1209	-0.0000	179.9	3.6737	90.0
<i>V/CR = 0.30</i>						
0.1	0.1993	2.3880	2.2402	0.8	1.2232	0.0
15.0	0.2427	2.3418	1.8188	49.0	1.2651	6.5
30.0	0.3636	2.0644	1.2519	64.1	1.3888	13.3
45.0	0.5367	1.7862	0.8300	77.0	1.5889	20.4
60.0	0.7238	1.5723	0.5430	89.5	1.8551	27.9
75.0	0.8774	1.4153	0.3460	101.7	2.1723	35.7
90.0	0.9461	1.3016	0.2091	113.6	2.5199	43.6
105.0	0.8929	1.2210	0.1147	125.2	2.8734	51.6
120.0	0.7201	1.1660	0.0512	136.5	3.2063	59.5
135.0	0.4763	1.1302	0.0106	147.5	3.4938	67.3
150.0	0.2347	1.1087	-0.0138	158.4	3.7147	74.9
165.0	0.0621	1.0974	-0.0265	169.2	3.8535	82.5
179.9	0.0000	1.0939	-0.0304	179.9	3.9008	90.0
<i>V/CR = 0.40</i>						
0.1	0.2199	2.4037	2.1325	0.4	1.3355	0.0
15.0	0.2595	2.3374	1.8064	42.6	1.3758	5.7
30.0	0.3723	2.0881	1.2919	60.9	1.4958	11.9
45.0	0.5418	1.8165	0.8729	75.4	1.6920	18.7
60.0	0.7429	1.5916	0.5680	89.0	1.9576	26.2
75.0	0.9338	1.4179	0.3492	102.0	2.2804	34.2
90.0	1.0487	1.2895	0.1948	114.5	2.6407	42.5
105.0	1.0203	1.1999	0.0902	126.4	3.0126	50.8
120.0	0.8340	1.1413	0.0232	137.7	3.3661	59.0
135.0	0.5508	1.1057	-0.0172	148.5	3.6727	67.1
150.0	0.2690	1.0858	-0.0395	159.1	3.9086	74.9
165.0	0.0705	1.0761	-0.0504	169.6	4.0567	82.5
179.9	0.0000	1.0733	-0.0535	179.9	4.1071	90.0

TABLE 1.1, CONT. MODE I, MU = 2/7

THETA	RY/RYI	S1	S2	THETA 1	$\hat{U}$	THETA U
$\nu/CR = 0.50$						
0.1	0.2640	2.3795	1.9463	0.3	1.5109	0.0
15.0	0.2973	2.3112	1.7366	34.3	1.5491	4.8
30.0	0.3946	2.1093	1.3284	55.8	1.6638	10.1
45.0	0.5524	1.8598	0.9351	72.7	1.8544	16.5
60.0	0.7686	1.6231	0.6090	88.1	2.1184	23.8
75.0	1.0203	1.4230	0.3555	102.5	2.4483	32.1
90.0	1.2211	1.2720	0.1741	115.8	2.8268	40.9
105.0	1.2419	1.1702	0.0560	128.0	3.2260	49.7
120.0	1.0314	1.1082	-0.0143	139.2	3.6107	58.4
135.0	0.6774	1.0739	-0.0529	149.8	3.9464	66.8
150.0	0.3260	1.0567	-0.0720	160.0	4.2048	74.8
165.0	0.0844	1.0492	-0.0803	170.1	4.3670	82.5
179.9	0.0000	1.0472	-0.0826	179.9	4.4222	90.0
$\nu/CR = 0.60$						
0.1	0.3650	2.2770	1.6552	0.2	1.7920	0.0
15.0	0.3871	2.2334	1.5613	25.7	1.8276	3.6
30.0	0.4540	2.1083	1.3266	48.2	1.9353	7.9
45.0	0.5787	1.9160	1.0181	68.2	2.1176	13.5
60.0	0.8021	1.6751	0.6780	86.7	2.3780	20.7
75.0	1.1558	1.4334	0.3682	103.3	2.7162	29.2
90.0	1.5302	1.2467	0.1446	117.6	3.1202	38.6
105.0	1.6577	1.1297	0.0099	130.0	3.5605	48.3
120.0	1.3980	1.0658	-0.0619	141.1	3.9933	57.7
135.0	0.9054	1.0348	-0.0963	151.4	4.3739	66.5
150.0	0.4260	1.0217	-0.1108	161.1	4.6675	74.7
165.0	0.1083	1.0171	-0.1159	170.6	4.8514	82.5
179.9	0.0000	1.0161	-0.1170	179.9	4.9140	90.0
$\nu/CR = 0.70$						
0.1	0.6285	2.0700	1.2614	0.1	2.2795	0.0
15.0	0.6285	2.0633	1.2502	18.4	2.3116	2.2
30.0	0.6297	2.0404	1.2124	38.0	2.4097	5.3
45.0	0.6618	1.9695	1.0997	60.2	2.5798	9.8
60.0	0.8486	1.7655	0.8011	84.0	2.8324	16.5
75.0	1.3844	1.4548	0.3946	104.4	3.1790	25.2
90.0	2.1686	1.2098	0.1017	120.1	3.6196	35.5
105.0	2.5632	1.0754	-0.0511	132.7	4.1250	46.3
120.0	2.1789	1.0134	-0.1200	143.5	4.6370	56.7
135.0	1.3705	0.9888	-0.1470	153.2	5.0925	66.1
150.0	0.6233	0.9813	-0.1552	162.4	5.4442	74.6
165.0	0.1547	0.9802	-0.1564	171.3	5.6643	82.4
179.9	0.0000	0.9803	-0.1562	179.9	5.7390	90.0

TABLE 1.1, CONT. MODE I, MU = 2/7

THETA	RY/RYI	S1	S2	THETA 1	$\hat{U}$	THETA U
$\nu/CR = 0.80$						
0.1	1.5126	1.7741	0.8131	0.1	3.2729	0.0
15.0	1.4592	1.7888	0.8336	12.9	3.3000	0.7
30.0	1.2869	1.8420	0.9093	27.3	3.3840	2.1
45.0	1.0200	1.9425	1.0582	46.6	3.5342	5.3
60.0	0.9479	1.9256	1.0324	77.4	3.7696	10.9
75.0	1.8400	1.5028	0.4546	106.3	4.1211	19.7
90.0	3.9073	1.1535	0.0370	123.7	4.6174	31.2
105.0	5.1782	1.0041	-0.1302	136.0	5.2408	43.6
120.0	4.3335	0.9508	-0.1883	146.2	5.9048	55.3
135.0	2.5786	0.9365	-0.2039	155.3	6.5053	65.5
150.0	1.1155	0.9362	-0.2042	163.8	6.9698	74.4
165.0	0.2684	0.9391	-0.2011	172.0	7.2597	82.4
179.9	0.0000	0.9404	-0.1996	179.9	7.3579	90.0
$\nu/CR = 0.90$						
0.1	6.9605	1.4422	0.3790	0.1	6.2538	-0.0
15.0	6.6897	1.4557	0.3958	9.0	6.2706	-1.0
30.0	5.7509	1.5100	0.4636	18.6	6.3254	-1.4
45.0	3.9058	1.6676	0.6679	30.5	6.4328	-0.4
60.0	1.7331	2.0755	1.2706	55.6	6.6226	3.5
75.0	3.2479	1.6344	0.6239	110.2	6.9588	11.6
90.0	13.0324	1.0628	-0.0652	128.7	7.5574	24.5
105.0	19.6631	0.9122	-0.2300	140.0	8.4812	39.7
120.0	15.2202	0.8790	-0.2656	149.3	9.5705	53.6
135.0	8.1852	0.8793	-0.2654	157.7	10.5832	64.9
150.0	3.2951	0.8874	-0.2567	165.4	11.3678	74.3
165.0	0.7620	0.8943	-0.2493	172.8	11.8561	82.4
179.9	0.0000	0.8969	-0.2465	180.0	12.0212	90.0
$\nu/CR = 0.99$						
0.1	796.0292	1.1521	0.0354	0.0	58.9705	-0.0
15.0	778.7952	1.1570	0.0410	6.3	58.8533	-2.8
30.0	711.9910	1.1776	0.0646	12.8	58.5375	-5.1
45.0	547.3641	1.2452	0.1427	19.7	58.1203	-6.6
60.0	234.5932	1.5360	0.4966	27.3	57.7344	-5.7
75.0	73.0905	2.0855	1.2875	125.2	57.6274	-0.0
90.0	1266.7075	0.9284	-0.2127	134.8	58.9850	14.2
105.0	2029.9112	0.8103	-0.3385	144.1	64.2511	34.2
120.0	1266.2131	0.8084	-0.3405	152.5	72.4102	51.4
135.0	579.9428	0.8251	-0.3229	160.0	80.3816	64.2
150.0	213.2879	0.8412	-0.3059	167.0	86.5705	74.1
165.0	47.1763	0.8516	-0.2949	173.6	90.4075	82.4
179.9	0.0020	0.8551	-0.2911	180.0	91.7017	90.0

TABLE 1.2 STRESS AND DISPLACEMENT FOR DYNAMIC MODE II CRACK TIP  
 POISSON'S RATIO, MU = 2/7, CR/CL = 0.506734, CR/CS = 0.925165

THETA	RY/RYI	S1	S2	THETA 1	U	THETA U
$\nu/CR = 0.01$						
0.1	3.0000	0.5768	-0.5779	45.1	1.1022	-89.7
15.0	2.8524	0.4997	-0.6543	52.4	1.3252	-52.4
30.0	2.4498	0.4105	-0.7413	59.4	1.8103	-29.7
45.0	1.9020	0.2958	-0.8507	65.5	2.3437	-16.6
60.0	1.3585	0.1385	-0.9965	69.6	2.8292	-8.1
75.0	0.9688	-0.0618	-1.1752	70.3	3.2238	-2.1
90.0	0.8418	-0.2258	-1.3157	67.5	3.5092	2.1
105.0	1.0163	-0.2435	-1.3305	64.7	3.6839	4.9
120.0	1.4503	-0.1699	-1.2684	65.4	3.7609	6.3
135.0	2.0319	-0.0935	-1.2028	69.5	3.7652	6.4
150.0	2.6091	-0.0400	-1.1561	75.6	3.7299	5.2
165.0	3.0300	-0.0097	-1.1295	82.6	3.6903	2.9
179.9	3.1839	-0.0000	-1.1209	90.0	3.6736	0.0
$\nu/CR = 0.30$						
0.1	3.0000	0.5768	-0.5779	45.1	1.2232	-89.7
15.0	2.8650	0.4983	-0.6558	52.6	1.4300	-54.7
30.0	2.4880	0.4078	-0.7439	59.8	1.8957	-32.1
45.0	1.9527	0.2917	-0.8546	66.2	2.4228	-18.4
60.0	1.3933	0.1299	-1.0043	70.7	2.9115	-9.2
75.0	0.9713	-0.0846	-1.1950	71.8	3.3130	-2.7
90.0	0.8275	-0.2653	-1.3487	68.5	3.6051	1.8
105.0	1.0249	-0.2731	-1.3553	64.9	3.7846	4.9
120.0	1.5166	-0.1817	-1.2785	65.6	3.8648	6.4
135.0	2.1633	-0.0966	-1.2054	69.8	3.8725	6.4
150.0	2.7878	-0.0403	-1.1564	75.9	3.8418	5.2
165.0	3.2318	-0.0097	-1.1294	82.8	3.8065	2.9
179.9	3.3917	-0.0000	-1.1209	90.0	3.7916	0.0
$\nu/CR = 0.40$						
0.1	3.0000	0.5768	-0.5779	45.1	1.3355	-89.8
15.0	2.8754	0.4969	-0.6571	52.7	1.5291	-56.6
30.0	2.5204	0.4054	-0.7463	60.2	1.9774	-34.1
45.0	1.9979	0.2880	-0.8580	66.9	2.4974	-19.9
60.0	1.4264	0.1228	-1.0108	71.8	2.9873	-10.2
75.0	0.9747	-0.1043	-1.2121	73.1	3.3942	-3.3
90.0	0.8131	-0.3019	-1.3791	69.4	3.6918	1.6
105.0	1.0307	-0.3000	-1.3775	65.2	3.8750	4.8
120.0	1.5766	-0.1916	-1.2869	65.8	3.9579	6.4
135.0	2.2840	-0.0989	-1.2075	70.0	3.9685	6.5
150.0	2.9517	-0.0406	-1.1566	76.1	3.9416	5.2
165.0	3.4165	-0.0096	-1.1294	82.9	3.9098	2.9
179.9	3.5818	-0.0000	-1.1209	90.0	3.8964	0.0

TABLE 1.2, CONT. MODE II, NU = 2/7

THETA	RY/RYI	S1	S2	THETA 1	$\hat{U}$	THETA U
$\nu/CR = 0.50$						
0.1	3.0000	0.5768	-0.5779	45.1	1.5109	-89.8
15.0	2.8898	0.4948	-0.6592	53.0	1.6866	-59.2
30.0	2.5668	0.4015	-0.7499	60.7	2.1088	-36.9
45.0	2.0662	0.2827	-0.8631	67.9	2.6159	-22.1
60.0	1.4806	0.1131	-1.0196	73.4	3.1054	-11.7
75.0	0.9831	-0.1322	-1.2361	75.2	3.5186	-4.2
90.0	0.7898	-0.3591	-1.4260	70.8	3.8234	1.2
105.0	1.0366	-0.3408	-1.4110	65.5	4.0118	4.8
120.0	1.6685	-0.2054	-1.2985	65.9	4.0982	6.5
135.0	2.4713	-0.1019	-1.2100	70.3	4.1129	6.6
150.0	3.2054	-0.0408	-1.1568	76.4	4.0912	5.3
165.0	3.7018	-0.0095	-1.1293	83.1	4.0643	2.9
179.9	3.8753	-0.0000	-1.1209	90.0	4.0529	0.0
$\nu/CR = 0.60$						
0.1	3.0000	0.5768	-0.5779	45.1	1.7920	-89.8
15.0	2.9097	0.4915	-0.6624	53.3	1.9447	-62.4
30.0	2.6341	0.3955	-0.7557	61.5	2.3280	-40.8
45.0	2.1733	0.2748	-0.8704	69.4	2.8111	-25.3
60.0	1.5765	0.1010	-1.0306	75.9	3.2951	-14.0
75.0	1.0085	-0.1690	-1.2676	78.6	3.7141	-5.5
90.0	0.7538	-0.4500	-1.4992	73.3	4.0278	0.6
105.0	1.0408	-0.4042	-1.4625	66.0	4.2223	4.6
120.0	1.8135	-0.2243	-1.3144	66.2	4.3140	6.6
135.0	2.7712	-0.1053	-1.2130	70.7	4.3342	6.7
150.0	3.6104	-0.0408	-1.1569	76.8	4.3197	5.3
165.0	4.1563	-0.0094	-1.1292	83.3	4.2993	2.9
179.9	4.3430	-0.0000	-1.1209	90.0	4.2905	0.0
$\nu/CR = 0.70$						
0.1	3.0000	0.5768	-0.5780	45.1	2.2795	-89.8
15.0	2.9394	0.4858	-0.6680	53.9	2.4021	-66.3
30.0	2.7409	0.3855	-0.7653	62.9	2.7267	-46.0
45.0	2.3621	0.2632	-0.8814	71.8	3.1636	-30.0
60.0	1.7775	0.0683	-1.0420	79.8	3.6271	-17.4
75.0	1.0984	-0.2080	-1.3007	84.3	4.0468	-7.6
90.0	0.7060	-0.6000	-1.6162	78.2	4.3699	-0.3
105.0	1.0400	-0.5104	-1.5469	66.8	4.5731	4.4
120.0	2.0643	-0.2504	-1.3363	66.4	4.6705	6.7
135.0	3.2984	-0.1092	-1.2163	71.2	4.6986	6.8
150.0	4.3196	-0.0407	-1.1567	77.3	4.6941	5.4
165.0	4.9510	-0.0092	-1.1290	83.6	4.6823	2.9
179.9	5.1608	-0.0000	-1.1209	90.0	4.6770	0.0

TABLE 1.2, CONT. MODE II, MU = 2/7

THETA	RY/RYI	S1	S2	THETA 1	$\hat{U}$	THETA U
$V/CR = 0.80$						
0.1	3.0000	0.5767	-0.5780	45.1	3.2730	-89.9
15.0	2.9950	0.4745	-0.6791	55.1	3.3543	-70.9
30.0	2.9555	0.3668	-0.7833	65.5	3.5836	-53.0
45.0	2.7957	0.2459	-0.8975	76.0	3.9230	-36.9
60.0	2.3514	0.0857	-1.0444	86.4	4.3212	-22.8
75.0	1.5063	-0.2036	-1.2970	94.4	4.7166	-11.0
90.0	0.7100	-0.8127	-1.7738	90.0	5.0425	-1.8
105.0	1.0316	-0.7169	-1.7040	68.1	5.2548	4.1
120.0	2.5966	-0.2878	-1.3674	66.6	5.3613	6.8
135.0	4.4319	-0.1133	-1.2199	71.7	5.4016	6.9
150.0	5.8379	-0.0401	-1.1562	77.8	5.4122	5.4
165.0	6.6512	-0.0088	-1.1287	84.0	5.4130	2.9
179.9	6.9118	-0.0000	-1.1209	90.0	5.4126	0.0
$V/CR = 0.90$						
0.1	3.0000	0.5764	-0.5783	45.1	6.2538	-89.9
15.0	3.1948	0.4429	-0.7099	58.7	6.2617	-76.3
30.0	3.7854	0.3247	-0.8234	72.1	6.2924	-62.2
45.0	4.7188	0.2284	-0.9138	85.2	6.3656	-47.6
60.0	5.5587	0.1373	-0.9976	97.9	6.5083	-32.4
75.0	4.8786	-0.0213	-1.1397	109.7	6.7339	-17.5
90.0	1.8749	-0.6076	-1.6219	116.1	7.0004	-4.8
105.0	1.0795	-1.2545	-2.0659	72.3	7.2149	3.4
120.0	4.4938	-0.3460	-1.4153	66.8	7.3397	6.9
135.0	8.5148	-0.1174	-1.2234	72.4	7.4071	7.1
150.0	11.2853	-0.0390	-1.1552	78.5	7.4477	5.5
165.0	12.7535	-0.0083	-1.1283	84.3	7.4721	2.9
179.9	13.2022	-0.0000	-1.1209	90.0	7.4806	0.0
$V/CR = 0.99$						
0.1	3.0009	0.5723	-0.5824	45.5	58.9705	-89.9
15.0	22.7692	0.2963	-0.8503	84.8	58.2002	-81.7
30.0	89.0979	0.2367	-0.8593	96.1	55.9299	-72.7
45.0	223.3409	0.2934	-0.8530	104.6	52.3193	-62.1
60.0	447.9558	0.3015	-0.8454	113.2	47.8036	-48.5
75.0	659.8280	0.2869	-0.8591	122.8	43.4713	-30.8
90.0	380.3559	0.1149	-1.0180	133.3	41.1205	-11.2
105.0	22.8238	-1.8282	-2.3450	132.7	40.9381	2.0
120.0	124.6452	-0.4382	-1.4897	66.7	41.3463	7.0
135.0	277.8349	-0.1207	-1.2262	73.1	41.7838	7.3
150.0	370.2391	-0.0372	-1.1537	79.2	42.1735	5.6
165.0	414.3484	-0.0077	-1.1277	84.7	42.4486	3.0
179.9	427.1087	-0.0000	-1.1209	90.0	42.5482	0.0

TABLE 2.1 STRESS AND DISPLACEMENT FOR DYNAMIC MODE I CRACK TIP

POISSON'S RATIO, MU = 2/6, CR/CL = 0.466263, CR/CS = 0.932526

$$((\text{PRIM STRSS})/Y)(R/RYI)^{0.5} \quad U/((Y/E)(R+RYI)^{0.5})$$

THETA	RY/RYI	S1	S2	THETA 1	U	THETA U
V/CR = 0.01						
0.1	0.1111	3.0026	2.9973	44.1	0.8890	0.0
15.0	0.1595	2.8069	2.1588	56.2	0.9344	7.5
30.0	0.2912	2.2534	1.3268	67.5	1.0676	15.0
45.0	0.4698	1.8637	0.8321	78.7	1.2795	22.5
60.0	0.6459	1.6165	0.5388	90.0	1.5557	30.0
75.0	0.7698	1.4548	0.3538	101.3	1.8772	37.5
90.0	0.8057	1.3449	0.2307	112.5	2.2223	45.0
105.0	0.7411	1.2683	0.1461	123.8	2.5675	52.5
120.0	0.5904	1.2144	0.0872	135.0	2.8891	60.0
135.0	0.3913	1.1770	0.0465	146.3	3.1652	67.5
150.0	0.1950	1.1524	0.0199	157.5	3.3771	75.0
165.0	0.0521	1.1384	0.0049	168.8	3.5103	82.5
179.9	0.0000	1.1339	-0.0000	179.9	3.5558	90.0

POISSON'S RATIO, MU = 2/8, CR/CL = 0.530817, CR/CS = 0.919402

THETA	RY/RYI	S1	S2	THETA 1	U	THETA U
V/CR = 0.01						
0.1	0.2500	2.0017	1.9982	43.9	1.2501	0.0
15.0	0.2960	2.0602	1.5845	56.2	1.2927	7.5
30.0	0.4208	1.8746	1.1038	67.5	1.4176	15.0
45.0	0.5884	1.6654	0.7436	78.7	1.6162	22.5
60.0	0.7500	1.5000	0.5000	90.0	1.8751	30.0
75.0	0.8572	1.3786	0.3353	101.3	2.1766	37.5
90.0	0.8751	1.2904	0.2214	112.5	2.5001	45.0
105.0	0.7925	1.2264	0.1413	123.8	2.8237	52.5
120.0	0.6251	1.1801	0.0847	135.0	3.1252	60.0
135.0	0.4117	1.1475	0.0454	146.3	3.3841	67.5
150.0	0.2043	1.1258	0.0195	157.5	3.5828	75.0
165.0	0.0545	1.1134	0.0047	168.8	3.7076	82.5
179.9	0.0000	1.1094	-0.0000	179.9	3.7502	90.0

TABLE 2.1, CONT. MODE I, MU = 2/6

THETA	RY/RYI	S1	S2	THETA 1	U	THETA U
$((\text{PRIN STRESS})/\text{Y})(\text{R}/\text{RY})^{0.5}$ $\text{U}/((\text{Y}/\text{E})(\text{R}/\text{RYI})^{0.5})$						
0.1	683.3745	1.1693	0.0383	0.0	53.4540	-0.0
15.0	667.1053	1.1745	0.0438	6.3	53.4319	-3.5
30.0	605.9894	1.1963	0.0675	12.9	53.3838	-6.6
45.0	461.0425	1.2680	0.1458	19.8	53.3484	-8.6
60.0	191.5183	1.5882	0.5062	27.6	53.3452	-8.2
75.0	48.6796	2.3634	1.4761	123.4	53.4301	-2.7
90.0	1127.9636	0.9262	-0.2205	134.5	54.6202	12.1
105.0	1796.6727	0.8102	-0.3409	144.1	59.6712	33.2
120.0	1105.4541	0.8119	-0.3392	152.6	67.7375	51.1
135.0	507.7994	0.8309	-0.3196	160.1	75.6171	64.1
150.0	188.2664	0.8484	-0.3015	167.0	81.7136	74.1
165.0	41.9094	0.8596	-0.2899	173.6	85.4839	82.4
179.9	0.0018	0.8634	-0.2859	180.0	86.7542	90.0

MODE I, MU = 2/8

$\text{V}/\text{CR} = 0.99$						
0.1	894.0848	1.1376	0.0334	0.0	63.1519	-0.0
15.0	875.8611	1.1422	0.0390	6.3	62.9675	-2.3
30.0	803.8354	1.1620	0.0627	12.8	62.4616	-4.2
45.0	622.3601	1.2261	0.1410	19.7	61.7697	-5.2
60.0	274.1182	1.4918	0.4895	27.0	61.1039	-4.0
75.0	97.9131	1.9064	1.1676	126.6	60.9477	1.8
90.0	1375.2361	0.9297	-0.2059	135.0	62.2960	15.7
105.0	2210.0289	0.8106	-0.3360	144.1	67.6809	34.8
120.0	1394.1226	0.8061	-0.3408	152.4	75.8855	51.6
135.0	638.5356	0.8211	-0.3247	160.0	83.9114	64.3
150.0	233.8941	0.8361	-0.3086	166.9	90.1618	74.1
165.0	51.5549	0.8459	-0.2980	173.6	94.0449	82.4
179.9	0.0022	0.8492	-0.2943	180.0	95.3560	90.0

TABLE 2.2 STRESS AND DISPLACEMENT FOR DYNAMIC MODE II CRACK TIP

POISSON'S RATIO, NU = 2/6, CR/CL = 0.466263, CR/CS = 0.932526

$$((\text{PRIM STRSS})/Y)(R/RY)^{0.5} \quad U/((Y/E)(R+RY)^{0.5})$$

THETA	RY/RYI	S1	S2	THETA 1	U	THETA U
$\nu/CR = 0.01$						
0.1	3.0000	0.5768	-0.5779	45.1	0.8890	-89.7
15.0	2.8512	0.4999	-0.6545	52.4	1.1617	-46.0
30.0	2.4450	0.4109	-0.7420	59.4	1.7081	-23.7
45.0	1.8913	0.2966	-0.8531	65.5	2.2788	-11.7
60.0	1.3403	0.1394	-1.0032	69.6	2.7845	-4.0
75.0	0.9419	-0.0627	-1.1919	70.3	3.1873	1.4
90.0	0.6055	-0.2308	-1.3450	67.5	3.4713	5.2
105.0	0.9707	-0.2491	-1.3614	64.7	3.6368	7.6
120.0	1.3959	-0.1732	-1.2929	65.4	3.6986	8.6
135.0	1.9700	-0.0950	-1.2215	69.5	3.6843	8.3
150.0	2.5413	-0.0405	-1.1714	75.6	3.6307	6.5
165.0	2.9587	-0.0098	-1.1430	82.6	3.5774	3.6
179.9	3.1113	-0.0000	-1.1339	90.0	3.5557	0.0

POISSON'S RATIO, NU = 2/8, CR/CL = 0.530817, CR/CS = 0.919402

THETA	RY/RYI	S1	S2	THETA 1	U	THETA U
$\nu/CR = 0.01$						
0.1	3.0000	0.5768	-0.5779	45.1	1.2501	-89.8
15.0	2.8536	0.4996	-0.6542	52.4	1.4456	-55.9
30.0	2.4543	0.4102	-0.7406	59.4	1.8900	-33.6
45.0	1.9117	0.2950	-0.8486	65.5	2.3953	-19.9
60.0	1.3750	0.1377	-0.9905	69.6	2.8642	-10.9
75.0	0.9934	-0.0610	-1.1606	70.3	3.2510	-4.5
90.0	0.8750	-0.2214	-1.2905	67.5	3.5356	-0.0
105.0	1.0581	-0.2386	-1.3040	64.7	3.7154	3.0
120.0	1.5001	-0.1671	-1.2472	65.4	3.8018	4.7
135.0	2.0885	-0.0923	-1.1864	69.5	3.8179	5.1
150.0	2.6709	-0.0395	-1.1426	75.6	3.7945	4.2
165.0	3.0952	-0.0096	-1.1175	82.6	3.7636	2.4
179.9	3.2502	-0.0000	-1.1094	90.0	3.7501	0.0

TABLE 2.2, CONT. MODE II, MU = 2/6

 $\langle \langle \text{PRIN STRESS} \rangle \rangle (R/RY)^{0.5}$     $U/\langle \langle Y/E \rangle \rangle (R/RY)^{0.5}$ 

THETA	RY/RYI	S1	S2	THETA 1	U	THETA U
$V/CR = 0.99$						
0.1	3.0007	0.5726	-0.5821	45.5	53.4539	-89.9
15.0	19.2174	0.2931	-0.8565	84.0	52.7339	-81.6
30.0	73.6083	0.2817	-0.8675	95.8	50.6103	-72.5
45.0	184.0928	0.2903	-0.8592	104.6	47.2305	-61.7
60.0	372.5352	0.3023	-0.8477	113.3	43.0061	-47.8
75.0	562.9642	0.2941	-0.8556	123.0	38.9987	-29.3
90.0	325.9776	0.1316	-1.0107	133.5	36.9820	-8.7
105.0	11.9639	-2.3032	-2.8836	133.2	36.9420	4.9
120.0	99.9380	-0.4246	-1.5172	66.3	37.1965	9.5
135.0	225.7058	-0.1141	-1.2391	72.8	37.3534	9.4
150.0	300.9732	-0.0348	-1.1662	78.9	37.4689	7.0
165.0	337.1164	-0.0072	-1.1406	84.6	37.5532	3.7
179.9	347.6404	-0.0000	-1.1339	90.0	37.5850	0.0

## MODE II, MU = 2/8

THETA	RY/RYI	S1	S2	THETA 1	U	THETA U
$V/CR = 0.99$						
0.1	3.0010	0.5720	-0.5827	45.5	63.1519	-89.9
15.0	25.8302	0.2983	-0.8456	85.4	62.3449	-81.8
30.0	102.3916	0.2897	-0.8534	96.3	59.9679	-72.9
45.0	256.7300	0.2950	-0.8486	104.7	56.1914	-62.4
60.0	511.0028	0.3003	-0.8437	113.2	51.4712	-49.0
75.0	738.7557	0.2811	-0.8614	122.8	46.9177	-31.8
90.0	425.7251	0.1020	-1.0218	133.1	44.3450	-13.0
105.0	34.9534	-1.5787	-2.0589	132.0	44.0718	0.1
120.0	148.2616	-0.4442	-1.4597	67.1	44.6009	5.2
135.0	324.7832	-0.1249	-1.2131	73.4	45.2532	5.9
150.0	432.0945	-0.0389	-1.1421	79.3	45.8501	4.6
165.0	483.2176	-0.0081	-1.1163	84.8	46.2680	2.5
179.9	497.9592	-0.0000	-1.1094	90.0	46.4180	0.0

## REFERENCES

Achenback, J. D.  
Bazant, Z. P. 1975 "Elastodynamic Near-Tip Stress and Displacement Fields for Rapidly Propagating Cracks in Orthotropic Materials," *J. Appl. Mech., Trans. A.S.M.E.* v. 42, 183-189.

Chitaley  
McClintock, F. A. 1971 "Elastic-Plastic Mechanics of Steady Crack Growth under Anti-Plane Shear," *J. Mech. Phys. Solids* v. 19, 147-163.

Flügge, W., ed. 1962 Handbook of Engineering Mechanics, McGraw-Hill, N.Y., p. 64-15.

Freund, L. B. 1975 Personal Communication

Kinra, V. K.  
Kolsky, H. 1977 "The Interaction Between Bending Fractures and the Emitted Stress Waves," *Eng. Fracture Mech.* v. 9, 423-432.

Levy, N.  
Marcal, P. V.  
Ostergren, W. J.  
Rice, J. R. 1971 "Small Scale Yielding near a Crack in Plane Strain: A Finite Element Analysis," *Int. J. Fracture Mech.* v. 7, 143-156.

McClintock, F. A.  
Irwin, G. R. 1965 "Plasticity Aspects of Fracture Mechanics," *Symposium on Fracture Toughness Testing and its Applications*, ASTM STP 381, Am. Soc. Test. Mat., Philadelphia, pp. 30-83.

Rice, J. R. 1968 "Mathematical Analysis in the Mechanics of Fracture," *Fracture* v. 2, H. Liebowitz, ed., Academic Press, N.Y., pp. 191-311.

Tracey, D. 1976 "Finite Element Solutions for Crack-Tip Behavior in Small-Scale Yielding," *J. Eng. Mat. & Tech., Trans. A.S.M.E.* v. 98H, 146-151.

Tsai, Y. M. 1974 "Dynamic Stress Distribution Around the Tip of a Running Crack," *Eng. Fracture Mech.* v. 6, 509-522.

SHOCK FRONT PROPAGATION AND THE STABILITY  
OF IMPLODING SURFACES

J. J. Gilman

A primary phenomenon in the operation of impact systems used extensively by the DoD and to a lesser extent to the DOE is the motion of shock waves through solids. In traditional systems this phenomenon has played an important role, but not a crucial role in the sense that ineffective shock propagation could be readily compensated for by increasing the driving force or by some other redesign. However, in some modern systems the role played by shock propagation has become crucial; such as systems in which thermonuclear fusion is intended to be inertially driven and confined. In these latter systems the propagation and stability characteristics of the fronts of shock waves and the stability of the subsequent motion of spherical surfaces clearly determine the success or failure of the primary fusion process. Thus the importance of an understanding of the motion of shock waves and spherical surfaces to these systems cannot be overemphasized.

Over a period of many years, the pressure/volume relationships (Hugoniot diagrams) obtained for shock waves have been studied using both experiments and theories. As a result,

shock wave propagation for pressure jumps up to about 100kb is reasonably well understood. Far less understood are the phenomena that occur when shocks emerge from free surfaces or strike discontinuous interfaces. For pressure jumps greater than 100kb experiments become very difficult to perform and interpret. Also, there is a great paucity of information and understanding about the structures of shock fronts; particularly at the high end of the cited pressure range (strong shocks).

In order to develop a predictive understanding of shock propagation and stability any model must start with either assumptions or knowledge of the structure of the shock front. Some of the features that need to be specified are:

- a. width: the best present experimental resolution is  $\approx 3$  sec.  $\approx 3 \times 10^5 \text{ \AA}$  and the lower limit is the granularity of the medium  $\approx 3 \text{ \AA}$ ; hence the uncertainty ranges over five orders of magnitude.
- b. distributions of atoms, ions, and electrons: present knowledge is very rudimentary. Best speculations are dislocation models.

Until these geometric features are specified, further modeling is impotent.

As for any other interface, it is important to define the interfacial free energy of a shock front because this may strongly influence its behavior.

When a strong shock front passes through a solid material the large densification that suddenly occurs causes strong interactions between the atoms which tend to disorganize them; and often converts a crystalline solid into a liquid while simul-

taneously raising the temperature and density of the material to high values. Dissipation accompanies this process, and this can be described as a drag pressure (or a viscous resistance) impeding the motion of the shock front. This may cause it to decelerate and attenuate significantly.

At the end of its passage through a material, a shock front passes through a free surface (or an interface). If this surface is initially smooth it may become unstable as it decelerates and develop protuberances (Taylor instability). If it is initially rough, the shock front may induce micro-jetting or micro-spalling. If it is concave it may rumple due to plastic instability. These phenomena depend strongly on the properties of the material. A knowledge of the magnitude of the viscosity of the material behind the shock front is especially important.

The phenomena outlined above were studied and discussed by some members of the MRC before and after a two day meeting with representatives from LASL. The program of this meeting is attached.

SHOCK-INTERFACE PROBLEMS  
July 17-18, 1978

D. H. Sharp, Moderator

J. F. Barnes	Introduction. Role of Fluff and Surface Instability in Fusion Devices.
K. A. Meyer	Taylor Instability
D. C. Wallace	Elastic-Plastic Flow at High Strain Rates
G. K. Straub	Molecular Dynamics Calculations
B. R. Suydam	Viscosity in Dense Materials

The questions of principal concern during the meeting were:

1. What is the appropriate magnitude of the viscosity of a material behind a strong shock front? Is it of order 1P or of order  $10^6$ P?
2. What features of real materials control Rayleigh-Taylor instability?
3. How does micro-jetting (and spall) depend on materials parameters?

The first two of these questions received the most discussion and the following recommendations were made:

- A. Improve understanding of the pressure dependence of viscosity for liquid metals.
  - a. study existing experimental literature
  - b. consider making new measurement, including quasi-static ones.
  - c. study scaling laws and analogs.
- B. Develop static and transport theory for very high density, high temperature metals. (>100Mb and >20eV temperature).
- C. Consider miniaturization of experimental equipment for shock-loading measurements.

- D. Enlarge studies of Taylor instability growth rates for solids, especially for spherical geometry or its analog.
  - a. effect of initial amplitude
  - b. dependence on static yield stress and on the shear modulus
  - c. wavelength/grain size ratio
  - d. influence of strain-hardening rate (at constant yield stress)
  - e. effect of coherent (integral) surface hardening.
- E. Study plastic rumpling of imploding shells caused by flow localization.
- F. Molecular dynamic models of fluid have been studied (Ashurst and Hoover, 1975) in which viscosity can be found directly. We recommend strongly that efforts be made to run such a model to mega-bar pressures with parameters representative of real liquids such as Hg or H<sub>2</sub>O.

ON THE KINK MODE OF FAILURE  
OF FIBER REINFORCED COMPOSITES  
D. C. Drucker and A. G. Evans

Some fiber reinforced composites (e.g., graphite-carbon) have been observed to fail in a kinking mode when subjected to compressive load parallel to the fibers. The geometric change shown in the accompanying figure carries the fibers from their straight configuration to their kinked twin position in which their total length returns to the length prior to the kink. During the motion, however, if the vertical dimension  $l$  is unchanged, the fibers must shorten appreciably from  $l$  to  $l\cos\beta$  for a compressive strain of  $1-\cos\beta$  where  $\beta$  is the angle of inclination of the kink plane to the horizontal plane normal to the fibers. Further rotation of the fiber toward its twin position releases load in the fiber and provides a driving force or instability.

The kink mode involves large matrix shear and so favors  $\beta = 45^\circ$  for an isotropic matrix and  $\beta = 0$  for the fiber. At  $\beta = 30^\circ$  the maximum fiber strain  $1-\cos\beta$  is a little over 0.13, an extremely large value that would bring an elastic fiber to its theoretical strength. Therefore, the transition from the straight configuration to the kinked configuration cannot occur simultaneously or nearly so over the entire plane at normal

static loads. This high resistance to almost simultaneous kinking is not overcome by the usual techniques of permitting the vertical distance to increase while the compressive load is increased because half of the  $0.13^+$  strain still is enormous for both the matrix in extension and the fiber in contraction. (Almost simultaneous kinking may well be possible under strong shock loading.)

Perhaps this result should come as no surprise. It is analogous to the situation for displacements of one row of atoms with respect to another that led to the dislocation concept of moving atoms one at a time. A closer analogy may be that an edge dislocation moves through a lattice much more easily by the lateral spreading of a kink than by the entire dislocation line moving forward simultaneously.

The implication would appear to be that fiber kinking under static loads requires an imperfection (crack or cavity) of several fiber spacings that overload the fibers immediately adjacent to the imperfection, cause them to buckle and so permit a kink to generate and then to propagate aided by successive local fiber buckling in advance of the spreading kink.

Of course, any appropriate inclination  $\alpha$  of the fibers from the direction of the compressive load reduces the strain needed for a kink to  $1 - \cos(\beta - \alpha)$ . Buckling of the fibers can give an  $\alpha$  comparable to  $\beta$  at which stage the fiber provides a driving force for the kink instability.

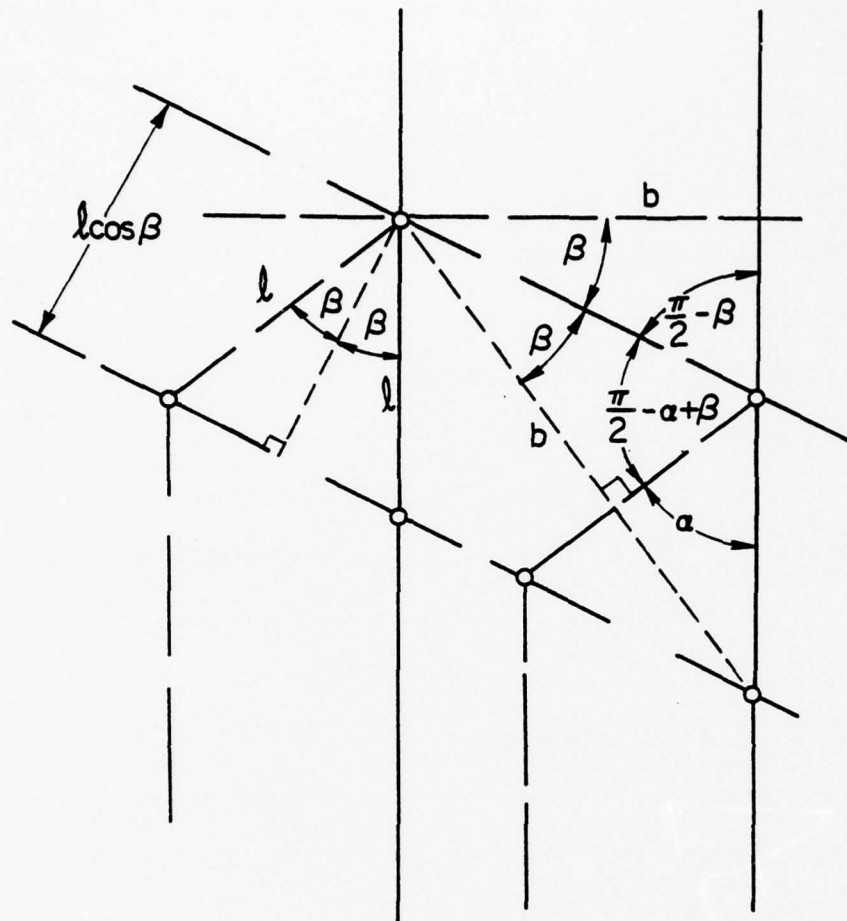


Figure 1. Kinking of Fibers

Acknowledgement

This research was supported by the Defense Advanced Research Projects Agency of the Department of Defense under Contract No. MDA903-76C-0250 with The University of Michigan.

ON THE THERMODYNAMICS OF ADSORPTION AT INTERFACES  
AS IT INFLUENCES DECOHESION

J. P. Hirth and J. R. Rice

ABSTRACT

Earlier computations on the work of separation of boundaries with adsorbed solute atmospheres are reconsidered in terms of reversible work cycles. The results are consistent with the limiting cases treated before and include the extension to more general cases of solute interactions, including multi-component systems. The work terms are conveniently represented on diagrams of chemical potential versus surface excess solute concentration.

ON THE THERMODYNAMICS OF ADSORPTION AT INTERFACES  
AS IT INFLUENCES DECOHESION

J. P. Hirth and J. R. Rice

INTRODUCTION

There are a number of embrittlement phenomena, such as temper embrittlement and hydrogen embrittlement, in which solute adsorption at a grain boundary or other interface degrades its mechanical properties and leads to intergranular separation. A limiting case of separation, tractable for thermodynamic analysis, occurs when no work terms other than interface creation and destruction are involved in the process. The analysis is also applicable to the situation first considered by Thomson<sup>1</sup> where plastic flow occurs but where dislocations screen the crack tip from the remote stress field and the local crack tip region separates as in the limiting case.

Seah<sup>2</sup> first considered the difference between two types of boundary separation as influenced by solute adsorption: quasi-equilibrium separation with the chemical potential of solute maintained throughout the system and "rapid" separation in such a manner that the excess amount of solute initially residing in the boundary remains attached to the created free surfaces with no solute exchange taking place with bulk phases. However, Rice<sup>3</sup> presented an analysis of the work terms in the two limits for

the grain boundary case, and his work suggests that details of Seah's<sup>2</sup> analysis are incorrect. In particular, the Rice analysis disagrees with Seah's conclusion that adsorption has no effect on the work of separation in the fixed composition (rapid) limit, although Rice does conclude that the effect of adsorption on the work in this limit is less than for separation at the fixed potential (slow) limit. The problem has also been considered by Asaro<sup>4</sup> and by Hirth<sup>5</sup>; Asaro extending Rice's work to interphase interfaces and Hirth discussing a number of irreversible phenomena which can cause deviations in work from that predicted for the limiting case.

In this presentation, we first discuss various mechanisms of interface separation, together with the appropriate variables giving the work term. Rice's<sup>3</sup> analytical result, expressed in terms of Helmholtz free energies related to stress-displacement variables for an interface separating uniformly, is given in terms of a reversible work cycle in chemical potential-composition space. An alternate reversible work cycle is then presented for surface energy area variables. Finally, the results are extended to several cases of interface separation other than the two previously treated.

#### Modes of Separation

There are various modes of separation of an interface, amenable to calculation of surface energies for a hypothetical reversible path, three of which are illustrated in Fig. 1. These produce different stress (or local force) -displacement curves

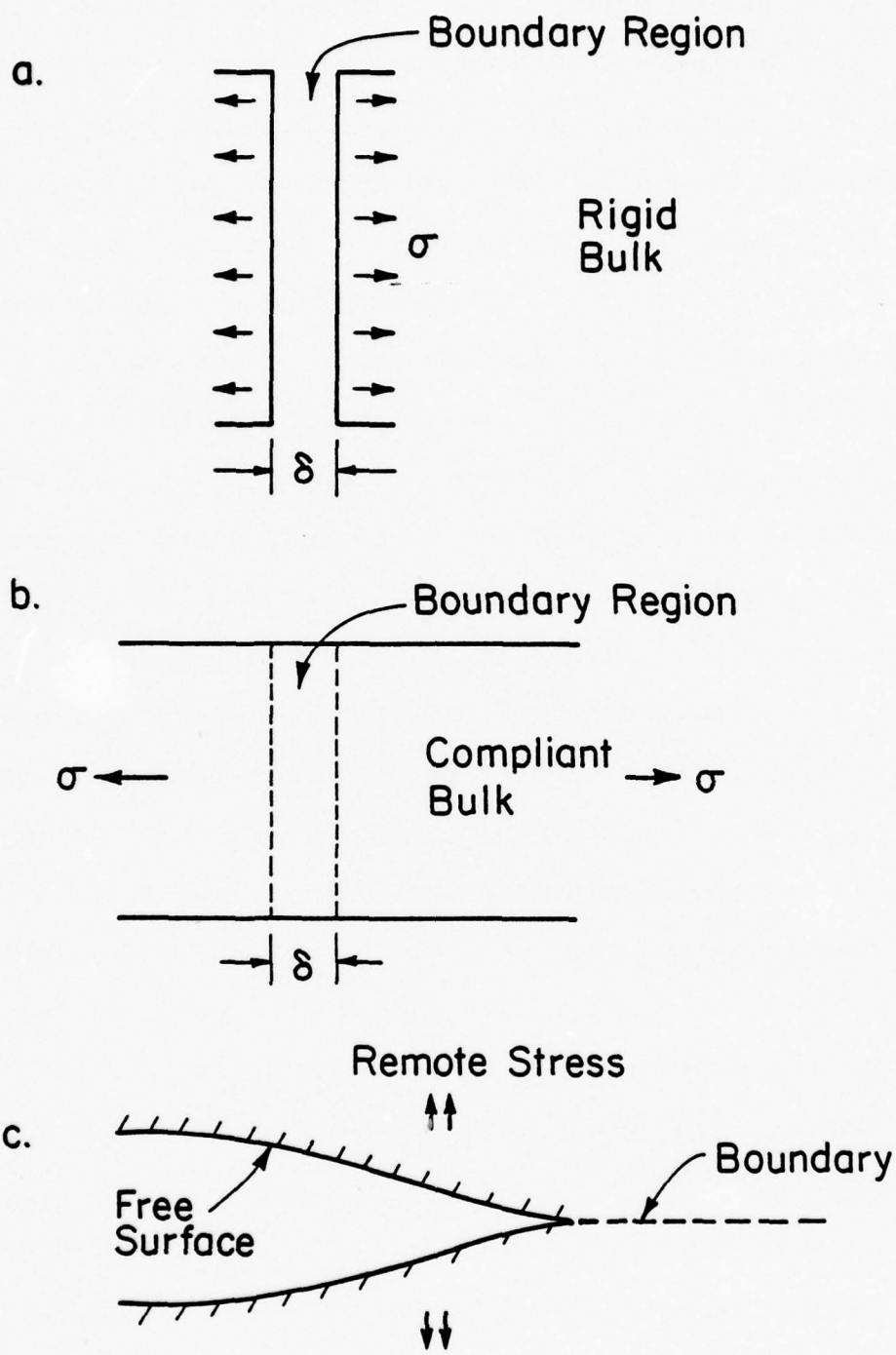


Figure 1. Mechanisms of boundary separation.

as shown in Fig. 2. However, the surface energy, equal to the integral of the stress-displacement curve from an unstressed equilibrium separation  $\delta_0$  to infinity, is the same for all three paths (assuming that all three correspond to one of the limiting composition states discussed above). Mode a in Fig. 1 corresponds to rigidly clamping the two bulk phases and separating the boundary regions, the path used by Rice<sup>3</sup>, Asaro<sup>4</sup> and in an atomic calculation by Zaremba<sup>6</sup>. The initial slope of the  $\sigma$ - $\delta$  curve for case a, determined by a weighted average of phonon frequencies<sup>6</sup> is larger than the elastic constant corresponding to the tensile extension of the bicrystal in base b. For case c, a crack is supposed to reversibly propagate along the boundary. A given atom pair being separated will undergo a stress-displacement excursion which differs from the other cases because of the varying stress field to the right of the crack tip and the varying compliance to the left and surrounding the crack tip, although initially it would coincide with case b. The force on the crack can be imagined to be applied in a double-cantilever beam mode so that advance of the crack has the net effect of removing unit area of unstressed boundary and creating unit area of separated surfaces.

For reversible extension, the work is performed by the external device applying the stress  $\sigma$  equals the free energy change in creating the surface. In all cases the work term performed by the external device, i.e., the negative of work done by the system, for this reversible extension is

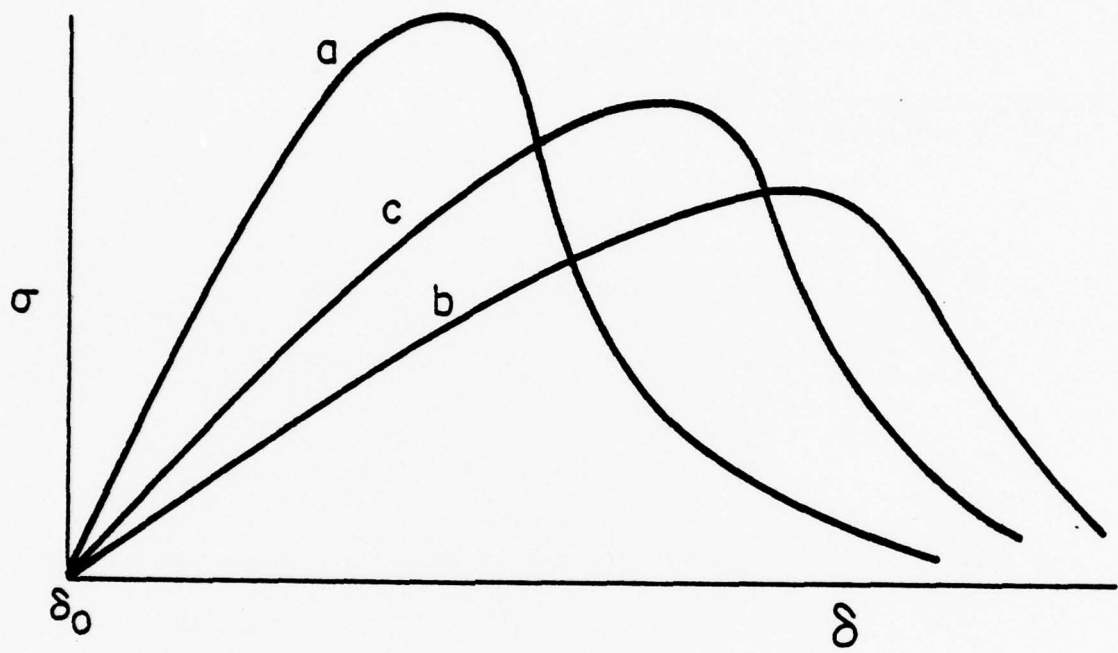


Figure 2. Stress-displacement curves corresponding to the processes of Figure 1.

$$w = \int_{\delta_0}^{\infty} \sigma d\delta \quad (1)$$

Relevant thermodynamic expressions for a system containing bulk phases and a boundary at uniform temperature and potentials, and subject to uniform pressure, are: for the total system Gibbs and Helmholtz free energies

$$dG = VdP - SdT + \mu_i dn_i + \gamma dA \quad (2)$$

$$dF = -PdV - SdT + \mu_i dn_i + \gamma dA ; \quad (3)$$

the Gibbs-Duhem relation, normalized to unit area of interface

$$d\gamma = [V]dP - [S]dT - \Gamma_i d\mu_i ; \quad (4)$$

the reduced form of (4) for the case of a binary solution where the Gibbs dividing surface (or size of the boundary region) is defined such that  $\Gamma_i = 0$ ,

$$d\gamma = [V]dP - [S]dT - \Gamma d\mu ; \quad (5)$$

and the Gibbs and Helmholtz surface free energies

$$f = g = \gamma + \mu\Gamma \quad (6)$$

which, together with (2) and (3) give

$$df = -Pd[V] - [S]dT + \mu d\Gamma + \gamma dA \quad (7)$$

$$dg = [V]dP - [S]dT + \mu d\Gamma + \gamma dA \quad (8)$$

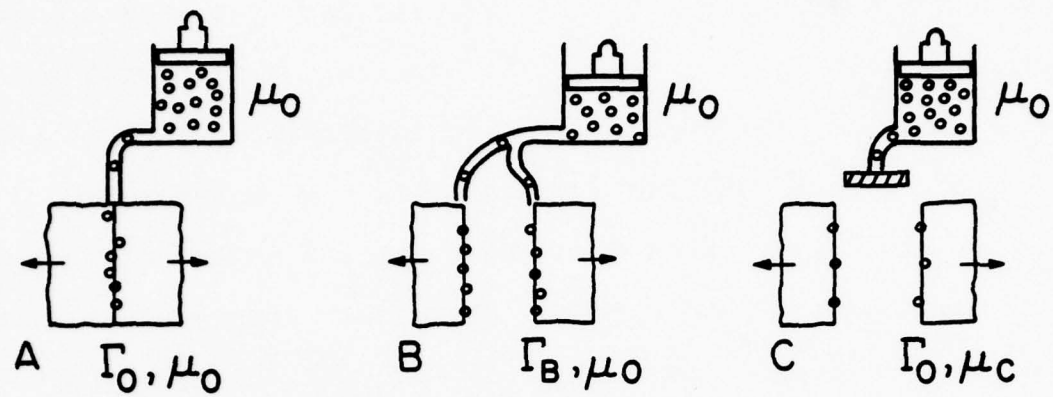
The surface excess quantities  $[V]$ ,  $[S]$  and  $\Gamma_i$  can be considered either in the Gibbsian sense<sup>7</sup> of excesses of the total extensive variable minus its amount residing in hypothetical bulk phases uniform up to a dividing surface or in the sense used by Guggenheim<sup>8</sup> of excesses over the average bulk amount in a boundary region finite in extent. Where only component 2 has a surface excess amount, as in Eqs. (5) and (6), the subscript 2 on  $\mu$  and  $\Gamma$  is dropped for simplicity in representation. Note that for the coherent interface  $\gamma = \gamma_b$  and  $\Gamma = \Gamma_b$ , whereas for the pair of free surfaces created by separation,  $\delta = 2\delta_s$  and  $\Gamma = 2\Gamma_s$ .

#### Separation of Initially Equilibrated Boundary

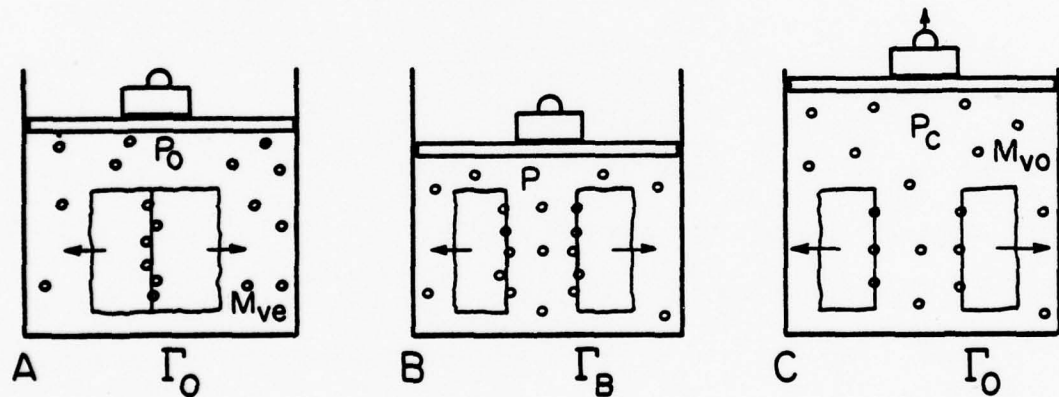
We first reconsider the boundary separation process treated by Rice<sup>3</sup>, shown in Fig. 3a and represented in  $\mu - \Gamma$  space in Fig. 4. The system is imagined to be initially in complete equilibrium, A (for which  $\mu = \mu_0$  and  $\Gamma = \Gamma_0$ ), and to be separated reversibly in one of two ways. One is path I (A to B, Fig. 3a), separation at constant  $\mu$ , T and P. The other is path III (A to C, Fig. 3a), separation in such a manner that the excess amount residing on the created unit areas of free surface equals the amount initially residing on the boundary

$$2\Gamma_s^C = \Gamma_b^A \equiv \Gamma_0$$

(schematically, the system is shown as blocked from access to a matter reservoir in Fig. 3a). For path III, constrained equilibrium is assumed in which there is no exchange between surface and bulk phases but in which the solute is imagined to distribute



(a)



(b)

Figure 3. Schematic representation of system in states A, B and C. For (a) the interface is imagined to have contact with (state B) or to be blocked from (state C) a matter reservoir. For (b) all processes are carried out under equilibrium with the surrounding vapor phase.

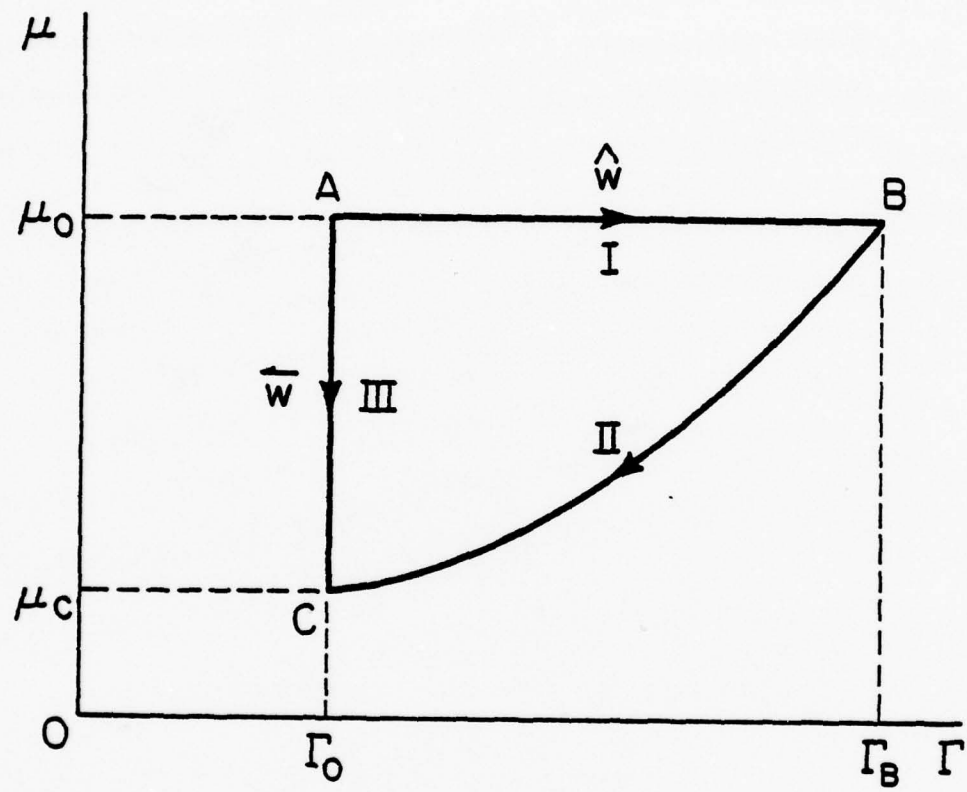


Figure 4. Work cycle representation of boundary separation process.

evenly between the two created surfaces and to equilibrate to a surface state which would be in equilibrium with a reduced chemical potential  $\mu_c$ . In this case the  $\mu$  coordinate in Fig. 4 corresponds to  $\mu$  for the progressively separating interface, and this value of  $\mu$  differs from  $\mu$  in the bulk phase.

With constrained equilibrium as described above, the volume change work in step IV is essentially zero. Thus, considering  $\sigma d\delta$  stretching work coordinates in place of  $\gamma dA$  coordinates in Eq. (3), and since  $dF = df$  for the case of Fig. 1a, Rice<sup>3</sup> obtained for step III

$$\sigma d\delta = d\bar{w} = df; \quad \bar{w} = \Delta f = 2f_s^c - f_b^A \quad (9)$$

Using Eq. (6) this becomes

$$\bar{w} = 2\gamma_s^c - \gamma_b^A + \int_{\mu_0}^{\mu_c} \Gamma_0 d\mu \quad (10)$$

Rice then introduced the Legendre transform

$$d\gamma = d(f - \mu\Gamma) = \sigma d\delta - \Gamma d\mu$$

or for the constant chemical potential path I

$$\sigma d\delta = d\hat{w} = d\gamma; \quad \hat{w} = \Delta\gamma = 2\gamma_s^B - \gamma_b^A \quad (11)$$

The difference in work terms in the two cases is thus

$$\hat{w} - \bar{w} = 2\gamma_s^B - 2\gamma_s^c - \int_{\mu_0}^{\mu_c} \Gamma_0 d\mu$$

$$\begin{aligned}
 &= \int_{\mu_0}^{\mu_C} (\Gamma - \Gamma_0) d\mu \\
 &= - \int_{\Gamma_0}^{\Gamma_B} (\mu - \mu_0) d\Gamma
 \end{aligned} \tag{12}$$

where, in the second step, we have used Eq. (5) in the form of the Gibbs adsorption equation,  $d\gamma = -\Gamma d\mu$ , for the pair of free surfaces created by separation. The third step in Eq. (12) involves an integration by parts, to put the result in the form given by Rice<sup>3</sup>, and it is to be understood that  $\Gamma \equiv 2\Gamma_s$  and that the  $\Gamma$  and  $\mu$  appearing in the integrals are functions of one another according to the adsorption isotherm  $\Gamma = \Gamma(\mu) = 2\Gamma_s(\mu)$  for the pair of free surfaces.

In actuality, as noted by Gibbs<sup>7</sup>, it is unlikely that both  $[V]$  and  $\Gamma_1$  can be maintained equal to zero for process III: Gibbs<sup>7</sup> (p. 219) discusses this point in terms of arbitrariness of the terms on the right side but the invariance of  $d\gamma$  in Eq. (4), a point also considered in some detail by Cahn<sup>8</sup>. While this is likely to be a second order effect, one can construct a Gibbs reversible work cycle which identically reproduces the results of Eqs. (10), (11) and (12). The separation processes are illustrated in Fig. 3b and again correspond to Fig. 4 in  $\mu - \Gamma$  space. In this case the created surfaces are assumed to be equilibrated with the vapor phase, but, as in the previous case, to be constrained not to equilibrate with the bulk solid phase. As a

concrete example consider adsorption of, say, oxygen on a separating copper interface. An analogous situation would hold with a fluid phase replacing the vapor phase.

The relevant reversible work term for the process in Fig. 3b is the external device work minus the  $PdV$  work done by the weight but this is precisely the change in  $G$  for the system for constant  $P$  processes. Otherwise, it is  $\Delta F = \Delta G - \int VdP$ . For process I at constant  $P$ ,  $T$ ,  $\mu$  and  $\mu_i$ , Eq. (2) gives

$$\hat{w} = \Delta G = \Delta g = 2\gamma_s^B - \gamma_b^A \quad (13)$$

For process III we separate the interface at equilibrium with the vapor but continuously alter  $P$  during separation to maintain a constant mass  $M_v = M_{vo}$  in the vapor phase, where  $M_{vo}$  is the vapor mass in state A. This simulates separation at constant  $\Gamma$ . During the process the volume of the vapor is  $V = M_{vo}v$  where  $v = v(P)$  is its specific volume, and the device work is  $\bar{w} = \Delta G - \int VdP$ . But the  $\Delta G$  for this process can alternatively be calculated by the hypothetical reversible sequence: (i) remove boundary at constant vapor pressure  $P_o$  with device work  $\Delta w = -\gamma_b^A$  for unit area; (ii) expand the vapor, now of mass  $M_{vo} + \Gamma_o$ , from  $P_o$  to  $P_c$ ; and (iii) create the pair of free surfaces at vapor pressure  $P_c$  with device work  $2\gamma_s^s$ . Thus

$$\begin{aligned} \bar{w} &= \Delta G - M_{vo} \int_{P_o}^{P_c} v dP = \Delta g \\ &= [-\gamma_b^A + (M_{vo} + \Gamma_o) \int_{P_o}^{P_c} v dP + 2\gamma_s^s] - M_{vo} \int_{P_o}^{P_c} v dP \end{aligned}$$

$$= 2\gamma_s^c - \gamma_b^A + \int_{\mu_0}^{\mu_c} \Gamma_0 d\mu \quad (14)$$

(since  $d\mu = v dP$ ). Thus, the results for  $\hat{w}$  and  $\bar{w}$  are identical to Eqs. (10) and (11). Moreover, in the process of creation and removal of interfaces, the Gibbs dividing surface can be chosen independently for each surface so that  $\Gamma_1 = 0$  and, as is evident from Eqs. (2) or (8), the result is also independent of  $[V]$ . Hence Rice's result, Eqs. (10) to (12), is exact.

Interestingly  $\bar{w}$  in Eq. (14) equals  $\Delta g$  but while  $g$  and  $f$  are defined by the same equation,  $\bar{w}$  no longer equals  $\Delta f$  for the process of Fig. 3b. This seeming anomaly arises because of the difficulty in selecting both  $\Gamma_1$  and  $[V]$  equal to zero as discussed earlier. Hence, formally, the appropriate  $\Gamma$  term for steps (i) and (iii) above may not be precisely the same.

The difference between  $\hat{w}$  and  $\bar{w}$  is again given by Eq. (12) but one can obtain the result directly by evaluation of  $\Delta G$  for process II in Fig. 4. This corresponds to a reversible transition from B to C in Fig. 3b by desorption of matter from the free surfaces. During this process  $dG = VdP$  and  $V = M_V v = (M_{vo} + \Gamma - \Gamma_0)v$ . Since  $\Delta G_I + \Delta G_{II} = \Delta G_{III}$ ,

$$\hat{w} + \int_{P_0}^{P_c} (M_{vo} + \Gamma - \Gamma_0) v dP = \bar{w} + M_{vo} \int_{P_0}^{P_c} v dP,$$

$$\text{or } \hat{w} - \bar{w} = - \int_{\mu_0}^{\mu_c} (\Gamma - \Gamma_0) d\mu \quad (15)$$

in agreement with Eq. (12). Regarded as a closed cycle I + II - III

the results of Eqs. (13) to (15) give

$$2\gamma_s^0 - 2\gamma_s^c = - \int_{\mu_c}^{\mu_0} \Gamma d\mu \quad (16)$$

in agreement with the Gibbs relation (5).

We are now in a position to review Seah's<sup>2</sup> analysis of separation at constant  $\Gamma$ . He correctly remarks that  $(2\Gamma_s)_c = (\Gamma_b)_A \equiv \Gamma_0$  for such a process. But he assumes that the appropriate device work term in this case is  $\bar{w} = 2\gamma_s^c - \gamma_b^A$ . Instead, the correct result, Eq. (9), is  $\bar{w} = 2f_s^c - f_b^A$ , and this differs from what Seah assumed by the term  $\Gamma_0(\mu_c - \mu_0)$ . Thus, Seah's evaluation of  $\bar{w}$  is equivalent to ignoring the  $\Gamma_0$  term in (10) or (14). In particular, his demonstration for the dilute concentration case that  $\bar{w}$  is independent of  $\Gamma_0$  is not supported by the present analysis.

The Gibbs adsorption relation (16) and the analogous relation for changes of  $\gamma_b$  may be combined with the previous expressions for  $\hat{w}$  and  $\bar{w}$  to give Rice's<sup>3</sup> equations

$$\begin{aligned} \hat{w} &= (w)_{\Gamma=0} - \int_{-\infty}^{\mu} [2\Gamma_s(\mu) - \Gamma_b(\mu)] d\mu \\ \bar{w} &= (w)_{\Gamma=0} - \int_0^{\Gamma} [\mu_b(\Gamma) - \mu_s(\Gamma/2)] d\Gamma \end{aligned} \quad (17)$$

where  $(w)_{\Gamma=0} = (2\gamma_s - \gamma_b)_{\Gamma=0} = (2f_s - f_b)_{\Gamma=0}$  pertains to separation in the absence of the solute, and where  $\Gamma_s = \Gamma_s(\mu)$  and  $\Gamma_b = \Gamma_b(\mu)$ , or  $\mu = \mu_s(\Gamma_s)$  and  $\mu = \mu_b(\Gamma_b)$ , represent adsorption isotherms for the free surface and unstressed grain boundary, respectively.

In application of the expressions derived for  $\bar{w}$  to practical cases of separation at fixed composition, it is well to remember that there is a tacit assumption of local equilibrium within the adsorbed layer during separation. This implies some atomic mobility over distances comparable to the layer thickness, and such mobility requirements may not always be met for fracture on practical time scales. An unresolved question is, then, that of by how much the work of separation at a completely "frozen" composition differs from  $\bar{w}$ .

#### General Separation Paths

We have considered two special separation paths: constant  $\Gamma$  ( $w = \bar{w}$ ), and constant  $\mu$  ( $w = \hat{w}$ ). More generally, and with reference to Fig. 5, we may regard separation as a transition from a state  $\Gamma_0, \mu_0$  along the isotherm for grain boundary adsorption to a state  $\Gamma_F, \mu_F$  along the isotherm for free surface adsorption. Assuming that there is local equilibrium within the adsorbed layer during separation, the separation process can be represented as a path in  $\Gamma, \mu$  as shown.

The actual details of the path are governed by the kinetics of matter transport by diffusion to the separating interface. The details will be different for the different modes of separation illustrated in Fig. 1, and in the crack case there is the possibility of transport from the surrounding environment. Nevertheless, it is generally to be expected that stressing the grain boundary tends to lower the potential there and induces a flow of matter to the separating interface. Hence the typical case is  $d\mu < 0$  and

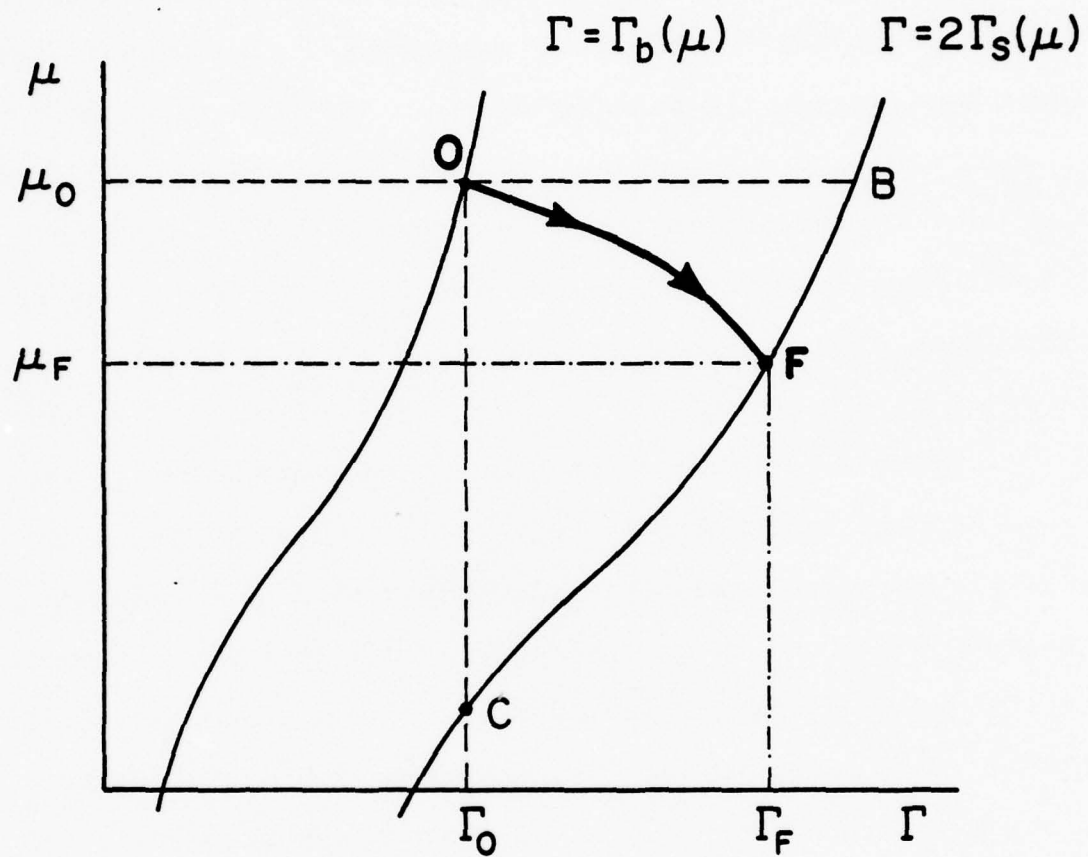


Figure 5. General separation path, from state "O" along adsorption isotherm for unstressed grain boundary to state "F" along adsorption isotherm for separated surfaces.

$d\Gamma > 0$  during separation, as for the path OF shown in Fig. 5.

To relate  $w_{OF}$  to work terms such as  $\hat{w}_{OB}$  or  $\bar{w}_{OC}$ , we use the result

$$dw \equiv \sigma d\delta = df - \mu d\Gamma = d\gamma + \Gamma d\mu \quad (18)$$

Since  $\gamma$  is a function of state in  $\Gamma, \mu$  space,

$$\oint dw = \oint \Gamma d\mu \quad (19)$$

where the cycle integrals will be understood to correspond to a closed path in the  $\Gamma, \mu$  plane. For example application of this result to the path OCBO gives

$$\bar{w}_{OC} - \hat{w}_{OB} = \oint_{OCBO} \Gamma d\mu \quad (20)$$

The integrals represent the areas OCFO and OFBO and are positive for the path shown. Hence for separation paths with  $d\mu \leq 0$ ,  $d\Gamma \geq 0$

$$\bar{w} \geq w \geq \hat{w} \quad . \quad (22)$$

The cycle equality (19) also provides a concise basis for derivation of Eq. (17). For example, consider the cycle: separate the interface at potential  $\mu$  with work  $\hat{w}$ , move up the free surface isotherm by  $d\mu$ , close the interface at potential  $\mu + d\mu$  with work  $-(\hat{w} + d\hat{w})$ , and move down the grain boundary isotherm by  $d\mu$ . Hence

$$\hat{w} - (\hat{w} + d\hat{w}) = -d\hat{w} = [2\Gamma_s(\mu) - \Gamma_b(\mu)]d\mu \quad (23)$$

which integrates to the form in Eq. (17). Similarly, a cycle involving separation at  $\Gamma$  and closing at  $\Gamma + d\Gamma$  gives

$$\bar{w} - (\bar{w} + d\bar{w}) = -d\bar{w} = [\mu_b(\Gamma) - \mu_s(\Gamma/2)]d\Gamma \quad (24)$$

which integrates to the form in Eq. (17).

### Three Component System

In the temper embrittlement case, there is evidence for coupled solute effects of a three component type with two dilute solute concentrations. The preceding analysis can be extended to the three component case as illustrated in Fig. 6. As shown there, it is now necessary to retain subscripts to distinguish the dilute components 2 and 3.

Proceeding as before, we find for step III, separation at constant chemical potential

$$\hat{w} = 2\gamma_s^B - \gamma_b^A \quad (25)$$

In order to compute the reversible work term for step II, the process is separated into two stages, a change of  $\mu_2$  at constant  $\mu_3$  followed by a change of  $\mu_3$  at constant  $\mu_2$  giving

$$\Delta\hat{w} = \hat{w} - \bar{w} = - \int_{\mu_2^0}^{\mu_2^C} (\Gamma_2 - \Gamma_2^0) \mu_3^0 d\mu_2 - \int_{\mu_3^0}^{\mu_3^C} (\Gamma_3 - \Gamma_3^0) \mu_2^C d\mu_3 \quad (26)$$

From Eqs. (25) and (26), the result for the "rapid" separation stage I is then

$$\bar{w} = 2\gamma_s^C - \gamma_b^0 - \int_{\mu_2^0}^{\mu_2^C} \Gamma_2^0 d\mu_2 - \int_{\mu_3^0}^{\mu_3^C} \Gamma_3^0 d\mu_3$$

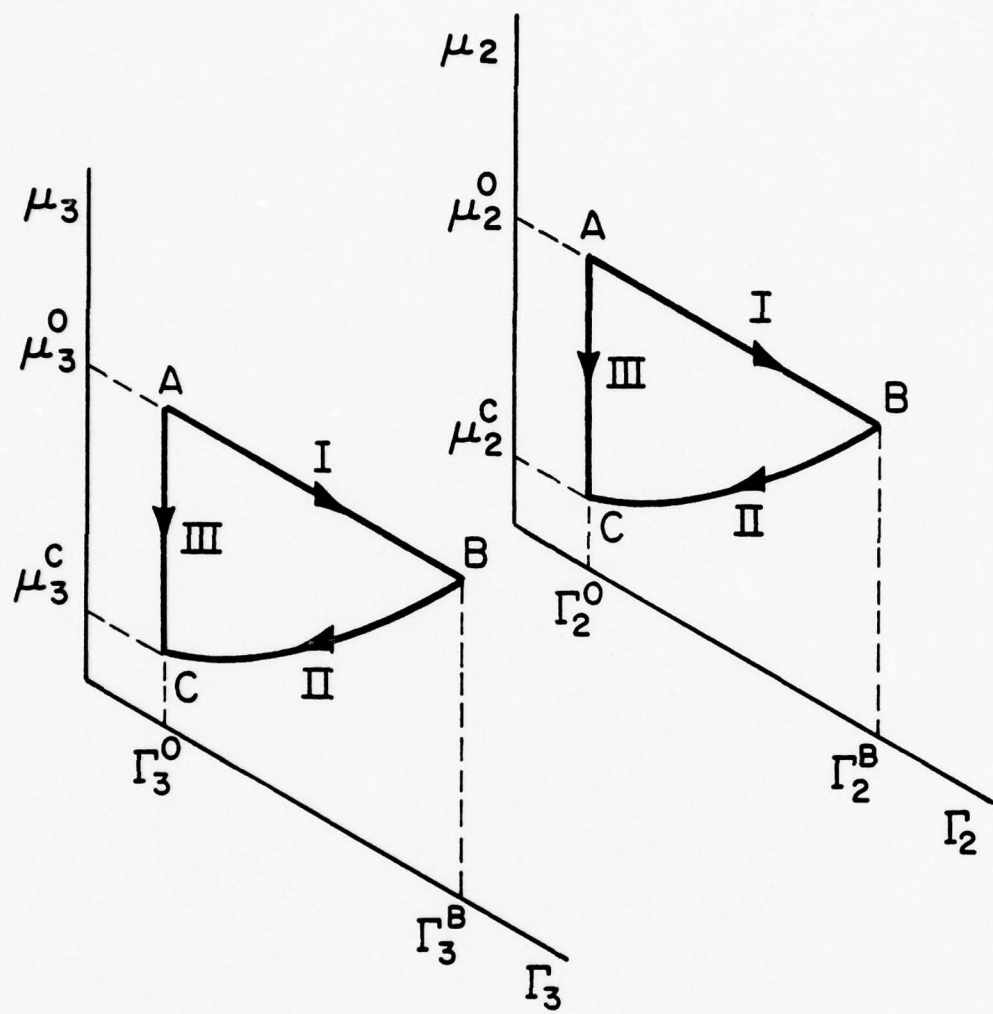


Figure 6. Work cycle for interface separation in three component system.

$$\hat{w} + \int_{\mu_2^0}^{\mu_2^c} (\Gamma_2 - \Gamma_2^0) \mu_3^0 d\mu_2 + \int_{\mu_3^0}^{\mu_3^c} (\Gamma_3 - \Gamma_3^0) \mu_2^0 d\mu_3$$

By analog with the cases treated for the binary case in the preceding section, and with the above expressions as a guide, equivalent expressions can be developed for the three component case. Indeed, Asaro<sup>4</sup> has extended the Rice formulation to multicomponent adsorption in a manner consistent with the above result.

#### Summary

A reversible work cycle in terms of Gibbs free energies precisely reproduces Rice's<sup>3</sup> result for the work of separation of interfaces at constant chemical potential of the components or at constant excess solute concentration at the interface. The work can be conveniently represented on graphs of solute chemical potential versus excess solute concentration. In terms of these developments, one can express the work of separation for arbitrary paths of chemical potential and excess solute concentration for binary or for multicomponent systems.

These results provide a basis for determining the work of separation from data on solute adsorption obtained either from experiment or by statistical thermodynamical prediction. The extent to which the assumptions of the model apply to separation at low temperature remain to be explored quantitatively, for example, the relaxation time for local equilibrium to be attained on the surface in the "rapid" separation case. However, even with substantial contributions to the total work of separation by plastic flow, for example, the crack tip may be screened by

dislocation fields so that the local work of separation relating to solute adsorption governs the separation behavior.

Acknowledgement

This research was supported by the Defense Advanced Research Projects Agency of the Department of Defense under Contract No. MDA903-76C-0250 with The University of Michigan.

References

1. C. Hsieh and R. M. Thomson, *J. Appl. Phys.* 44, 2051 (1973).
2. M. P. Seah, *Surface Sci.* 53, 168 (1975); *Proc. Roy. Soc. (London)* A349, 539 (1976).
3. J. R. Rice, in *Effect of Hydrogen on Behavior of Materials*, AIME, New York, 1976, p. 455.
4. R. J. Asaro, *Met. Sci. J.*, in press (1978).
5. J. P. Hirth, *Phil. Trans. Roy. Soc. (London)*, in press (1978).
6. E. Zaremba, *Solid State Comm.* 23, 347 (1977).
7. J. W. Gibbs, *Collected Works*, Vol. 1, Yale Univ. Press, New Haven, Conn., 1948, p. 219.
8. E. A. Guggenheim, *Thermodynamics*, North Holland, Amsterdam, 1950, p. 35.
9. J. W. Cahn, in *Surface Thermodynamics*, Am. Soc. Metals, Metals Park, Ohio, in press (1978).

CONTACT PROBLEMS IN CERAMIC COMPONENTS

A. G. Evans  
F. A. McClintock

ABSTRACT

Ceramic turbine design invariably involves a number of ceramic/ceramic or ceramic/metal contacts that are subject to lateral forces during service. The influence of the lateral forces on the contact stress fields is evaluated in terms of the friction coefficient and the material compliance. Then the relative probabilities of fracture are derived to determine the specific advantages that can be accrued by reducing the friction coefficient compared to increasing the compliance or improving the quality of the surface layers in the vicinity of the contact.

## CONTACT PROBLEMS IN CERAMIC COMPONENTS

A. G. Evans and F. A. McClintock

### INTRODUCTION

The design of ceramic engines invariably involves some ceramic or ceramic/metal contacts that exhibit relative lateral motion. The quantity and criticality of these contacts can be minimized by employing the appropriate design criteria, such as the maximum use of integrated units. However, the problem will almost invariably need to be addressed at some locations within the engine. The present paper examines the problem of elastic contact in the presence of lateral forces, and identifies the specific roles of the friction coefficient, the compliance, and the surface quality on the incidence of fractures in the vicinity of the contact site.

### CONTACT STRESSES

The problem of an elastic contact subjected to a lateral force was firstly examined in detail by Mindlin.<sup>1</sup> He demonstrated that, in the absence of sliding, the tangential tractions  $\sigma_x$  over the contact area exhibit a singularity at the contact periphery  $a$  (Fig. 1);

$$\sigma_x = \left( \frac{P_x}{2\pi a^2} \right) [1 - (r/a)^2]^{-\frac{1}{2}} \quad (r < a) \quad (1)$$

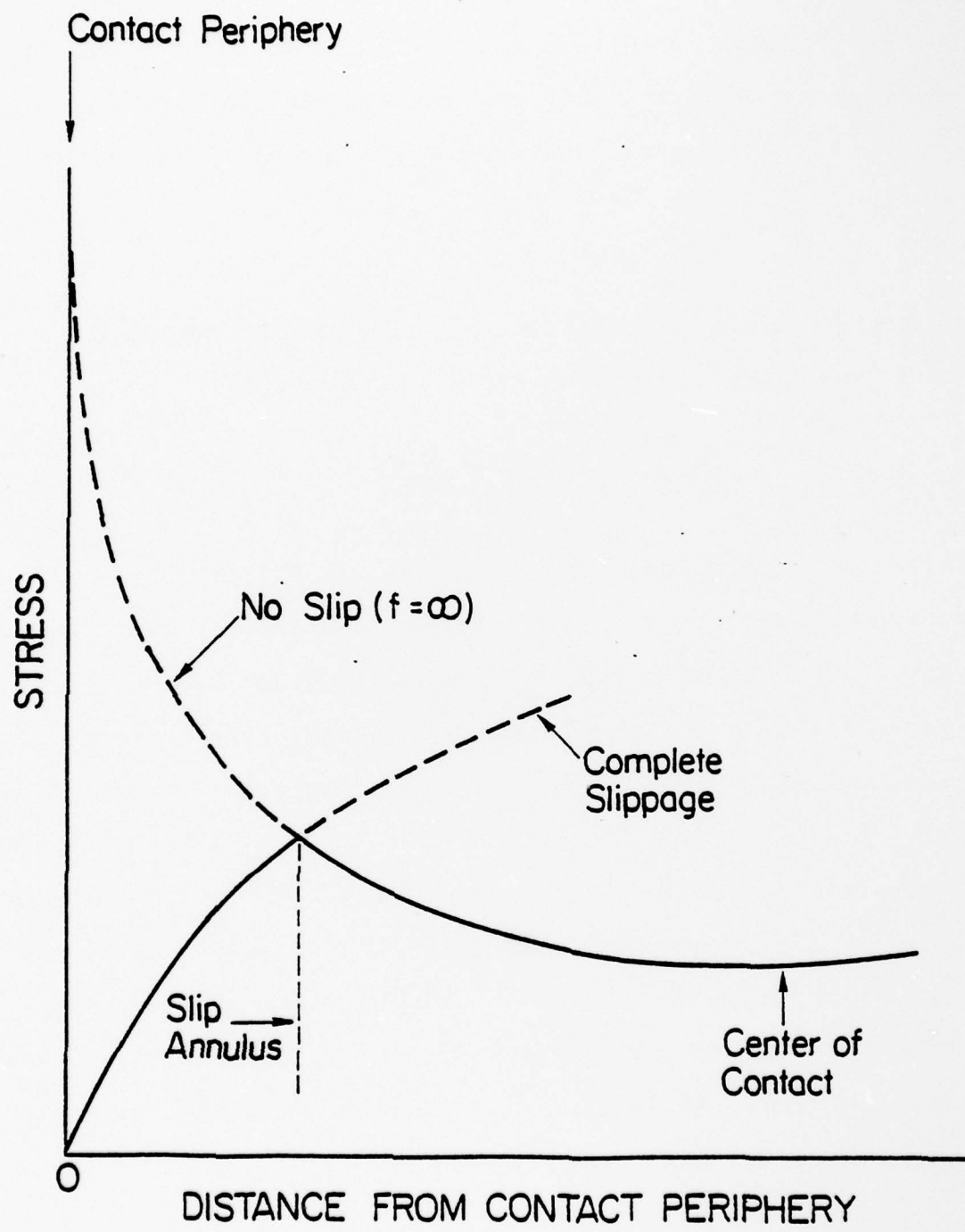


FIGURE 1.

where  $P_x$  is the lateral force. However, in the presence of a finite friction coefficient,  $f$ , sliding will occur over an outer annulus  $a^*$  (Fig. 1), with the stresses in this annulus then being related to the normal stresses  $\sigma_y$  by the usual relation;

$$\sigma_x = f\sigma_y = \frac{3fP_y}{2\pi a^2} [1 - (r/a)^2]^{1/2} \quad (a^* < r < a) \quad (2)$$

where  $P_y$  is the normal force. Mindlin<sup>1</sup> also related the annulus of sliding to the ratio of forces;

$$\frac{a^*}{a} = \left( 1 - \frac{P_x}{fP_y} \right)^{1/3} \quad (3)$$

Complete sliding will thus initiate ( $a^* = 0$ ) when  $P_x > fP_y$ , whereupon the tangential tractions can be fully described by Eq. (2). This condition will be assumed for subsequent calculation, although it is emphasized that many real cases will not involve complete sliding. For these cases the following analysis will provide an upper bound for the fracture probability (because the stresses in the stationary annulus have been overestimated).

The stresses corresponding to the distribution of tractions defined by Eq. (2) have been determined by Hamilton and Goodman.<sup>2</sup> Tensile stresses occur in the surface, primarily outside the zone of contact (Fig. 2) and behind the sliding direction, given by;

$$\begin{aligned} \sigma &= \left( \frac{3fP}{2\pi a^2} \right) \xi \cos \theta \left[ (1 + v \sin^2 \theta) [\tan^{-1} (\xi^2 - 1)^{-1/2} - \xi^{-1} (\xi^2 - 1)^{1/2}] \right. \\ &\quad \left. + (v/4) (3 - 4 \cos^2 \theta) [2 \xi^{-4} (\xi^2 - 1)^{3/2} - \tan^{-1} (\xi^2 - 1)^{-1/2} - \xi^{-1} (\xi^2 - 1)^{1/2}] \right] \\ &\equiv (3fP/2\pi a^2) F(\xi, \theta, v) \end{aligned} \quad (4)$$

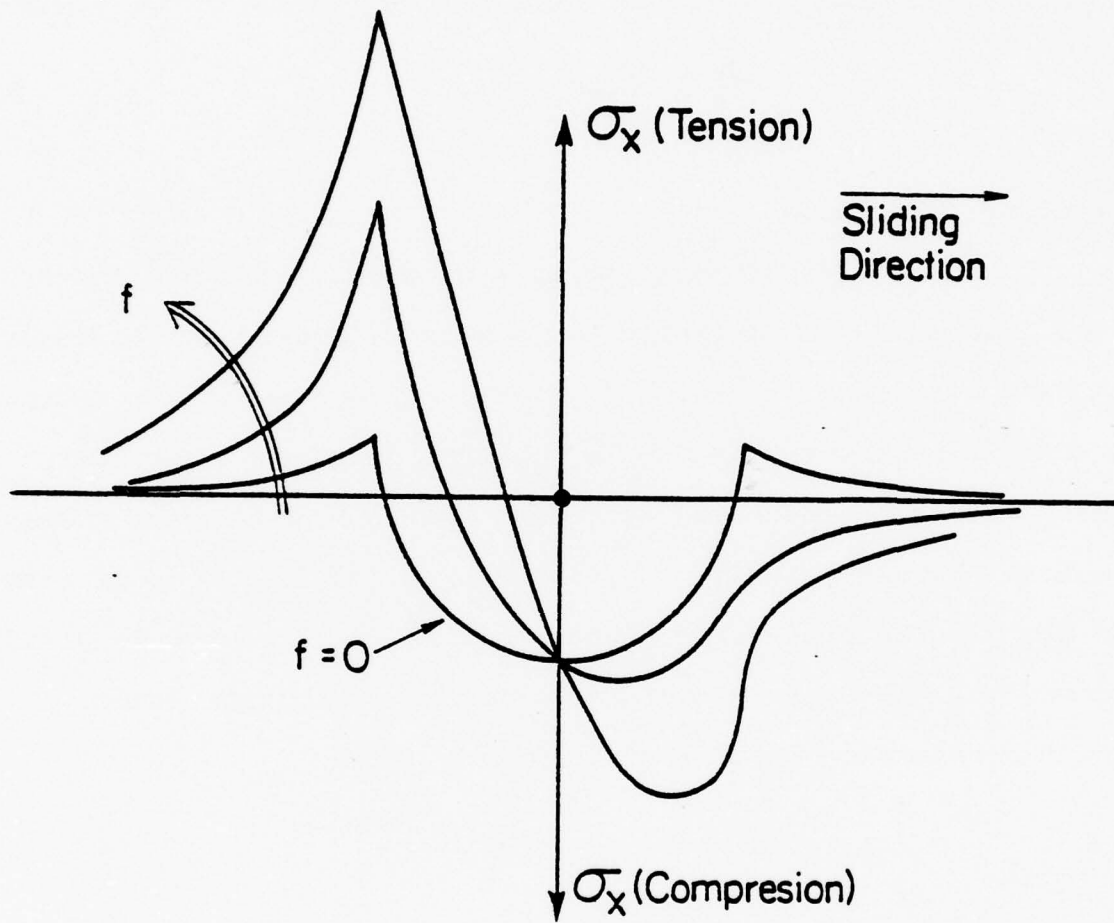


FIGURE 2.

where  $\xi = r/a$  and  $\theta$  is the inclination to the sliding direction; note that the stresses are tensile in the range  $\theta = \pm\pi/2$ . The tensile stresses outside the contact area will be augmented by the stresses from the normal tractions, given by;

$$\sigma = \frac{P}{2\pi a^2 \xi^2} (1-2\nu) \quad (5)$$

#### FRACTURE INITIATION

The distribution of tensile stress outside the contact zone interacts with pre-existent surface micro-cracks to generate surface initiated fractures (Fig. 2). The pre-existent micro-cracks will belong to a population that depends on the micro-structure of the surface layers and the mode of surface preparation. This population can, in general, be described in terms of the distribution of local stress  $\sigma$  required to induce their extension. A convenient and versatile distribution function is the two-parameter Weibull distribution;

$$\Phi(\sigma, \Delta A) = 1 - \exp \left[ -\frac{\Delta A}{A_0} \left( \frac{\sigma}{\sigma_0} \right)^m \right] \quad (6)$$

where  $\Delta A$  is a surface element subjected to the stress  $\sigma$ ,  $\sigma_0$  is the scale parameter,  $m$  is the shape parameter,  $A_0$  is a constant and  $\Phi$  is the cumulative probability of crack extension. Inserting the tensile stress from Eqs. (4) and (5) into Eq. (6) and integrating over the zone of tension yields the following expression for the fracture probability

$$-\ln[1-\Phi(P, f)] = \frac{\pi a^2}{A_0^{(m-1)}} \left[ \frac{P(1-2\nu)}{2\sigma_0 \pi a^2} \right]^m \quad (7)$$

$$+ \frac{2a^2}{A_0} \left( \frac{3fP}{2\sigma_0 \pi a^2} \right)^m \int_0^{\pi/2} \int_1^{\infty} [F(\nu, \theta, \xi)]^m \xi d\xi d\theta \\ \equiv \left( \frac{P}{2\sigma_0 \pi} \right)^m \left( \frac{a^{2-m}}{A_0} \right) I(f, m, \nu) \quad . \quad (8)$$

Values of  $I(m, f)$  are plotted in Fig. 3 for  $\nu = 0.25$ . It is now instructive to replace the load dependent contact radius  $a$  in Eq. (8) using;<sup>2</sup>

$$a^3 = \frac{3}{4} PR \left[ \frac{(1-\nu_1^2)}{E_1} + \frac{(1-\nu_2^2)}{E_2} \right] \equiv \kappa PR \quad (9)$$

where  $R$  is the radius of curvature at the contact,  $E$  is Young's modulus and the subscripts 1 and 2 refer to the two materials in contact; then,

$$-\ln[1-\Phi(P, f)] = \frac{2(m+1)/3}{A_0^{(2\pi\sigma_0)^m} R^{(m-2)/3} \kappa^{(m-2)/3}} I(f, m, \nu) \quad . \quad (10)$$

The ratio  $\alpha$  of the fracture loads with and without friction is;

$$\alpha = [I(f, m, \nu)/I(m, \nu)]^{-\frac{3}{2}(m+1)} \quad . \quad (11)$$

The dependencies of the fracture probability or the fracture load on the contact conditions are now fully specified. It is directly evident that small values of the normal load and the

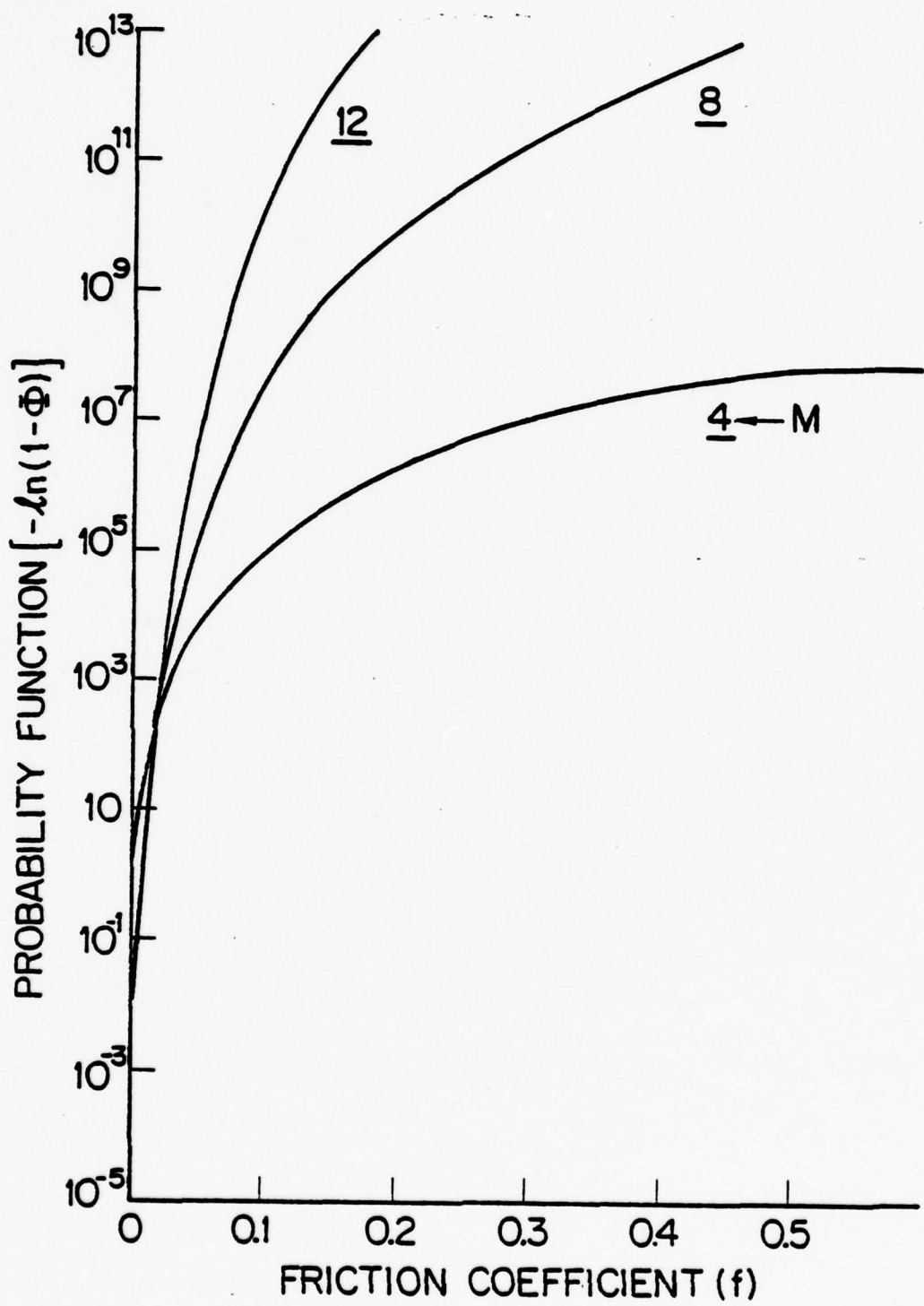


FIGURE 3.

friction coefficient and large values of the contact curvature are required. Additionally, the  $\kappa$  term (Eq. 9) indicates that a low elastic modulus of one constituent (not necessarily both) of the contact will be of considerable benefit.

#### IMPLICATIONS

The preceding analysis has indicated that the incidence of fracture at ceramic contacts is influenced by the normal force, the curvature, the friction coefficient, the elastic moduli and the distribution of pre-existent near-surface cracks. These influences suggest a combination of effects that can be used to retard fracture initiation, other than the self-evident effects of reducing the normal force and increasing the curvature by improved design. Firstly, since the fracture probability can be appreciably decreased by reducing the elastic modulus of one constituent of the contact, a compliant elastic interlayer should be beneficial. An elastic interlayer of low modulus, but adequate compressive strength, implies an elastic material containing a large proportion of porosity, distributed on the finest possible scale. Alternatively, available compliant materials, such as graphite, may be used when the ambient conditions are appropriate. Secondly, the low friction coefficient requirement suggests the incorporation of a solid lubricant. This might be particularly appropriate for the porous elastic interlayer concept, because the lubricant could be contained by the pores near the surface of the interlayer. Finally, the influence of the near-surface flaw

distribution suggests that superior surfaces in the vicinity of the contact area would be beneficial. This might be achieved, for example, by depositing a thin surface layer of high quality onto the contact region using chemical vapor deposition techniques; a layer with a slightly larger expansion coefficient than the substrate-leading to residual surface compression stress - would be particularly appropriate.

#### ACKNOWLEDGEMENT

This research was supported by the Defense Advanced Research Projects Agency of the Department of Defense under Contract No. MDA903-76C-0250 with The University of Michigan.

#### References

1. P. D. Mindlin, J. Appl. Mech. 16, 259 (1949).
2. G. M. Hamilton and L. E. Goodman, J. Appl. Mech. 33, 371 (1966).

## HIGH TEMPERATURE CAVITY GROWTH IN CERAMICS

A. G. Evans

### ABSTRACT

Observation of high temperature crack growth in ceramic polycrystals have indicated that a viscous phase is often contained near the crack tip. The role of this liquid phase on high temperature crack growth is explored in this paper. The liquid is shown to be subjected to a tensile pressure during steady state crack growth, and this pressure influences the chemical potential gradients. Also, crack extension is shown to occur by either a solution/reprecipitation process within the crack or by atom transport from the crack through the adjacent grain boundaries; the latter being the more prevalent. Approximate expressions for the crack growth are derived and their implications are discussed.

## HIGH TEMPERATURE CAVITY GROWTH IN CERAMICS

A. G. Evans

### INTRODUCTION

Recent studies of high temperature crack growth in polycrystalline alumina<sup>1</sup> have indicated that the cracks progress along grain boundaries with an amorphous phase contained at the tip (Fig. 1a). Fracture surface observations indicate that the amorphous material bridging the crack faces (Fig. 1b). These observations also suggest that the amorphous phase should be regarded as a viscous liquid at the test temperature. Some of the consequences of such a liquid phase on high temperature crack growth are examined in this paper.

Rigorous analyses of diffusive crack growth along grain boundaries have recently been performed by Chuang and colleagues.<sup>2,3</sup> Crack growth relations have been derived for transport occurring along both the surfaces of the crack and the adjacent grain boundaries. A similar approach is adopted herein, to examine the possible modes of crack extension that can occur in the presence of a liquid phase. This is preceded by a preliminary analysis of the pressures that develop in the liquid phase, in an attempt to rationalize the cavitation observations and as a basis for assessing the influence of the pressure on the crack growth.

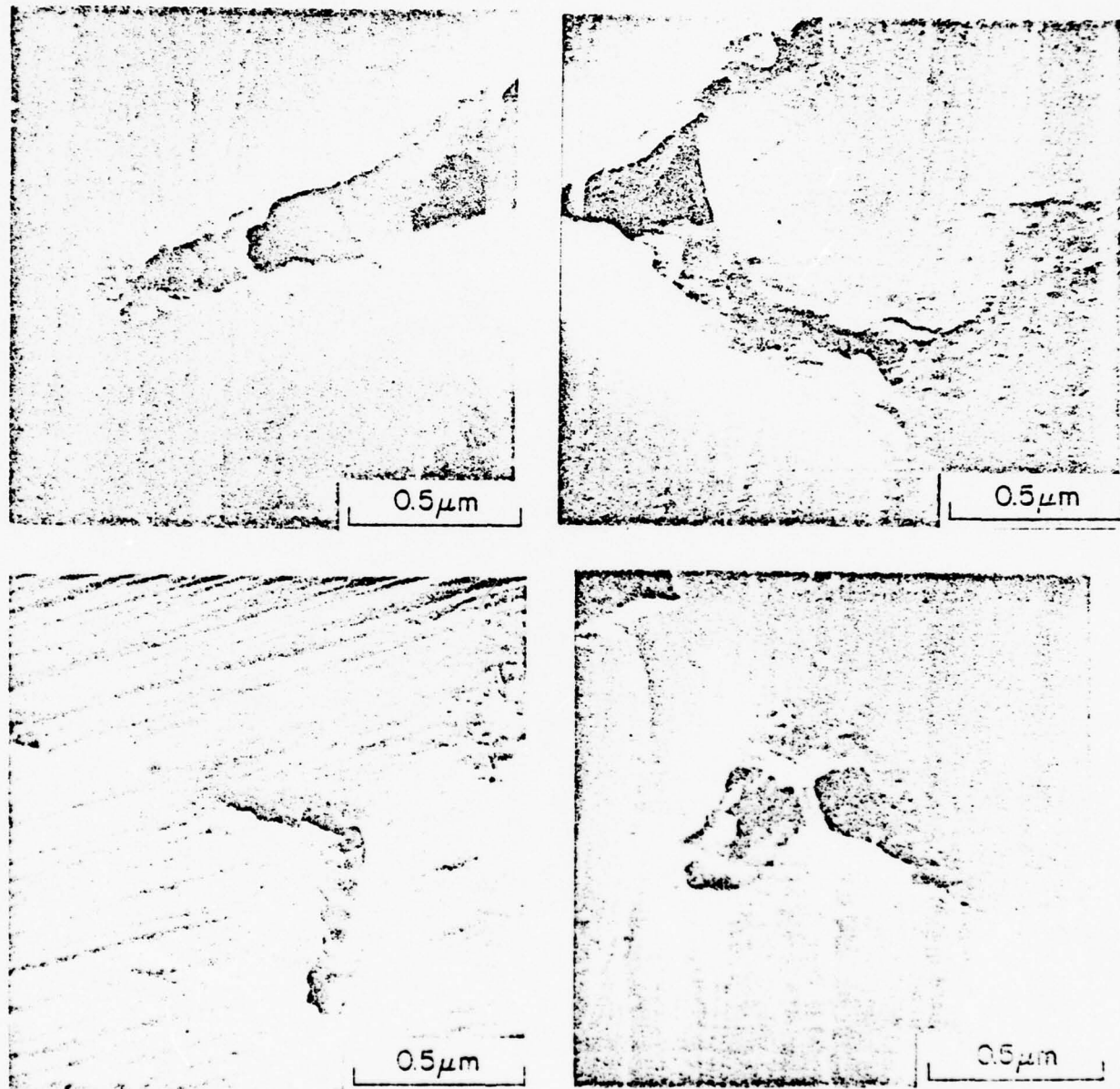


Figure 1a. Scanning electron micrograph of a crack in hot pressed alumina formed at 1550°C. The location of the viscous phase is indicated.

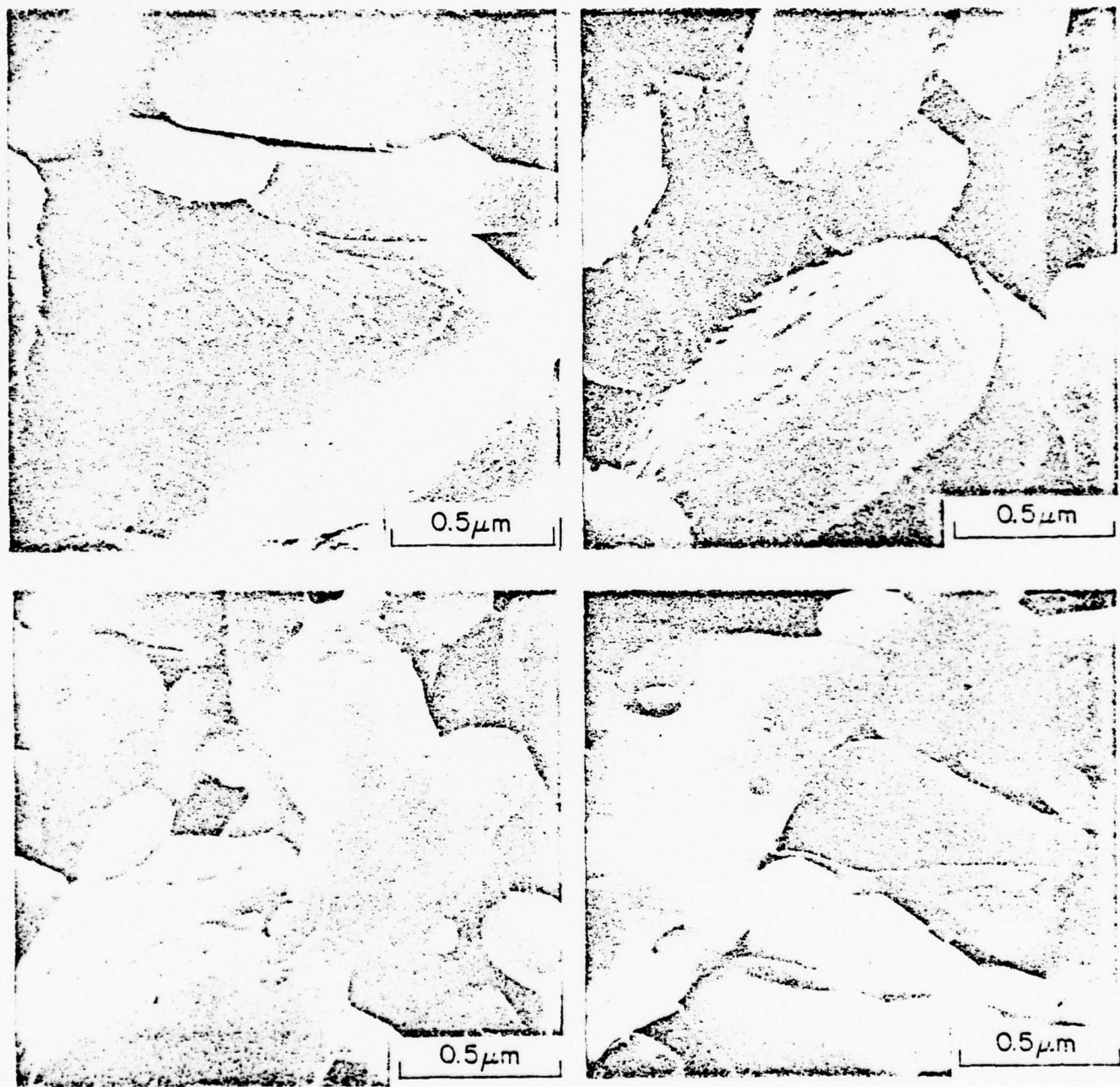


Figure 1b. A scanning electron micrograph of a fracture surface indicating networks of the amorphous phase.

## STRESS DISTRIBUTIONS IN LIQUID CONTAINING CRACKS

When a stressed crack contains a liquid phase, the liquid transmits stresses that depend on the compressibility ( $\kappa$ ) and viscosity ( $\eta$ ). For a stationary crack, radius  $2a$  and center separation  $2b$  (Fig. 2a), filled with liquid, the liquid develops a hydrostatic tension  $\bar{\sigma}$  given by<sup>4</sup>

$$\bar{\sigma}/\sigma_{\infty} = \left[ \frac{4a(1-\nu^2)}{2E} \right] \left[ \frac{b}{\kappa} + \frac{4a(1-\nu^2)}{2E} \right]^{-1} \quad (1)$$

where  $\sigma_{\infty}$  is the remote stress. However, if  $\bar{\sigma}$  exceeds the stress needed to initiate a vapor bubble in the liquid, the stress will decrease to a more modest level, dictated by the radius of curvature  $\rho_{LV}$  of the liquid vapor interface

$$\bar{\sigma} = \frac{2\gamma_{LV}}{\rho_{LV}} \quad (2)$$

where  $\rho_{LV}$  is related to the crack surface separation. When the crack starts to move, the liquid will tend to flow along with the crack and vapor cavities may initiate and propagate within the liquid. For the liquid to move with the crack, a stress gradient must develop in the liquid, related to the crack growth rate  $v$ , the liquid viscosity, and the cavity distribution. If we assume that the flow of liquid with the crack is analogous to steady state flow through a channel, the governing equation for a steady-state velocity  $v$  and a two-dimensional crack is simply

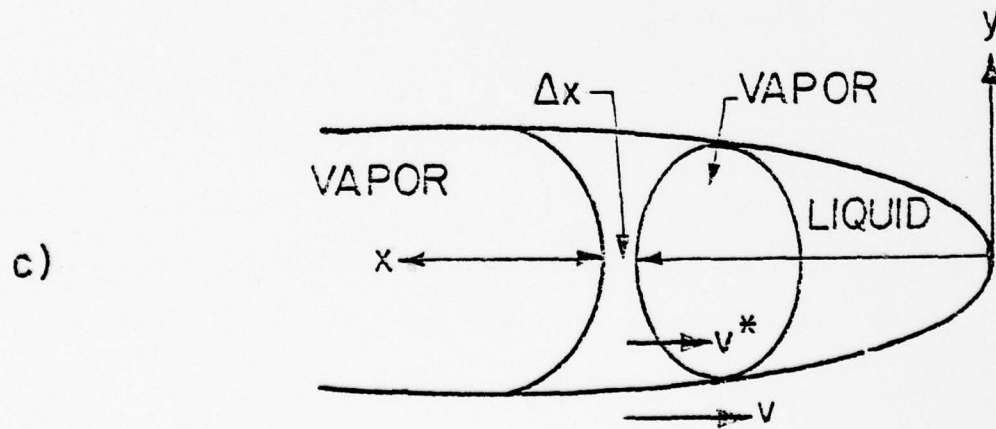
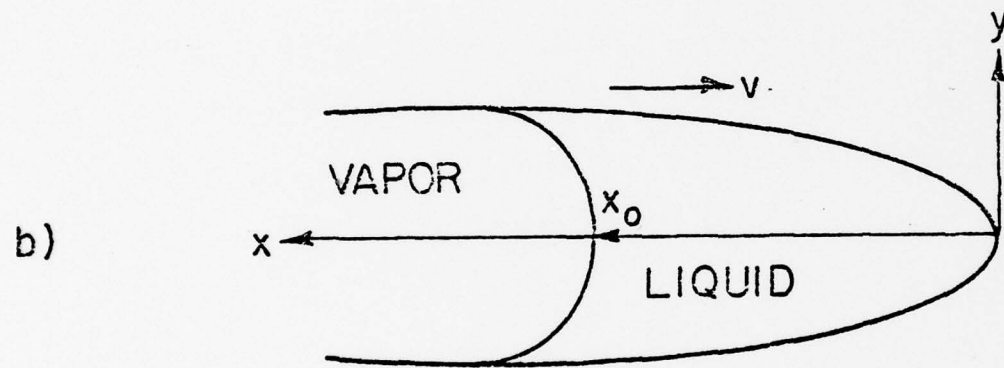
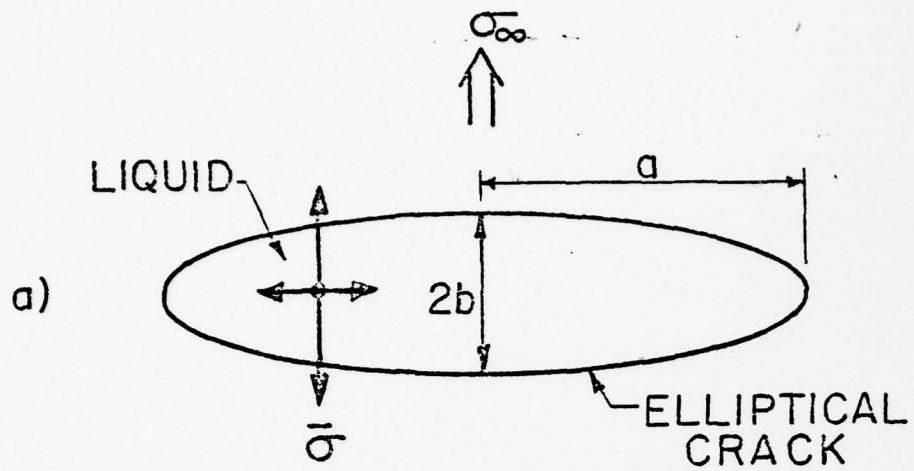


Figure 2a. A schematic view of a liquid filled crack.  
 2b. A crack containing a liquid phase near the tip.  
 2c. A fully contained cavity within the crack tip liquid phase.

$$v = - \frac{y^2}{3} \left( \frac{d\bar{\sigma}}{dx} \right) \quad (3)$$

where  $2y$  is the crack surface separation. If we now consider an elliptical crack with a liquid volume that is small compared to the total cavity volume, the cavity surface profile can be described by

$$y^2 \sim \frac{2b^2 x}{a} \quad (4)$$

where  $2a$  and  $2b$  are the major and minor axes of the ellipse respectively, and  $x$  is the distance from the tip (Fig. 2b). Substituting Eq. (4) into (3), and noting that the pressure must satisfy equilibrium requirements [Eq. (2)] at the vapor interface, gives

$$\bar{\sigma} = \frac{\gamma_{LS}}{b} \sqrt{\frac{2a}{x_0}} + \frac{3\gamma_{av}}{2b^2} \ln \left( \frac{x_0}{x} \right) \quad (5)$$

where  $x_0$  is the distance between the vapor interface and the crack tip. The magnitude of  $x_0$  can be estimated by examining the stability conditions for a fully contained cavity (Fig. 2c). The stress gradient from the primary vapor interface to the cavity interface causes the intervening liquid ligament to move at a velocity  $v^*$ , in approximate accord with Eq. (3). The stress gradient  $\Delta\bar{\sigma}$  (again neglecting vapor pressure effects) is given by

$$\Delta\bar{\sigma} \approx \frac{\gamma_{LS}\sqrt{2a}}{b} \left[ \frac{1}{\sqrt{x}} - \frac{1}{\sqrt{x+\Delta x}} \right] \equiv \frac{\gamma_{LS}}{bx^{3/2}} \sqrt{\frac{a}{b}} \Delta x \quad (6)$$

$(\Delta x \ll x_0)$

Substituting for  $\Delta\bar{\sigma}/\Delta x$  in Eq. (3) then gives

$$x \approx \frac{2}{a} \left( \frac{b\gamma_{LS}}{3\eta v^*} \right)^2 \quad . \quad (7)$$

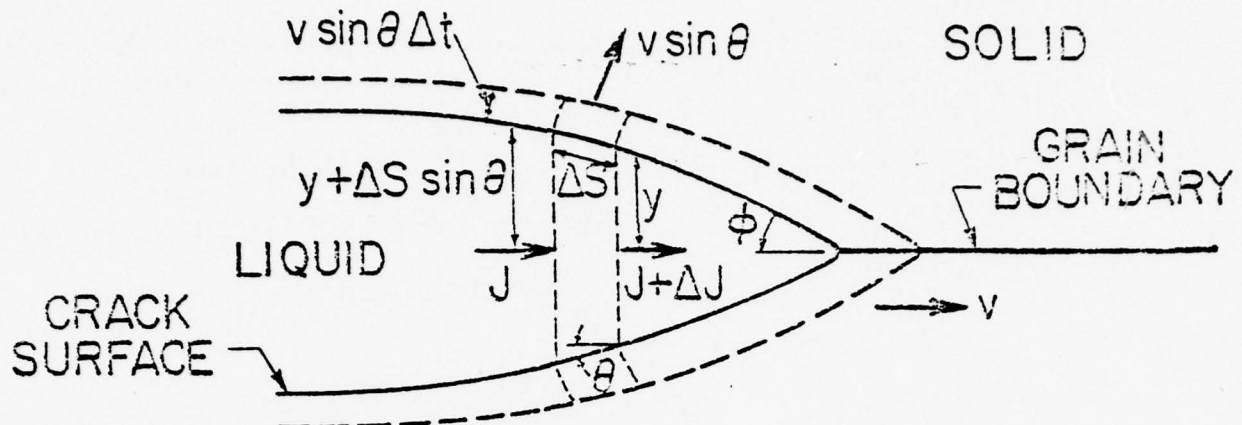
Equating  $v^*$  to  $v$  gives the steady state location  $x_0$  of the primary vapor interface. Cavities will form when the liquid volume exceeds that required to maintain the interface at  $x_0$ . Inserting this value for  $x_0$  into Eq. (5) yields the final expression for the stress distribution,

$$\bar{\sigma} = \frac{3\eta av}{b^2} \ln \left[ \left( \frac{2}{ax} \right)^{\frac{1}{2}} \left( \frac{b\gamma_{LS}}{3\eta v} \right) \right] \quad . \quad (8)$$

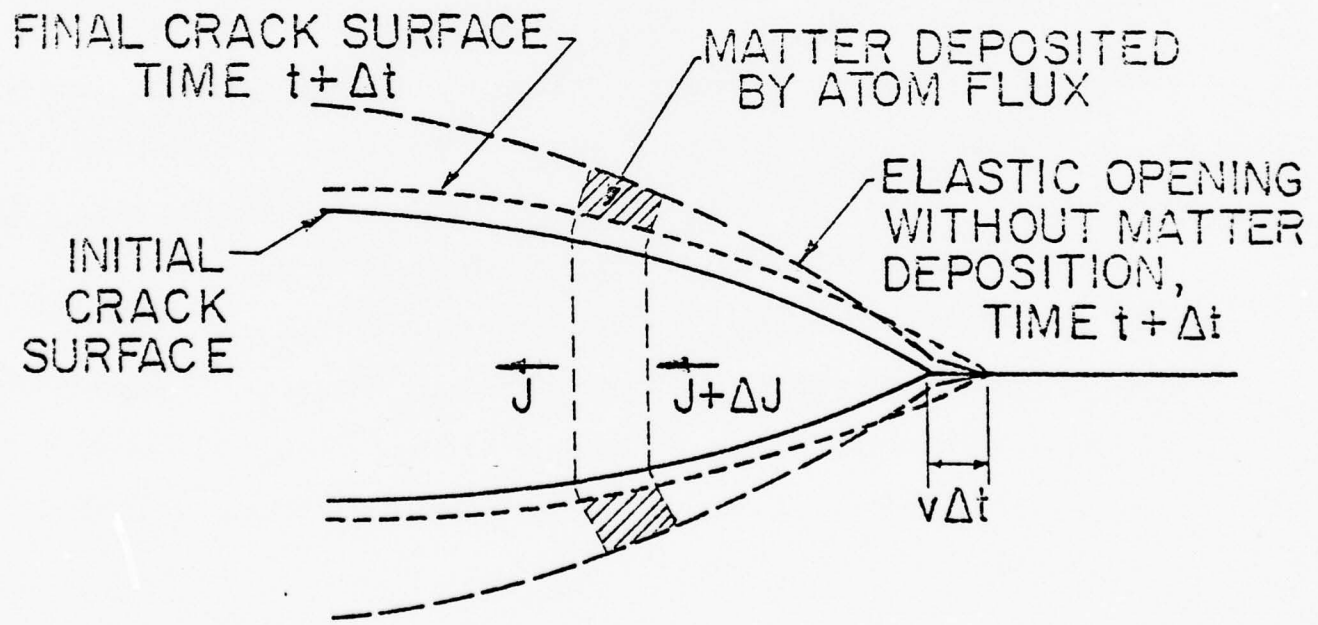
Inspection of Eq. (8) indicates that the stress increases as the crack tip is approached ( $x$  decreases), and as  $\eta$  or  $v$  increase (i.e., Eq. (8) has no maximum for finite  $v$ ). The presence of crack surface tractions created by the tensile stress in the liquid will reduce the stress intensity factor below the applied value ( $\sigma_{\infty}\sqrt{\pi a}$ ), and will modify the chemical potential of atoms on the crack surface. The latter effect is examined in subsequent sections.

#### GENERALIZED CRACK GROWTH RELATIONS

The motion of a crack in a stressed solid is considered to occur by mass transport through a liquid phase contained near the crack tip (Fig. 3). When the crack tip is followed by a detached vapor interface, the crack can extend in a steady state



a) DIFFUSIONAL GROWTH



b) SOLUTION REPRECIPITATION

Figure 3. A schematic indicating the atom fluxes through the liquid phase for (a) differential growth, (b) solution/reprecipitation.

mode, at a velocity  $v_s$ . The crack velocity prescribes the atom flux that must pass through each element of liquid. This flux is, in turn, related to the chemical potential gradient and hence to the crack profile. There are unique relations between the crack profile and the crack velocity that depend on the dominant mass transport process, the surface energies between the liquid, vapor and solid phases, and the imposed boundary conditions. The relations needed to obtain the crack profiles are developed in this section, following an assessment of the conditions that accompany the primary modes of crack growth.

#### Chemical Potentials

The chemical potential  $\mu$  contains terms associated with changes in the surface energy, strain energy, and the work done by the distribution of forces.<sup>5</sup> For atoms located along the surface of a crack, addition of an atom (at a ledge) has the following effects: the surface energy changes through the usual radius of curvature term, work is done against the traction normal to the crack surface (the stress  $\bar{\sigma}$  in the liquid phase), and the strain energy  $U$  of the system increases (for fixed grip conditions). Consideration of these three contributions leads to a chemical potential<sup>5</sup>

$$\frac{\mu}{\Omega} = \gamma_{LS} \kappa - \bar{\sigma} + \left[ \frac{(1-v^2)(\sigma_L^2 + \bar{\sigma}^2)}{2E} - \frac{v(1+v)\sigma_L \bar{\sigma}}{E} \right] \quad (9)$$

where  $\kappa$  is the local curvature ( $1/\rho$ ),  $\sigma_L$  is the local tangential

stress at the crack surface, and  $\Omega$  is the atomic volume. In situations where appreciable boundary diffusion occurs, the stress  $\sigma_L$  is relatively low ( $\ll E$ ) and the strain energy term can be neglected. Crack growth then occurs by the migration of vacancies, formed at grain boundaries, into the crack tip (i.e., a flow of atoms into the grain boundary). However, in the absence of boundary diffusion, the strain energy term is not negligible and crack growth can occur by a solution/reprecipitation process involving the liquid phase. This process requires a net flux of atoms (through the liquid) away from the crack tip and hence, that the potential gradient be negative, i.e., for  $\sigma_L \gg \bar{\sigma}$ ,

$$\frac{d}{dr} \left[ \frac{(1-\nu^2) \sigma_L^2}{2E} - \bar{\sigma} + \gamma_{LS}^K \right] < 0 \quad (10)$$

where  $r$  is the distance from the crack tip. To estimate the conditions under which this crack growth process prevails, an elliptical crack profile will be assumed and the chemical potential terms calculated near the crack tip.

The tangential stresses around an elliptical crack normal to a uniaxial applied stress are given by<sup>6</sup>

$$\frac{\sigma}{\sigma_\infty} = \frac{\sinh 2u_0 + e^{2u_0} \cos 2\theta - 1}{\cosh 2u_0 - \cos 2\theta} \quad (11)$$

where  $\theta$  is the angle between the crack plane and the crack surface ( $\theta = 0$  at the crack tip) and  $u_0 = \tanh^{-1}(b/a)$ . For a

narrow crack,  $b \ll a$ , Eq. (11) reduces to

$$\frac{\sigma_L}{\sigma_\infty} \approx \frac{2(b/a) - \theta^2}{(b/a)^2 + \theta^2} . \quad (12)$$

Near the crack tip, small  $\theta$ , the following relations can be applied:

$$\theta \approx y/a , \quad y = b\sqrt{2r/a} .$$

Substitution into Eq. (12) then gives

$$\sigma_L = \sigma_\infty \left[ \frac{2a^2}{b(a+r)} \right] , \quad (13a)$$

$$\frac{U}{\Omega} = \frac{4(1-\nu^2)\sigma_\infty^2 a^4}{b^2(a+r)^2 E} \equiv \frac{4Ga^3}{\pi(a+r)^2 b^2} \quad (13b)$$

where  $G$  is the strain energy release rate. For relatively narrow cracks ( $b \ll a$ ) the curvature is

$$\kappa \approx \frac{d^2y}{dr^2}$$

and hence near the crack tip,

$$\kappa = - \frac{b\sqrt{2}}{4r^{3/2}} a^{\frac{1}{2}} . \quad (14)$$

Substituting the derivatives of  $U$ ,  $\kappa$ , and  $\sigma$  of Eq. (3) into Eq. (10), now gives

$$\frac{4Ga^3}{\pi b^2(a+r)^3} > \frac{3b\gamma_{SL}}{4(2a)^{\frac{1}{2}} r^{\frac{5}{2}}} + \frac{3\nu a}{2b^2 r} . \quad (15)$$

At a location near the crack tip,  $r \approx b$ , Eq. (15) reduces to

$$G > \frac{3\pi}{8} \left[ \frac{\gamma_{SL}}{2} \sqrt{\frac{b}{2a}} + v\eta \left( \frac{a}{b} \right) \right] \quad (16)$$

A solution/reprecipitation crack growth process can thus occur at large  $G$ : the incidence of this mode of crack growth being encouraged by small values of the solid/liquid surface energy and of the liquid viscosity. (Note that the dependence of the final result, [Eq. (15)], on  $r$  indicates that the steady state crack shape, if steady state exists, cannot be characterized by an ellipse.)

#### The Atom Flux

The atom flux through the liquid phase for steady state crack extension can be derived from the requirements of mass conservation (see Appendix I). For example, for a positive flux gradient directed toward the crack tip, (Fig. 3a)

$$\frac{dJ}{dy} = \frac{v}{\Omega b} \quad (17)$$

$$J = \frac{v}{\Omega} \left( \frac{y}{b} - 1 \right) \quad .$$

Also, the flux is related to the chemical potential gradient by<sup>7</sup>

$$J = - \frac{D_L C_L}{kT\Omega} \left( \frac{d\mu}{dr} \right) \quad (18)$$

where  $D_L$  is the diffusion coefficient in the liquid phase, and

$c_L$  is the molecular fraction of the solid material dissolved in the liquid. Substituting for the chemical potential gradient from Eq. (9), differentiating, and equating to Eq. (17), then gives a differential equation for the crack shape. For example, for diffusion controlled crack growth, the strain energy term can be neglected, and the governing differential equation is:

$$\frac{d^4y}{dr^4} + \frac{dy}{dr} \left[ \left( \frac{v}{\gamma_{LS}} \right) \left( \frac{kT}{2D_L c_L \Omega b} - \frac{6n}{y^3} \right) \right] = 0 \quad (19)$$

The differential equations that describe the crack shape in the presence of a liquid phase typically require numerical solution. These solutions are not attempted in the present study. Instead, approximate analytic solutions are developed, in order to provide an appreciation for the important physical phenomena.

#### APPROXIMATE SOLUTIONS

To obtain approximate analytic solutions for cavity growth, the gradients of pressure and strain energy are linearized. The pressure linearization is analogous to invoking a parallel-sided crack and therefore, is most pertinent to narrow cracks ( $b \ll a$ ). The linearized stress gradient [c.f. Eq. (3)] is

$$\frac{d\bar{\sigma}}{dr} = - \frac{2\eta v}{\tilde{y}^2} \quad (20a)$$

$$\bar{\sigma} = \frac{2\gamma_{LS}}{y_o} + \frac{3\eta n}{\tilde{y}^2} (x_o - r) \quad (20b)$$

where  $\tilde{y}$  is some averaged value of the crack surface separation, and  $y_0$  is the separation at  $x_0$ .

The linearized strain energy term is adapted from the solution for an ellipse [c.f. Eqs. (9) and (12)] in the region near the crack tip ( $r \ll a$ ); viz,

$$\frac{U}{\Omega} = \frac{4Ga}{\pi b^2} \left[ 1 - \frac{2r}{a} \right] , \quad (21a)$$

$$\frac{1}{\Omega} \left( \frac{dU}{dr} \right) = - \frac{8G}{\pi b^2} . \quad (21b)$$

Recall, however, that this term is only important when grain boundary diffusion is not occurring.

#### Diffusion Controlled Crack Growth

The linearized differential equation governing the crack shape for a flux directed toward the tip (as pertains to diffusion control) is obtained directly from Eq. (19) as

$$\frac{d^4y}{dr^4} + \left( \frac{kTv}{D_L c_L \gamma_{LS} b \Omega} \right) \frac{dy}{dr} = 0 . \quad (22)$$

Specifying the crack tip location and equilibrium angle,  $\sigma(\cos\phi = \gamma_B/2\gamma_{SL})$ , by:  $y = 0$ ,  $r = 0$ , and  $dy/dr = \phi$ , the solution to Eq. (22) becomes

$$y = \phi \alpha^{-1/3} [1 - \exp(-\alpha^{1/3} r)] \quad (23)$$

where  $\alpha = kTv/D_L c_L \gamma_{LS} b \Omega$ . This shape is depicted in Fig. 4. The

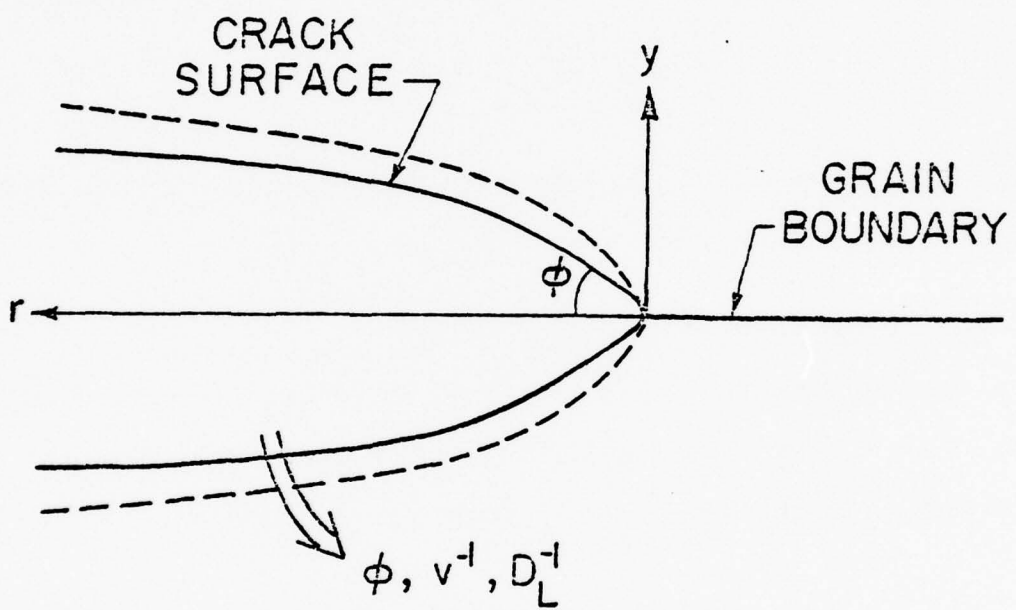


Figure 4. The shape of the crack surface predicted by the analysis.

crack surface curvature is

$$\kappa = -\phi \alpha^{1/3} \exp[-\alpha^{1/3} r] . \quad (24)$$

The chemical potential of atoms at the crack surface can now be obtained from Eq. (9) as

$$\frac{\mu}{\Omega} = -\gamma_{LS} \left[ \frac{2}{\tilde{y}} + \frac{3\eta v(x_o - r)}{\tilde{y}^2 \gamma_{LS}} + \alpha^{1/3} \phi \exp(-\alpha^{1/3} r) \right] ,$$

and at the crack tip

$$\frac{\mu_{tip}}{\Omega} = -\gamma_{LS} \left[ \frac{2}{y_o} + \frac{3\eta v x_o}{\tilde{y}^2 \gamma_{LS}} + \alpha^{1/3} \phi \right] . \quad (25)$$

The chemical potential of atoms at the crack tip is also related to the tensile stress at the tip,  $\sigma_{tip}$ , by<sup>5</sup>

$$\frac{\mu_{tip}}{\Omega} = -\sigma_{tip} . \quad (26)$$

Equating Eq. (28) with Eq. (27) yields a value for the crack tip stress,

$$\sigma_{tip} = \gamma_{LS} \left[ \frac{2}{y_o} + \frac{3\eta v x_o}{\tilde{y}^2 \gamma_{LS}} + \sigma \left( \frac{kT v}{D_L C_L \gamma_{LS} b \Omega} \right)^{1/3} \right] \quad (27)$$

An extension of this result can be achieved if it is assumed that there is no atom flux through the vapor phase (so that  $b \approx y_o$ ), and that the crack length is sufficiently large that the crack width  $b \approx y$  at  $r = \infty$ ; viz,

$$b = \phi \alpha^{1/3} . \quad (28)$$

If it is also assumed that the average crack surface separation  $\tilde{y}$  is related to  $b$  by

$$\tilde{y} \sim \xi b$$

where  $\xi$  is a constant ( $\sim 0.8$  for the present crack shape), the tip stress becomes

$$\sigma_{tip} \approx \left( \frac{vkT \gamma_{LS}}{D_L c_L \Omega \phi^3} \right)^{1/2} \left[ \phi^2 + 2 + \frac{3\eta x_0 v^{3/2}}{\xi^2} \left( \frac{kT}{D_L c_L \Omega \phi^3 \gamma_{LS}^3} \right)^{1/2} \right]. \quad (29)$$

This result should be used with caution, because the above set of assumptions overspecify conditions on the atom flux. Nevertheless, the result does provide useful insights, as noted below.

The flux of atoms through the crack tip into the grain boundary is

$$J_{tip} = \frac{v}{\Omega} \quad . \quad (30)$$

The equivalent grain boundary flux at the tip is<sup>5</sup>

$$(J_b)_{tip} = \frac{D_b \delta_b}{2kT} \sigma'_{tip} \quad (31)$$

where  $\sigma'_{tip}$  is the derivative of the stress in the grain boundary at the crack tip. Equating Eqs. (30) and (31) gives

$$\sigma'_{tip} = \frac{2kTv}{\Omega D_b \delta_b} \quad . \quad (32)$$

For a given crack morphology, the quantities  $\sigma_{tip}$  and  $\sigma'_{tip}$  can be related to the applied stress  $\sigma_\infty$ . For example, for a collinear array of cracks of length  $2a$  separated by a distance  $2b$ ,<sup>5</sup>

$$\sigma_{\infty} = \frac{b-a}{b} \left( \sigma_{\text{tip}} + \frac{b-a}{3} \sigma'_{\text{tip}} \right) \quad (33)$$

Combining with Eqs. (29) and (32) then gives a relation between the crack velocity and the applied stress;

$$\frac{b\sigma_{\infty}}{(b-a)} = Av^{\frac{1}{2}} + Bv + Cv^2$$

where

$$A = (2+\phi^2) \left( \frac{kT\gamma_{LS}}{\phi^3 \Omega D_L C_L} \right)^{\frac{1}{2}},$$

$$B = \frac{2(b-a)kT}{3\Omega D_b \delta_b},$$

$$C = \frac{3\eta x_0 kT}{\Omega D_L C_L \gamma_{LS} \phi^3 \xi^2}.$$

Large values of the coefficients A, B and C yield low values of the crack velocity. Note that the coefficients containing  $\phi$  in the denominator only apply in the presence of the liquid phase. They reflect an enhancement of the crack tip stresses due to the viscous action of the liquid; which in turn, reduce the driving force for boundary diffusion.

#### Solution/Reprecipitation

The linearized governing differential equation for solution/reprecipitation can be derived from Eq. (18) and (A17) as

$$\frac{d^4 y}{dr^4} + \frac{v k T}{b^2 \Omega D_L C_L \gamma_{LS}} (\beta * \tilde{y} - b) \frac{dy}{dr} = 0 \quad (34)$$

The solution is the same as that given by Eq. (23) (if dissolution at the crack tip occurs rapidly enough, so that the equilibrium crack tip angle  $\phi$  is maintained), except that  $\alpha$  is now given by

$$\alpha = \frac{vkT}{b^2 \Omega D_L C_L \gamma_{LS}} (\beta^* \tilde{y} - b) \quad . \quad (35)$$

The atom flux is thus

$$J = - \frac{D_L C_L}{kT} \left[ \frac{3\eta v}{\tilde{y}^2} - \frac{G}{\pi b^2} + \gamma_{SL} \phi \alpha^{2/3} \exp(-\alpha^{1/3} r) \right] \quad . \quad (36)$$

Equating this flux to the flux obtained from the steady state growth requirements [Eq. (A16)] then relates the crack driving force  $G$  to the crack velocity  $v$ ,

$$G = \frac{\pi b^2}{8} \left[ \frac{3\eta v}{\tilde{y}^2} + \alpha \gamma_{SL} \left( b - \frac{\phi}{\alpha^{1/3}} \right) \right] \quad (37)$$

Substituting for  $\alpha$  from Eq. (35) yields a relatively complex expression relating  $G$  and  $v$ , in terms of the liquid viscosity and diffusivity.

#### DISCUSSION

The approximate solutions for high temperature crack growth provide a basis for estimating the importance of certain material variables on high temperature failure in the presence of a viscous phase. The prevalent steady state regime of crack growth entails diffusion of atoms from the crack into the grain boundaries, using the liquid phase as a medium for enhanced

diffusion. Prominent influences in this regime derive from the diffusivities in the solid (grain boundary) and the liquid, and from the liquid/solid equilibrium angle  $\phi$ . Large values of the diffusivities encourage crack extension, as might be anticipated; but their relative influence depends on the magnitude of several other variables. The influence of  $\phi$  is interesting. Intuitively it might be anticipated that small values of  $\phi$ , i.e. narrow cracks, would encourage crack growth. However, the stresses with the liquid become very large as the crack width decreases and this tends to reduce the stress gradient in the solid: thereby reducing the driving force for grain boundary atom migration. Hence, the crack growth rate actually tends to increase as  $\phi$  increases. This is the opposite trend to that found for crack growth dictated by diffusion along the crack surface.<sup>5</sup> The importance of  $\phi$  depends, again, on other variables: notably the viscosity of the liquid.

A solution/reprecipitation mode of crack extension seems possible under conditions which prohibit solid state atom migration. Crack extension occurs only above a minimum applied  $G$ , and then the growth rate is related in quite complex fashion to  $G$  and the other influential variables (such as the liquid diffusivity and viscosity, the equilibrium angle  $\phi$  and the surface energy).

#### ACKNOWLEDGEMENTS

This work was supported by the Division of Material Science, Office of Basic Energy Sciences, U.S. Department of Energy.

## APPENDIX: ATOM FLUX DUE TO MATTER CONSERVATION

The volume  $\Delta V_J$  of material removed per unit width from a crack surface element of length  $\Delta S$ , in time  $\Delta t$  by a positive flux gradient toward the crack (Fig. 3a) is

$$\begin{aligned}\Delta V_J &= \Omega [(J + \Delta J)y - J(y + \Delta S \sin\theta)] \Delta t \\ &= \Omega [\Delta J y - \Delta S J \sin\theta] \Delta t\end{aligned}\quad (A1)$$

where  $\theta$  is the angle defined in Fig. 3a. The volume  $\Delta V_v$  of material removed per unit crack width by the steady state motion,  $v$ , of the crack in time  $\Delta t$  is

$$\Delta V_v = v \Delta t \sin\theta \Delta S . \quad (A2)$$

Hence, in the absence of elastic crack opening effects, conservation of matter requires that these volumes be equal, and hence,

$$\frac{\Delta J}{\Delta S \sin\theta} = \frac{V}{\Omega} + J . \quad (A3)$$

Noting that  $\Delta y \equiv \Delta S \sin\theta$ , Eq. (A3) can be expressed in differential form as

$$y \frac{dJ}{dy} = \frac{V}{\Omega} + J . \quad (A4)$$

Solution of Eq. (A4) gives

$$\frac{Y}{C} = \frac{V}{\Omega} + J \quad (A5)$$

where  $C$  is a constant. Applying the boundary condition,  $J = 0$  at  $y = b$  (the crack center), Eq. (A5) becomes

$$J = \frac{v}{\Omega} \left( \frac{y}{b} - 1 \right) ,$$

and

$$\frac{dJ}{dy} = \frac{v}{b\Omega} . \quad (A6)$$

This result is modified if appreciable elastic crack opening effects are involved (Fig. 3b). The contribution due to elastic opening can be explicitly calculated for conditions that exclude stress relaxation due to boundary or lattice diffusion. Then the crack opening, near the tip, created by a remote stress  $\sigma_\infty$  is

$$u = \frac{\sigma_\infty (1 + v)}{2\sqrt{2E}} (ra)^{\frac{1}{2}} . \quad (A7)$$

In time  $\Delta t$ , the change in displacement at a distance  $r$  from the tip of a crack moving with a velocity  $v$  is thus

$$\begin{aligned} \Delta u &= \frac{\sigma_\infty (1 + v)}{2\sqrt{2E}} r^{\frac{1}{2}} \left[ (a + v\Delta t)^{\frac{1}{2}} - a^{\frac{1}{2}} \right] \\ &= \frac{\sigma_\infty (1 + v)}{4\sqrt{2E}} \left( \frac{r}{a} \right)^{\frac{1}{2}} v\Delta t \equiv \left[ \frac{G(1 + v)r}{2\pi E(1 - v)} \right]^{\frac{1}{2}} \frac{v\Delta t}{4a} . \end{aligned} \quad (A8)$$

The increase in crack volume  $\Delta V_C$  associated with an element of surface  $\Delta S$  at position  $r$  is then

$$\Delta V_C = \Delta S \Delta u \cos\theta \equiv \left[ \frac{G(1 + v)r}{2\pi E(1 - v)} \right]^{\frac{1}{2}} \frac{v \cos\theta \Delta S \Delta t}{4a} . \quad (A9)$$

For a crack with an approximately elliptic profile, Eq. (A9) becomes

$$\Delta V_C \approx \left[ \frac{G(1+v)}{4\pi E(1-v)a} \right]^{\frac{1}{2}} \frac{yv \cos\theta \Delta S \Delta t}{4b} . \quad (A10)$$

The prevalent mode of crack extension in the absence of diffusion is solution/reprecipitation; this involves a flux directed toward the crack center, such that atoms are deposited on each element of crack surface (Fig. 3b). When this diminution of the crack opening is more than counteracted by the elastic opening, a steady state growth can be achieved, as depicted in Fig. 3b, i.e.,

$$\Delta V_V = \Delta V_C - \Delta V_J . \quad (A11)$$

Substituting for these volumes from Eqs. (A1), (A2), and (A9) gives

$$y \frac{dJ}{dy} = J - \frac{v}{\Omega} + \frac{\beta r^{\frac{1}{2}}}{a\Omega} v \cot\theta \quad (A12)$$

where  $\beta^2 = G(1+v)/32\pi E(1-v)$ . For relatively narrow cracks,  $\cot\theta \sim dr/dy$ ;

$$y \frac{dJ}{dy} = J - \frac{v}{\Omega} + \frac{\beta r^{\frac{1}{2}}}{\Omega} \frac{v dr}{dy} . \quad (A13)$$

Assuming a crack with an approximately elliptic profile, Eq. (A13) reduces to

$$y \frac{dJ}{dy} - J - \beta^* \left( \frac{v}{b} \right)^2 \frac{v}{\Omega} + \frac{v}{\Omega} = 0 \quad (A14)$$

where  $\beta^* = \beta a^{\frac{1}{2}}/\sqrt{2b}$ . The standard solution for this first order differential equation is

$$J = \frac{v}{\Omega} + C^* + \beta^* \left(\frac{y}{b}\right)^2 \frac{v}{\Omega} \quad (A15)$$

where  $C^*$  is a constant. Applying the boundary condition,  $J = 0$  at  $y = b$ , the flux becomes

$$J = \frac{v}{\Omega b^2} (y - b) (\beta^* y - b) \quad (A16)$$

$$\frac{dJ}{dy} = \frac{v}{b\Omega} \left| \frac{2\beta^* y}{b} - \beta^* - 1 \right| . \quad (A17)$$

The linearized flux gradient is

$$\frac{dJ}{dy} = \frac{v}{b^2 \Omega} (\beta^* \tilde{y} - b) . \quad (A18)$$

#### REFERENCES

1. A. G. Evans, D. R. Clarke and B. I. Davis, to be published.
2. T.-j. Chuang and J. R. Rice, *Acta Met.* 21 (1975) 653.
3. T.-j. Chuang, K. I. Kagawa, J. R. Rice and L. B. Sills, *Acta Met.*, to be published.
4. B. Budiansky and R. J. O'Connell, *Intl. J. Solids Structure* 12 (1976) 81.
5. T.-j. Chuang, Ph.D. Thesis, Division of Engineering, Brown University (1974).
6. C. E. Inglis, *Trans. Inst. Naval Archit.* 55 (1913) 219.
7. R. L. Stocker and M. F. Ashby, *Review of Geophys. & Space Phys.* 11 (1973) 391.

USE OF NUCLEAR MAGNETIC RESONANCE TO MEASURE  
COOLING RATES IN RAPIDLY SOLIDIFIED METALS

H. Reiss

ABSTRACT

No "real time" method for following temperature in rapidly quenched liquid metal drops has existed, and investigators have been forced to rely on the uncertain ex post facto method involving dendrite arm spacing. The liquid drops under consideration are generally less than  $100\mu$  in diameter and are quenched at rates of  $10^5$ - $10^6$  deg K sec $^{-1}$ . Nuclear magnetic resonance (NMR) offers a potential method for measuring cooling rate.

NMR is performed at radio frequencies (rf) such that a typical penetration depth into the metal is of the order of several hundred microns. Thus the entire volume of the drop will be exposed to the radiation. Furthermore, in other contexts, there exist several examples of the application of NMR to assemblies of small liquid metal drops.

The configuration envisioned in the NMR measurement of cooling rate has the drops shot through low temperature helium gas between the pole pieces of the NMR magnet in a steady stream. In this steady process the NMR absorption line shape

can be measured as it is affected by changing temperature due to cooling.

We have calculated these line shapes for the case of cooling characterized by a linear dependence of temperature upon time. Along the way it is necessary to solve the Bloch equations for the bulk magnetization of the drops under the condition that both spin-lattice and spin-spin relaxation times are time dependent (through their temperature dependences). Surprisingly, analytical solutions of these complicated simultaneous equations are possible.

The results appear quite promising although they are different for metals like lithium with a quite long spin-lattice relaxation time ( $\sim 80$  milliseconds) and more typical metals ( $\sim 100$  microseconds). The line shapes are quite sensitive to cooling rate (especially line broadening). It appears as though NMR may offer a practical technique for the real time determination of cooling rate.

USE OF NUCLEAR MAGNETIC RESONANCE TO MEASURE  
COOLING RATES IN RAPIDLY SOLIDIFIED METALS

H. Reiss

INTRODUCTION

No "real time" method exists for the measurement of cooling rates in rapidly solidified metal droplets. The best available technique involves the measurement of dendrite arm spacing<sup>1</sup> and this method is limited to an ex post facto examination of the solidified material. The problem is complicated by the fact that if crystallization indeed occurs the released latent heat (actually observable through the phenomenon of recalescence) leads to a decidedly complicated functional dependence of temperature on time. If a glassy metal should be formed there will be no dendrites and in this case, the one available method cannot be used. It is therefore important to examine other possibilities for measurement, and to estimate the likelihood of success in each case.

Given the overall problem it is not surprising that almost no "other possibilities" exist. The only one which comes to mind involves some application of nuclear magnetic resonance (NMR) which we shall investigate here. NMR is particularly suited to metals since it is a radio frequency (rf) technique and the penetration of the rf radiation into the metal is of the

order of several hundred microns. Since the rapidly cooled metal drops are less than  $100\mu$  in diameter the full volume of each drop will therefore be exposed to the rf radiation. Actually, metal drops have already been studied<sup>2, 3, 4, 5</sup> by NMR in other contexts.

The general configuration contemplated in the proposed measurement is one in which the drops are shot, with cool helium gas, between the pole pieces of the magnet supplying the static field at which time they are also exposed to the rf signal. In passing between the pole pieces they are therefore continually cooled at a rate which presumably affects the absorption line shape. It is this line shape and its dependence on cooling rate which we shall attempt to calculate. First, however, it is necessary to introduce some conditions which will make analytical solutions of the problem possible. Consider the cooling process. If a drop is at temperature  $T_0$  when time  $t$  is zero, and its radius is  $R$ , then the temperature at a distance  $r$  from its center at time  $t$  will be well approximated by<sup>6</sup>

$$T = T_0 f(r) e^{-(6Kt/R^2)} \quad (1)$$

where  $K$  is the thermal diffusivity. Equation (1) is predicated on the assumption that at the boundary of the drop, at  $r = R$ ,  $T = 0$ . Thus the drop cools at all its interior points approximately exponentially and the temperature depends on position within the drop as well as its radius  $R$ .

The first simplification we shall make is that the drops all have the same radius and that the temperature is independent of position within the drop. Furthermore we shall assume the cooling rate to be linear rather than exponential. This last condition will be approximately true until  $T = T_0/2$ . The more realistic process, not subject to these conditions, is easily amenable to full numerical solution. There, however, we will be primarily interested in determining whether a measurable signal, dependent on cooling rate, is possible in the first place and we therefore choose the simplest conditions.

If the drops move at a velocity  $v$  and the length of the sensing region is  $l$ , the time  $t_c$  during which they absorb rf radiation is

$$t_c = \frac{l}{v} \quad (2)$$

Assuming a linear cooling rate we will have

$$T = T_0 - \beta t \quad (3)$$

where  $\beta$  is the cooling rate.

We will consider different rf frequencies as well as different values of  $\beta$ , but  $t_c$  will be maintained constant. This is likely to be true in the experimental arrangement since both  $l$  and  $v$  will be approximately invariant, although, in practice it may be relatively easy to vary  $v$ .

Steady states of droplet flux will be considered so that the number density of droplets between the pole pieces will be

constant at  $\rho$ . Our results apply more naturally to cases in which crystallization is avoided (glassy materials) since, then, the more complicated temperature-time pattern associated with the appearance of latent heat is avoided. However, by numerical analysis it should even be possible to treat the more complicated situation.

#### LINE SHAPE

We now consider the quantity we need to calculate in more detail. Consider a single drop passing between the pole pieces of the magnet and being cooled in transit. The bulk nuclear magnetization,  $\vec{M}$ , of the drop will be time dependent for several reasons. First  $\vec{M}$  will be time dependent because the drop enters the steady field with zero  $\vec{M}$  and relaxes towards the equilibrium value,  $\vec{M}_0$  of  $\vec{M}$ . Second, there will be a time dependence because the drop will be subject to a constant rf field (which for simplicity we assume to be experienced by the drop simultaneously with the steady field) which will generate a periodic component of  $\vec{M}$ . Third, and most important, there will be time dependence because the drop is being cooled and the spin relaxation times will be time dependent. This component of the time dependence will allow us to sense the cooling rate.

The energy absorbed by the drop from the rf field in the time  $dt$  is given by

$$dE = V_D \vec{H}_1(t) \cdot \frac{d\vec{M}}{dt} dt \quad (4)$$

where  $\vec{H}_1(t)$  is the instantaneous magnetic induction due to rf

field and  $V_D$  is the drop volume. The total energy absorbed by the drop during  $t_c$ , the time it is in the sensing region, is then

$$E(t_e) = V_D \int_{t_e}^{t_c+t_e} \vec{H}_1(t) \cdot \frac{d\vec{M}}{dt} dt \quad (5)$$

where  $t_e$  is the time at which the drop enters the region.

Now consider a stream of drops, all the same size, and of number density  $\rho$ . Then the flux density of drops will be  $\rho v$  and if the cross sectional area of the stream is  $A$  the number of drops entering the sensing region in time  $dt_e$  will be

$$\begin{aligned} dN &= \rho v A dt_e \\ &= \Omega dt_e \end{aligned} \quad (6)$$

where

$$\Omega = \rho v A_e \quad (7)$$

Clearly, the energy absorbed by this group of drops in its passage through the sensing distance  $l$  in time  $t_c$  will be

$$\Omega E(t_e) dt_e \quad (8)$$

In the steady state of flow the drops "filling" the sensing region will have entered over a period of time such that the range of  $t_e$  values extends over an interval of time  $t_c$ . Then the energy absorbed by the group filling the sensing space (in its passage through that space) is given by

$$\Delta E = \int_{t_e^0}^{t_e^0 + t_c} \Omega E(t_e) dt_e \quad (9)$$

where  $t_e^0$  is time at which the leading edge of the group enters the space.

If  $t_c$  consists of a whole number of cycles of the rf field  $\Delta E$  will be independent of  $t_e^0$ . Alternatively, if it consists of a large number of cycles plus a fraction of a cycle it will depend negligibly on  $t_e^0$  since the dependence can only arise from the fraction of a cycle which is less than one out of many. In general we shall be interested in  $t_c$  values consisting of many thousands of cycles so that  $\Delta E$  may be considered independent of  $t_e^0$ .

Consequently, each succeeding group of drops filling the sensing region will absorb the same amount of energy and therefore the steady absorption of energy in the time  $t_c$  will be  $\Delta E$  which corresponds to a power

$$P = \frac{\Delta E}{t_c} = \frac{\Omega}{t_c} \int_0^{t_c} E(t_e) dt_e \quad (10)$$

where in the integral on the right we have set  $t_e^0 = 0$  since  $\Delta E$  does not depend on it.

In order to evaluate  $E(t_e)$  from Eq. (5) it is necessary to know  $\dot{M}(t)$  for the rapidly cooled drops. We address this problem in the following sections.

### THE BLOCH EQUATIONS

The most direct route to the bulk magnetization is through the Bloch equations<sup>7</sup> which provide a classical phenomenological description of  $\vec{M}$ . Fortunately the Bloch equations have been shown to apply fairly well to the nuclear magnetism of liquids and are therefore especially appropriate to the present case.

Before writing these equations a few comments about coordinate systems are in order. In the laboratory frame the direction of the steady magnetic field is chosen as the z-direction. The x-direction is determined by the direction of polarization of magnetic vector of the rf field. In dealing with magnetic moment precession it is convenient to work with the familiar rotating frame<sup>8</sup> with z-axis parallel to the z-axis of the fixed frame and rotating about that axis with the angular frequency  $\omega$  where  $\omega$  is also the frequency of the rf field. In the rotating frame a component of the rf field is constant and the component at right angles to it averages (as a practical matter) to zero and can be ignored.

The Bloch equations are expressed in terms of the rotating frame and the components of nuclear magnetization in this frame are written as  $M_x$ ,  $M_y$ , and  $M_z$ . These equations express the time dependence of  $\vec{M}$  in the presence of the rf field (polarized in the x-direction) whose magnetic vector (in that direction) is

$$H_1 = 2H_1 \cos \omega t \quad (11)$$

The equations also account for the effect of the steady field,  $\vec{H}_0$ , in the z-direction. The equations are

$$\frac{dM_x}{dt} = \gamma M_y (H_0 - \frac{\omega}{\gamma}) - \frac{M_x}{T_2} \quad (12)$$

$$\frac{dM_y}{dt} = \gamma M_z H_1 - \gamma M_x (H_0 - \frac{\omega}{\gamma}) - \frac{M_y}{T_2} \quad (13)$$

$$\frac{dM_z}{dt} = -\gamma M_y H_1 + \frac{M_0 - M_z}{T_1} \quad (14)$$

where  $\gamma$  is the magnetogyric ratio and  $M_0$  is the equilibrium magnetization<sup>3</sup> in the steady field,

$$M_0 = \left\{ \frac{n\gamma^2 \hbar^2 I(I+1)}{3k_B T} \right\} H_0 \quad (15)$$

Here  $n$  is the number density of spins,  $\hbar = h/2\pi$  where  $h$  is Planck's constant,  $k_B$  is the Boltzmann constant,  $T$ , the temperature and  $I$ , the nuclear spin. In Eqs. (12)-(14),  $T_1$  and  $T_2$  are the spin-lattice and spin-spin (or transverse) relaxation times respectively. In liquid metals  $T_1$  and  $T_2$  are approximately equal<sup>5</sup> and we will assume them to be strictly equal and denote both of them by

$$\tau = T_1 = T_2 \quad (16)$$

It is important to know that in liquids  $1/\tau$  depends approximately linearly<sup>10</sup> on  $T$  so that we may write

$$\frac{1}{\tau} = \alpha T \quad (17)$$

where  $\alpha$  is a constant. We note that Eq. (15) may be written as

$$M_o = \frac{\xi}{T} \quad (18)$$

where  $\xi$  is independent of  $T$  and given by

$$\xi = \frac{n\gamma^2 \hbar^2 I(I+1)H_o}{3k_B} \quad (19)$$

Since we will be considering cooling rates such that  $T$  depends linearly on time we may write

$$T = T_o - \beta(t - t_e) \quad (20)$$

where  $\beta$  is the cooling rate and  $T_o$  is the temperature at which the drop enters the sensing region.

#### THE ISOTHERMAL CASE

It is instructive to deal first with the isothermal case in which  $\beta = 0$ . Then  $\tau = T_1 = T_2$  is a constant and we may write Eqs. (12) through (14) as

$$\frac{dM_x}{dt} = h_o M_y - aM_x \quad (21)$$

$$\frac{dM_y}{dt} = h_1 M_z - h_o M_x - aM_y \quad (22)$$

$$\frac{dM_z}{dt} = -h_1 M_y - aM_z + aM_o \quad (23)$$

where

$$h_1 = \gamma H_1 \quad (24)$$

$$h_o = \gamma (H_o - \frac{\omega}{\gamma}) \quad (25)$$

$$a = \frac{1}{\tau} \quad (26)$$

The solution of these equations is facilitated by defining  $u$ ,  $v$ , and  $w$  by the equations

$$M_x = ue^{-at} \quad (27)$$

$$M_y = ve^{-at} \quad (28)$$

$$M_z = we^{-at} \quad (29)$$

When these equations are substituted into Eqs. (21) through (23) the resulting linear equations for  $u$ ,  $v$ , and  $w$  are easily solved subject to

$$u = v = w = 0, \quad t = t_e \quad (30)$$

which follows from

$$M_x = M_y + M_z = 0, \quad t = t_e \quad (31)$$

The solutions are

$$M_x = (K_1 \sin[h(t-t_e)] + K_2 \cos[h(t-t_e)]) e^{-a(t-t_e)} - \frac{M_0 h_0 h_1}{h^2} e^{-a(t-t_e)} + \frac{M_0 h_0 h_1}{a^2 + h^2} \quad (32)$$

$$M_y = \frac{h}{h_0} (K_1 \cos[h(t-t_e)] - K_2 \sin[h(t-t_e)]) e^{-a(t-t_e)} + \frac{a M_0 h_1}{(a^2 + h^2)} \quad (33)$$

$$M_z = -\frac{h}{h_0} (K_1 \sin[h(t-t_e)] + K_2 \cos[h(t-t_e)]) e^{-a(t-t_e)} + \frac{M_0 h_1^2}{h^2} e^{-a(t-t_e)} + M_0 \left(1 - e^{-a(t-t_e)}\right) - \frac{M_0 h_1^2}{a^2 + h^2} \quad (34)$$

where

$$K_1 = - \frac{a M_0 h_0 h_1}{h(a^2 + h^2)} \quad (35)$$

$$K_2 = \frac{M_0 a^2 h_0 h_1}{h^2 (a^2 + h^2)} \quad (36)$$

and

$$h = (h_0^2 + h_1^2)^{\frac{1}{2}}$$

We now need to evaluate  $E(t_e)$  prescribed by Eq. (5), but first we must express  $\bar{M}$ , defined in the laboratory frame, in terms of  $M_x$  and  $M_y$  in the rotating frame. Actually, since  $H(t)$  is defined by Eq. (11) it has only an x-component in the laboratory frame and the scalar product in Eq. (5) therefore only requires the x-component of  $\bar{M}$  which is

$$M_x = M_x \cos \omega t + M_y \sin \omega t \quad (38)$$

since the rotating frame rotates with the angular frequency  $\omega$ .

Then Eq. (5) becomes

$$E(t_e) = V_D \int_{t_e}^{t_c + t_e} (2H_1 \cos \omega t) \frac{d}{dt} \{M_x \cos \omega t + M_y \sin \omega t\} dt \quad (39)$$

We can substitute Eqs. (32) and (33) for  $M_x$  and  $M_y$  in this equation. Before doing this we integrate by parts to get

$$E(t_e) = 2H_1 V_D \{ \cos \omega (t_c + t_e) [M_x^* \cos \omega (t_c + t_e) + M_y^* \sin \omega (t_c + t_e)] + \omega \int_0^{t_c} \sin \omega (t' + t_e) [M_x \cos \omega (t' + t_e) + M_y \sin \omega (t' + t_e)] dt' \} \quad (40)$$

where  $M_x^*$  and  $M_y^*$  are the values of  $M_x$  and  $M_y$  at  $t = t_c + t_e$  and where we have set  $M_x(t'=0)$  and  $M_y(t'=0)$  equal to zero in accordance with Eq. (31). Furthermore we have introduced  $t'$  defined by

$$t' = t - t_e \quad (41)$$

The integrand in the integral of Eq. (40) may be expanded trigonometrically to yield

$$\begin{aligned} \text{integrand} = & M_x \sin \omega t' \cos \omega t' [\cos^2 \omega t_e - \sin^2 \omega t_e] \\ & + M_x [\cos^2 \omega t' - \sin^2 \omega t'] \sin \omega t_e \cos \omega t_e \\ & + M_y [\sin^2 \omega t' \cos^2 \omega t_e + \cos^2 \omega t' \sin^2 \omega t_e] \\ & + M_y [2 \sin \omega t' \cos \omega t' \sin \omega t_e \cos \omega t_e] \end{aligned} \quad (42)$$

Now we turn to Eq. (10) and note that  $E(t_e)$  given by Eq. (40) must be integrated over  $t_e$ . This integration can be performed before the integration over  $t'$  in Eq. (40). If  $t_c$  is set equal to a whole number of cycles, i.e.,

$$t_c = \frac{2\pi g}{\omega} \quad (43)$$

where  $g$  is an integer, then most of the terms in the integrand expressed in the form of Eq. (42) will integrate (over  $t_e$ ) to zero since  $\cos^2 \omega t_e$  and  $\sin^2 \omega t_e$  have the same integral over a whole number of cycles. The second and fourth terms will integrate to zero because  $\sin \omega t_e \cos \omega t_e$  is an odd function. Finally, because  $\sin^2 \omega t_e$  and  $\cos^2 \omega t_e$  have the same integral the third term may be retained in the form

$$M_Y [\sin^2 \omega t' + \cos^2 \omega t'] \sin^2 \omega t_e = M_Y \sin^2 \omega t_e \quad (44)$$

Thus we get

$$\text{integrand} = M_Y \sin^2 \omega t_e \quad (45)$$

Substitution into Eq. (40) gives for the integral

$$\text{integral} = \omega \sin^2 \omega t_e \int_0^{t_c} M_Y(t') dt' = \frac{2\pi g}{\omega} M_Y(t_c) \quad (46)$$

The first term on the right of Eq. (40) may similarly be expanded trigonometrically, and, upon examination in relation to integration over a whole number of cycles of  $t_e$ , the surviving term is simply

$$\text{first term} = M_X^* \sin^2 \omega t_e \quad (47)$$

Substitution into Eq. (40) gives

$$E(t_e) = 2H_1 V_D \left\{ M_X^* + \omega \int_0^{t_c} M_Y(t') dt' \right\} \sin^2 \omega t_e \quad (48)$$

Substitution of Eq. (48) into Eq. (10) then gives

$$\begin{aligned} P &= \frac{2V_D \Omega H_1}{t_c} \int_0^{t_c} \left\{ M_X^* + \omega \int_0^{t_c} M_Y(t') dt' \right\} \sin^2 \omega t_e dt_e \\ &= \frac{\omega V_D \Omega H_1}{\pi g} \int_0^{t_c} \left\{ M_X^* + \omega \int_0^{t_c} M_Y(t') dt' \right\} \sin^2 \omega t_e dt_e \quad (49) \\ &= V_D \Omega H_1 \left\{ M_X^* + \omega \int_0^{t_c} M_Y(t') dt' \right\} \end{aligned}$$

Substitution of Eqs. (32) through (36) into Eq. (49) yields

$$\frac{P}{V_D \Omega H_1} = \frac{M_O h_0 h_1 a}{h(a^2 + h^2)} \left\{ \frac{a}{h} \cos \frac{2\pi g h}{\omega} - \sin \frac{2\pi g a}{\omega} \right\} e^{-\frac{2\pi g a}{\omega}} - \frac{M_O a h_1 \omega}{(a^2 + h^2)^2} \left\{ h + \frac{a^2}{h} \right\} e^{-\frac{2\pi g a}{\omega}} \sin \frac{2\pi g h}{\omega} + \frac{2\pi g a h_1 M_O}{(a^2 + h^2)} \quad (50)$$

With the definitions Eqs. (24) through (26) this equation gives the scaled power absorbed as a function of applied frequency  $\omega$ . It is therefore the line shape formula. For large  $g$  (i.e., large  $t_c$ ) it reduces to the last term which is the usual steady state formula.

#### EFFECT OF COOLING ON LINE SHAPE

We now consider the case in which temperature changes linearly with time in accordance with Eq. (20). It is convenient to use the symbol  $\theta$  for the temperature, in place of  $T$ . Thus

$$\theta = T_0 - \beta(t - t_e) \quad \text{or} \quad t = \frac{T_0 - \theta}{\beta} + t_e \quad (51)$$

Introducing Eqs. (17) and (18) into Eqs. (21) through (23) together with

$$dt = -\frac{1}{\beta} d\theta \quad (52)$$

leads to the set

$$\frac{dM_x}{d\theta} = k\theta M_x - k_0 M_y \quad (53)$$

$$\frac{dM_y}{d\theta} = k\theta M_y + k_0 M_x - k_1 M_z \quad (54)$$

$$\frac{dM_z}{d\theta} = k\theta M_z + k_1 M_y - m \quad (55)$$

where

$$k = \frac{\alpha}{\beta} \quad (56)$$

$$k_0 = \frac{h_0}{\beta} \quad (57)$$

$$k_1 = \frac{h_1}{\beta} \quad (58)$$

$$m = \frac{\alpha \xi}{\beta} \quad (59)$$

We now make the following substitutions

$$M_x = xe^{\frac{k\theta^2}{2}} \quad (60)$$

$$M_y = ye^{\frac{k\theta^2}{2}} \quad (61)$$

$$M_z = ze^{\frac{k\theta^2}{2}} \quad (62)$$

Substitution of these into Eqs (53) through (55) yields

$$\frac{dx}{d\theta} = -k_0 y \quad (63)$$

$$\frac{dy}{d\theta} = -k_1 z + k_0 x \quad (64)$$

$$\frac{dz}{d\theta} = k_1 y - me^{-\frac{k\theta^2}{2}} \quad (65)$$

These equations admit of an analytical solution subject to the initial conditions

$$M_x(t_e) = M_y(t_e) = M_z(t_e) = 0 \quad (66)$$

or in terms of  $x$ ,  $y$ ,  $z$  and  $\theta$

$$x(T_0) = y(T_0) = z(T_0) = 0 \quad (67)$$

For example, substituting  $y$  from Eq. (63) into Eq. (65) gives

$$\frac{d}{d\theta} \left( z + \frac{k_1}{k_o} x \right) = -me^{-\frac{k\theta^2}{2}} \quad (68)$$

This can be integrated subject to Eq. (67) to give

$$z + \frac{k_1}{k_o} x = m \left( \frac{\pi}{2k} \right)^{\frac{1}{2}} \left[ \operatorname{erf} \left( T_o \sqrt{\frac{k}{2}} \right) - \operatorname{erf} \left( \theta \sqrt{\frac{k}{2}} \right) \right] \quad (69)$$

Differentiating Eq. (63) once with respect to  $\theta$  gives

$$\frac{d^2 x}{d\theta^2} = -k_o \frac{dy}{d\theta} \quad (70)$$

Now Eqs. (64) and (69) may be substituted into Eq. (70) to yield

$$\frac{d^2 x}{d\theta^2} + s^2 x = k_o k_1 m \left( \frac{\pi}{2k} \right)^{\frac{1}{2}} \left[ \operatorname{erf} \left( T_o \sqrt{\frac{k}{2}} \right) - \operatorname{erf} \left( \theta \sqrt{\frac{k}{2}} \right) \right] \quad (71)$$

where

$$s^2 = k_o^2 + k_1^2 \quad (72)$$

The solution of Eq. (71) is immediate. Thus we have

$$\begin{aligned} x &= \frac{k_o k_1 m}{s^2} \left( \frac{\pi}{2k} \right)^{\frac{1}{2}} \operatorname{erf} \left( T_o \sqrt{\frac{k}{2}} \right) \\ &\quad - \frac{k_o k_1 m}{s^2} \left( \frac{\pi}{2k} \right)^{\frac{1}{2}} e^{-is\theta} \int_0^\theta e^{2is\theta'} \left\{ \int_0^{\theta'} e^{-is\theta''} \operatorname{erf} \left( \theta'' \sqrt{\frac{k}{2}} \right) d\theta'' \right\} d\theta' \quad (73) \\ &\quad + A \sin(s\theta) + B \cos(s\theta) \end{aligned}$$

where  $A$  and  $B$  are constants to be determined by Eq. (67), and  $i$  is  $\sqrt{-1}$ .

Substitution of Eq. (73) into Eq. (60) then gives

$$M_x = e^{\frac{k\theta^2}{2}} A \sin(s\theta) + B \cos(s\theta) + \frac{k_0 k_1 m}{s^2} \left(\frac{\pi}{2k}\right)^{\frac{1}{2}} \operatorname{erf}\left(T_0 \sqrt{\frac{k}{2}}\right) \\ - \frac{k_0 k_1 m}{s^2} \left(\frac{\pi}{2k}\right)^{\frac{1}{2}} e^{-is\theta} \int_0^\theta e^{2is\theta'} \int_0^{\theta'} e^{-is\theta''} \operatorname{erf}\left(\theta'' \sqrt{\frac{k}{2}}\right) d\theta'' d\theta' \quad (74)$$

From this expression we may determine  $M_y$  by substituting  $M_x$  into Eq. (53). In fact we discover

$$M_y = -e^{\frac{k\theta^2}{2}} \frac{As}{k_0} \cos(s\theta) - \frac{Bs}{k_0} \sin(s\theta) \\ + \frac{ik_1 m}{s} \left(\frac{\pi}{2k}\right)^{\frac{1}{2}} e^{is\theta} \int_0^\theta e^{-is\theta'} \operatorname{erf}\left(\theta' \sqrt{\frac{k}{2}}\right) d\theta' \quad (75)$$

We may now use Eqs. (74) and (75) in Eq. (40) to determine  $E(t_e)$ . However it is first convenient to rewrite this equation in terms of  $\theta$ . Thus, using Eqs. (51) and (52) we get

$$E(t_e) = 2H_1 V_D \{ \cos\omega(t_c + t_e) [M_x^* \cos\omega(t_c + t_e) + M_y^* \sin\omega(t_c + t_e)] \\ - \frac{\omega}{\beta} \int_{T_0}^{T_0 - \beta^+} \sin\omega(\psi + t_e) [M_x(\theta) \cos\omega(\psi + t_e) + M_y \sin\omega(\psi + t_e)] d\theta \} \quad (76)$$

where

$$\psi = \frac{T_0 - \theta}{\beta} \quad (77)$$

We can in fact use the same trigonometric expansion as in the case of Eq. (42) and we find (again for  $t_c$  corresponding to a whole number of cycles, in place of Eq. (48),

$$\varepsilon(t_e) = 2H_1 V_D \left\{ M_x^* - \frac{\omega}{\beta} \int_{T_0}^{T_0 - \frac{2\pi g \beta}{\omega}} M_y(\theta) d\theta \right\} \sin^2 \omega t_e \quad (78)$$

This may be substituted into Eq. (10) to give

$$P = V_D \Omega H_1 \left\{ M_x^* - \frac{\omega}{\beta} \int_{T_0}^{T_0 - \frac{2\pi g \beta}{\omega}} M_y(\theta) d\theta \right\} \quad (79)$$

which takes the place of Eq. (49). In Eq. (79) both  $M_x^* = M_x(T_0 - \frac{2\pi \beta}{\omega})$  and  $M_y(\theta)$  are obtained from Eqs. (74) and (75).

Equations (74) and (75) may be manipulated into more convenient forms, before the constants A and B are determined. This is accomplished by performing the integrations, in these formulas, by parts between the limits 0 and  $\theta'$  (for  $\theta''$ ), in Eq. (74), and between 0 and  $\theta$  (for  $\theta'$ ), in Eq. (75). The results are

$$M_x = e^{\frac{k\theta^2}{2}} \left\{ A \sin(s\theta) + B \cos(s\theta) - \frac{mk_0 k_1}{s^2} \left( \frac{\pi}{2k} \right)^{\frac{1}{2}} \left[ \operatorname{erf} \left( \theta \sqrt{\frac{k}{2}} \right) - \operatorname{erf} \left( T_0 \sqrt{\frac{k}{2}} \right) \right] \right. \\ \left. + \frac{mk_0 k_1}{s^2} \int_0^{\theta} [\cos(s(\theta - \theta'))] e^{-\frac{k}{2}(\theta')^2} d\theta' \right\} \quad (80)$$

and

$$M_y = -e^{\frac{k\theta^2}{2}} \left\{ \frac{As}{k_0} \cos(s\theta) - \frac{Bs}{k_0} \sin(s\theta) - \frac{mk_1}{s} \int_0^{\theta} [\sin(s(\theta - \theta'))] e^{-\frac{k}{2}(\theta')^2} d\theta' \right\} \quad (81)$$

These forms have the advantage, among other things, of displaying  $M_x$  and  $M_y$  as real variables. The constants A and B may be determined by making use of Eq. (67), where  $x(T_0)$  is given by

$$e^{-kT_0^{1/2}} M_x(T_0), \text{ etc.}$$

In order to examine the feasibility of determining the cooling rate in this manner we need to compare the scaled power,  $P/V_D \Omega H_1$  given by Eq. (79) with the same quantity for the case in which there is no cooling, i.e., with  $P/V_D \Omega H_1$  specified by Eq. (30) with  $a$  and  $M_0$  set to the values they have at  $\theta = T_0$ . For convenience we denote the scaled power given by Eq. (79) as  $\phi'$  and that given by Eq. (50) as  $\phi$ . Then feasibility requires  $\phi'/\phi$  to be non-zero (i.e.,  $\phi'$  should be relatively measurable) but not unity. If the ratio were unity  $\phi'$  would be measurable, but cooling would exhibit no effect which means that cooling rate would not be measurable.

For convenience we set the various pertinent parameters at the following not untypical values:

$$\beta = 10^7 \text{ K sec}^{-1}$$

$$\alpha = 10 \text{ K sec}^{-1}$$

$$h_1 = 10 \text{ sec}^{-1}$$

$$s = 10^{-3} \text{ K}^{-1}$$

$$h_0 = 0 \text{ sec}^{-1} (\omega = \omega_0 = \gamma H_0, \text{ for resonance}) \quad (82)$$

$$\omega = 10^8 \text{ sec}^{-1}$$

$$g = 800$$

$$T_0 = 1000 \text{ K}$$

$$\xi = 3 \times 10^{-3} \text{ ergs K gauss}^{-1}$$

In order to apply Eq. (79) it is necessary to evaluate  $M_x$  and  $M_y$  given by Eqs. (80) and (81) for use in Eq. (79). The

quadratures in these equations are best obtained numerically. However we can easily obtain order of magnitude estimates by another procedure. We return to Eq. (71). In this equation we approximate  $\text{erf}\left(\theta\sqrt{\frac{k}{2}}\right)$  by a two piece function, namely,

$$\begin{aligned}\text{erf}\left(\theta\sqrt{\frac{k}{2}}\right) &= \left(\frac{2k}{\pi}\right)^{\frac{1}{2}}\theta \quad , \quad \theta \leq \left(\frac{\pi}{2k}\right)^{\frac{1}{2}} \\ \text{erf}\left(\theta\sqrt{\frac{k}{2}}\right) &= 1 \quad , \quad \theta > \left(\frac{\pi}{2k}\right)^{\frac{1}{2}}\end{aligned}\tag{83}$$

This amounts to replacing  $\text{erf}\left(\theta\sqrt{\frac{k}{2}}\right)$  by a linear function having the same initial slope as the erf functions until the value of the approximate function reaches unity, the limiting value of the erf functions. Thereafter, erf is approximated as the constant, unity.

Substitution of Eq. (83) into Eq. (71) yields

$$\begin{aligned}\frac{d^2x}{d\theta^2} + s^2x &= k_0 k_1 m [T_1 - \theta], \quad \theta \leq T_1 \\ \frac{d^2x}{d\theta^2} + s^2x &= 0 \quad , \quad \theta > T_1\end{aligned}\tag{84}$$

where

$$T_1 = \left(\frac{\pi}{2k}\right)^{\frac{1}{2}}\tag{85}$$

With the values selected in Eq. (82) we find

$$T_1 = 1253K\tag{86}$$

and since  $T_0 = 1000K$ , this means that the entire domain of our calculation is restricted to the first of equations (84), whose solution is

$$x = A \sin(s\theta) + B \cos(s\theta) + \frac{k_0 k_1 m}{s^2} (T_1 - \theta) \quad (87)$$

where A and B are constants of integration. We determine y from x by using Eq. (63) and find,

$$y = -\frac{s}{k_0} \{A \cos(s\theta) - B \sin(s\theta)\} + \frac{k_1 m}{s^2} \quad (88)$$

Finally A and B are determined by substituting Eqs. (87) and (88) into Eq. (67). Then  $M_x$  and  $M_y$  are obtained from Eqs. (60) and (61). The final results are

$$M_x = \frac{k_0 k_1 m}{s^2} \{T_1 - \theta - (T_1 - T_0) \cos[s(T_0 - \theta)] - \frac{1}{s} \sin[s(T_0 - \theta)]\} e^{\frac{k\theta^2}{2}} \quad (89)$$

and

$$M_y = \frac{k_1 m}{s^2} \{1 + s(T_1 - T_0) \sin[s(T_0 - \theta)] - \cos[s(T_0 - \theta)]\} e^{\frac{k\theta^2}{2}} \quad (90)$$

It is easy to show that, with the values of parameters chosen in Eq. (82), the following approximations are accurate.

$$e^{\frac{k\theta^2}{2}} = 1 - \frac{k\theta^2}{2} \quad (91)$$

$$\sin[s(T_0 - \theta)] = s(T_0 - \theta) \quad (92)$$

$$\cos[s(T_0 - \theta)] = 1 - \frac{s^2 (T_0 - \theta)^2}{2} \quad (93)$$

Substitution of Eqs. (91) through (93) into Eqs. (89) and (90) and the results into Eq. (79) gives

$$\begin{aligned}
 \phi' = & \frac{1}{2} \left( 1 - \frac{kT_2^2}{2} \right) k_0 k_1 m (T_1 - T_0) (T_0 - \theta)^2 \\
 & + k_1 m T_0 \left( T_1 - \frac{T_0}{2} \right) \left( T_0 - T_2 \right) - \frac{1}{2} T_1 \left( T_0^2 - T_2^2 \right) \\
 & + \frac{1}{6} \left[ 1 - kT_0 \left( T_1 - \frac{T_0}{2} \right) \right] \left( T_0^3 - T_2^3 \right) \\
 & + \frac{1}{8} kT_1 \left( T_0^4 - T_2^4 \right) - \frac{1}{20} k \left( T_0^5 - T_2^5 \right)
 \end{aligned} \tag{94}$$

in which

$$T_2 = T_0 - \frac{2\pi g \beta}{\omega} \tag{95}$$

Substituting the values in Eq. (82) we find

$$\phi' = 1.23 \times 10^{-4} \text{ ergs gauss}^{-1} \tag{96}$$

Employing the same values in Eq. (50) with  $a = \alpha T_0$  and  $M_0 = \zeta/T_0$  gives

$$\phi = 3.16 \times 10^{-3} \text{ ergs gauss}^{-1} \tag{97}$$

Thus we have

$$\frac{\phi'}{\phi} = 0.039 \tag{98}$$

which is neither zero nor unity, thereby demonstrating the potential feasibility of the method.

### CONCLUSION

Our conclusion is simple. On the basis of a first analysis it seems possible to measure large cooling rates by NMR techniques. Other configurations and other NMR experiments may lead to more expeditious means of measurement. We have in

mind "spin echo" and "rotating frame" methods, but the utility of these still remains to be analyzed.

ACKNOWLEDGEMENTS

This research was supported by the Defense Advanced Research Projects Agency of the Department of Defense under Contract No. MDA903-76C-0250 with The University of Michigan.

### References

1. H. Metyja, B. C. Giessen, and N. J. Grant, *J. Inst. Metals* 96, 30 (1969).
2. J. S. Murday and R. M. Cotts, *J. Chem. Phys.* 48, 4938 (1968), *Z. Naturforsch* 26A, 94 (1971).
3. C. J. Kruger, W. Muller-Warmuth and A. Klemm, *Z. Naturforsch* 26A, 94 (1971).
4. W. W. Warren, Jr., and W. G. Clark, *Phys. Rev. B1*, 24 (1970).
5. A. L. Kerlin and W. G. Clark, *Phys. Rev.*, B12, 3533 (1975).
6. H. S. Carslaw and J. C. Jaeger, "Conduction of Heat in Solids," p. 200 (Oxford 1947).
7. R. T. Schumacher, "Introduction to Magnetic Resonance," p. 34 (W. A. Benjamin, New York, 1970).
8. *Ibid.*, p. 10.
9. *Ibid.*, p. 30.
10. C. P. Poole, Jr., and H. A. Farach, "Relaxation in Magnetic Resonance," Ch. 6 (Academic Press, New York, 1971).

DAMAGE THRESHOLDS IN CERAMICS CAUSED BY WATER DROP IMPACT

A. G. Evans

ABSTRACT

Models for the initiation of fractures by near surface tensile pulses created by water impact and the subsequent surface chipping created by lateral jetting are developed. These models highlight the influence of parameters such as the surface micro-toughness, the wave velocity ( $\sqrt{\text{modulus/density}}$ ), the pre-existent surface microcrack population, as well as the projectile size, velocity and density on the incidence of damage. Several implications for the design of materials with superior rain erosion resistance are then presented.

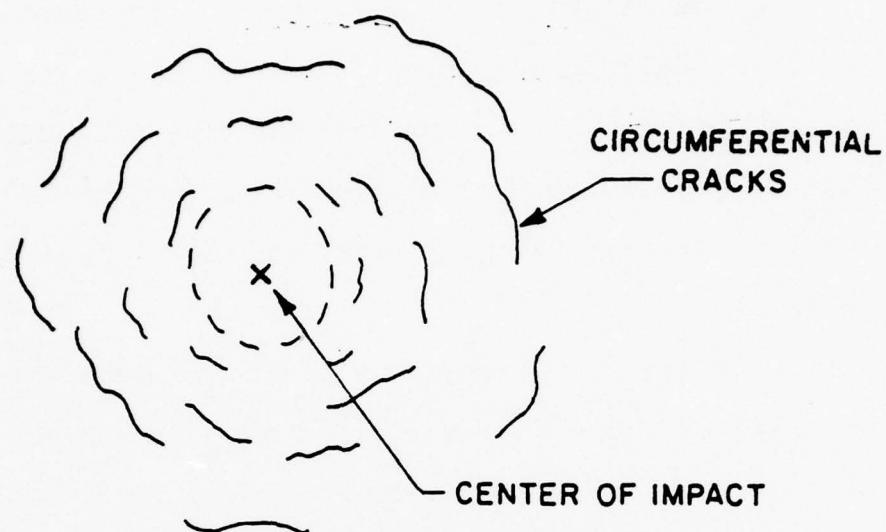
## DAMAGE THRESHOLDS IN CERAMICS CAUSED BY WATER DROP IMPACT

A. G. Evans

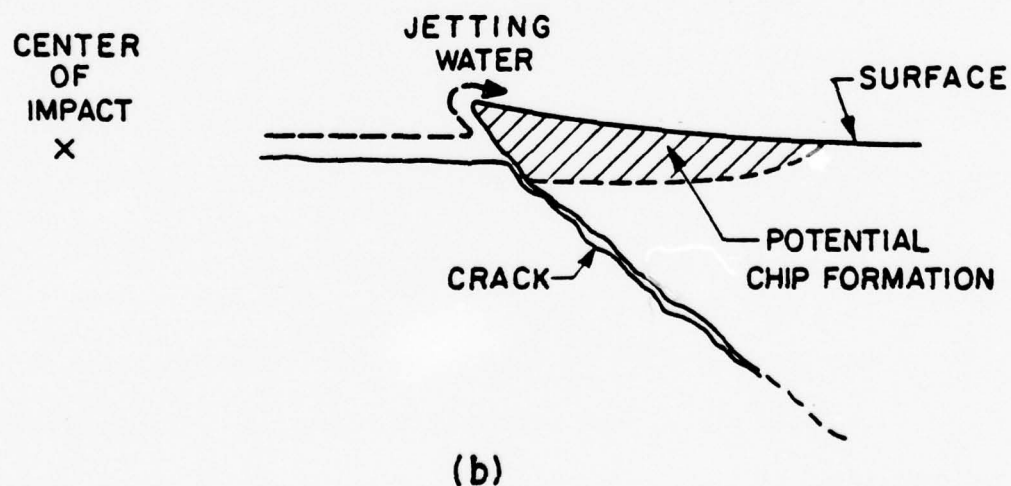
### INTRODUCTION

The mechanisms of rain erosion damage on ceramics have been identified in several recent studies.<sup>1,2,3,4</sup> At the damage threshold, it is evident that the damage consists of short circumferential surface cracks (Fig. 1a) produced by the relatively large amplitude, short duration tensile pulse associated with the propagation of the Rayleigh wave. The cracks, once formed, always exhibit a residual displacement normal to the surface (Fig. 1b), exposing a protuberance to the impact center.<sup>4</sup> This protuberance interacts with the water drop after lateral jetting, to cause local chipping and possibly, to extend the cracks (Fig. 1b).

The configuration of the cracks - a large number of small cracks in the vicinity of the high stress, short duration stress pulse - indicates that the crack formation depends on both the amplitude and duration of the pulse. An interpretation of the damage might, therefore, be based on an analysis of the time dependent activation of surface cracks by a tensile Rayleigh wave pulse.<sup>3</sup> An approximate analysis that indicates the relative roles of the material and projectile variables on the damage threshold is described in the first part of this paper. The analysis uses (and correlates with) selected numerical results.<sup>5</sup>



(a)



(b)

Figure 1.

The chipping damage at surface protuberances is a particularly deleterious form of damage, vis-a-vis the resultant optical properties. A preliminary analysis of this mode of damage is presented in the second section of the paper, in an attempt to identify the parameters that influence the extent of chipping.

Finally, the implications of the analyses for the suppression of the cracking and chipping thresholds are discussed, with particular reference to materials development suggestions pertinent to the design of more erosion resistant window materials.

#### CRACK FORMATION THRESHOLD

Analyses of the stress intensity factor at finite stationary cracks subjected to a normal tensile stress pulse have indicated<sup>6</sup> that  $K$  varies with time,  $t$ ; initially as  $t^{1/2}$  and then as a damped sinusoid about the quasi-static stress intensity factor  $K_s$  (Fig. 2). An approximate  $K(t,a)$  function that contains the essence of the time and crack length,  $a$ , dependence is given by;<sup>7</sup>

$$(K/K_s)^2 = 1.44[1 + (\pi^2/4)(a/c)]^{-1} \quad (1)$$

where  $c$  is the wave velocity (the Rayleigh velocity for surface cracks). For time dependent pulse profiles, a solution for  $K$  can be obtained by summing  $K$  due to each prior time increment,<sup>7</sup>

$$K(t_0) = 1.2 \int_0^{K_s} \frac{(t_0-t)^{1/2} dK_s}{[t_0-t + (\pi^2/4)(a/c)]^{1/2}} \quad (2)$$

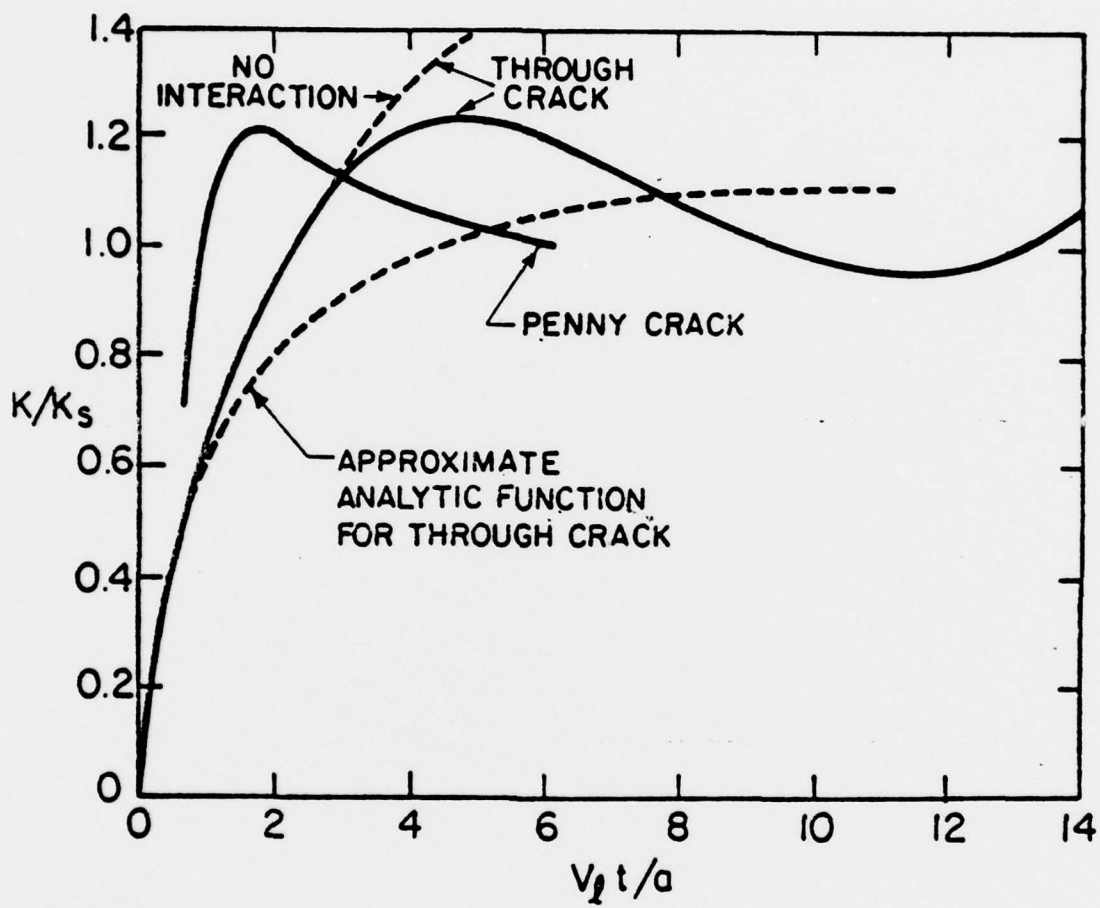


Figure 2.

The quasi-static stress intensity factor can be obtained from the stress  $\sigma(z, r)$  associated with the Rayleigh wave by applying the Green's function<sup>3</sup>

$$K_s(r) = 2 \left(\frac{a}{\pi}\right)^{\frac{1}{2}} \int_0^a \frac{\sigma(z, r) [1 + F(z/a)] dz}{(a^2 - z^2)^{\frac{1}{2}}} \quad (3)$$

where

$$\begin{aligned} F(z/a) = & (1-z/a)(0.295-0.39(z/a)^2+0.77(z/a)^4-0.99(z/a)^6 \\ & + 0.51(z/a)^8]. \end{aligned}$$

The stress gradient at the radial location where the surface stress is a maximum has been computed numerically<sup>5</sup> and shown to vary as;

$$\sigma = \hat{\sigma} \exp -(z/z_o)^{\frac{1}{4}} \quad (4)$$

where  $\hat{\sigma}$  is the stress of the surface and  $z_o$  is a measure of the stress gradient. Inserting  $\sigma$  from Eq. (4) into Eq. (3) gives,

$$K_s = 2\hat{\sigma} \sqrt{a/\pi} I(a/z_o) \quad (5)$$

where  $I(a/z_o)$  is plotted in Fig. 3: a convenient analytic approximation for  $I(a/z_o)$ , is found to be:

$$I \approx \pi/2 \sqrt{1+(a/z_o)^2} \quad (6)$$

so that

$$K_s \approx \hat{\sigma} [\pi a / (1 + a/z_o)]^{\frac{1}{2}} \equiv \alpha \hat{\sigma} \quad (7)$$

The pulse profiles predicted by the numerical calculations<sup>1, 5</sup>

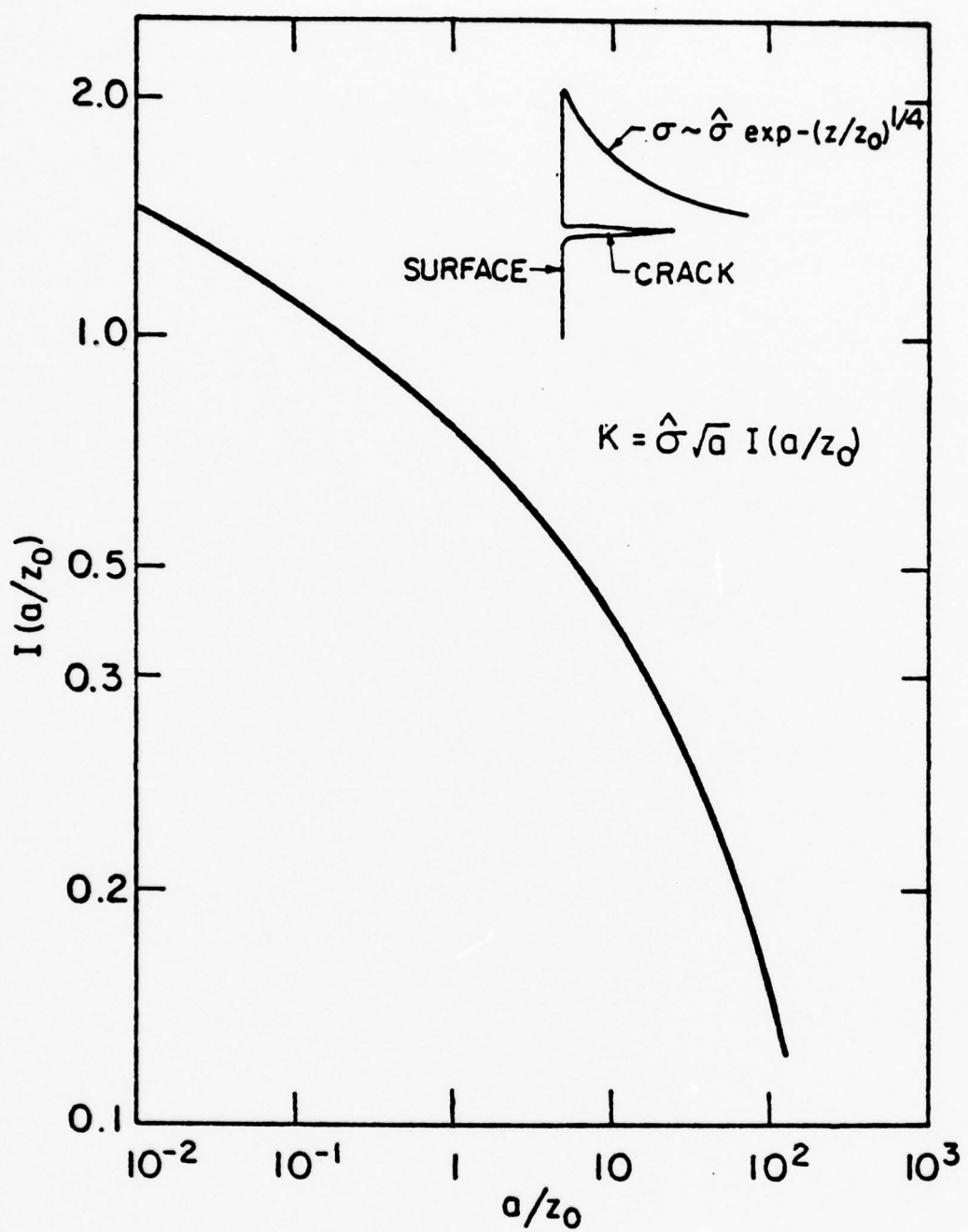


Figure 3.

(Fig. 4) can be approximated by triangular pulses, characterized in terms of stressing rate  $\dot{\sigma}_L$  and an unstressing rate  $\dot{\sigma}_u$ . Substituting these rates into Eqs. (2) and (7) yields the stress intensity factor

$$\frac{K(t_o)}{1.2\alpha} = \dot{\sigma}_L \int_0^{t_m} \left[ \frac{t_o - t}{t_o + \beta - t} \right]^{\frac{1}{2}} dt + \dot{\sigma}_u \int_{t_m}^{t_o} \left[ \frac{t_o - t}{t_o - \beta - t} \right]^{\frac{1}{2}} dt \quad (8)$$

where  $\beta = (\pi^2/4)(a/c)$  and  $t_m = \hat{\sigma}_m/\dot{\sigma}_L$ :  $\hat{\sigma}_m$  being the peak value of the surface stress (Fig. 4). Integration of Eq. (8) gives;

$$\begin{aligned} \frac{K(t_o)}{1.2\alpha} = & \dot{\sigma}_L \sqrt{t_o^2 + \beta t_o} - \sqrt{(t_o - t_m)^2 + \beta(t_o - t_m)} \\ & + \beta \ln \left[ \frac{\sqrt{t_o - t_m + \beta} + \sqrt{t_o - t_m}}{\sqrt{t_o + \beta} + \sqrt{t_o}} \right] \quad (9) \\ & - \dot{\sigma}_m \sqrt{(t_o - t_m)^2 + \beta(t_o - t_m)} + \beta \ln \left[ \frac{\sqrt{\beta}}{\sqrt{t_o - t_m + \beta} + \sqrt{t_o - t_m}} \right] \end{aligned}$$

Numerical results indicate that  $\dot{\sigma}_L/\dot{\sigma}_m \approx 3$ . Applying this ratio of stress rates,  $K/1.2 \hat{\sigma}_m \alpha$  derived from Eq. (9) is plotted in Fig. 5 as a function of  $t_o/t_m$  for several  $\beta \dot{\sigma}_L/\dot{\sigma}_m$ . It is noted that the peak stress intensity factor  $\hat{K}$  develops after the maximum stress has been reached, in accord with recent numerical results (Table 1). An approximate expression for  $\hat{K}$  is

$$\hat{K} \approx 1.2 \hat{\sigma}_m \left[ \frac{\pi a}{(1+a/z_o) [1 + (\pi^2/4)(a \dot{\sigma}_L/c \hat{\sigma}_m)]} \right]^{\frac{1}{2}} \quad (10)$$

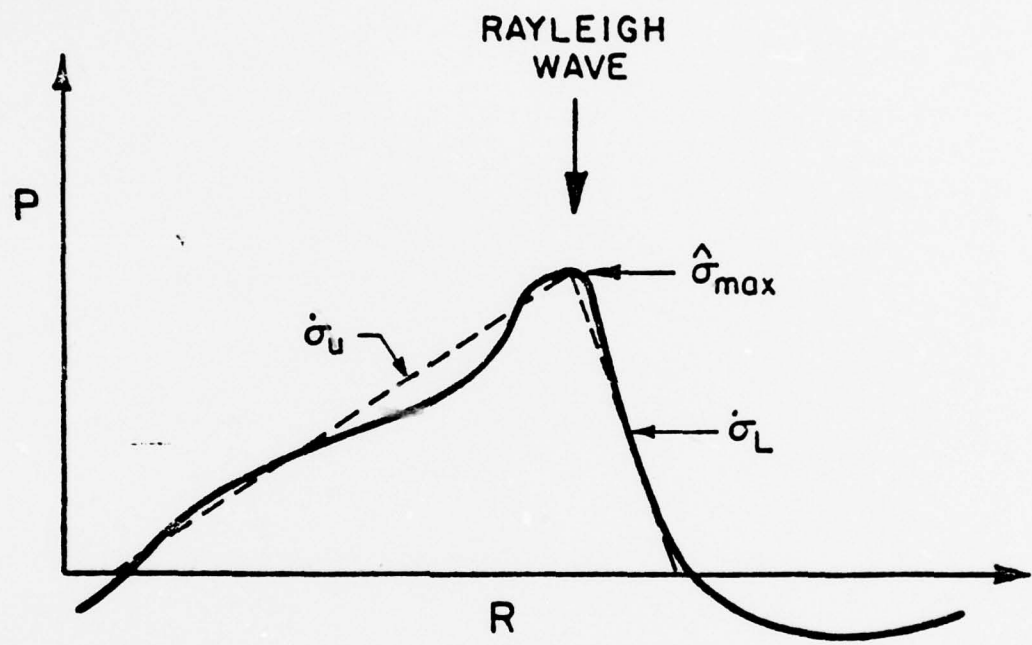


Figure 4.

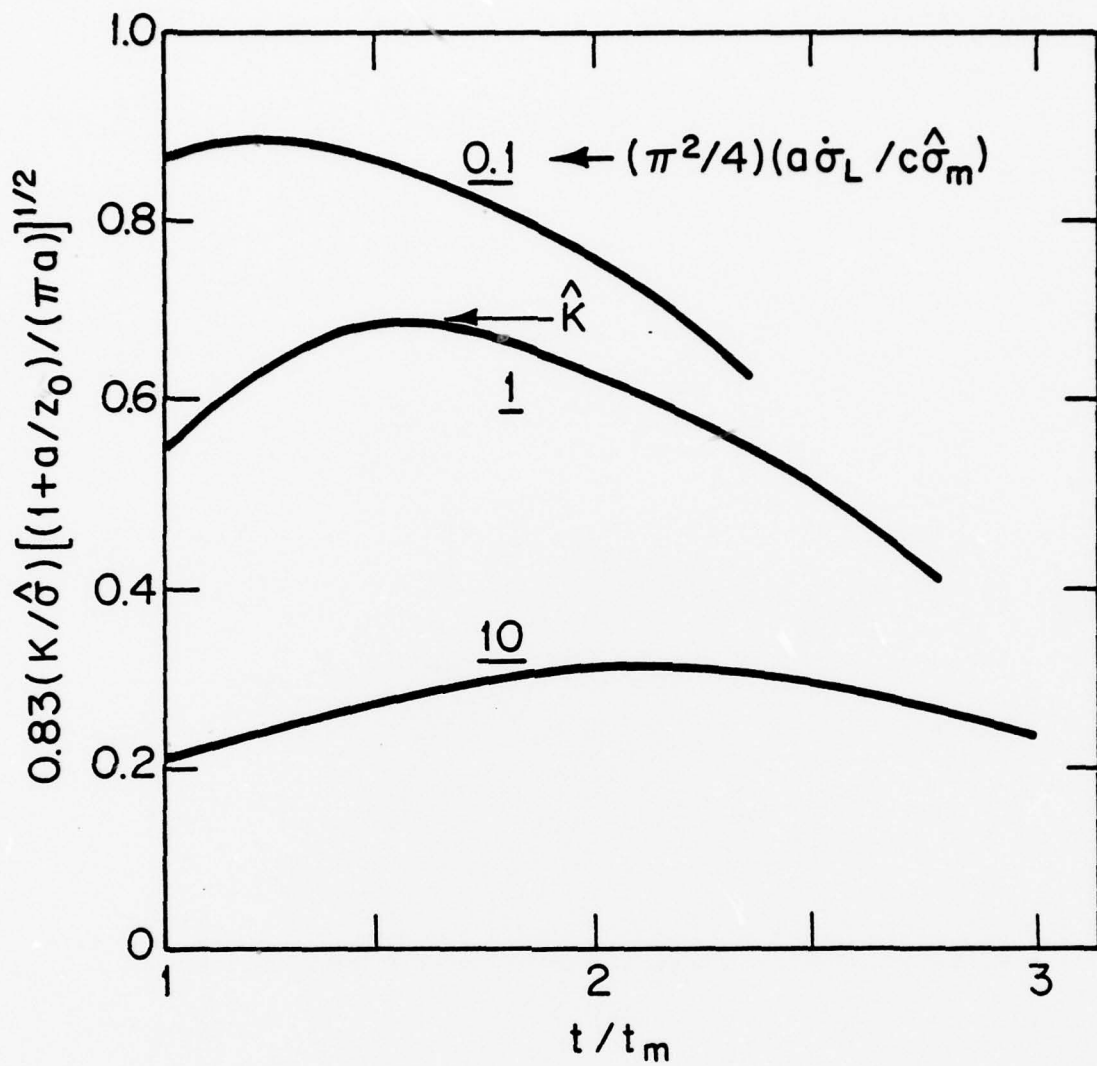


Figure 5.

Note that the quantity,  $a\dot{\sigma}_L/c\dot{\sigma}$  is just the ratio of the loading time  $t_m$  to the time taken for a stress wave to traverse the length of the crack,  $t_c (a/c)$ . At this juncture the approximate validity of the analysis is established by comparing the crack length dependence of  $\hat{K}$  with numerical computations<sup>5</sup> (Table I). For relatively steep stress pulses,  $t_L \gtrsim 0.2t_c$ , and large cracks,  $a \gtrsim 0.2z_0$ , Eq. (10) reduces to;

$$\hat{K} \sim 2.4 (\dot{\sigma}_m)^{3/2} \left[ \frac{z_0 c}{\pi a \dot{\sigma}_L} \right]^{1/2} \quad (11)$$

indicating a inverse dependence on  $a^{1/2}$ , in very good agreement with the numerical results (Table I). Now, by equating  $\hat{K}$  to  $K_c$  (the crack extension condition) the value of the peak stress at the threshold,  $\sigma_c$ , can be found. In general, from Eq. (10);

$$\sigma = \frac{K_c \sqrt{1+a/z_0}}{\sqrt{\pi a}} \cos(\phi/3) \quad (12a)$$

where

$$\phi = \cos^{-1} \left[ \frac{13.2 \dot{\sigma}_L a^{3/2}}{K_c c \sqrt{1+a/z_0}} \right] .$$

The two limit solutions are of interest. For long relative loading times ( $c\sigma \gg a\dot{\sigma}_L$ ),

$$\sigma_c \sim \frac{K_c}{1.2} \left( \frac{1+a/z_0}{\pi a} \right)^{1/2} \quad (12b)$$

TABLE I. Summary of Numerical Results (Ito and Rosenblatt)

Crack Length ( $\mu\text{m}$ )	$K_{\max}$ (MPa $\sqrt{\text{m}}$ )	Time at $K_{\max}$ ( $\mu\text{s}$ )
25	2	0.143
50	1.4	0.159
100	0.9	0.180
0	---	0.136

whereas, for short relative loading times ( $c\sigma \ll a\dot{\sigma}_L$ );

$$\sigma_c \sim \left[ \frac{\pi(1+a/z_o) K_c^2 \dot{\sigma}_L}{4.6c} \right] \quad (12c)$$

It is now possible to express the threshold in terms of the critical target and projectile parameter by invoking the dimensionless material independent quantities  $T$ ,  $Z$ ,  $P$ , utilized by Blowers<sup>8</sup> in his analytic stress analysis, viz.

$$T = \frac{2c^2 t}{(rv)_p} , \quad Z = \frac{2cz}{(rv)_p} , \quad P = \frac{\sigma}{(\rho cv)_p} .$$

Inserting these quantities into Eqs. (12) we obtain a threshold impact velocity  $v_p^c$ . It is found that three conditions prevail, which can be referred to relative values of the quantity  $r_p v_p / ac$  and the two material independent quantities  $T_L$  (the time taken to attain the peak stress at the location of interest vis-a-vis the impact center) and  $Z_o$  (a measure of the sub-surface stress gradient at the same location). The three results are; for  $v_p r_p / ac$  larger than both  $2/T_L$  and  $2/Z_o$  (quasi-static),

$$v_p^c \sim \beta_1 K_c / \rho_p c_p \sqrt{a} ; \quad (13a)$$

for  $v_p r_p / ac$  between  $2/T_L$  and  $2/Z_o$

$$v_p^c \sim \beta_2 [K_c^2 c / r_p c_p^2 \rho_p^2]^{1/3} ; \quad (13b)$$

and for  $v_p r_p / ac$  less than both  $2/T_L$  and  $2/Z_o$  (fully dynamic),

$$v_p^c \sim \beta_3 [a(K_c c / r_p c_p \rho_r)^2]^{\frac{1}{4}} ; \quad (13c)$$

where  $\beta_1, \beta_2$  and  $\beta_3$  are material independent constants.

Inspection of Eqs. (13a,b,c) indicates the unambiguous advantage of a high target toughness, a low projectile density and a low projectile wave speed (low impedance). Usually, a large target wave velocity and a small projectile radius will also be preferred, except for very large values of  $v_p r_p / ac$  with respect to the stress pulse parameters  $T_L^{-1}, z_o^{-1}$ . The most regime dependent parameter is the crack length,  $a$ ; the threshold can increase, decrease or remain invariant as the crack length increases. It is particularly important, therefore, to identify the relevant regime before anticipating the influence of the crack length.

#### CHIP FORMATION

The problem of chip formation is addressed using a quasi-static analysis. The formation of the protuberance is presumed to occur because the crack follows a mixed mode trajectory; the relative displacement of the crack faces is then restrained from full restoration by frictional effects associated with the non-planar character of the fracture surface (Fig. 1b). The residual displacement is thus assumed to be related to the displacement  $\delta$  during propagation; this is given approximately by;

$$\delta \sim K_c \sqrt{a} / 4 \mu \sqrt{2\pi} \quad (14)$$

where  $\mu$  is the shear modulus. Further, we note that the arrest

crack length depends on the toughness and wave velocity;<sup>3,7</sup> an approximate relation ( $\Delta a \gg a_0$ ), expressed in terms of the material independent parameters is

$$\Delta a \sim \beta_4 \frac{\rho^2 c^2 v_p^3 r_p}{K_c^2 c} \quad (15)$$

where  $\beta_4$  is a constant. Combining Eqs. (14) and (15) the displacement  $\delta$  becomes;

$$\delta \sim \beta_5 \frac{\rho c v_p^{3/2} r_p^{1/2}}{c^{1/2}} \quad (16)$$

Note that  $\delta$  is independent of the fracture toughness.

The magnitude of the pressure applied to the protuberance by the jetting water depends on the local velocity  $v_j$ . It is assumed that there is no significant boundary layer development, the pressure  $p$  (after an initial transient of  $\rho c v_j$ ) is;

$$p \sim \rho v_j^2 / 2 \quad (17)$$

This pressure, acting over the area of the protuberance, generates tensile stresses along the surface of the crack. The magnitude of the stress depends on both the crack angle,  $\theta$ , and the distance  $r$  from the protuberance and is given approximately by (B. Budiansky, private communication)\*:

$$\sigma \approx 2p[(\theta/\sin\theta)^2 - 1]^{-1} (1 + \delta/r)^{-1} \quad (18)$$

These tensile stresses will initiate chip formation if they exceed the stress needed to extend the small secondary cracks that

---

\*The exact solution is rather complex and deviates appreciably from Eq. (18) in the limits  $r \rightarrow 0$  and  $r \rightarrow \infty$ . However, the approximate form does provide a useful analytic solution for the chipping problem.

are distributed along the surface of the major cracks. These secondary cracks are dictated by the microstructure, and typically are of the order of the grain size  $G$  in length. The extension stress,  $\sigma_s$ , for the secondary cracks is thus:

$$\sigma_s \sim 2K_l/\pi G^{\frac{1}{2}} \quad (19)$$

where  $K_l$  is the extension resistance of the secondary cracks (usually  $< K_c$ ).

The chip formation problem can now be analyzed by considering a distribution of secondary cracks, related to the distribution of grain sizes, subjected to the stress distribution supplied by the jetting water (Eq. 18). If we consider that the important secondary cracks are dominated by the large grain size extreme, an appropriate expression for the probability  $\phi(G) dG$  that the secondary crack size will be in the range  $G$  to  $G+dG$  is,<sup>9</sup>

$$\phi(G) dG = (G_o/G)^k d(G/G_o) \quad (20)$$

where  $G_o$  and  $k$  are the scale and shape parameters respectively. If we also recognize that the separation between secondary cracks is related to the grain size, an expression for the probability  $\delta\phi(G)$  of finding secondary cracks larger than  $G$  in an area  $\delta A$  of crack surface can be written as;

$$\delta\phi(G) = (\delta A/G_A^2) \int_G^{\infty} G_o^{k-1} G^{-k} dG \equiv (\delta A/G_A^2) (G_o/G)^{k-1} (k-1)^{-1} \quad (21)$$

where  $G$  is the average separation between cracks: given by some multiple of the scale parameter  $G_o$ . Now, substituting  $\sigma_s$  for  $G$  from Eq. (19), the probability  $\delta\phi(\sigma_s)$  that chip formation will

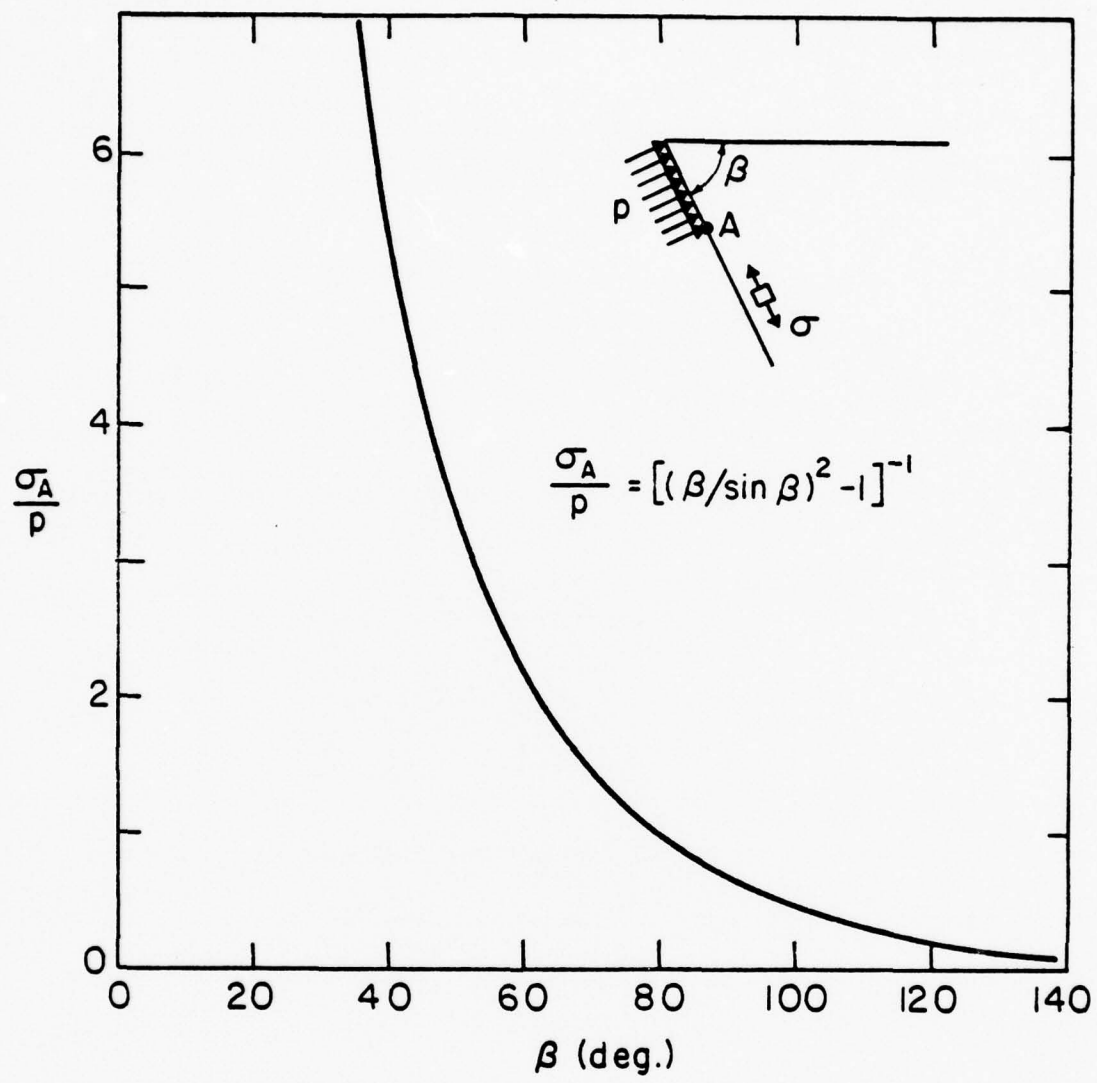


Figure 6.

initiate in the element  $\delta A$ , subjected to the stress  $\sigma_s$ , becomes;

$$\delta\phi(\sigma_s) = 2(\pi/2K_l)^{2k-2}(\delta A/G_A^2) [G_O^{k-1}/(k-1)] \sigma_s^{2k-2} \quad (22)$$

The total probability  $\Phi$  of chip function over the surface of the crack is thus  $(A/\delta A \rightarrow \infty)$ ; <sup>10</sup>

$$1-\Phi = \prod_1^{A/\delta A} [1-\delta\phi(\sigma_s)] \approx \exp[-2(\pi/2K_l)^{2k-2}(b/G_A^2) [G_O^{k-1}/(k-1)] \int_0^a \sigma_s^{2k-2} dr] \quad (23)$$

where  $b$  is the crack width and  $a$  the crack depth. Substituting the distribution of crack surface stress given by Eq. (18), then gives;

$$1-\Phi(\delta, v_j) = \exp[-2(\pi/2K_l)^{2k-2}(b/G_A^2) [G_O^{k-1}/(k-1)] [\rho v_j / (\theta/\sin\theta)^2 - 1]^{2k-2} \int_0^a \left[ (r/\delta) [1 + (r/\delta)]^{-1} \right]^{2k-2} dr] \quad (24)$$

The integral can be readily evaluated for specific values of  $k$ . For example, for  $k=2$  the integral is,  $(2a^3\delta + 3a^2\delta^2 + 2a\delta^3)/\delta^2(a+\delta) + 2\delta \ln(1+a/\delta)$ . Inspection of Eq. (24) indicates that, except for small  $k$ , the chip formation probability depends strongly on the local toughness  $K_l$ , the grain size  $G_O$ , the crack length  $a$ , and the jetting velocity  $v_j$ ; in the sense that large toughness and small grain size materials are preferred. There is a relatively small influence of the displacement  $\delta$  which, from Eq. (16), implies that large wave velocities could slightly suppress chip formation.

## IMPLICATIONS

The primary implications of both the theory and experiment are that the damage threshold in the elastic response regime is influenced by both the wave velocity and toughness of the material. The wave velocity is a microstructure-insensitive property, and its influence on the damage has implications primarily for the basic choice of the material, i.e., materials with a large modulus and low density such as  $\text{Si}_3\text{N}_4$ ,  $\text{SiC}$ ,  $\text{Al}_2\text{O}_3$ . By contrast, the toughness is highly microstructure sensitive, and substantial opportunities exist for increasing the damage resistance by attending to the material's toughness. However, it is critical to recognize that the pertinent crack growth resistance relates to the extension of surface or near-surface cracks. This immediately establishes the importance of a fine surface grain size. A fine-scale microstructure also enhances the shipping threshold and thus has a dual advantage. The requirement for a fine-scale microstructure essentially eliminates one important mode of toughening, controlled microfracture, which only pertains to relatively coarse grained ( $\sim 10 \mu\text{m}$ ) materials or to relatively coarse multiphase systems. Also, relatively tough two-phase metal/ceramic systems (e.g., WC/Co) may not be effective because of perturbations caused by deformation of the metal phase. Nevertheless, several attractive toughening approaches that can be applied to essentially single-phase systems, e.g., stress-induced phase transformations and grain pull-out, seem pertinent.

The role of the pre-existent crack size is more complex. Decreasing the surface crack size can either increase or decrease the damage threshold, depending on the details of the stress pulse. It is believed that many important practical problems are in a dynamic regime, in which large cracks are preferred to small cracks; but this should not be regarded as a universal result. Further numerical studies are needed to completely define the conditions that lead to the three regimes of crack activation behavior.

#### ACKNOWLEDGEMENT

This research was supported by the Defense Advanced Research Projects Agency of the Department of Defense under Contract MDA903-76C-0250 with The University of Michigan.

### References

1. W. F. Adler, J. Mater. Sci. 12, 1253 (1977).
2. A. G. Evans and T. R. Wilshaw, 12, 97 (1977).
3. A. G. Evans, J. Appl. Phys. 49, 3304 (1978).
4. F. P. Bowden and J. E. Field, Proc. Roy. Soc. A282, 321 (1965).
5. M. Ito and M. E. Rosenblatt, private communication.
6. L. B. Freund, J. Mech. Phys. Solids 21, 47 (1973).
7. A. G. Evans, Treatise of Materials Science and Technology (Ed. C. M. Preece) Academic Press, N.Y., in press.
8. R. M. Blowers, J. Inst. Math. Appl. 5, 167 (1969).
9. A. G. Evans, B. R. Tittmann, L. Ahlberg, B. T. Khuri-Yakub and G. S. Kino, J. Appl. Phys. 49 (1978).
10. J. R. Matthews, F. A. McClintock and W. J. Shack, J. Am. Ceram. Soc. 59, 304 (1976).

A REMARK ON SOME REPORTED MEASUREMENTS OF THE VISCOSITY  
OF WATER AT VERY HIGH PRESSURES

G. H. Vineyard

An interesting method of measuring the behavior of a fluid behind a shock wave front has been devised by Al'tschuler, et al,<sup>1</sup> and applied in an effort to determine the viscosity of water at pressures between 30 and 80 kbar. The viscosity was found to be greater by five orders of magnitude than the viscosity of water under normal conditions. These results are consistent with very high viscosities for water, mercury, and other liquids deduced from rippled-front shock wave experiments by other Russian workers. Because these very high viscosities are difficult to rationalize (by orders of magnitude) and because such viscosities, if real, would be important in stabilizing shock fronts, it is of considerable interest to know how much reliance to place in this work.

Unfortunately, the paper by Al'tschuler, et al appears to have a serious flaw. The method of measurement is to place fine wires of copper or tungsten in the fluid, in a superposed magnetic field. The wires are aligned parallel to the shock front and are connected in some fashion to an oscillosograph. Passage of the shock front displaces the wires along the direction of the particle motion behind the front and, by virtue of the magnetic

field, induces an EMF that is observed on the oscillograph. This allows the velocity of the wire to be determined as a function of time. Thin foils are also deployed and measure in the same way the velocity of the fluid behind the front as a function of time. Ascribing the motion of the wire to the drag exerted by the moving fluid, (i.e., assuming quasi-static conditions) the observations determine the drag. Since the relative velocity of fluid and wire is also known, drag is converted into viscosity by employing known values of the drag coefficient for a cylinder. The drag coefficient is a function of the Reynolds number,

$$R = \frac{\rho d(u-v)}{\eta} ,$$

where  $\rho$  is the density of the fluid,  $d$  the diameter of the cylinder,  $u$  the instantaneous velocity of the fluid,  $v$  the instantaneous velocity of the wire, and  $\eta$  is the viscosity of the fluid.

Al'tschuler, et al use the drag coefficients measured by Tritton<sup>2</sup>. However, Tritton's data cover the range  $0.5 < R < 100$ . For larger Reynolds numbers the drag coefficient has complex behavior, and over a large range is nearly independent of  $R$ .

If one assumes  $\eta$  to be the order of  $10^3$  Poise, the relevant values of  $\rho$ ,  $u$ , and  $v$  give  $R$  in the range 5 to 20 or so, which is in the realm to which Tritton's data apply. However, if  $\eta$  is very much smaller than  $10^3$ , as other considerations would argue<sup>3</sup>, then the Reynold's number is far above Tritton's range,

and it would appear to be very difficult to determine it from the Al'tschuler data. If, for example,  $\eta$  is 0.01 Poise (the value at normal pressure) the Reynolds number for these experiments is in the range  $10^5$  to  $10^6$ .

Al'tschuler, et al actually calculate velocity-time curves for the test wires which come out in moderately good agreement with the observations over the time range  $\sim 0.5$  to  $3\mu\text{sec}$ , as well as can be judged from the very small-scale figure given in their article. However, moderate changes in the deduced drag coefficient would allow the curves in the figure to be fit about as well by the very different assumption that  $R \gg 1$ , (the highly turbulent realm) implying that  $\eta$  is near, or not enormously higher than, its zero pressure value. Therefore, the high viscosities of shocked water reported by Al'tschuler, et al should be taken with reserve. Indeed, if  $R$  is above 100, it is doubtful whether an unambiguous determination of  $\eta$  can be made by this method.

Incidentally, a formula for viscosity as a function of pressure is also given in the Al'tschuler paper. It is an activation volume type of formula, which has some theoretical basis (see Frisch, Eyring, and Kincaid, J. Appl. Phys. 11, 75 (1940) and which can fit the data presented.

However, to fit the data it is necessary for the authors to assume an activation volume for shear which is close to one molar volume. This is surprisingly large for flow in an ordinary fluid. Thus Frisch, et al find the activation volume for liquid

mercury between 0 and 6 kilobars to be a little less than one twentieth of the molar volume; for water they find the activation volume to vary from a very small fraction of a molar volume up to one seventh of a molar volume at 5 kilobars. Such activation volumes, of course, go with a much more modest variation of viscosity with pressure.

I have attempted to reproduce the calculations by which Al'tschuler et al found viscosities from their data. The effort is made difficult by their failure to present their data in any form other than a minute graph of all of the velocity-time curves. Nevertheless, it is illuminating to make the attempt. Reading velocities and accelerations from their curves (their Fig. 1) as best as one can, and assuming not more than about 10% accuracy in the process, I find the following:

<u>Expt. No.</u>	<u>Time Range Used (<math>\mu</math> sec)</u>	<u><math>C_D</math></u>	<u>R</u>	<u><math>\eta \times 10^{-3}, P</math></u>	<u>Pressure kb</u>
1	0.2 - 1.5	5. - 22.	3.5 - .31	2.2 - 5.	81 - 61
2	0.2 - 3.0	4.8 - 3.2	4. - 3.2	2.6 - .29	81 - 41
3	0.8 - 3.0	2.9 - 9.7	10.5 - 1.1	1.8 - 7.	31 - 28
5	2	2.0	23	.19	31 - 27

Here  $C_D$  is the derived drag coefficient, R is the Reynolds number found from  $C_D$  with the use of Tritton's data, and the viscosity is derived from the Reynolds number so found. The pressures are as stated by the experimenters. Experiment 4 was not recalculated. The two values quoted for  $C_D$ , R, and  $\eta$  are the

extremals at the earliest and latest times, and are given in that order. Experiment 2 appears anomalous because  $C_D$  falls as time increases, and as a consequence the predicted values of  $\eta$  increase. Since the pressure is falling during the time of measurement, the viscosity should decrease. Also, the ranges of values of  $C_D$ ,  $R$ , and  $\eta$  are quite large. The 3 microsecond value of  $\eta$  in experiment 2 is very small, and the value of  $\eta$  derived from experiment 5 is strangely small. These features do not have a ready explanation within the framework of assumptions given in the paper.

Another consideration is the relaxation time of the flows involved. If one assumes that transient flow in a viscous fluid requires a characteristic time  $\tau$  to reach steady state,  $\tau$  may be calculated as the ratio of kinetic energy per unit volume to rate of energy dissipation per unit volume. For flow at a velocity  $v$  with characteristic shear rate  $\dot{\epsilon}$ , this ratio is

$$\tau \approx \frac{\rho v^2}{\eta \dot{\epsilon}^2} .$$

gives

$$\tau \approx \frac{\rho d^2}{\eta} = \frac{Rd}{v} \quad (1)$$

where  $R$  is the Reynolds number,  $\frac{\rho d^2}{\eta}$ . For the flows in the Al'tschuler experiment  $R = 0.3$  to  $22$ ,  $d \approx 5 \times 10^{-2}$  cm,  $v \approx 10^5$  cm/sec, and  $\eta = 200$  to  $5000$ . The range of  $\tau$  predicted by the above equation is then about  $0.15$  to  $10$   $\mu$ sec, with a middle value of about  $3$   $\mu$ sec. Since the exact numerical constants that may be required in Equation (1) have not been developed, these

numbers should be considered order-of-magnitude estimates only. Nevertheless, they indicate that steady state conditions may not have been reached in the Russian experiments, even employing the high viscosities the Russians favor. With more ordinary viscosities the relaxation time would be very much longer still. This consideration may also explain some of the oddities in the data reported.

In summary, it is felt that the viscosities reported by Al'tschuler, et al should be taken with reserve.

#### Acknowledgement

This research was supported by the Defense Advanced Research Projects Agency of the Department of Defense under Contract No. MDA903-76C-0250 with The University of Michigan.

#### References

1. L. V. Al'tschuler, G. I. Kanel, and B. S. Chekin, *Zh. Eksp. Teor. Fiz.* 72, 663 (1977) [Sov. Phys. *JETP* 45(2), 348 (1977)].
2. D. Tritton, *J. Fluid Mech.* 6, 547 (1959).
3. See J. J. Gilman, "Resistance to Shock Front Propagation in Solids", 1977 ARPA Materials Research Council Report. Compare also the data on electrical conductivity of aqueous solutions of electrolytes under shock compression up to 135 kilobard reported by S. D. Hamann and M. Linton, (*J. Appl. Phys.* 40, 913 (1969)), which are consistent with a viscosity of water not very different from its normal value.

SOURCE MONOCHROMATICITY CONSIDERATIONS

FOR OPTICAL INTERFEROMETRY

Amnon Yariv

ABSTRACT

The requirements on optical source monochromaticity in applications involving distance interferometry are examined. Limiting sensitivities and bandwidth requirements are obtained.

SOURCE MONOCHROMATICITY CONSIDERATIONS  
FOR OPTICAL INTERFEROMETRY

Amnon Yariv

Numerous applications exist which use optical interferometry to detect extremely small displacements. A generic experimental arrangement common to most of these situations is shown in Fig. 1.

To illustrate the basic problem consider first the case where the incident light beam is perfectly monochromatic

$$E_0(t) = E_0 \cos \omega t = E_0 \operatorname{Re}(e^{i\omega t}) \quad (1)$$

and the mirror motion is modulated sinusoidally at some "acoustic" frequency  $\Omega$  ( $\Omega \ll \omega$ )

$$l_2 = l_{20} + (\Delta l) \cos \Omega t. \quad (2)$$

In this case the total field at the detector input can be written as

$$E_s(t) = E_0 e^{i\omega t} + E_0 e^{i[\omega t - \frac{\omega}{c}(l_{20} - l_1) - \frac{\omega}{c}(\Delta l) \cos \Omega t]}. \quad (3)$$

The current output from the detector is given by the "long-time" average<sup>1</sup>

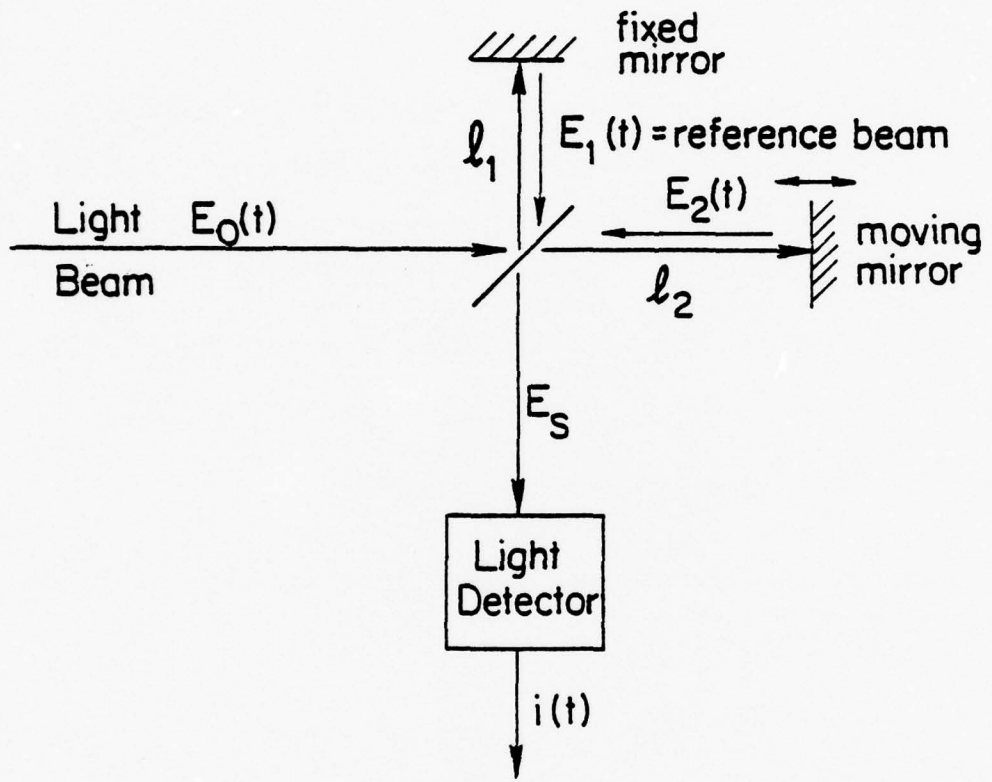


Figure 1. A Michelson interferometer used to detect small motions.

$$i(t) = \frac{aE_s^2}{aE_o^2} (t) = aE_o^2 \frac{1 + e^{-i[\frac{2\omega}{c}(\ell_{20} - \ell_1) + \frac{2\omega}{c}(\Delta\ell) \cos\Omega t]}}{1 + e^{i[\frac{2\omega}{c}(\ell_{20} - \ell_1) + \frac{2\omega}{c}(\Delta\ell) \cos\Omega t]}} \quad (4)$$

$$= aE_o^2 \{ 2 + 2\cos[\phi_o + \delta \cos\Omega t] \}$$

$$= 2aE_o^2 [1 + \cos\phi_o \cos(\delta \cos\Omega t) - \sin\phi_o \sin(\delta \cos\Omega t)] \quad (5)$$

where

$$\phi_o \equiv \frac{2\omega}{c}(\ell_{20} - \ell_1) \quad (6)$$

is the phase shift due to the difference in path length of the two arms of the interferometer and

$$\delta \equiv \frac{2\omega}{c} \Delta\ell \quad (7)$$

Since the expected motion  $\Delta\ell$  is very small compared to an optical wavelength we have  $\delta \ll 1$  so that

$$i(t) \approx 2aE_o^2 [1 + \cos\phi_o - \delta \cos(\Omega t) \sin\phi_o] \quad (8)$$

The output current thus contains a component oscillating at the acoustic frequency  $\Omega$  with an amplitude proportional to the maximum displacement  $\Delta\ell = \frac{\delta c}{\omega}$ . A practical difficulty which will be considered below, is the need to keep  $\phi_o$ , the phase shift corresponding to the path difference of the two arms a constant to within a fraction of an optical wavelength. If  $\phi_o$  is equal (or is nearly equal) to some multiple of  $\pi$ , the output current

at  $\Omega$  will be zero. This difficulty can be avoided by using a heterodyne scheme as will be discussed further on.

A fundamental issue in this type of distance interferometry is the minimum excursion  $\Delta\ell$  which can be detected. This minimum value  $(\Delta\ell)_{\min}$  is ultimately limited by the noise at the output of the detector at frequencies near that of the signal  $\Omega$ . If a perfectly monochromatic laser is used as the source and dark current is neglected then the main noise mechanism is shot noise current due to the mean current generated by the light. The mean square value of the shot noise current is

$$(i_n^2)_{\text{shot}} = 2eI_o\Delta\nu = 4eaE_o^2\Delta\nu \quad (9)$$

where  $I_o = 2aE_o^2$  is the dc current at the output of the detector and  $\Delta\nu$  is the detection bandwidth.

The signal current at  $\Omega$  (assuming  $\sin\phi_o = 1$ ) has, according to (8), an amplitude

$$i_s = 2aE_o^2\delta \quad (10)$$

so that the signal-to-noise power ratio at the output is

$$\frac{i_s^2}{(i_n^2)_{\text{shot}}} = \frac{2a^2E_o^4\delta^2}{4eaE_o^2\Delta\nu} = \frac{aE_o^2\delta^2}{2e\Delta\nu} = \frac{P_o\eta\delta^2}{4h\nu\Delta\nu} \quad (11)$$

where we used  $2aE_o^2 = P_o\eta/h\nu$  where  $P_o$  = total incident optical power and  $\eta$  the quantum efficiency of the detector. The minimum excursion  $(\Delta\ell)_{\min}$  is obtained by setting  $i_s^2/(i_n^2)_{\text{shot}} = 1$  and using (7). The result is:

;

$$(\Delta\ell)_{\min} = \frac{\lambda}{2\pi\sqrt{\frac{h\nu\Delta\nu}{P_0\eta}}} . \quad (12)$$

This result is often referred to as the "photon-noise limited" detectable excursion since the only noise mechanism considered was shot noise generated by the signal. It represents the ideal limit of detection.

It is thus imperative to determine how this ideal goal of shot noise limited detection can be approached. In what follows we will show that if the optical source is not sufficiently monochromatic then the output of the detector will contain additional noise that may far overshadow the shot noise and thus increase the minimum detectable signal to levels far in excess of the ideal limit.

Before embarking on a detailed mathematical analysis let us illustrate the physical origin of the noise which arises when the optical source has a finite spectral width. Let the optical spectrum have a constant value  $A$  over a narrow spectral region  $B$  and be zero elsewhere as shown in Fig. 2. Two optical fields oscillating at two frequencies, say,  $f_1$  and  $f_2$  will beat with each other to yield an output current oscillating at  $f_1 - f_2$ . If  $f_1 - f_2$  is near  $\Omega$ , the signal frequency, then this new current "contaminates" the signal and constitutes a new noise source in addition to the shot noise. Since this noise results from the self-beating of the optical field it is referred to as homodyne noise due to the finite spectral width of the source and to

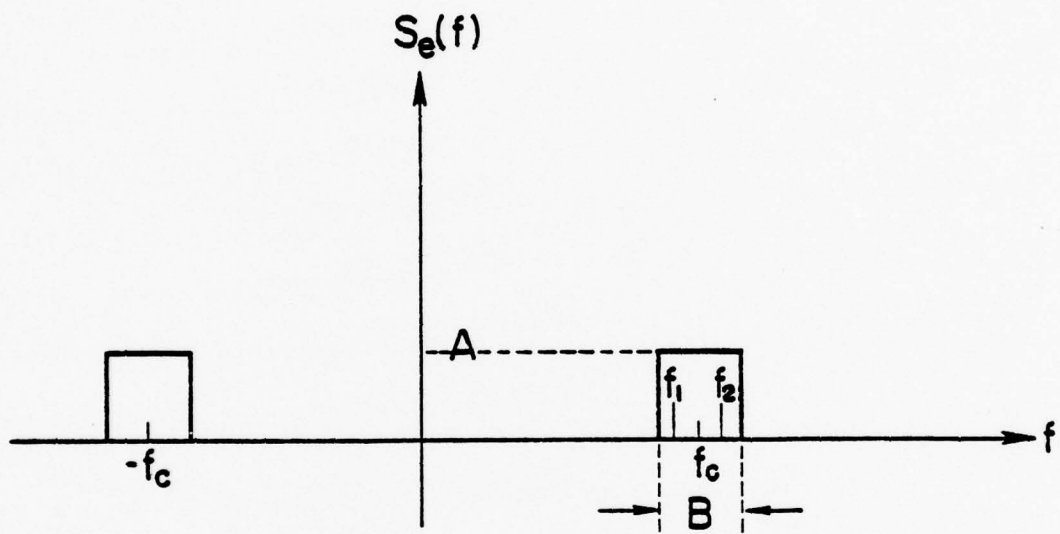


Figure 2. The spectral density function  $S_e(f)$  of the field  $e(t)$  incident on the detector.

compare it to that of shot noise at frequencies near that of the acoustic signal.

In calculating the noise spectrum of the current due to the finite spectral width of the optical source we take the optical field as  $e(t)$  and the output current as

$$i(t) = ae^2(t) \quad (13)$$

with the understanding that all current components of  $i(t)$  at optical frequencies are suppressed by the finite response time of the detector. We regard the field  $e(t)$  as a random stationary Gaussian process. It follows directly<sup>2</sup> that

$$\langle e_1^2 e_2^2 \rangle = \langle e^2 \rangle^2 + 2 \langle e_1 e_2 \rangle^2 \quad (14)$$

where  $e_1 = e(t_1)$  and the  $\langle \rangle$  symbol denotes ensemble averaging.

Letting the autocorrelation functions of the field and current be

$$R_e(\tau) = \langle e(t)e(t+\tau) \rangle \quad (15)$$

$$R_i(\tau) = \langle i(t)i(t+\tau) \rangle = a^2 \langle e^2(t)e^2(t+\tau) \rangle$$

respectively, we obtain from (14) letting  $e_1 \rightarrow e(t)$ ,  $e_2 \rightarrow e(t+\tau)$ ,  $i(t) \rightarrow i_1$ ,  $i_2 \rightarrow i(t+\tau)$

$$\begin{aligned} R_i(\tau) &= a^2 \{ \langle e^2(t) \rangle^2 + 2 \langle e(t)e(t+\tau) \rangle^2 \} \\ &= a^2 \{ R_e^2(0) + 2R_e^2(\tau) \} \quad . \end{aligned} \quad (16)$$

The spectral density function of the output current is the Fourier transform of the current autocorrelation function

$$S_i(f) = a^2 \int_{-\infty}^{\infty} [R_e^2(0) + 2R_e^2(\tau)] e^{-i2\pi f\tau} d\tau \quad (17)$$

$$= a^2 R_e^2(0) \delta(f) + 2a^2 \int_{-\infty}^{\infty} R_e^2(\tau) e^{-i2\pi f\tau} d\tau .$$

To evaluate the integral we use the relation

$$R_e(\tau) = \int_{-\infty}^{\infty} S_e(\tau) e^{i2\pi f'\tau} df'$$

so that

$$\begin{aligned} \int_{-\infty}^{\infty} R_e^2(\tau) e^{-i2\pi f\tau} d\tau &= \int_{-\infty}^{\infty} d\tau R_e(\tau) \int_{-\infty}^{\infty} df' S_e(f') e^{i2\pi f'\tau} e^{-i2\pi f\tau} \\ &= \int_{-\infty}^{\infty} df' S_e(f') \int_{-\infty}^{\infty} d\tau R_e(\tau) e^{-i2\pi(f-f')\tau} \\ &= \int_{-\infty}^{\infty} df' S_e(f') S_e(f-f') \end{aligned}$$

leading to

$S_i(f) = a^2 R_e^2(0) \delta(f) + 2a^2 \int_{-\infty}^{\infty} S_e(f') S_e(f-f') df' .$

(18)

This is the basic result relating the current spectral density  $S_i(f)$  to the optical spectral density function  $S_e(f)$ .

If the optical spectrum can be approximated as in Fig. 2 by a constant over a spectral band  $B$  centered on  $f_c$  and zero elsewhere, then the current spectrum  $S_i(f)$  is shown in Fig. 3. It consists of a delta function at  $f = 0$  and triangular regions centered on  $f = 0$  and  $f = \pm f_c$ . The area under the delta function is  $a^2 R_e^2(0) = 4a^2 A^2 B^2$  since

$$R_e(0) = \langle e^2(t) \rangle = P_o = 2AB \quad (19)$$

where  $P_o$  is the total optical power incident on the detector.

In practice, no optical detectors can respond at optical frequencies so that the noise bands centered on  $\pm f_c$  do not exist and we need concern ourselves only with that portion of the noise spectrum in Fig. 3 which is centered on  $f = 0$ .

Since acoustic frequencies which we may wish to detect are typically very small,  $\Omega \ll B$ , the noise spectral density which interferes with the measurements of acoustic signals is given by  $S_i(0)$ . The ratio of this noise to the shot noise is

$$\frac{S_i(0)}{S_{\text{shot}}} = \frac{S_i(0)}{(i_n^2)_{\text{shot}}/\Delta\nu} = \frac{2a^2 P_o^2/B}{2eI_o} = \frac{a^2 P_o^2 h\nu}{Be^2 P_o n} \quad . \quad (20)$$

$I_o$ , the dc current output, is given by

$$I_o = a \langle e^2 \rangle = a P_o = \frac{P_o e n}{h f_c} \quad (21)$$

where  $n$  is the quantum efficiency (electrons per photon) of the detector. It follows that  $a = \frac{en}{hf_c}$  so that

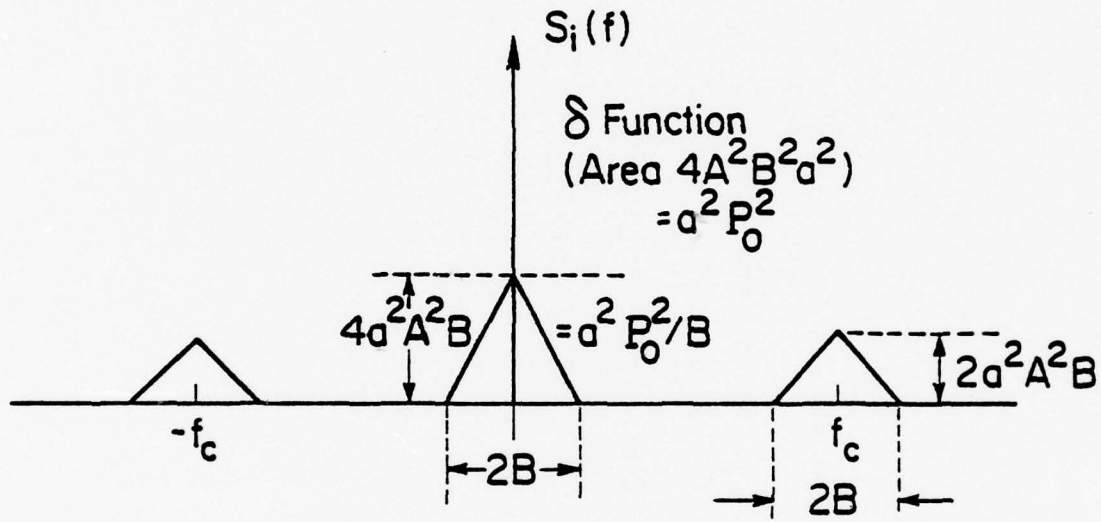


Figure 3. The spectral density of the current output of a square law optical detector illuminated with light whose spectrum is shown in Figure. 2. The two triangles at  $f = \pm f_c$  do not exist in practice since present day detectors cannot respond at optical frequencies.

$$\frac{S_i(0)}{S_{\text{shot}}} = \frac{P_o \eta}{h f_c B} .$$

(22)

The ratio of homodyne ( $S_i(0)$ ) to shot noise in a typical case involving the use of a light emitting diode as the source is evaluated using the following data:

$$P_o = 1 \text{ mW}$$

$$\eta = 0.5$$

$$\lambda = 1 \mu\text{m}$$

$$f_c = \frac{c}{\lambda} = 3 \times 10^{14}$$

$$B = 6 \times 10^{11} \text{ (corresponding to a } 20\text{\AA} \text{ linewidth)}$$

This results in

$$\frac{S_i(0)}{S_{\text{shot}}} \approx 4000 .$$

In words: The homodyne noise under these circumstances is far (X4000) larger than the shot noise and any system consideration based on interferometry with wide spectrum light must take it into account. This can be done simply by replacing the shot noise term  $i_n^2$  in Eq. (9) or (11) with  $S_i(0)$ . In the present example the minimum detectable signal will be larger by  $\sqrt{4000}$ .

The conclusion of the above treatment is that for sensitive interferometry one must use sources with spectral width B

narrower than the acoustic frequency  $\Omega$  to be detected so that the latter falls outside the region  $f \gtrsim B$  occupied by the homodyne noise. This situation is illustrated in Fig. 4.

The spectral purity which is required for detection of acoustic signals in the, say, KHz range is available only from coherent sources such as lasers.

When considering the spectral requirements of lasers we need to distinguish between frequency modulation (FM) noise and amplitude modulation (AM) noise.<sup>3</sup> The homodyne noise considered above is due to AM alone (a square-law detector does not respond to phase fluctuations). It is then possible that a laser with a "broad" spectrum,  $B > \Omega$ , can still be used for "acoustic" detection provided the FM component of the noise is sufficiently narrow so that  $B_{FM} < \Omega$ . This, fortunately, is the case with most lasers where amplitude fluctuation (i.e., AM noise) are smoothed by gain saturation.<sup>3</sup>

We mentioned at the outset that for a maximum signal out of the detector one need satisfy, according to Eq. (8), the condition  $\phi_0 = \pi/2$ . This requires (see Eq. (6)) that the path difference between the two arms of the interferometer  $l_{20} - l_1$  be stable to within a fraction of the optical wavelength  $\lambda$ . This requirement is extremely difficult to satisfy in practice. This problem can be solved by shifting the reference beam  $E_0 e^{i\omega t}$  (see Fig. 1) in frequency (say, by acoustic Bragg diffraction) to a frequency  $\omega_1 + \omega_{If}$ . ( $\omega_{If}$  will be called the intermediate

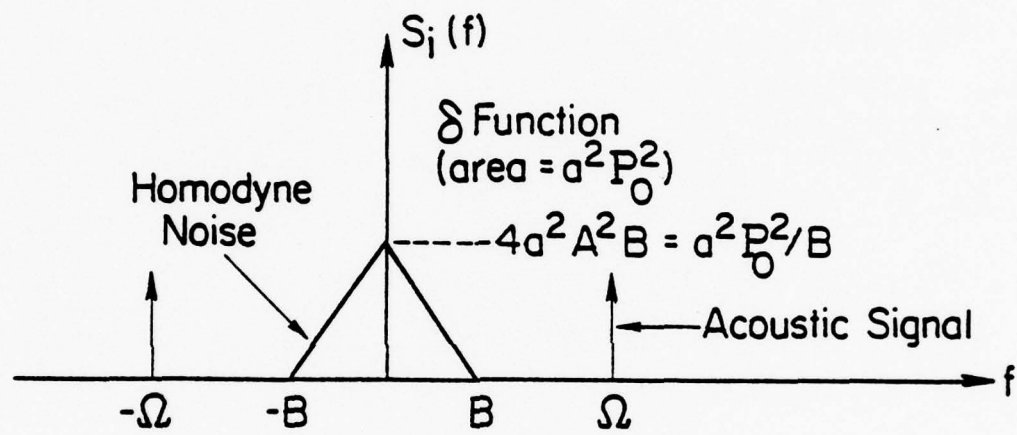


Figure 4. The noise and signal spectra in the case of narrow spectral sources.

frequency.) The total field at the detector is given, instead of by Eq. (3), by

$$E_s(t) = E_0 e^{i\omega_1 t} + E_0 e^{i(\omega t - \phi_0 - \delta \cos \Omega t)} \quad (23)$$

The detector output current is then

$$i(t) = \overline{aE_s^2(t)} = 2E_0^2 \{1 + \cos[(\omega_1 - \omega)t + \phi_0 + \delta \cos \Omega t]\} \quad (24)$$

The signal spectrum is thus one of phase modulation and is centered about the intermediate frequency (IF)  $\omega_1 - \omega$ . The need for maintaining  $\phi_0$  a constant is now obviated. All that is needed of  $\phi_0$  is that its variation be small during an acoustic period  $2\pi/\Omega$ . The spectral purity of the laser, more precisely, that due to its frequency modulation, must still satisfy  $B < \Omega$ . The signal is recovered by conventional phase demodulation of  $i(t)$ .

In summary, we have examined the basic noise mechanisms which interfere with the detection of small acoustic vibrations by means of optical interferometry. The limitation on sensitivity due to the finite optical spectral width was derived. The main conclusion is that the AM spectral width of the source need be small compared to the lowest acoustic frequency if the sensitivity is to approach the quantum photon noise limit.

#### ACKNOWLEDGEMENT

This research was supported by the Defense Advanced Research Projects Agency of the Department of Defense under Contract MDA903-76C-0250 with The University of Michigan.

### References

1. A. Yariv, "Introduction to Optical Electronics," 2nd ed., Holt, Rinehart & Winston, New York, 1976, p. 3.
2. W. B. Davenport and W. L. Root, "An Introduction to the Theory of Random Signals and Noise." McGraw-Hill Gook Co., Inc., New York, 1958.
3. See, for example: A. Yariv, "Quantum Electronics," 2nd ed., J. Wiley & Sons, New York, 1975, p. 300 and references cited therein.

## METHOD FOR MEASURING SHOCK FRONT RISETIMES

J. J. Gilman and A. Yariv

Knowledge of the structures of shock fronts is presently limited by available techniques for measuring the time duration of the pressure rise through the shock front. The best method is the laser interferometer which has a time resolution limit of about  $3 \times 10^{-9}$  sec. For a shock front speed of  $10^6$  cm/sec this yields a spatial resolution limit of about  $3 \times 10^{-3}$  cm. However, the intrinsic limiting shock front thickness in a solid is an atomic dimension; say  $3 \times 10^{-8}$  cm. Thus the experimental observational limit may be as much as  $10^5$  times too large.

The time resolution needed for an accurate determination of the shock front risetime might be as small as  $3 \times 10^{-14}$  sec. It is unlikely that such resolution can be achieved in the foreseeable future, but laser pulses as short as  $10^{-12}$  sec are presently available and could be used to improve the state of knowledge by up to three orders of magnitude.

The conditions needed to improve the resolution by one order of magnitude will be considered here because study of the problem quickly indicates that synchronization of the arrival of a picosecond light pulse and a shock wave at a free surface presents a severe experimental difficulty.

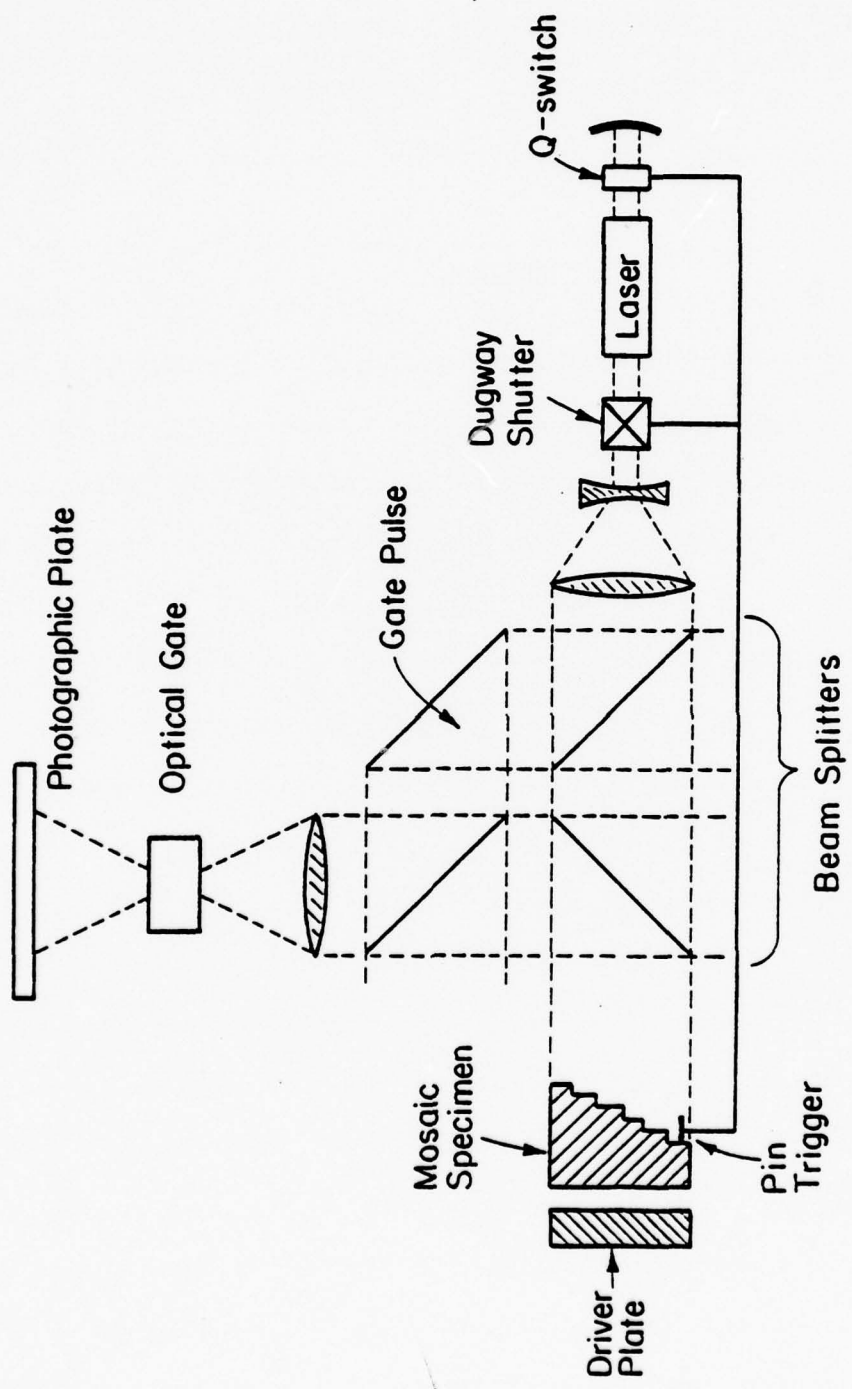
A mode-locked laser normally emits a train of light pulses in which each pulse lasts about  $10^{-12}$  sec and the pulses are spaced about  $3 \times 10^{-9}$  sec apart. Thus the ratio of "on time" to "off time" is about  $3 \times 10^{-4}$  which is the probability of synchronization if a shock front arrives at a free surface at a random time relative to the train of light pulses. By increasing the length of each pulse to about  $10^{-11}$  sec and reducing the laser cavity length from 100 to 30 cm, the on-off ratio could be increased to about  $10^{-2}$ .

Next, by dividing the free surface at which the shock front emerges into a mosaic of 100 small mirrors each spaced in a sequence  $10^{-4}$  cm apart in the direction of shock propagation (so that a total range of  $10^{-2}$  is covered), the probability that at least one mirrored position would simultaneously be struck by the emerging shock front and a light pulse could be increased to unity.

As indicated in the attached figure, a fast non-linear optical gate could be used to isolate single picosecond pulses while a pin contact (with  $10^{-9}$  sec resolution) could be used to trigger a Q-switched, mode-locked laser and an optical shutter so as to produce a single picosecond pulse at the time of arrival of a shock wave. A photographic film is placed to record specimen mosaic when at least one of the mosaic elements coincides with the shock front. The intensity of the image would provide a measure of the time duration of the interaction.

**ACKNOWLEDGEMENT**

This research was supported by the Defense Advanced Research Projects Agency of the Department of Defense under Contract No. MDA903-76C-0250 with The University of Michigan.



ACOUSTIC WAVEGUIDES FOR UNDERSEA ACOUSTIC  
DETECTORS AND TRANSMITTERS

G. S. Kino

ABSTRACT

It is shown that acoustic fiber waveguides can be employed in much the same manner as the optical waveguides in the FOSS system, but with much reduced sensitivity. This is because of the longer wavelengths and hence smaller phase shifts of the acoustic waveguide modes employed, as well as the shorter usable waveguide lengths (meters rather than kilometers).

An alternative approach analogous to the electromagnetic dielectric rod antenna is suggested. A waveguide consisting either of a liquid filled pipe or of a helically coiled rod is employed. The waveguide mode is chosen to have the same propagation velocity along its axis as the acoustic wave in water. At the same time the coupling of this mode to the wave in the surrounding water medium is deliberately chosen to be very weak. Thus full coupling between the waves in the two media takes place over several tens of wavelengths.

By this means an antenna is formed with extremely high directivity. The angular range of acceptance of this antenna is  $\Delta\theta = \lambda/2\pi l$  where  $l$  is the antenna length and the leak rate  $\alpha$  is chosen so that  $\alpha l \approx 1.3$ .

The antenna is in the form of a helix or a simple liquid filled cylinder. It should therefore have small drag and generate a relatively small amount of noise.

ACOUSTIC WAVEGUIDES FOR UNDERSEA ACOUSTIC  
DETECTORS AND TRANSMITTERS

G. S. Kino

The employment of fiber optic waveguides has been demonstrated as an important new technique for detection of acoustic fluctuations in the sea. Stimulated by these results we began to examine the implications of using an acoustic waveguide rather than a fiber optic waveguide as an acoustic detector or transmitter<sup>1</sup>.

Initially we examined the direct analogy, the interaction of a low frequency wave in the water with a high frequency waveguide mode. This device is very closely related also to the parametric antennas which utilize parametric interactions in water between high frequency and low frequency signals. The analysis of such interactions showed that because the wavelength of the acoustic waveguide modes that could be used was of the order of 100  $\mu\text{m}$  and the maximum allowable length of the guide only a few meters, the phase shifts caused by the received signals is decreased by five orders of magnitude from that of the equivalent optical system. Because the acoustic waveguide signals can have much larger power than the equivalent optical mode, and much smaller bandwidth, some of the decrease in sensitivity can be recovered. So even these devices may be interesting.

However, we then began to realize that a linear rather than nonlinear interactions could be used to construct antennas analogous to waveguide or dielectric rod electromagnetic antennas with extremely high sensitivity and outstanding directional characteristics. So we shall concentrate on this mode of operation, and only briefly consider the parametric mode of operation.

We consider two forms of acoustic guide to be used as antennas. The first illustrated in Fig. 1a consists of a liquid column between one half and several wavelengths in a diameter enclosed in a metal or plastic tube in which the acoustic velocity is normally much higher than that in the liquid. The wave in this guide is arranged to have a velocity identical to the natural velocity of acoustic waves in the medium outside the guides normally the sea. As the wave has a slower velocity than that in the hollow enclosing tube, its amplitude falls off essentially exponentially in the tube, so there is only weak coupling to the medium outside the tube. By this means the device behaves like a wedge coupler to an acoustic surface wave, and with the right choice of waveguide length approximately 80% of the power in the guide can be coupled into a wave propagating in the axial direction in the sea.

A second possibility is to use a waveguide mode in a faster solid medium such as fused quartz. In this case the solid is made in the form of a rod which is coiled in the form of a helix, so that the wave velocity along its axis is equal to that of a wave in water.

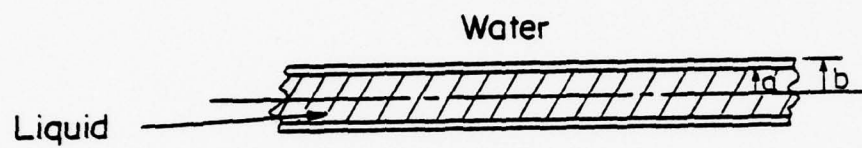


Figure 1a. A waveguide in the form of a pipe.

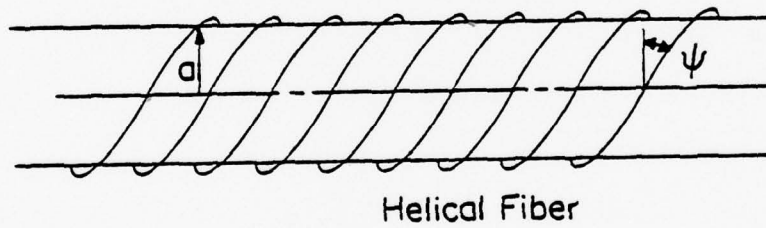


Figure 1b. A fiber guide wrapped into a helix.

The velocity of sound in water is  $v_w = 1.5 \times 10^5$  cm/sec, the velocity of a torsional wave or symmetric radial mode in a quartz waveguide is approximately  $v_g = 3.5 \times 10^5$  cm. Suppose now the quartz fiber is coiled into a helical form of radius  $a$  and  $n$  turns per cm. Let the angle the axis of the fiber makes with a place perpendicular to the axis of the helix be  $\psi$ , as shown in Figure 1b. Then

$$2\pi a n \tan\psi = 1$$

The effective velocity of the guided wave in the axial direction is

$$v = v_g \sin\psi$$

so it follows that

$$v = \frac{v_g}{\sqrt{1 + 4\pi^2 a^2 n^2}}$$

When  $v = v_w$  there will be a cumulative interaction along the axial direction between the waveguide in the fiber and that in the water receiver or transmitter. Thus for  $v = 1.5 \times 10^5$  cm/sec,  $v_g = 3.5 \times 10^5$  cm/sec,  $\sin\psi = .429$ ,  $\psi = 25.38^\circ$ ,  $\tan\psi = .474$ . So for  $a = 0.2$  meters,  $n = 16.7$  turns/meter. Such guides could be used both as a receiving or transmitting antennas if excited in the mismatch in  $k$  at an angle  $\theta$  off axis will be  $k \sin\theta \approx k\theta$ . Therefore the response of the antenna can be shown to vary as

$$R = \frac{\sin(k\theta/2)}{k\theta/2}$$

The 4db points of this response cover an angular range  
 $\Delta\theta$  where

$$\Delta\theta = \lambda/2\pi l$$

So for an antenna length of 5 meters and a wavelength of 15 cm (10kHz) the main lobe has an angular spread of .00477 or 0.27 degrees.

The antenna itself is in the form of a cylinder or helix, supported on a cylinder or on fins. In both cases the drag or noise caused by dragging the antenna through the water could be made very small.

A detailed calculation of the performance of this antenna could be made. Based on the theory worked out for wedge transducers<sup>2</sup>, the leak rate from the waveguide mode to the water wave mode would be  $\alpha$  with

$$\alpha l \approx 1.3$$

for optimum coupling of 80% of the power from or to the waveguide mode, over at least one octave bandwidth.

## APPENDIX

### Comparison of Acoustic and Optical Parametric Detectors

#### Operating in the Homodyne Mode

If we consider the acoustic waveguide mode to have a frequency of the order of 30 MHz, the acoustic wavelength would be of the order of  $100\mu\text{m}$ . The acoustoelastic effect, i.g., the relative change of acoustic velocity with pressure applied to the guide is of the same order as the elasto optic effect; both relative changes of velocity are themselves of the same order as the applied strain. Therefore, as the optical wavelength employed is approximately  $1\mu\text{m}$ , the phase change per unit length due to applied pressure will be approximately  $10^{-2}$  of that obtained for the equivalent optical guide. The attenuation at 30 MHz of the doped quartz used in these experiments is approximately 1.8db/meter. So a further reduction in sensitivity would be expected because the fiber lengths that could be employed would be of the order of  $10^{-3}$  of those usable in an optical detector. Thus the basic phase change obtained in an acoustic device of this type is of the order of  $10^{-5}$  of that to be expected in the equivalent optical device.

On the other hand homodyne detection in an acoustic device should be much more sensitive than in the optical device because an essentially noiseless narrow band reference signal can be employed.

Consider an optical system with an optical source of power  $P_o$ . The current in the detector will be  $I_o$  where  $I_o = \eta P_o / h\nu$ . Therefore, the shot noise current fluctuations  $\langle i^2 \rangle$  per cycle bandwidth will be

$$\langle i^2 \rangle = 2eI_o = \frac{2e\eta P_o}{h\nu}$$

where  $\eta$  is the quantum efficiency and  $\nu$  is the center frequency of the light source.

The shot noise power delivered into a resistive load  $R_o$  is therefore

$$P_s = \frac{2e^2 \eta P_o R_o}{h\nu} \text{ per cycle}$$

So the noise figure is  $N = 1 + P_s/kT$  or

$$N_s = 1 + \frac{2e}{h\nu} \frac{e}{kT} P_o R_o = 1 + \alpha_s$$

Taking  $h\nu/e = 1$  volt,  $kT/e = .027$  volt,  $P_o = 1$  mV,  $R_o = 50$  ohms we find that

$$N_s = 6.7 \text{ dBs}$$

But in a paper given at this meeting Yariv<sup>3</sup> has shown that the ratio of homodyne noise to shot noise is

$$\frac{P_h}{P_s} = \frac{P_o \eta}{2h\nu B}$$

where  $B$  is the bandwidth of the optical source. Yariv shows that this ratio  $\approx 2000$  for an LED source. So this would imply a noise figure of approximately 38 dBs due to homodyne noise.

An acoustic source could easily produce 1 watt at a frequency of 30 MHz, with an extremely narrow bandwidth. So in homodyne operation we would expect to use a 1 meter length and lose a factor of  $10^{-5}$  in the basic phase change. By using a 1 watt reference instead of a 1 mw reference the homodyne output would increase by a factor  $10^3 \times 10^{-10} = 10^{-7}$ . Now the noise figure of the detection system should be near to 0 dbs. So the sensitivity of the acoustic system would be 70 dbs - 38 dbs  $\sim$ 30 dbs worse than that of the optical system.

#### Acknowledgement

This research was supported by the Defense Advanced Research Projects Agency of the Department of Defense under Contract Mo. MDA903-76C-0250 with The University of Michigan.

#### References

1. G. D. Boyd, L. A. Coldren and R. N. Thurston, "Acoustic Waveguide with a Cladded Core Geometry," *Appl. Phys. Lett.* 26, 31-34, January 1975.
2. H. L. Bertoni and T. Tamir, "High Efficiency Wedge Transducers," *IEEE Trans.* 50-19, 413, 1972.
3. A. Yariv, "Comparison of Homodyne Noise and Shot Noise in Optical Detection." Private communication.

THE PRESSURE SENSITIVITY OF A CLAD OPTICAL FIBER

B. Budiansky, D. C. Drucker, G. S. Kino and J. R. Rice

ABSTRACT

Experiments carried out by Bucaro, et al. suggest that an optical fiber acoustic wave detector coated with a plastic coating several times its diameter exhibits greatly increased sensitivity compared to an uncoated fiber. In this paper we show that this effect should be expected because when hydrostatic pressure is applied to the plastic coating, it contracts in the axial direction. As the area of the plastic coating is much larger than that of the fiber, the fiber tends to contract in the axial direction and expand in the radial direction. The longitudinal strain in the fiber is therefore much larger than it would be in the uncoated fiber.

The calculations which have been made lead to the conclusion that with a coating of a teflon-like plastic, the longitudinal strain in the fiber is increased by a factor of 13 leading to a corresponding increase in the effective phase change.

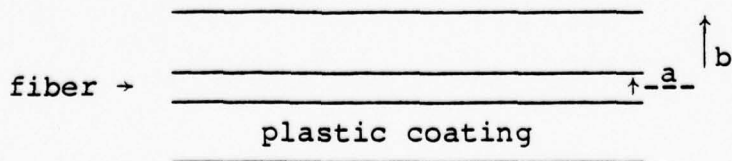
## THE PRESSURE SENSITIVITY OF A CLAD OPTICAL FIBER

B. Budiansky, D. C. Drucker, G. S. Kino, and J. R. Rice

### INTRODUCTION

It was suggested by experiments of Bucaro, et al. described during the MRC meeting on optical fiber acoustic wave detectors that greatly enhanced acoustic sensitivity can be obtained using a clad optical fiber rather than an unclad fiber. In this paper we show that this is to be expected because of the high Poisson's ratio and low elastic constant of the fiber normally employed. When a plastic coating, whose diameter is several times that of the fiber is subjected to an external radial hydrostatic pressure, it contracts in the axial direction and expands in the radial direction. As the diameter of the fiber is small, the fiber contracts in the axial direction along with the plastic coating, so that the strain  $\epsilon_z$  in the z-direction is basically controlled by the plastic coating. For this reason the strain in the fiber is very much larger than it would otherwise be at the same pressure in the unclad fiber alone.

### THEORY OF THE INTERACTION



We consider an isotropic cylindrical glass fiber of radius,  $a$ , clad with a plastic coating of radius,  $b$ , and write  $f = (a/b)^2$ . Typically,  $f \ll 1$ . We take the Young's moduli and Poisson's ratio of the glass fiber and plastic to be  $E_g$ ,  $\nu_g$ , and  $E_p$ ,  $\nu_p$ , respectively.

For determination of stresses in the fiber under pressure loading, we observe that the problem is one of generalized plane strain (i.e., the axial strain  $\epsilon_z$ , which is the same for both glass and plastic, is unknown). Boundary conditions are

$$\sigma_{rp}|_{r=b} = -p, \quad \text{and} \quad (1)$$

$$f\sigma_{zg} + (1-f)\sigma_{zp} = -p. \quad (2)$$

The latter condition assures that the net stress on the fiber ends is  $-p$ . In writing the condition we have made use of the observation that the exact elasticity solution (i.e., the Lamé solution) which gives spatially uniform  $\sigma_z$  stresses within the glass and plastic. Two continuity conditions must be met:

$$\sigma_{rg}|_{r=a} = \sigma_{rp}|_{r=a} \quad (3)$$

$$u_g|_{r=a} = u_p|_{r=a} \quad (4)$$

where  $u$  is the radial displacement.

The solution is such that  $\sigma_{rg}$  and  $\sigma_{\theta g}$  are constant. Call their common value  $-q$ :

$$\sigma_{rg} = \sigma_{\theta g} = -q . \quad (5)$$

From the Lamé solution

$$\sigma_{rp} = - \frac{(q-p)fb^2}{(1-f)r^2} + \frac{(qf-p)}{1-f} \quad (6)$$

$$\sigma_{\theta p} = \frac{(q-p)fb^2}{(1-f)r^2} + \frac{(qf-p)}{1-f} . \quad (7)$$

Hence the value of  $\sigma_{rp} + \sigma_{\theta p}$  is:

$$\sigma_{rp} + \sigma_{\theta p} = 2(qf-p)/(1-f) . \quad (8)$$

Now, both glass and plastic are subject to the same (unknown) axial strain  $\epsilon_z$ :

$$\begin{aligned} \epsilon_z &= \frac{\sigma_{zg}}{E_g} - \frac{\nu_g}{E_g} (\sigma_{rg} + \sigma_{\theta g}) \\ &= \frac{\sigma_{zp}}{E_p} - \frac{\nu_p}{E_p} (\sigma_{rp} + \sigma_{\theta p}) . \end{aligned} \quad (9)$$

Using the results of (5) and (8), this gives

$$\frac{\sigma_{zg}}{E_g} - \frac{\sigma_{zp}}{E_p} = \frac{2\nu_p}{(1-f)E_p} p - \left( \frac{2\nu_g}{E_g} + \frac{2f\nu_p}{(1-f)E_p} \right) q . \quad (10)$$

This may be solved simultaneously with (2) to give

$$\sigma_{zg} = - \frac{(1-2\nu_p)p + 2[(1-f)\nu_g E_p/E_g + f\nu_p]q}{f + (1-f)E_p/E_g} . \quad (11)$$

Note that at this point  $q$  remains undetermined. Later we shall indicate how it can be found, but for practical cases

exact knowledge of  $q$  is unessential. This is because the cladding material and geometry used is such that

$$f \ll 1, \quad E_p/E_g \ll 1. \quad (12)$$

Further, we expect  $q$  to be of the same size as  $p$  (indeed, one anticipates  $0 \leq q \leq p$ ). Now, the terms multiplying  $q$  in (11) are all of order  $f$  or  $E_p/E_g$ , and hence small compared to those multiplying  $p$ . Thus a first approximation, which is especially accurate for the practical range  $f \ll 1$ ,  $E_p/E_g \ll 1$  is to neglect  $q$  and hence write

$$\sigma_{zg} \approx - \frac{(1-2\nu_p)p}{f + (1-f)E_p/E_g} . \quad (13)$$

A somewhat improved approximation, which is accurate to the same order when (12) are met, but which gives the correct result in several limiting cases, is to write  $q \approx p$ . That is,

$$\sigma_{rg} = \sigma_{\theta g} = -q \approx -p \quad (14)$$

and, from (11),

$$\sigma_{zg} = - \frac{1 - 2(1-f)\nu_p + 2(1-f)\nu_g E_p/E_g}{f + (1-f)E_p/E_g} . \quad (15)$$

These formulae for the stresses in the glass are good approximations at small  $f$  and  $E_p/E_g$ , and happen also to give the exact results when: (i) there is no cladding,  $f = 1$ ; (ii) the glass and its cladding have identical properties,  $\nu_g = \nu_p$ ,  $E_g = E_p$ ; and (iii) both materials are incompressible,  $\nu_g = \nu_p = 1/2$ .

In order to solve exactly for  $q$  (which is, evidently, not necessary in practical cases), we must make use of the continuity condition (4), ignored in the solution as thus far discussed. The details are given in the Appendix.

To obtain the strains in the glass, the first approximation (i.e., Eq. (13) for  $\sigma_{zg}$  and neglecting  $\sigma_{rg}$  and  $\sigma_{\theta g}$ ) gives

$$\begin{aligned}\varepsilon_{zg} &= -\frac{(1-f\nu_p)p}{fE_g + (1-f)E_p} \\ \varepsilon_{\theta g} &= \varepsilon_{rg} = -\nu_g \varepsilon_{zg} = \frac{\nu_g (1-2\nu_p)p}{fE_g + (1-f)E_p}\end{aligned}\tag{16}$$

and these are accurate when  $f \ll 1$  and  $E_p/E_g \ll 1$ . At the expense of more complicated expressions, a somewhat better approximation to the strains is given by using the stresses of Eqs. (14) and (15) to obtain

$$\begin{aligned}\varepsilon_{zg} &= -\frac{1-2(1-f)\nu_p - 2f\nu_g}{fE_g + (1-f)E_p} p \\ \varepsilon_{\theta g} &= \varepsilon_{rg} = p \frac{g(1-2\nu_p) - f(1-\nu_g - 2\nu_g \nu_p) - (1+\nu_g)(1-2\nu_g)(1-f)E_p/E_g}{fE_g + (1-f)E_p}.\end{aligned}\tag{17}$$

Finally, for the sake of completeness, we record fully exact (usually superfluously so) formula for the strains in the fiber:

$$\begin{aligned}\varepsilon_{zg} &= \frac{1 + \left[ \frac{4f(1-\nu^2)}{A(1-2\nu_p)} \right] \left[ \nu_p - \nu_g \right]}{1 + \left\{ \frac{2f(1-f)(1-2\nu_p)}{\left[ A \left( \frac{fE_g}{E_p} - 1 \right) + 1 \right]} \right\} \left[ \nu_p - \nu_g \right]^2} \\ \varepsilon_{\theta g} &= \frac{2f(1-f)(1-2\nu_p)}{\left[ A \left( \frac{fE_g}{E_p} - 1 \right) + 1 \right]} \left[ \nu_p - \nu_g \right]^2\end{aligned}\tag{18}$$

where  $\epsilon_{zg}^0$  is given by the zero'th order approximation of Eq. (16); and

$$A = [1+v_p][1+f(1-2v_p)] + \frac{E_p}{E_g} [1+v_g][1-2v_g][1-f] . \quad (19)$$

Also

$$\epsilon_{rg} = \epsilon_{\theta g} = -v \epsilon_{zg} - q \frac{(1+v_g)(1-2v_g)}{E_g} \quad (19)$$

where  $q$  is given by Eq. (A-5) of the Appendix.

It is interesting to note that  $\epsilon_{zg} = \epsilon_{zg}^0$  exactly for  $v_p = v_g$ .

#### PHASE DELAY CHANGE

The phase of a wave of frequency  $\omega$  propagating in a fiber of length  $l$  is

$$\phi = \frac{\omega l}{v} . \quad (20)$$

Therefore when  $l$  and  $v$  are changed

$$\frac{\Delta\phi}{\phi} = \frac{\Delta l}{l} - \frac{\Delta v}{v} = \epsilon_{zg} + \frac{\Delta n}{n} \quad (21)$$

where  $n$  is the change in refractive index.

Now consider the photoelastic tensor. For an isotropic medium we can write in normal tension notation

$$\Delta n_{ij} = - \frac{n^2 p_{ijkl}}{2} \epsilon_{kl} . \quad (22)$$

In our case we have three components of strain present  $\epsilon_{rg} = \epsilon_1$ ,  $\epsilon_{\theta g} = \epsilon_2$  and  $\epsilon_{zg} = \epsilon_3$  in reduced tensor notation. We are interested in  $\Delta n_1 = \Delta n_{11}$  and  $\Delta n_2 = \Delta n_{22}$  for the optical

wave. So we require the components  $p_{12} = p_{1122}$  and  $p_{11} = p_{1111}$ . The tensor that is normally measured in Bragg scattering experiments by longitudinal waves is  $p_{12}$ , while for scattering by a shear wave the effective tensor is  $p_{44} = p_{1212}$ . Because this is a 4th rank tensor of an isotropic material, it follows the analogous properties of the elastic tensor. So we can write

$$p_{12} = p_{11} - 2p_{44} . \quad (23)$$

Because  $\varepsilon_1 = \varepsilon_2$ , it follows that

$$\frac{\Delta\phi}{\phi} = \varepsilon_3 - \frac{n^2}{2} [\varepsilon_1 (p_{11} + p_{12}) + \varepsilon_3 p_{12}] \quad (24)$$

$$\frac{\Delta\phi}{\phi} = \varepsilon_3 - \frac{n^2}{n} [2\varepsilon_1 (p_{11} - p_{44}) + \varepsilon_3 (p_{11} - 2p_{44})] . \quad (25)$$

Taking  $p_{11} = 0.27$ ,  $p_{44} = .075$ ,  $n = 1.46$  for fused quartz

$$\begin{aligned} \frac{\Delta\phi}{\phi} &= \varepsilon_3 - .42\varepsilon_1 - .13\varepsilon_3 \\ &= .87\varepsilon_3 - .42\varepsilon_1 . \end{aligned}$$

The results for the unclad fiber ( $f = 1$ ) using the materials constants of pyrex glass for the mechanical properties;  $E_g = 6.2 \times 10^{10}$  newtons/m<sup>2</sup>,  $v_g = 0.24$  are

$$\varepsilon_1 = \varepsilon_3 = -8.4 \times 10^{-12} p$$

where  $p$  is in newtons/m<sup>2</sup>. So

$$\frac{\Delta\phi}{\phi} = -3.8 \times 10^{-12} p .$$

For the clad fiber with  $f \ll 1$  or a very large diameter ratio, we can use the approximate theory with  $f = 0$ . Taking  $E_p = .076 \times 10^{10}$  newtons/m<sup>2</sup>,  $v_p = 0.458$  corresponding to polyethylene, we find that

$$\epsilon_3 = -1.1 \times 10^{-10} p$$

$$\epsilon_1 = .154 \times 10^{-10}$$

and

$$\frac{\Delta\phi}{\phi} = -1.026 \times 10^{-10} p .$$

In the limiting case  $\Delta\phi/\phi$  has been increased by a factor of 27 due to cladding. The value of  $\Delta\phi/\phi$  has been calculated from the exact solution of Eq. (18) as a function of  $b/a$ . In Fig. 1 we observe that for  $b/a = 6$ , the value of  $\Delta\phi/\phi$  is increased by a factor of 8.8 over that of the unclad fiber.

#### ACKNOWLEDGEMENTS

The authors would like to thank A. Yariv for helpful discussions. This research was supported by the Defense Advanced Research Projects Agency of the Department of Defense under Contract No. MDA903-76C-0250 with The University of Michigan.

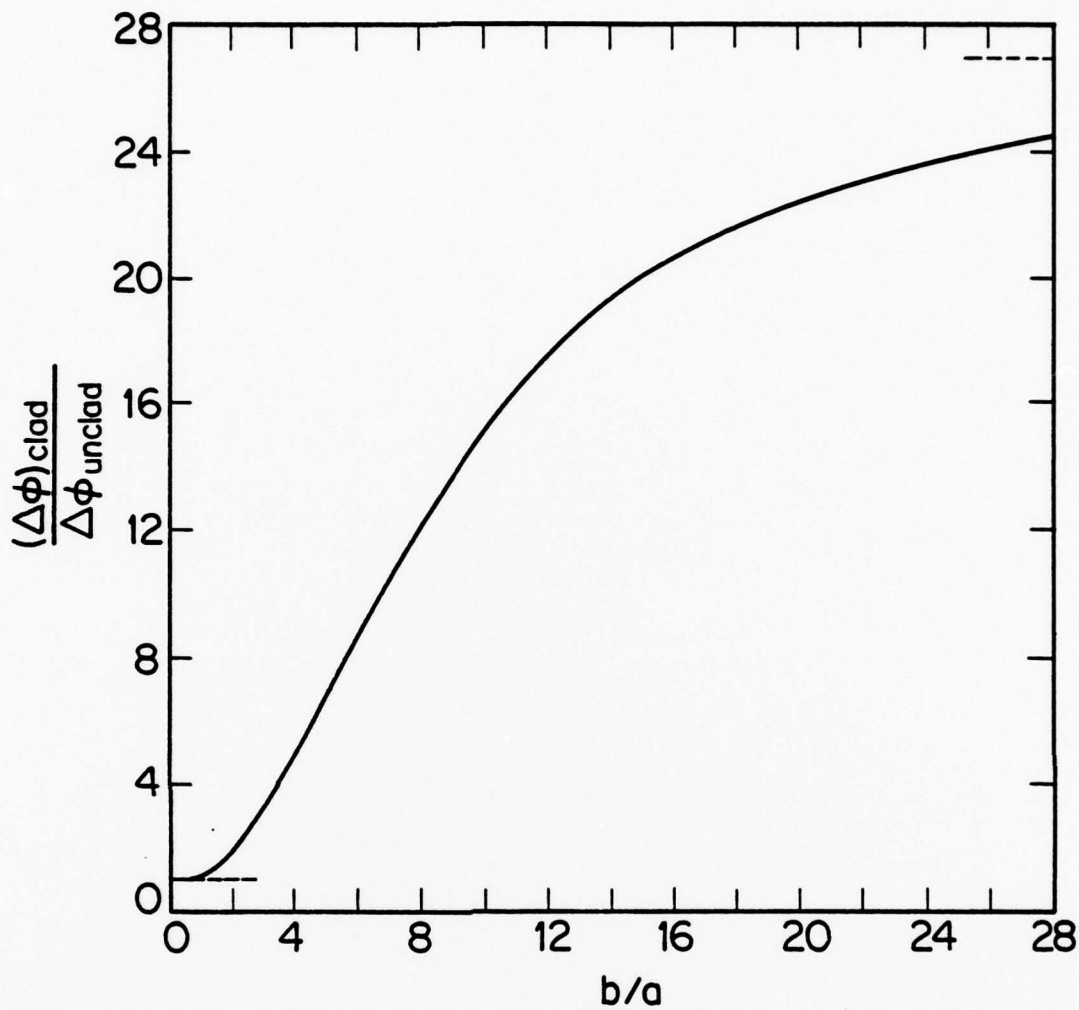


Figure 1. A calculation of  $(\Delta\phi)_{\text{clad}}/\Delta\phi_{\text{unclad}}$  as a function of  $b/a$  for a glass fiber in plastic.

$$\begin{aligned}
 E_g &= 6.2 \times 10^{10} \text{ newtons/m}^2, & v_g &= 0.24, \\
 E_p &= 0.076 \times 10^{10} \text{ newtons/m}^2, & v_p &= 0.458, \\
 p_{11} &= 0.27, p_{44} = 0.075, & n &= 0.46.
 \end{aligned}$$

## APPENDIX

### Exact Solution for q

As discussed in the text, the continuity condition (4) must be imposed. Since  $\varepsilon_\theta = u/r$ , this can conveniently be re-written in the form

$$\varepsilon_{\theta g} \Big|_{r=a} = \varepsilon_{\theta p} \Big|_{r=a} , \quad (A1)$$

or

$$\left[ \frac{\sigma_{\theta g}}{E_g} - \frac{v_g}{E_g} (\sigma_{rg} + \sigma_{zg}) \right] \Big|_{r=a} = \left[ \frac{\sigma_{\theta p}}{E_p} - \frac{v_p}{E_p} (\sigma_{rp} + \sigma_{zp}) \right] \Big|_{r=a} \quad (A2)$$

or, using (5-7) and rearranging

$$\frac{v_p \sigma_{zp}}{E_p} - \frac{v_p \sigma_{zp}}{E_p} = - \frac{2}{(1-f) E_p} p = \left( \frac{(1+f) + v_p (1-f)}{(1-f) E_p} + \frac{1-v_g}{E_g} \right) q . \quad (A3)$$

Now, using (10) to eliminate  $\sigma_{zp}$ , we obtain

$$\frac{(v_p - v_g) \sigma_{zg}}{E_g} = - \frac{2(1-v_p^2)}{(1-f) E_p} p + \left( \frac{(1+v_p)[1+f(1-2v_p)]}{(1-f) E_p} + \frac{1-v_g - 2v_g v_p}{E_g} \right) q \quad (A4)$$

which is a second relation between  $\sigma_{zg}$ ,  $p$  and  $q$ , complementary to (11). The two may be solved simultaneously and there results

$$q = \left[ \frac{2(1-v_p^2)}{(1-f) E_p} - \frac{(v_p - v_g)(1-2v_p)}{f E_g + (1-f) E_p} \right] \frac{p}{B} \quad (A5)$$

$$B = \frac{(1+\nu_p)[1+f(1-2\nu_p)]}{(1-f)E_p} + \frac{1-\nu_g-2\nu_g\nu_p}{E_g} \\ + \frac{2(\nu_p-\nu_g)[(1-f)\nu_g E_p/E_g + f\nu_p]}{fE_g + (1-f)E_p} \quad (A6)$$

A simple limit of this expression, when  $E_p/E_g$  is replaced by zero, is

$$q = \frac{2(1-\nu_p)}{1 + (1-2\nu_p)f} p \quad (A7)$$

For  $\nu_p = 0.458$ , this gives

$$q = \frac{1.084}{1 + 0.084f} p \quad (A8)$$

and suggests that the approximation  $q = p$ , leading to Eqs. (14) and (15), is quite reasonable.

## THREE DIMENSIONAL VLSI DEVICES

G. S. Kino

### ABSTRACT

A proposed design for a three dimensional VLSI device is discussed. The purpose is to obtain a very large number of individual elements without severe requirements on their size, and to minimize the interconnect problem between individual chips.

We propose to lay down silicon by vacuum deposition and laser anneal it, ion implant in and form an LSI circuit. Then a layer of polyimide will be deposited on the Si to form a level surface. This is covered with a thick  $\text{SiO}_2$  layer then a further Si layer which is laser annealed, and used to form a second LSI circuit. The process is then repeated to form a multiple layer device.

In this system, vertical interconnecting bus bars are formed by deposition of metal layers approximately  $20\mu\text{m}$  thick in holes in the  $\text{SiO}_2$  using a lift off technique to form the  $200\mu\text{m} \times 200\mu\text{m}$  connectors.

Heat dissipation in this device is a severe problem. So it would not be expected that very high speed devices could be made in this way. However it would be expected that such

devices would be suitable for large capacity memories or slow speed logic.

## THREE DIMENSIONAL VLSI DEVICES

G. S. Kino

The major limitations on the number of elements in LSI devices are caused by the lower limit on size of an individual element, and by the interconnect problem both on the chip and between chips. Biological systems are not subject to such severe limitations because they are three dimensional rather than two dimensional, so that the number of individual elements in the human brain is many orders of magnitude larger than can be envisaged even in VLSI systems. We suggest that an effort should be made to construct three dimensional semiconductor devices, using elements with a basic size comparable to that or larger than that employed in present day technology, and without trying for the ultimate in speed so as to limit power dissipation. We give here a "blue skies" design which we hope will provide an initial conceptual form of a three dimensional device.

The basic requirement for such a system is a technology for laying down multiple layers of semiconductors, metal interconnecting conductors, and insulators. In addition there must be provision for vertical interconnections or bus bars. We suggest that the basic technique should be to construct normal LSI devices laid down, one on top of the other, with insulation and interconnecting metal bus bars between them. The total

surface area of the device is not much larger than in a standard LSI device, while its volume may be increased many times. Therefore we might expect there to be a power dissipation problem. For this reason, such 3D devices might be expected to be slower than VLSI devices and may require more elaborate cooling techniques, such as the use of liquid coolants.

#### THE SEMICONDUCTOR

We must be able to deposit high quality semiconductor layers on amorphous substrates. It would appear that laser annealing of the type proposed by Gibbons could, in the end, lead to such materials. The silicon would be E beam evaporated onto an amorphous substrate in the form of amorphous silicons and then laser annealed to form a high quality semiconductor layer.

#### THE OXIDES

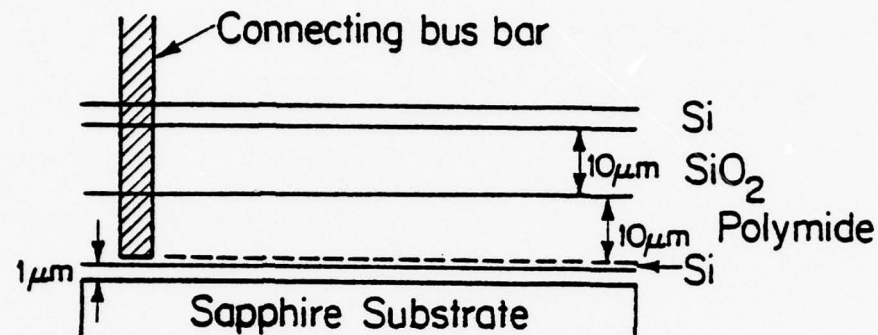
The choice of metals and insulators employed between the layers will dictate to some extent the type of oxide employed. Ideally we would prefer to use a thermal oxide of silicon. However, if the intermediate layers cannot stand the temperatures required and, furthermore, this large volume device is sensitive to thermal cracking, it would be better to use an oxide with a lower deposition temperature. Here the silane process would seem to be appropriate. Perhaps a further improvement in oxide quality near the semiconductor surface would be obtained by an initial thermal oxidation with pulse laser heating in steam, or by pulse laser heating of the silicon once the  $\text{SiO}_x$  layer is formed by silane deposition.

### THE INSULATING LAYERS

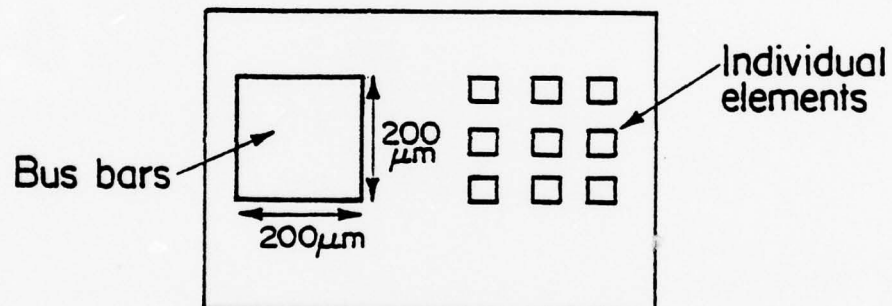
Insulating layers are needed between the various semiconductor layers. These must have level surface so that the next semiconductor layer will be level. Furthermore, they must be several microns thick in order to limit the capacity of the gates and connecting lines on the substrate below them. This would imply that a self-leveling liquid which later solidifies be used for the purpose. The most obvious choice at the moment is probably the use of high polymer plastics such as the polyimides which can withstand temperatures up to 400°C. These would have the advantage that they would have sufficient flexibility to allow for differences in thermal expansion between the different layers of the three dimensional device.

### THE STRUCTURE

We propose a structure of the type shown in Fig. 1. The first semiconductor layer is made by vacuum depositing polysilicon on sapphire. This silicon is then laser annealed, ion implanted and so on, and metal and polysilicon interconnecting leads are deposited to make a conventional LSI structure. Provision is made for vertical metal bus bars several hundred microns in cross-section by vacuum depositing metal in holes cut in the  $\text{SiO}_2$ . These layers are then built up by electroplating to a thickness of the order of  $20\mu\text{m}$  before removing and photoresist. This could also be done by a fast vapor deposition and use of a lift off procedure.



(a)



(b)

Figure 1. (a) Two layers of a 3D VLSI device  
(b) View from the top

A layer of polyimide of the order of  $10\mu\text{m}$  thick is now laid down to provide a flat top surface. On top of this layer, a  $10\mu\text{m}$  layer of  $\text{SiO}_x$  is laid down by silane deposition or by fast sputtering with a magnetron discharge. This is to provide a thermal insulation for the anneal of the next silicon layer, so the polyimide will not be affected by the annealing process. Another layer of silicon is then laid down upon the  $\text{SiO}_2$  layer and the whole process is then repeated.

#### LASER ANNEALING

The thermal conductivity of silicon is approximately 100 times that of  $\text{SiO}_2$  while the specific heat is of the same order. If the front surface of the  $\text{SiO}_2$  is brought to a temperature  $T_0$  as a step function, its back surface temperature becomes

$$T \approx T_0 \text{ erfc} [\ell/2\sqrt{\sigma t/c}]$$

where  $\ell$  is the thickness of the  $\text{SiO}_2$ ,  $\sigma$  its thermal conductivity,  $c$  its specific heat,  $t$  the time after application of the step, and

$$\text{erfc}\xi = 1 - \frac{2}{\sqrt{\pi}} \int_0^{\xi} e^{-y^2} dy$$

The work of Gibbons indicates that with a  $1\mu\text{m}$  thickness of Si the laser beam need only be applied for times of the order of 1 msec to obtain annealing. Calculations based on the model given indicate that it takes only a few microseconds for the temperature through the  $1\mu\text{m}$  layer of Si to become essentially

uniform. So we suggest that the solid epitaxial regrowth phenomenon itself takes a time of the order of 1 msec and that the temperature rise in the Si is basically uniform in the top layer, but only becomes large enough after 1 msec to allow annealing.

It follows that because the specific heat of the  $\text{SiO}_2$  is comparable to that of the Si its thermal capacity is ten times higher, so that its temperature cannot reach much more than 1/10 of that of the Si if the laser is only incident on the Si for 1 msec. It also follows from the thermal diffusion analysis that, in fact, the temperature of the  $\text{SiO}_2$  rises relatively slowly at its back surface because the thermal conductivity of the  $\text{SiO}_2$  is so poor. Hence, it would appear to be reasonable to assume that the polyimide layer will not be affected by the annealing process.

#### THERMAL PROPERTIES OF THE 3D DEVICE

The device itself has intermediate layers of  $\text{SiO}_2$  and polyimide with poor thermal conductivity. However, these layers are only  $10\mu\text{m}$  thick, while normal semiconductor substrates are normally  $300\mu\text{m}$  thick. We might therefore assume that the thermal properties of even a multiple layer device will not be too drastically affected by these intermediate layers. On the other hand, the packing density of the devices is now very large. So we would expect that even with liquid cooling, only relatively low speed devices could be constructed. However, such devices could be useful for large scale memories as well as for lower speed logic operations.

ACKNOWLEDGEMENT

This research was supported by the Defense Advanced Research Projects Agency of the Department of Defense under Contract No. MDA903-76C-0250 with The University of Michigan.

A PROPOSED TECHNIQUE FOR MEASUREMENTS OF IMMINENT  
FAILURES IN CERAMIC TURBINES IN OPERATION

G. S. Kino

During operation ceramic turbines are rotating at 60,000 rpm. When faults develop, the blades shatter and it is very difficult to obtain any useful information on the cause of the problem. We suggest here a simple optical technique for observing the development of flaws while the system is in operation.

The ceramic parts are normally operating at high temperature, so they are emitting visible light. Normally under such conditions, because of the change in heat distribution around a crack, surface cracks in a hot ceramic can be clearly seen. We therefore suggest the use of a high speed moving mirror streak camera for observation of the blades and rotor in the turbine, as well as the use of simpler photography for observation of the fixed parts of the structure.

The engine housing is, of course, not normally transparent. However, it should be possible to use small sapphire windows let into the housing to carry out the observations. Suppose we require a definition of  $d_s = 50\mu\text{m}$  from a distance  $Z = 3\text{cm}$ . The diameter  $D$  of the aperture required is then given by the relation  $d_s = \frac{Z\lambda}{D}$ . For  $\lambda = 0.5\mu\text{m}$ ,  $Z = 3 \times 10^4\mu\text{m}$ ,  $d_s = 50\mu\text{m}$ ,

$D = \frac{3 \times 10^4 \times 5 \times 10^{-1}}{50} = 300 \mu\text{m}$ . So the window required in the housing would only be of the order of 1mm. By scanning with a moving mirror one could hope to observe a region of the order of 3cm square. However, with a larger window the problem of observation would become far simpler.

Acknowledgement

This research was supported by the Defense Advanced Research Projects Agency of the Department of Defense under Contract No. MDA903-76C-0250 with The University of Michigan.

## COVALENT BONDED MATERIALS

R. L. Coble

The recent emphasis on sintering and hot pressing of covalent materials (silicon carbide, silicon nitride, sialons) and the development of high density products from each has given a self-consistent rationale for the processing requirements in these systems. First, that a coarsening inhibitor must be present. Secondly, a sintering aid must be present.

The properties of elemental silicon or germanium show one feature that distinguishes these from ionic solids: the lattice diffusion coefficients are very low at temperatures just below their melting temperatures ( $10^{-11} \text{ cm}^2/\text{sec}$ ) for germanium and that the relative vapor pressures are high in comparison to metals or ionic materials. Thus neck growth and coarsening by vapor transport is reasonable to expect in these relative to lattice transport which could produce densification. Similarly, control of the oxygen pressure in order to suppress vapor transport (through  $\text{SiO}$ ) for the silicon containing ceramic is readily understandable. In the absence of data on boundary diffusion the requirement that sintering aids be included can also be accepted on the basis of the low lattice diffusion coefficients. More basic data are needed on the influences of dopants on all of the fundamental parameters: surface energies,

grain boundary energies, interfacial energies as well as on the transport coefficients, surface reaction coefficients and modifications in the vapor pressures.

For ionic materials the general status is: they are readily sinterable if a suitable small particle size is utilized, if agglomeration is avoided and a grain growth inhibitor to suppress discontinuous grain growth is included. We have no rationale to understand the selection of suitable dopants. A systematic study of the influence of dopants on grain boundary diffusion and on the rates of grain growth provide the best basis to advance our understanding in this area while serving technology requirements as well.

#### Acknowledgement

This research was supported by the Defense Advanced Research Projects Agency of the Department of Defense under Contract No. MDA903-76C-0250 with The University of Michigan.

## DESIGN OF HIGH CURRENT BRUSHES

J. L. Margrave

The design parameters for high-current brushes materials include high electrical conductivity, stability at elevated temperatures, low frictional coefficient and wear rate, mechanical strength and fatigue resistance, oxidation resistance, and various other surface properties. Among the prototype brushes recently prepared and studied at Westinghouse<sup>1</sup> are silver-graphite brushes of various compositions (55-85 weight per cent Ag); copper-graphite brushes of various compositions (55-85 weight per cent Cu) and metal-coated carbon fiber brushes (Ag-Ni and Cu-Ag-Ni coatings on graphite fibers) metal-coated powders of pleophilic and phosphate-impregnated graphites were studied as well as with dichalcocide additives ( $\text{MoS}_2$  or  $\text{NbSe}_2$ ) to see if brush performance was enhanced.

Also, brush operations were studied in moist and dry  $\text{CO}_2$ ; in moist and dry helium or argon; in moist and dry nitrogen; and in  $\text{CO}_2$  or He or Ar or  $\text{N}_2$  atmospheres to which small amounts of hydrocarbon vapors have been added, these gases are intended to transport airborne brush debris out of the brush-rotor interface and thus, to minimize wear and prevent short circuits, as well as to minimize arcing and electrical erosion.

It would appear that further improvements of the performance of high current brushes could be achieved by:

- (1) Operation in an SF<sub>6</sub>-atmosphere to suppress arcing.
- (2) Use of fluorocoated fibers to provide self-lubrication by "CFX" as well as enhanced metal-graphite bonding.
- (3) Use of fluorocoated graphite powders in the sintered metal-graphite composites to provide self-lubrication as well as enhanced metal-graphite binding.

The introduction of fluorinated graphite, "CFX" would take advantage of the well-known thermal stability and lubricant properties of this material<sup>2</sup> while improving the metal-fiber or metal-powder surface interactions and minimally affecting the conductivity. Another advantage of CFX-additives over MoS<sub>2</sub> additives in practical service is the decomposition of CFX to form C (or CO<sub>2</sub>) + CF<sub>4</sub> which are stable and non-corrosive even in humid atmospheres.

#### References

1. "Advanced Current Collection Research," Annual Report, February 28, 1978, Contract N00014-76-C-0683, ARPA Order No. 3153, Westinghouse Electric Corporation, R&D Center, Churchill, Pennsylvania 15235.
2. (a) P. Kamarchik and J. L. Margrave, J. Therm. Anal. 11, 259 (1977).  
(b) P. Kamarchik and J. L. Margrave, Accts. Chem. Res., October 1978.

A CHEMICAL INTERPRETATION  
OF THE EFFECT OF OXYGEN ADDITIONS TO  $\text{CF}_4$  IN PLASMA-ETCHING  
OF SILICON, SILICON OXIDES OR SILICON NITRIDES

J. L. Margrave

It has been unequivocally established that etch rates of silicon, silicon dioxide or silicon nitride in an RF-plasma containing  $\text{CF}_4$  are greatly enhanced by the addition of  $\text{O}_2$  in small percentages.<sup>1, 2, 3, 4, 5</sup> Actually, the enhancement is found with increasing oxygen partial pressure up to a point, and then the rate decreases.

Previous experiments have utilized microbalance weight loss measurements, visible and near ultraviolet spectroscopy, Auger spectroscopy, ESCA and mass spectroscopy of the effluent gases in efforts to understand and interpret the mechanism of plasma etching.<sup>6</sup> A combination of ion bombardment processes, ion-molecule reactions and neutral atom-molecule reactions is required to explain how plasma etch rates can be reduced or enhanced by factors of 10 or more by the use of additives like  $\text{H}_2$ ,  $\text{CH}_3\text{F}$ ,  $\text{H}_2\text{O}$  or  $\text{O}_2$ .

An argument which fits currently available data states that hydrogen-containing additives will suppress etch rates by reducing the concentrations of reactive F-atoms or  $\text{F}_2$  through formation of the very stable HF-molecule. In contrast, etch

rates for  $\text{CF}_4/\text{O}_2$  mixtures are greatly enhanced because of the possibility of forming the very stable bonds in  $\text{CO}$  and/or  $\text{CO}_2$  and leaving the fluorine to form  $\text{COF}_2$  or some other reactive intermediate like triplet  $\text{CF}_2$  or even negative ions like  $\text{F}^-$ ,  $\text{F}_2^-$ , or  $\text{CF}_2^-$ .

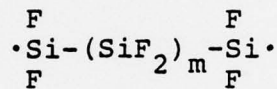
Current literature strongly invokes  $\text{COF}_2$  (or  $\text{COF}$ ) as the reactive oxyfluoride species, mainly on the basis of mass spectrometric studies<sup>2,5</sup> which showed mass 66 ( $\text{COF}_2$ ) and mass 47 ( $\text{COF}$ ) in direct sampling of  $\text{CF}_4/\text{O}_2$  plasmas operated in an  $\text{Al}_2\text{O}_3$  tube to eliminate any possible source of the coincident mass species  $\text{SiF}_2$  (mass 66) and  $\text{SiF}$  (mass 47). Transport of active fluorinating species for distances of 10-25 cm has been observed and attributed to  $\text{COF}_2$ .  $\text{CF}_2$  is ignored on the basis of an early report of a short lifetime in a  $\text{CF}_4$ -discharge.<sup>7</sup> Actually, an appreciable steady-state concentration of  $\text{CF}_2$  can be built up and optical spectra of  $\text{CF}_2$  from such plasmas have been recorded.<sup>3</sup> It is somewhat inconsistent for  $\text{COF}_2$  to play a major role as the fluorinating agent in such plasmas when its thermal decomposition occurs at relatively low temperatures.<sup>8</sup>

Even if  $\text{COF}$  and  $\text{COF}_2$  account for mass spectral peaks at masses 47 and 66 from  $\text{CF}_4/\text{O}_2$  plasmas, it is certain that  $\text{SiF}$  and  $\text{SiF}_2$  are formed in appreciable quantities when the fluorinating etchant reaction occurs. The arguments that were used to eliminate  $\text{SiF}/\text{SiF}_2$  as plasma species when an RF-plasma is formed from  $\text{CF}_4/\text{O}_2$  in the presence of  $\text{Si}$  or  $\text{SiO}_2$  have ignored the extensive mass spectrometric studies of the  $2\text{SiF} \rightleftharpoons \text{SiF}_2 + \text{Si}$  equilibrium.<sup>9</sup>

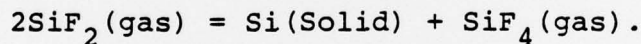
Furthermore, the reports of  $\text{Si}_2\text{F}_6$  and  $\text{C}_2\text{F}_6$  as products in the effluent gases are best explained by the insertion reactions.<sup>10</sup>



In summary, divalent fluorides of silicon and carbon are undoubtedly generated in  $\text{CF}_4/\text{O}_2/\text{SiF}_4$  plasmas and these "carbenes" are known to be stable and long-lived.<sup>7,9</sup> For example,  $\text{SiF}_2(\text{g})$  has a half-life of several minutes in  $\text{SiF}_2/\text{SiF}_4$  mixtures at pressures of 10-20 torr.<sup>9</sup> Gaseous dimers ( $\text{SiF}_4$ ) are not known but low-temperature condensates contain paramagnetic diradical species:



At elevated temperatures, the  $\text{SiF}_2$  molecule either reacts with  $\text{O}_2$  to form  $\text{SiOF}_2$  and similar species or disproportionates:



The  $\text{CF}_2$ -analog can form stable polymers, but also these species undergo thermal disproportionation and/or oxidation.

#### Acknowledgement

This research was supported by the Defense Advanced Research Projects Agency of the Department of Defense under Contract No. MDA903-76C-0250 with The University of Michigan.

### References

1. (a) Adir Jacob, U.S. Patent No. 3,795,557, March 1974.  
(b) Adir Jacob, Solid State Technology \_\_\_, 70-73, September 1976.
2. Horiike and M. Shibagaki, Japan J. Appl. Phys. 15, suppl., 13 (1976).
3. W. R. Harshbarger, R. A. Porter, T. A. Miller and P. Norton, Appl. Spect. 31, 201 (1977).
4. G. B. Bunyard and B. A. Raby, Solid State Tech. \_\_\_, 53, December, 1977.
5. H. F. Winters, J. W. Coburn and E. Kay, J. Appl. Phys. 48, 4973 (1977).
6. J. W. Coburn, H. F. Winters and T. J. Chuang, J. Appl. Phys. 48, 3532 (1977).
7. (a) P. Venkateswarlu, Phys. Rev. 77, 676 (1959).  
(b) See also F. Modica,
8. Janaf Tables, D. R. Stull, Ed., Dow Chemical Company, Midland, Michigan, Table \_\_\_, 19\_\_.
9. (a) T. C. Ehlert and J. L. Margrave, J. Chem. Phys. 41, 1066 (1964).  
(b) P. L. Timms, R. A. Kent, T. C. Ehlert and J. L. Margrave, J. Am. Chem. Soc. 87, 2824 (1965).
10. (a) P. Wilson and J. L. Margrave, Accts. Chem. Res. \_\_\_, (197\_\_).  
(b) D. Perry and J. L. Margrave, J. Chem. Ed. 53, 696 (1976).

EXTENSION OF FIBER SENSOR RESPONSE TO EXTREMELY HIGH FREQUENCIES

H. Winsor

ABSTRACT

Fiber sensors are not limited to sensing signals whose period is large compared to the transit time of the signal through the fiber. Simple geometry variations suffice to extend their frequency response to arbitrarily high frequencies. These geometries are not likely to be important for some time.

## EXTENSION OF FIBER SENSOR RESPONSE TO EXTREMELY HIGH FREQUENCIES

H. Winsor

The effects of the finite velocity of light on the frequency range over which a fiber optic acoustic sensor can be used was modelled in one of the viewgraphs presented in the FOSS briefing. The conclusion drawn was that the time for the light to pass through the fiber must be less than the period of the acoustic wave detected. It was also stated that the active length of the fiber sensor must be contained within a distance small with respect to an acoustic wavelength in order to be simultaneously insonified by the peak amplitude of the wave. The simple combination of these two effects leads to placing restrictions on the size and length of fiber optic sensors which are too restrictive. A considerably wider range of geometries is available as discussed below.

Consider first a straight fiber of length  $l$  as shown in Figure 1. Sound is incidental from a direction normal to the fiber. The acoustic amplitude is seen by a short pulse of light started at one end of the fiber at  $t = 0$ . The complex amplitude of the acoustic wave is  $A = A_0 e^{-i\omega At}$ . The acoustic pressure at any time,  $t$ , is the real part of  $A$ . The position of the pulse of light at time  $t$  is  $(\frac{C}{n}t, 0)$  where  $n$  is the index of refraction.

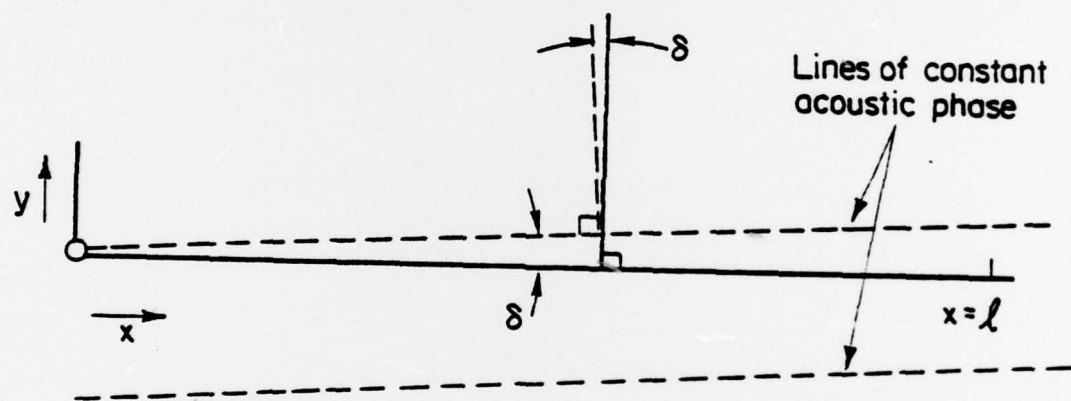


Figure 1.

At this position, the phase of the acoustic wave is  $\omega_A t = \omega_A \frac{nx}{c}$ . For normal incidence, we can see that a length of fiber given by

$$l_{2\pi} = \frac{2\pi c}{\omega_A n} \quad (1)$$

will cause the light pulse to sample an entire cycle of the acoustic wave. If the fiber is now tilted an amount  $\delta$  with respect to the acoustic wavefront, the position of the light pulse at time  $t$  is given by

$$(x, y) = \left( \frac{c}{n} t \cos \delta, \frac{c}{n} t \sin \delta \right). \quad (2)$$

The complex amplitude at this point is given by

$$A = A_0 e^{-i \frac{\omega_A n l}{c}} e^{i \omega_A \frac{l \sin \delta}{s}} \quad (3)$$

where  $l = \sqrt{x^2 + y^2} = \frac{ct}{n}$  and  $s$  is the speed of sound in the insonifying medium.

If the terms in the complex exponentials cancel, the traveling light pulse will see constant acoustic phase.

$$\frac{\omega_A n l}{c} = \omega_A \frac{\sin \delta l}{s} \quad (4)$$

or

$$\frac{ns}{c} = \sin \delta. \quad (5)$$

This implies that the fiber will retain optimum sensitivity for higher frequency waves only if they arrive from a distance  $\delta$  off the normal direction of the fiber. The spatial sense of the deviation in angle of arrival ( $\delta$ ) must be as shown in Fig. 1,

since the sound wavefront and the light pulse must travel along the optical fiber in the same direction.

To find the acoustic frequencies for which this effect is significant, we back substitute in Eq. (1) for  $\ell_{2\pi} = 10m-10^2m$  as in practical fiber sensors.

$$\omega_A = \frac{2\pi c}{\ell_{2\pi} n} \approx \frac{12 \times 10^5 \text{ km/sec}}{.01 \text{ km}} = 120 \text{ MHz}$$

$$\frac{12 \times 10^5 \text{ km/sec}}{1 \text{ km}} = 1.2 \text{ MHz}$$

If  $\omega_A$  exceeds about 1/10 of these frequencies, a substantial fraction of the light will start to see a lower than maximum pressure amplitude.

These frequencies are clearly in the active sonar frequency range for all currently practical fiber lengths. The angle  $\delta$  is independent of  $\omega_A$  and is about  $7.5 \mu\text{rad}$  for silica fiber in water. The same mechanism can be used to tailor the response of helical fiber sensor geometries to high frequencies arriving from a direction along the axis of the helix. The pitch (P) of the helix will be

$$\frac{P}{\pi D} = \frac{s}{\left(\frac{c}{n}\right)\pi} \approx 2.2 \times 10^{-6}$$

where D is the diameter of the helix.

These corrections are not likely to be of importance for the fiber optic hydrophone application, but they may well be worth considering if acoustic waveguide effects such as G. Kino<sup>1</sup>

has suggested are ever used. The pitch to diameter ratio for acoustic waveguides is about 1 as the speed of sound in the fiber is given by

$$c_f \approx 3c_s .$$

If fiber sensors are used for receiving electromagnetic radiation, the speed of light in the fiber is slower than the speed of light in free space, and the effect can be used only by immersing the fiber in a higher index material. Sensitivity variations, introduced by spatially modulating the coating or field strength, are more likely to be useful in such cases.

#### Acknowledgement

This research was supported by the Defense Advanced Research Projects Agency of the Department of Defense under Contract No. MDA903-76C-0250 with The University of Michigan

#### Reference

1. Acoustic Waveguides for Undersea Acoustic Detectors and Transmitters (1978 MRC Proceedings).

FIRST PRINCIPLES BAND THEORETIC AND PAIR POTENTIAL

CALCULATIONS OF THEORETICAL TENSILE STRESS

H. Ehrenreich

ABSTRACT

Two ab initio calculations of the theoretical tensile strength of an ideal crystalline metal (fcc Cu) done in collaboration with A. E. Carlsson, E. Esposito, and D. C. Gelatt (Harvard University) are presented. The first employs a full band-theoretic approach to compute the cohesive energy as a function of uniaxial lattice deformation. The second uses a new, non-empirical pair potential  $\phi$  that can be expressed formally in terms of the cohesive energy  $E$  and can be evaluated if  $E$  as a function of the interatomic distance  $r$ , is known. No experimental inputs are required. In the present case the necessary information is obtained from self-consistent first-principles band calculations for Cu. The stress-strain curves obtained using these two approaches are in fair agreement. The corresponding theoretical strengths differ by about 35%, but both are consistent with available measurements. Computed elastic constants are in satisfactory agreement with experiment in both cases.

AS TECHNOLOGIES APPROACH THEIR LIMIT

E. W. Montroll

ABSTRACT

As technologies approach their limits, increased operating costs, increased manufacturing costs, increased development costs, and increased failure rates are experienced. A qualitative analysis is presented on a diverse set of technologies ranging from naval architecture to accelerated design in computer construction.

An elementary mathematical model is presented to summarize the data.

THE RELATION BETWEEN IMAGING, TOMOGRAPHY  
AND FAR FIELD INVERSION TECHNIQUES

G. S. Kino

ABSTRACT

We have analyzed the relation between the inversion techniques used in the NDE field by Bleistein and others, acoustic imaging and tomographic techniques of the type used in the medical field. By using as an example the two-dimensional system consisting of a line reflector, it is shown that imaging with a narrow band signal is equivalent to the Bleistein method taken over a very narrow range of  $k$ . Imaging with pulsed signals is equivalent to a reconstruction with Fourier transform techniques, but weighting the integrals. This type of reconstruction turns out to be entirely equivalent to filtered back projection tomography.

By following these close analogues it is possible to make use of results obtained by any one of these methods. For instance, imaging theory leads to conclusions about the use of narrow apertures and a finite number of sample points. The Bleistein results lead to conclusions on what information is contained in the image in the low frequency limit. Similarly, the use of the mathematical methods developed for tomography

lead to methods for optimizing the pulse shape employed in an imaging system.

At the same time we have classified the reconstruction and imaging techniques. For instance, a synthetic aperture system which uses one element of an array as a transmitter and receiver in turn is equivalent to a bistatic reconstruction. This gives a transverse definition twice as good as that of a system which uses a separate transmitter whose position is fixed. Again, CW systems, such as holographic systems, give good transverse definition but poor range definition. But short pulse systems or wideband reconstruction systems addressing the field of view from only one angle give good range definition and poor transverse definition.